INFORMATION TO USERS

This manuscript has been reproduced from the microfilm master. UMI films the text directly from the original or copy submitted. Thus, some thesis and dissertation copies are in typewriter face, while others may be from any type of computer printer.

The quality of this reproduction is dependent upon the quality of the copy submitted. Broken or indistinct print, colored or poor quality illustrations and photographs, print bleedthrough, substandard margins, and improper alignment can adversely affect reproduction.

In the unlikely event that the author did not send UMI a complete manuscript and there are missing pages, these will be noted. Also, if unauthorized copyright material had to be removed, a note will indicate the deletion.

Oversize materials (e.g., maps, drawings, charts) are reproduced by sectioning the original, beginning at the upper left-hand corner and continuing from left to right in equal sections with small overlaps.

Photographs included in the original manuscript have been reproduced xerographically in this copy. Higher quality 6" x 9" black and white photographic prints are available for any photographs or illustrations appearing in this copy for an additional charge. Contact UMI directly to order.

ProQuest Information and Learning
300 North Zeeb Road, Ann Arbor, MI 48106-1346 USA
800-521-0600

STRESS ANALYSIS OF AN OPTICAL GROUND WIRE

MASOUD ROSHAN FEKR

Department of Civil Engineering
and Applied Mechanics
McGill University, Montreal
December 1999

A Thesis submitted to the Faculty of
Graduate Studies and Research in partial fulfillment
of the requirements of the degree of Doctor of Philosophy

To my parents

" ...And when you have reached the mountain top,
then you shall begin to climb ... "

K. Gibran

ABSTRACT

The main objective of this research was to create a finite element model for detailed three-dimensional stress analysis of an overhead optical ground wire (OPGW) typical of those used in transmission lines. The detailed model considers all possible mechanical effects, such as contact, friction, elongation, torsion, and bending for different end conditions.

The OPGW under study comprises four components: the external layer of fourteen aluminum alloy wires and ten inner aluminum clad steel wires, which are laid over an aluminum tube that houses a five-groove aluminum spacer. The optical fiber units are inserted in the aluminum spacer grooves. Three-dimensional solid elements are used to model the outer wires, the inner wires, and the aluminum spacer. The central aluminum tube is modeled with shell elements with large strain and deformation kinematics. All possible contacts between the components, with and without friction, are considered in the model.

The OPGW is assumed fixed at one end and pulled from the other with a prescribed displacement equivalent to the experimental elongation of 0.61% defined for all components. This elongation is based on the results of experiments carried out at Hydro-Québec's research institute (IREQ), where the cable was subjected to the sustained maximum tension in normal operation (MTNO) of 83.5 kN.

The finite element analysis predicts that the responses of the outer and inner wires are in the linear range, however the aluminum tube and spacer are yielded under the prescribed displacement. Therefore, a multilinear stress-strain law is used in the model. Three-dimensional contact surfaces are defined for contacts between the outer wires, the inner wires, between the outer and the inner wires, between the inner wires and the central tube, and between the central tube and the aluminum spacer. The latter was not observed in the analysis as the gap between the spacer and tube is too large and considering the end conditions specified in the model.

Two scenarios of loading were tested to apply the axial elongation on the wires; either only the central node or all the interior nodes of the wire cross sections are

prescribed a maximum axial displacement. In the two scenarios, the aluminum tube and the spacer cross sections are prescribed the same axial displacement. Two types of finite element meshes are considered for the outer and inner wires. The cross sections of the outer and inner wires are modeled with an 8-sided polygon in the coarser mesh while a 16-sided polygon is used in the finer mesh. The cross-sectional areas of the coarse and fine mesh models are smaller than the real cross sections by 10% and 2.6%, respectively.

Results of the finite element model are compared with those of the experiments performed at IREQ and with the analytical solutions of Machida and Durelli (1973) and Phillips and Costello (1973). The calculated axial forces of the cable in the coarse and fine mesh models are 61% and 70% of those predicted by the analytical solutions, respectively. However, the differences in stresses and strains of the coarse mesh model are in the range of ten percent only from the theoretical solutions. Nevertheless, the stresses and strains in the wires of the fine mesh model are almost identical with those of the analytical solutions. The friction effects on the wires are found negligible in static analysis, although they are a non-negligible source of damping in flexural vibrations. However, the effect of contact with friction between the inner wires and the central tube is significant on the response of the tube.

The effective modulus of elasticity of the finite element model increases with tension. For the maximum elongation, the effective modulus obtained with the coarse and fine mesh models is 62% and 70% respectively of the equivalent modulus of elasticity calculated neglecting all three-dimensional effects. As a result, the elongation of the cable is larger in the finite element model than in the theoretical calculation under the same tension. The central aluminum tube and spacer are yielded after only 36% and 62% of the load level corresponding to the maximum tension in normal operation, respectively. In a transmission line, the plastic deformation of the tube and spacer will be accumulated under periodic loading-unloading cycles, and the optical fibers are inevitably under stress. Therefore, permanent signal attenuation due to induced stresses in the fibers will occur.

This study shows the reliability and significance of using finite element modeling in predicting the detailed response of a complex cable, for which experiments and theoretical solutions are unable to yield complete results.

SOMMAIRE

L'objectif principal de la recherche était de créer un modèle d'éléments finis fiable pour l'analyse détaillée des contraintes dans un câble de garde à fibres optiques (CGFO) typique de ceux utilisés dans les lignes aériennes de transport d'électricité. Le modèle considère tous les effets mécaniques importants tels le contact et le frottement entre les composants, ainsi que l'allongement, la torsion et la flexion pour différentes conditions frontières.

Le CGFO étudié a un diamètre extérieur nominal de 19 mm et compte quatre composants. Une couche métallique externe de quatorze fils en alliage d'aluminium ainsi qu'une couche métallique interne de dix fils en acier enrobés d'aluminium sont toronnés sur un tube en aluminium, lequel loge une entretoise à cinq cannelures, également en aluminium. Les torons de fibres optiques sont insérés dans les cannelures de l'entretoise. Les fils des deux couches métalliques ainsi que l'entretoise sont modélisés à l'aide d'éléments finis solides. Le tube central est modélisé à l'aide d'éléments de coques minces pouvant accommoder des grandes déformations et des grands déplacements. Le modèle considère toutes les forces de contact présentes, avec ou sans l'influence du frottement.

Pour les fins du modèle, on suppose que le CGFO est parfaitement fixe à une extrémité et que l'autre extrémité est soumise à un déplacement uniforme équivalent à un allongement total de 0.61%, soit la valeur maximale mesurée lors d'essais de traction pour homologation. Cet allongement a été obtenu sous une charge de tension totale de 83,5 kN, correspondant à la tension maximale en opération normale (TMON) pour le câble étudié.

L'analyse par éléments finis prédit que le comportement de l'enveloppe métallique (couches de fils externes et internes) se maintient dans le domaine linéaire, alors que le tube central et l'entretoise d'aluminium sont plastifiés au niveau de déformation correspondant à la TMON. L'usage d'une loi constitutive non linéaire s'impose donc

pour ces deux derniers composants. Des surfaces de contact tri-dimensionnelles sont définies entre les fils de la couche externe, entre les fils de la couche interne, entre les fils des couches interne et externe, entre les fils de la couche interne et le tube central, et finalement entre le tube et l'entretoise d'aluminium. Toutefois, aucun contact ne se produit dans le modèle entre le tube central et l'espaceur, étant donné la taille de l'espace vide entre les deux composants et les conditions frontières définies.

Deux scénarios de chargement ont été testés pour imposer le déplacement de l'extrémité libre du modèle. Dans le premier, seuls les noeuds situés au centre de chaque fil de l'enveloppe métallique se voient imposer le déplacement, alors que dans le second, tous les noeuds définis à l'intérieur de la section de chaque fil se voient imposer le même déplacement. Dans les deux scénarios, le même déplacement axial est prescrit pour le tube central et l'entretoise. Deux types de maillage sont également considérés pour modéliser les fils de l'enveloppe métallique. Le maillage du modèle de référence utilise des éléments isoparamétriques solides à 8 noeuds alors que dans le maillage le plus fin utilise des éléments à 16 noeuds. Il en résulte que la section droite du premier maillage est inférieure à la section réelle des fils d'environ 10% alors cette différence n'est que de 2,6% dans le modèle plus fin.

Les résultats de l'analyse sont comparés aux mesures expérimentales faites à l'IREQ (Institut de recherche en électricité du Québec, Hydro-Québec) et aux solutions analytiques pour câbles toronnés standards publiées indépendamment en 1973 par Machida et Durelli et par Phillips et Costello. La force axiale totale obtenue par l'analyse par éléments finis est inférieure à celle prédite par les solutions théoriques, dans une proportion de 61% et 70%, selon qu'on réfère aux résultats obtenus avec le maillage de référence ou plus fin. Toutefois, les différences entres les contraintes et déformations de l'enveloppe métallique du modèle et celles des solutions analytiques sont inférieures à 10% pour le maillage de référence et, à toutes fins pratiques, les résultats du maillage fin et des solutions analytiques sont identiques. Les effets du frottement entre les fils sont par conséquent jugés négligeables sur la réponse statique des fils eux-mêmes. À noter que le frottement est toutefois une source importante

d'amortissement interne du câble en vibrations flexionnelles. Par contre, l'effet du contact et du frottement entre la couche interne de fils et le tube central est très significatif sur le comportement du tube.

Le module d'élasticité équivalent du câble, évalué à partir des résultats de force et d'allongement du modèle d'éléments finis, augmente avec la tension axiale dans le câble. Pour l'allongement maximum spécifié de 0.61%, le module équivalent obtenu respectivement pour le maillage de référence et le maillage fin, est de 62% et 70% de la valeur théorique calculée en négligeant les effets tri-dimensionnels de la réponse. Pour une force de tension donnée, le modèle d'éléments finis prédit donc un allongement plus grand qu'un calcul théorique. L'analyse par éléments finis prédit également la plastification du tube central et de l'entretoise à des niveaux d'allongement du câble qui ne correspondent qu'à 36% et 62% respectivement de l'allongement obtenu en condition TMON. Dans les conditions réelles d'une portée suspendue, la plastification du tube et de l'entretoise s'accumule sous l'effet des cycles périodiques de chargement et de déchargement, et les fibres optiques sont inévitablement sous contrainte résiduelle. Il en résulte un affaiblissement permanent et irréversible du signal.

En conclusion générale, l'étude démontre la fiabilité et la pertinence de la méthode des éléments finis pour prédire la réponse détaillée d'un câble de section complexe, ce qui n'est pas possible actuellement ni par les techniques expérimentales ni par les solutions théoriques connues.

ACKNOWLEDGMENTS

First and foremost, I want to thank God, the almighty, for the faith, knowledge and health he has blessed me with.

I would like to express my sincere gratitude and appreciation to my supervisors, Professor Ghyslaine McClure and Professor Masoud Farzaneh (University of Québec at Chicoutimi), for their guidance, continual interest and encouragement throughout the course of this work. I am particularly indebted to Professor Ghyslaine McClure for her valuable support, invaluable suggestions, long discussions and understanding to the student life.

I would like to acknowledge the contributions of Mr. Stephan Banville (Phillips Fitel) and Mr. Pierre Guilbault (Hydro-Québec, IREQ) in providing the data and experimental results. The experiments performed at McGill University by Mr. Marek Przykorski, and the ADINA support line, Dr. Pavel Bouzinov, in particular are also greatly appreciated.

The financial assistance provided by Le Fond pour la Formation de Chercheurs et l'Aide à la Recheche (Fonds FCAR) in the form of a team grant, by the industrial chair on atmospheric icing of power network equipment NSERC/Hydro-Québec/UQAC (CIGELE), and by the McGill Emil Nenniger Fellowship (1997) are greatly appreciated

I would also like to thank my fellow students and the staff in the Department of Civil Engineering and Applied Mechanics at McGill University, in particular, Dr. Robert William Cook, the computer system manager, for providing diligent assistance.

I wish to express my gratitude to my family, particularly my parents for their moral support, encouragement, and patience.

TABLE OF CONTENTS

CHAPTER THREE

ANALYTICAL SOLUTIONS

CHAPTER FOUR

NUMERICAL MODELING

CHAPTER FIVE

RESULTS AND DISCUSSION

APPENDIX II

LABORATORY TESTS

LIST OF SYMBOLS

A	cross-sectional area of a cable
A_h	cross-sectional area of a helical wire
A_c	cross-sectional area of a core wire
$\mathbf{B}^{(m)}$	strain-displacement matrix at time t
C_h	Contact compliance between a helical wires and a compliant layer
CFORCE	norm of contact force increment between two iterations
CFNORM	contact force norm
c	subscript to denote core wire
d_c	diameter of a core wire
d_h	helical wire diameter
E	modulus of elasticity
E_h	Young's modulus of a helical wire
E_o	Young's modulus of optical fibers
$\mathbf{F}$	nodal point forces vector at time t
F_c	contact force acting on a helical wire
F_{hc}	contact force exerted by the compliant layer on a helical wire
F_R	radial force per unit length of a wire
F_T	tangential force per unit length of a wire
f_F	friction force per unit length of a helical wire
f_{cF}	frictional force per unit length on a core with no slip between wires
f_{cAF}	frictional force per unit length on a core in the direction parallel to the wire axis with no slip between wires
f_{cTF}	frictional force per unit length on a core in the direction tangential to the wire axis with no slip between wires
f_{hF}	frictional force per unit length on a helical wire with no slip between wires
f_{hAF}	frictional force per unit length on a helical wire in the direction parallel to the wire axis with no slip between wires
f_{hTF}	frictional force per unit length on a helical wire in the direction tangential to the wire axis with no slip between wires
g	gap between two surfaces
H	horizontal tension
h	subscript to denote helical wire

h	length of a strand
I_h	second moment of area of the cross section of a helical wire
J_h	polar moment of inertia of the cross section of a helical wire
$\mathbf{K}$	stiffness matrix
K_n	cable axial rigidity in the non slipping part
L_T	transitional length adjacent to strand termination
l	length of a helical wire
M_c	twisting moment acting on a core wire
M	bending moment in a wire
M_b	bending moment in the plane of cable cross-section
M_b^h	component of internal moment resultant in b (binormal) direction
M^t	twisting moment in a wire
M_t^h	component of internal moment resultant in t (tangential) direction
M_t	total axial twisting moment acting on wires
m	number of helical wires in a strand
m_f	distribution friction torque
N_b^h	component of internal force resultant in b (binormal) direction
N'	component of the shearing force on a wire
$\mathbf{n}$	unit normal vector
P	axial load
P_h	axial load acting on a helical wire
P_n	interwire distributed force in the normal direction
p	pitch length of a helical wire
Q	contact force per unit length between two adjacent wires
R	radius of a cylinder on which the center line of a helical wire lies
$\mathbf{R}$	load vector
R'	deformed radius of a cylinder on which the center line of a wire lies
RCONSM	reference contact force level
RCTOL	contact force convergence tolerance
RESFAC	response smoothing factor
r_h	radius of a helical wire
STOL	user-input line search convergence tolerance
S_1	torsional stiffness of a core wire
S_2	axial stiffness of a core wire
S_3	bending stiffness of a helical wire
S_4	torsional stiffness of a helical wire

T_h	internal tension in a helical wire
t	aluminum tube thickness
t	tangential contact traction component
U	displacements vector
$\dot{u}$	tangential velocity
$^tV^{(m)}$	Volume of a body at time t
w	weight per unit length
X	nodal coordinate
X_c	contact force per unit length acting along the line of contact
X_h	external force components per unit length of a wire in the x direction
Y_h	external force components per unit length of a wire in the y direction
Z_h	external force components per unit length of a wire in the z direction
$\Delta\alpha$	change in helix angle of a wire
$\Delta\varphi_2$	change in twist per unit length of an inner wire
$\Delta\kappa'_2$	change in curvature of an inner wire
α	helix (lay) angle of a helical wire
α'	deformed helix angle, final angle between the tangent to the center line of a helical wire and the plane normal to the axis of the helix
β	contact angle
$\beta^{(i)}$	acceleration factor
δS_e	cable elastic extension
δ_x	cable axial displacement
ε	normal strain, axial strain of the strand
ε_E	energy tolerance (ETOL)
ε_h	axial strain of a helical wire
ε_N	parameter used in constraint function
ε_T	parameter used in frictional constraint function
ϕ_c	rotation per unit length of a core wire
γ	normalized rotation of one pitch length of the strand ($\Delta/2\pi$)
η	nonlinearity parameter
φ_h	angle of twist per unit length of a helical wire (in t direction)
κ_h	center line component of curvature of a helical wire in n direction
κ'_h	center line component of curvature of a helical wire in b direction
λ	normal contact traction components
μ	coefficient of static friction
ν	Poisson's ratio

$\bar{\nu}$	Poisson's ratio of a compliant layer
ρ	radius of curvature of the helical wire axis
ρ'	deformed radius of curvature of the helical wire axis
σ_b	bending stress
σ_c	normal stress in the wire core
σ_{Pl}	principal stress
σ_Q	maximum compressive stress due to contact
σ_t	average normal stress
σ_o	axial stress in outer wires
τ	shear stress
${}^t\tau^{(m)}$	stress matrix at time t

LIST OF TABLES

LIST OF FIGURES

1

INTRODUCTION

1.1 General

Overhead ground wires with optical fibers (OPGW) are being used widely in transmission lines. They have two functions: their primary function is to protect the line conductors electrically against lightning, while optical fibers incorporated in the core of the cable serve as telecommunication lines for automatic control of the transmission network. The traditional ground wire is composed of several galvanized steel strands that carry the cable self-weight and environmental loads (ice, snow, wind, and changes in temperature). On some power lines, the traditional ground wires have been replaced with ground wires carrying optical fibers that are protected inside the cable core. In most cable constructions, the optical fibers are enclosed in the core of the cable and are designed to be stress free or to resist only low stresses under normal operation loads.

The structure of optical fiber cables typically consists of several fiber optics arranged in ribbons or strands, which are either tightly or loosely inserted into

helically shaped slots on a spacer. The relative looseness of the fibers is created by the extra length of the fibers compared to that of the cable. The large diameter of the slots with respect to the diameter of the fiber ribbons or strands provides space for the additional length of the fibers, which is also referred to as *excess length* or *over length*. Due to compatibility of strains and displacements, the optical fibers will not experience any elongation and axial stresses until the cable extension exceeds the fiber over length.

The mechanical reliability of optical fibers needs to be assessed as excessive strains resulting from axial deformations (and or curvatures) cause signal degradation or attenuation. Several mechanical studies have been done on isolated optical fibers but not on fibers in cables. The difficulty is to understand and model the mechanical behavior of these cables of complex construction under a variety of loads. Experimental work supporting these analytical and numerical models is also necessary. Due to technological limitations, experimental testing alone is insufficient to fully characterize the mechanical response of each cable component. Therefore, reliable numerical models for stress analysis are needed. Three-dimensional modeling is necessary because of the complexity of the interaction between the components of the transverse direction (cross section), longitudinal direction, and the boundary conditions. Contact among the different components, i.e., between the outer wires, the inner wires, the outer and inner wires, the inner wires and the tube, and the tube and the aluminum spacer, needs to be properly accounted for in the stress analysis. In these contact problems, the effects of friction also have to be examined.

The proposed research is original since at present there is no reliable stress analysis model to predict the detailed mechanical response of optical fibers in optical ground wires. It is a complex problem that requires a thorough understanding of the interaction between the geometrical effects (fiber over length, depth and shape of slot of central core, lay angle of various components) and the friction amongst the different components in contact. It is worth noting that the present research and development approach used by cable manufacturers is almost exclusively experimental and limited to specific types of cables. It is believed that this research will prove directly useful for the mechanical design of optical ground wires.

1.2 Problem definition

As stated in the introduction, the reliability of ground wires with optical fibers must be properly evaluated. This evaluation relies on two components: 1) the characteristics of climatic and other loads that affect the transmission lines in general, and the OPGW in particular and 2) the mechanical response of the OPGW under the loads, i.e., the stresses and deformations of different components of the cable (metallic cover, central core, fibers) resulting from the applied forces.

Hydro-Québec has invested considerable resources in the characterization of the climatic loads on transmission lines for the last twenty years, and probabilistic models are known. On contrast, the mechanical response of OPGW is less understood and cannot be extrapolated directly from available data on traditional cables (conductors or ground wires). The present approach used by Hydro-Québec to characterize the behavior of OPGW is exclusively experimental. Although experimental studies are necessary, their conclusions are often limited to the parameters and types of experiments being carried out and are therefore difficult to generalize or extrapolate. Numerical modeling is therefore considered essential to pursue the assessment of the mechanical reliability of OPGW.

The complex cross section of an OPGW with its several different components (aluminum-clad steel wires, aluminum alloy wires, tube and spacer, and optical fibers) makes it difficult to understand its behavior under various types of loading. The OPGW investigated in this study is made by Phillips-Fitel and used widely by Hydro-Québec (see Figure 1.1).

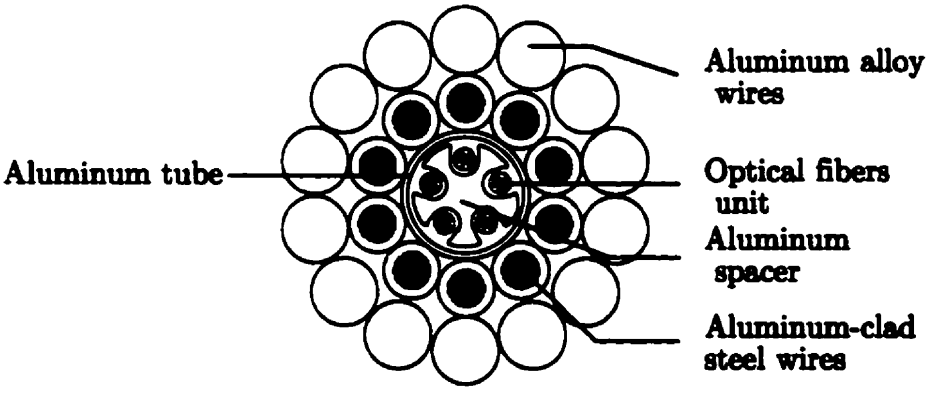

Figure 1.1 Cross-section of the 19-mm OPGW used by Hydro-Québec

Its external diameter is 18.94 mm and the outer layer is made of 14 aluminum alloy wires whose function is mainly to dissipate the electrical current generated by a lightning strike. The inner layer is made of 10 aluminum-clad steel wires that act as the main structural part. The core is composed of a 6.5 mm diameter aluminum tube, which encloses the optical fiber strands that are inserted in the grooves of an aluminum spacer.

1.3 Research objective and scope

The objective of this research is to model the mechanical behavior of a particular construction of optical ground wire (OPGW) used in overhead transmission lines, using the finite element method, in order to predict the state of stresses and deformations in each component of the cable and ultimately in the optical fibers, in view of estimating the opto-mechanical reliability of the cable under normal operation loads. The ADINA (1999) software was selected because of its proven efficiency in solving complex nonlinear contact problems (Bathe et al. 1999, Roshan Fekr et al. 1999).

1.4 Methodology

The research program is carried out mainly in finite element modeling of the OPGW, in the following stages:

- Three different lengths of cable segment are analyzed to limit the size of the model and to obtain the minimum/optimum length of the cable for numerical efficiency and accuracy. One, two, and three pitch lengths of only one inner wire are modeled with the central tube. A comparison of the stress and strain variations along the cable axis of the three models allows the appropriate length selection. It is noted that these models are incapable of representing the responses of the full OPGW, since the effects of the neighboring wires are neglected. However, they can be indicative of pitch length effects.
- Only one layer of the OPGW (all the inner wires and the central tube) is modeled with and without friction effects. Two different loading cases are adopted to induce elongation in the cable when only the wires are subjected to a prescribed displacement; 1) either at their central node or 2) at all the interior nodes of the wire cross sections. In this case, the tube remained unloaded in order to verify the effects of contact between the wires and the tube. The effects of friction are also considered in the model. A distributed

tensile force on the cross section and a concentrated force at the central nodes of the wires and tube were also considered, however, due to displacement compatibility between the components, the displacement-control approach is finally used.

- The inner-wire-and-tube model is studied where all components of the cable (inner wires and the tube) are assigned a prescribed axial displacement with and without the effects of friction. Both the wires and the tube are subjected to a compatible axial strain of 0.61%.
- The OPGW model is completed by adding the outer wires and the aluminum spacer to the previous model. Once again, two cases are considered; 1) when all the interior nodes of the wires are subjected to a prescribed displacement and 2) when only the central wire nodes are subjected to this same displacement. In both cases the aluminum spacer and the central tube are subjected to the same compatible displacement. The effects of friction are also included. It is worth noting that the initial gap between the aluminum spacer and the central tube is too large to produce contact when subjected to axial displacement; therefore, the aluminum spacer can be modeled separately.
- To validate the finite element mesh and the type of element selected for the wires (8-node 3-D solid element), a finer mesh with the same element is used. Two other types of elements (20- and 27-node 3-D solid) were also used to verify the accuracy of the 8-node element. The 20-node element model is used for the complete OPGW. However, the 27-node is only used in the inner-wire-and-tube model due to limitations in computational resource. Results of 20- and 27-node models are not presented in details.
- The theoretical solutions by Machida and Durelli (1973), Phillips and Costello (1973), and Costello (1997) are modified for the OPGW. The modification is carried out mainly to include the effect of the central tube as both analytical solutions consider a central wire instead of a central tube. The analytical calculations were carried out based on a 0.61% cable elongation. The internal forces and stresses in the OPGW components were calculated in the absence of contact and friction effects (see Appendix I).
- Due to the plastification of the central aluminum tube and spacer predicted in the finite element model, uniaxial tension tests were performed at McGill University on the central aluminum tube and spacer separately to obtain their nonlinear material law. The experimental stress-strain curve of each component was then used in the model.

- The finite element model and the two analytical solutions are compared with the results of 96-hour traction tests, which were performed at IREQ (IREQ 1996). In the experiments, it is unclear whether the internal components of the OPGW (inner wires, central tube, and the aluminum spacer) deform as much as the external envelope (outer wires).
- The finite element model is unloaded after reaching its maximum prescribed displacement. Due to plastification of the aluminum tube and spacer, permanent deformations remain when no axial forces are induced in those components.

1.5 OPGW construction

The geometrical characteristics and material properties of the OPGW presented in Figure 1.1 are summarized in Tables 1.1 and 1.2.

Table 1.1 19-mm OPGW construction

Outside diameter		mm	18.94
Outer aluminum alloy wires		No./mm	14/3.37
Inner aluminum clad steel wires		No./mm	10/2.85
Aluminum tube external radius		mm	6.5
Number of spacer grooves			5
Weight	Self weight	N/m	8.23
	with 35 mm ice	N/m	60.52
Breaking tensile strength		kN	116.8
Modulus of elasticity		MPa	97000
Thermal expansion coefficient		1/°C	17.1×10^{-6}

Source: IREQ (1994)

It is noted that the helix angles of the different layers of wires and components are in opposite directions. The helical shape of the outer wires is a "*Z* shape" while the opposite direction is called "*S*". The outer wires (aluminum alloy) are of *Z* shape with a pitch of 202 mm, while the inner wires (aluminum-clad steel, Ac) are of *S* shape with a 265.16-mm pitch length. Two of the optical fiber units consist of 8 fibers helically twisted (*S*-shape) around a straight fiber acting as a structural fiber (i.e., not meant to be used for communication purposes). The other three strands have the same structure but comprise only 6 fibers.

Table 1.2 Properties the OPGW components

	Outer Wires Al. Alloy (6201)	Inner Wires (Ac)	Aluminum Tube	Aluminum Spacer (6201)	Optical Fibers
Radius (mm)	1.685	1.425	3.25	-	-
Area (mm^2)	8.92	6.38	10.28	10.17	0.0123
Thermal expansion coefficient /°C	23×10^{-6}	13×10^{-6}	23×10^{-6}	23×10^{-6}	0.5×10^{-6}
Modulus of elasticity (GPa)	63.77	162	61.80	63.77	72.59
Mass (kg/km)	24.1	41.7	30.0	27.6	2.0
Allowable stress (MPa)	-	1250	-	-	-
Max. stress (MPa)	336	1474	162	280.6	-
Pitch length (mm)	202 (*Z*)	265.2 (*S*)	-	150 (*S*)	150

Source: Phillips-Fitel Inc. (cable manufacturer)

The optical fiber units are loosely inserted in the aluminum spacer which is helically (*S*) twisted with a 150-mm pitch length and 0.018% over length of the aluminum spacer length. The cladding of aluminum over the steel inner wires is 0.191 mm thick.

1.6 Organization of the thesis

The thesis consists of six chapters. The first chapter defines the problem and states the objective of the study. In the second chapter, a brief literature review is presented; A more detailed literature review on the subject was also published by the author in 1998 (Roshan Fekr 1998). The theoretical solutions are presented in chapter three. The numerical model and finite element procedure used to solve the mathematical model are covered in details in chapter four, followed by chapter five, which is devoted to results with complementary discussions. Conclusions are summarized in chapter six. Two appendices follow on detailed calculations pertaining to analytical solutions and experimental characterization of the OPGW under study.

1.7 Statement of originality

To the best of the author's knowledge, the following original contributions were carried out in finite element and stress analysis of complex cable structures.

1. The construction of a three-dimensional finite element model of a complex helical cable to estimate the stress distribution in the different components of the cable.
2. The contact analysis with and without friction effects of an OPGW cable is considered for the first time. These effects are presently impossible to predict using analytical solutions.
3. The large kinematics, large displacement with small and large strain in different components is considered in the state of deformation. Neither any theoretical solution nor numerical modeling is yet available in the literature that includes large deformations in the calculation of the stresses and deformations in a standard cable.
4. For the first time, this study shows that the detailed modeling of a complex strand (OPGW) including the exact geometry, full length (based on the longest pitch length), and all possible mechanical effects is feasible.

2

LITERATURE REVIEW

2.1 Helical Wires

2.1.1 Mechanics of wire ropes

Mechanical engineers have been interested in the design and analysis of wire ropes since the 1930's. One of the earliest investigations on stress analysis in wires is a study by Hall (1951). He considered a wire rope made of several strands, each strand being composed of wires as shown in Figure 2.1. The strands and the wires were helically twisted around each other. Hall determined stresses on a wire subjected to an axial load using the following three assumptions:

- the applied load was equally distributed amongst the strands and the wires in turn,
- there was neither friction nor bending in the wires and the strands,
- all strands and wires were tightly in contact with each other, such that only a static elongation of the rope would result from the loading.

However, many subsequent studies have revealed that these assumptions are unrealistic (Hruska 1951, Machida and Durelli 1973, Phillips and Costello 1973).

Considering the wire rope as a fully coupled cross section and distributing the load equally amongst its components means neglecting the essential characteristics of a wire rope. Applying his theoretical model, Hall predicted that stresses in the outer wires would be notably higher than those on the inner wires, and consequently, that the outer wires would likely break under the applied load before the inner wires. It is clear that the radial forces applied by the wires on the strands and by the strands on the core have significant effects on the stresses in wire ropes. Tangential forces generated from the axial load create a torque that changes the geometry of the strands and affects the stresses. Nevertheless, Hall's preliminary study revealed the complexity of stress analysis of wire ropes.

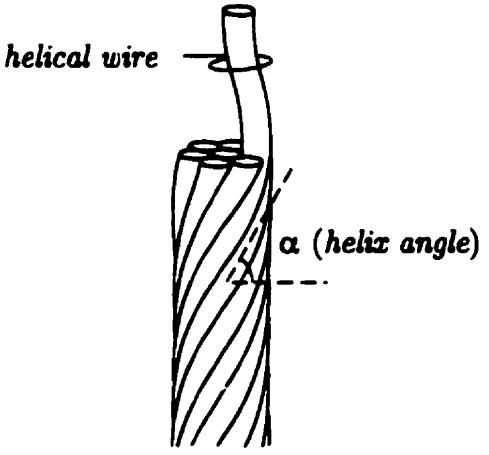

Figure 2.1 Typical wire configuration in a strand

Six months later, Hruska (1951) claimed that Hall had made a "principle error" when he assumed that there was no friction in the wire rope. Hruska stated that the elongation of all wires, under the axial load, was the same due to the great friction between the wires. According to Hruska, an axial load on a wire rope produces three components of forces: axial tension force, radial force, and tangential force. His analysis of the axial tension showed that the core in a strand was always more stressed than the other wires, which is in contradiction with Hall's prediction. He found that the stresses in the wire core, σ_c, and in the outer wires σ_o, were related as

$$\sigma_c = \frac{\sigma_o}{\cos^2 \alpha} \tag{2.1}$$

where α is the lay (helix) angle of the wires. According to Hruska (1952), the radial force F_R per unit length of a wire under an axial load P can be found as

$$F_R = \frac{P \sin^2 \alpha}{R} \tag{2.2}$$

where R is the radius of the cylinder on which the centerlines of the wires lie (see Figure 2.2).

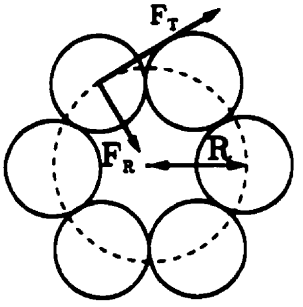

Figure 2.2 Radial and tangential forces on a wire rope cross section

Hruska (1953) also investigated tangential forces in wire ropes, and realized that these forces produced moments about the axis of the strand. He concluded that these tangential forces and the resulting moments would either cause rotation of the wires in free-ends boundary conditions, or be the moment reactions at the fixed supports. The tangential force, F_T, and the corresponding twisting moment, M_t, were determined as

$$F_T = P \sin \alpha \tag{2.3}$$

$$M_t = F_T R . \tag{2.4}$$

2.1.2 Stress analysis of helical wires

One of the first detailed studies carried out on helical wires is the work of Machida and Durelli (1973). They derived linear expressions to determine the axial load, bending and twisting moments of helical wires, and the axial force and twisting moment of a core subjected to axial and torsional displacements. They suggested that the analysis of a wire rope made of strands could be considered analogous to that of helical wires in a strand.

Machida and Durelli investigated three main static external loadings, namely axial loading, torsion, and bending. Although they ignored the interwire contact deformation and Poisson's effect due to axial strain, they considered tensional

loading and the combination of tensional and torsional loadings. According to their assumptions, two types of deformations could occur in a strand: a displacement in the axial direction, δ, and a rotation around the axis of the strand, Δ (see Figure 2.3). They categorized four types of internal forces or stress resultants (axial force, bending moment, twisting moment and contact forces) associated with strains and stresses of the helical wire, and expressed them as a function of δ and Δ.

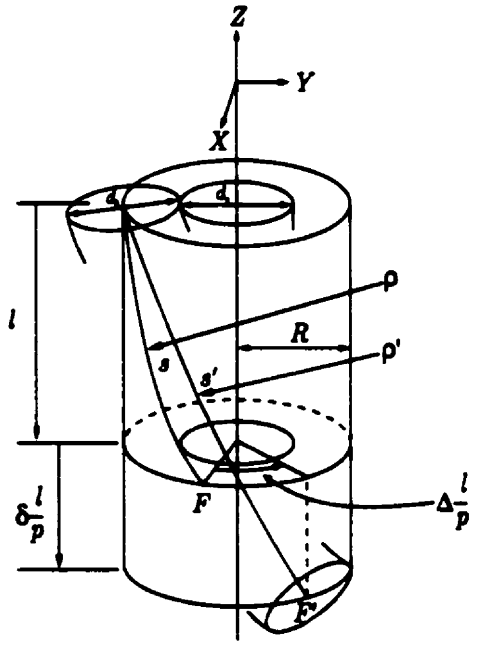

Figure 2.3 Axial displacement and rotation of a helical wire

On the basis of this study, the axial force P_h, the bending moment M, and the twisting moment M_t^h acting in a helical wire, and the resultant contact forces F_c on the wire can be found from the following equations:

$$P_h = A_h E_h (\varepsilon \sin^2 \alpha + \gamma \cos^2 \alpha) \tag{2.5}$$

$$M = \frac{2E_h I_h}{R} (\varepsilon - \gamma) \sin^2 \alpha \cos^2 \alpha \tag{2.6}$$

$$M_t^h = \frac{G_h J_h}{4R} (\varepsilon - \gamma) \sin 4\alpha \tag{2.7}$$

$$F_c = \frac{P_h}{\rho'} \approx \frac{P_h}{\rho} \tag{2.8}$$

where;

A_h cross-sectional area of a helical wire,

E_h Young's modulus,

I_h second moment of area of the cross section of a helical wire,

J_h polar moment of inertia of the cross section of a helical wire,

G_h shear modulus,

ε axial strain of the strand,

γ normalized rotation of one pitch length of the strand ($\gamma = \Delta/2\pi$),

ρ radius of curvature of the helical wire axis,

ρ' deformed radius of curvature of the helical wire axis.

Machida and Durelli also derived expressions for the external axial force and torque of a strand made of m helical wires with a central core as follows:

$$P = P_c + mP_h \sin\alpha' \tag{2.9}$$

$$M_t = M_c + m(M_t^h \sin\alpha' - M\cos\alpha' + P_h R\cos\alpha') \tag{2.10}$$

where indices c and h denote the core and the helical wire, respectively. The deformed helix angle α' and twisting moment M_c acting on the core can respectively be found as

$$\alpha' = \tan^{-1}\left(\frac{1+\gamma}{1+\varepsilon}\tan\alpha\right) \tag{2.11}$$

$$M_c = G_c J_c \frac{2\pi\gamma}{p} \tag{2.12}$$

As it can be seen, Machida and Durelli presented a rational model that took into account different possible loadings and the corresponding stresses. However, the effects of friction amongst the wires, Poisson's effect, and the contact pressure between the core and wires were all neglected in their model. It is noted that in their experimental work, an oversized epoxy model was used for which the effect of friction was actually negligible. Despite its limitations, their work remains an important contribution as most subsequent investigations on helical wires have been based on this study.

Not long after Machida and Durelli, Phillips and Costello (1973) introduced a method to determine stresses in twisted wire cables, with fewer limiting

assumptions than previous researchers. They considered a cable as consisting of thin wires subjected to an axial force and a torque with no friction between the wires. The general non-linear equations for the bending and twisting of a thin rod subjected to line loads were solved using the six non-linear equations of equilibrium for each wire. In the stress analysis, they neglected the radial force exerted by the core on the wires because the core was relatively soft in the example considered. An exact solution was presented to evaluate all stresses (axial, bending, shear, and contact) in the wire. Each single wire in a cable was assumed to be subjected to an external bending moment and the tension T was considered constant along the length. The resultant axial force P and torque M_t on the cable were determined by

$$P = m(P_h \sin\alpha' + N_b^h \cos\alpha') \tag{2.13}$$

$$M_t = m(M_t^h \sin\alpha' + M_b^h \cos\alpha' + P_h R' \cos\alpha' - N_b^h R' \sin\alpha') \tag{2.14}$$

where

N_b^h component of internal force resultant in *b* (binormal) direction (see Figure 2.4),

M_b^h, M_t^h components of internal moment resultant in *b* (binormal) and *t* (tangential) directions, respectively,

R' deformed radius of a cylinder on which the centerline of a helical wire lies,

α' deformed angle between the tangent to the centerline of a helical wire and the plane normal to the axis of the helix.

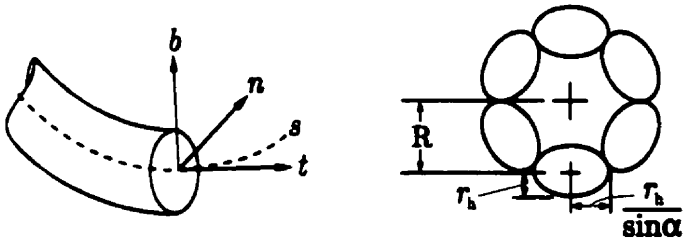

Figure 2.4 Normal (n), Binormal (*b*), and Tangential (*t*) directions of a helical wire and changes in the radius

The contact angle, β (see Figure 2.5), which locates the line of action of the contact loads, Q, on a wire due to its neighbors is given by

$$\beta = \sin^{-1}\left(1 + \frac{\sin^2\alpha}{\tan^2(\pi/2 - \pi/m)}\right)^{-1/2} \tag{2.15}$$

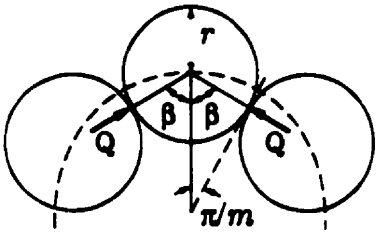

Figure 2.5 Contact between two adjacent helical wires

Phillips and Costello presented some numerical results for a few special cases. Given α' and P_h (obtained using a Newton-Raphson procedure to solve the nonlinear equations of equilibrium) the wire stresses can be calculated using Equations 2.16 to 2.18 (see Figure 2.6). The normal stress of the wire cross section due to direct tension was given by

$$\sigma_t = \frac{P_h}{A_h} \tag{2.16}$$

where A_h is the Cross-sectional area of the helical wire. The maximum bending stress, σ_b, and the maximum shearing stress, τ, due to St-Venant torsion were given by

$$\sigma_b = E_h r_h \left(\frac{\cos^2\alpha'}{R'} - \frac{\cos^2\alpha}{R}\right) \tag{2.17}$$

and

$$\tau = G_h r_h \left(\frac{\sin\alpha'\cos\alpha'}{R'} - \frac{\sin\alpha'\cos\alpha}{R}\right) \tag{2.18}$$

respectively.

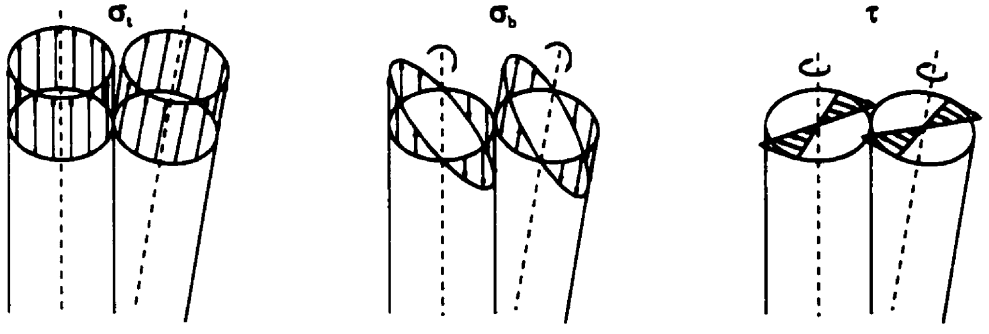

Figure 2.6 Normal stress (σ_t), Bending stress (σ_b), and Torsional shearing stress (τ) in wires

The maximum compressive stress due to contact is

$$\sigma_c = -\sqrt{\frac{QE_h}{\pi R}} \tag{2.19}$$

where Q is the contact force per unit length between two adjacent wires, as shown in Figure 2.5.

This theoretical analysis is incomplete due to the omission of frictional forces between the wires. The relative movements of the wires due to tension and twisting of the cable generate resisting forces that are closely related to the contact forces and stresses in the wires. Therefore, the friction forces will directly affect the stresses calculated by Phillips and Costello. Moreover, if there is more than one layer of wires, which is a common situation, the friction and contact forces between adjacent and lower wires, and also the friction between the wires and the core affect the stresses. The approach proposed by Phillips and Costello does not consider the case of many layers of wires with a hard core. Despite its limitations, however, it is recognized that their investigation was the first to account for the contact forces and their interaction with other forces.

2.1.3 Advanced analytical and experimental studies on cables

The response of wire rope strands to axial tensile loads was more recently investigated theoretically and experimentally by Uttings and Jones (1987 I, II). They were the first to present a mathematical model considering the change of helix angle under load, Poisson's effect in the wires, and the effects of friction and wire flattening at the contact surfaces.

The resultant axial force and torque were calculated using Equations (2.13) and (2.14) of the analysis by Phillips and Costello (1973), adding P_c and M_c to include the contribution of the core,

$$P_c = E_c A_c \varepsilon \quad \text{and} \quad M_c = E_c I_c \phi_c / (1 + \nu) \tag{2.20}$$

where P_c is the core tension and M_c is the torque resisted by the core, respectively (see Figure 2.7).

The axial strain of the strand is

$$\varepsilon = (1 + \varepsilon_h)\frac{\sin\alpha'}{\sin\alpha - 1} \tag{2.21}$$

where ε_h is the strain along the helical wire axis, and the rotation per unit length ϕ_c is

$$\phi_c = \frac{R(1+\varepsilon)}{R' \tan \alpha'} - \frac{1}{\tan \alpha}. \tag{2.22}$$

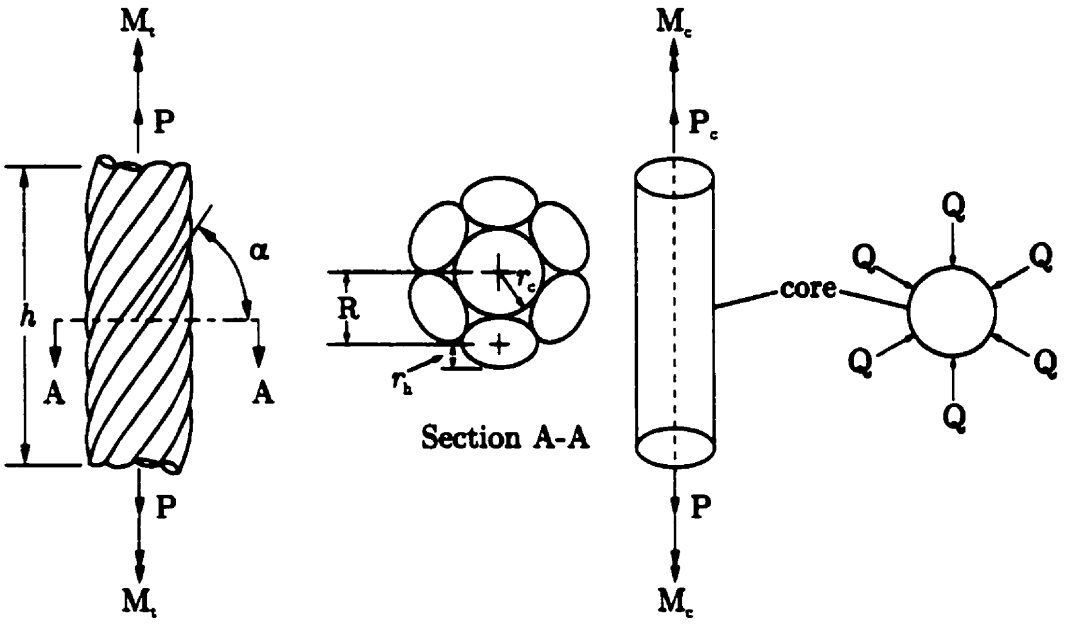

Figure 2.7 Geometry of a seven-wire strand

Neglecting wire flattening and Poisson's effect, the helix radius R is given by

$$R = (d_c + d_h) / 2 \tag{2.23}$$

where d_c and d_h are the core wire and helical wire diameters, respectively. Uttings and Jones considered several aspects of friction in their theoretical analysis, including Poisson's effect, zero friction between the wires, friction with zero slip, and friction with slip. They determined the helix radius of a strand under axial load considering Poisson's effect and equal moduli of elasticity for the core and helical wires.

$$R' = \{d_c(1 - \nu\varepsilon) + d_h(1 - \nu\varepsilon_h)\}/2 \tag{2.24}$$

They took the wire flattening into account by imposing $\delta_Q = f(Q)$ as a flattening effect on the wire radius, therefore modifying Equation. (2.24) as follows:

$$R' = \{d_c(1 - \nu\varepsilon) + d_h(1 - \nu\varepsilon_h)\}/2 - \delta_Q \qquad (2.25)$$

The wire flattening effect is determined empirically from experiments and considered as a function of Q, the contact force per unit length of helical wire (see Figure 2.7). However, it is not clear how important the effect of the contact force is on the reduction of the radius.

End effects were neglected in previous analyses by Machida and Durelli (1973), Phillips and Costello (1973), and Velinsky et al. (1984). Uttings and Jones assumed that when there was no friction between the wires, any change in the strand geometry occurs over a transitional length, L_T, at each end of the strand adjacent to the end grip. They postulated that when friction without slip between the wires was considered, the frictional resistance from the core wire prevents some of the rotation and bending of the helical wires about their axis. Furthermore, the friction force between the helical wires and the core was considered by treating each wire as a thin rod after Phillips and Costello (1973), and Love (1944).

A friction force per unit length of helical wire, f_F, acts as shown in Figure 2.8 with components f_{hTF} and f_{hAF} which are tangential and parallel to the wire axis along the line of contact, respectively. The equal and opposite force acting on the core wire has two components, f_{cTF} and f_{cAF}. Considering the core wire as a helical wire with α=90°, they calculated the total friction force on the core per unit length of core as

$$f_{cF} = m\sqrt{(f_{cAF}^2 + f_{cTF}^2)} \,/\, \sin\alpha \qquad (2.26)$$

where,

f_{cF} frictional force on the core per unit length of core with no slip between wires,

f_{cAF} frictional force on the core in the direction parallel to the wire axis per unit length of core with no slip between the wires,

f_{cTF} frictional force in the direction tangential to the wire axis per unit length of core with no slip between the wires.

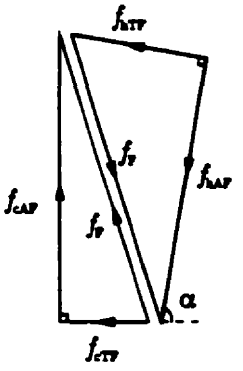

Figure 2.8 Interwire friction with no slip-forces

The frictional force acting on the helical wire per unit length is equal and opposite to the force acting on the core wire:

$$f_{hF} = \sqrt{f_{hAF}^2 + f_{hTF}^2} = \frac{f_{cF} \sin \alpha}{m} \tag{2.27}$$

where,

f_{hF} frictional force on the helical wire per unit length with no slip between the wires,

f_{hAF} frictional force on the helical wire in the direction parallel to the wire axis per unit length with no slip between the wires,

f_{hTF} frictional force on the helical wire in the direction tangential to the wire axis per unit length with no slip between the wires.

By applying thin rod theory, Uttings and Jones calculated f_{hAF} and f_{hTF} as

$$f_{hAF} = \frac{2(M_b B / S_3 - M_t^h A / S_4)}{m d_h L_T (A^2 - BC)} \tag{2.28}$$

$$f_{hTF} = \frac{2(M_t^h C / S_4 - M_b A / S_3)}{m d_h L_T (A^2 - BC)} \tag{2.29}$$

where

$$A = \sin\alpha \cos\alpha (1/S_2 - 1/S_1)$$

$$B = \sin^2\alpha/S_1 + \cos^2\alpha/S_2 + 1/m S_4 \tag{2.30a-c}$$

$$C = \cos^2\alpha/S_1 + \sin^2\alpha/S_2 + 1/m S_3$$

and,

S_1 torsional stiffness of the core wire, $S_1 = E_c I_c / \{r_c^2 \sin\alpha(1+\nu)\}$

S_2 axial stiffness of the core wire, $S_2 = E_c A_c / \sin \alpha$

S_3 bending stiffness of the helical wire, $S_3 = E_h I_h / r_h^2$

S_3 torsional stiffness of the helical wire, $S_4 = E_h I_h / \{r_h^2 (1 + \nu)\}$

L_T transitional length adjacent to strand termination,

Utting and Jones (1989 I) also concluded that if the friction between the core and the helical wires were insufficient to resist rolling contact, slip would occur. Therefore, slip occurs when the force acting on the core is greater than the contact force multiplied by the coefficient of static friction between the core and the helical wires. Uttings and Jones have modified the expression of Q given by Phillips and Costello (1973) concerning the reduced bending moment and torque in the helical wires in the presence of the friction. It should be noted that the theoretical analyses presented by Uttings and Jones do not account for more than one layer of helical wires. Also, the cable behavior will be even more complex if the core and the helical wires in different layers have different moduli of elasticity. Moreover, the large displacements of the wires and the core are not considered. In both of the analyses by Phillips and Costello (1973) and Uttings and Jones (1987), the cable is considered short and straight which is not appropriate in transmission lines and stayed bridges applications where the catenary configuration of the cable and the large displacements of the wires have significant effects on cable stresses.

Utting and Jones (1989 II) predicted that the strand extension under a given load is greater for strands with less torsional restriction such that the extension at the free-end was as much as 70% larger than in the fixed-end tests. All the computations and experiments were performed on seven-wire straight strand with helix angles ranging from 74° to 81° and with core and helical wire diameters of 3.94 and 3.73 mm. It is noted that friction effects, wire flattening, and Poisson's effects, which are all included in the work of Utting and Jones (1989), were neglected in the work of Machida and Durelli (1973).

Experimental results revealed that the theoretical predictions of the torque generated at the fixed end overestimated the measured torque by up to 5%. In the free-end loading, however, the wire rotations (unwinding motion) obtained

experimentally were smaller in all strands (with different pitch lengths) from 9.0 to 15.7%. They concluded that the difference is due to the effect of plastic yielding and wire flattening at contact points and migration of the effective line of contact between the core and the helical wires. The experiments also revealed that the load-torque relation was linear. However, the load-extension behavior was non-linear at low loads in the free-end case.

Surface strains revealed uneven load sharing between nominally identical helical wires, especially near the end grips.

Raoof and Hobbs (1988) have proposed an analytical model for analysis of multi-layered structural strands. They presented several graphs to determine the inter-wire and interlayer contact forces. Each layer of wires in a multi-layered strand was treated as a statically indeterminate orthotropic cylinder with an equivalent modulus of elasticity. The analysis assumed that the wires in each layer just touch each other when there is no axial load on the strand and that the strand was fixed against rotation at its ends. They determined the radial rigid body motion of the wires, which would occur due to the change in lay angle in the absence of a central core. The radial force calculated agreed with the force determined by Hall (1951)(Eq. 2.2).

LeClaire (1991) also extended a linear theory for wire ropes that considered individual wire geometry and equilibrium including the effects of contact deformation between the wires. After reviewing the approach of Velinski et al. (1984) and Costello (1983) for the axial response of a simple strand, LeClaire extended the method to include the effect of contact deformation of a compliant layer. The cross section of a simple strand illustrated in Figure 2.7 has a helix angle α, measured from the perpendicular axis of the strand and the helix radius, $R = r_h + r_c$, which locates the helical wire centerline. The components of curvature κ_h, κ'_h and twist φ_h, can be determined by Equations (2.31-32).

$$\kappa_h = 0 \quad \text{and} \quad \kappa'_h = \frac{\cos^2 \alpha}{R} \tag{2.31}$$

$$\varphi_h = \frac{\sin \alpha \cos \alpha}{R} \tag{2.32}$$

The length h of the strand and the length l of a helical wire are related as

$$h = l\sin\alpha \tag{2.33}$$

The ends of the helical wire of length h make an angle of θ with the strand axis where

$$R\theta = l\cos\alpha \tag{2.34}$$

Under axial load, both the helix angle and the helix radius change by small amounts $\delta\alpha$ and δR. The corresponding variation in lengths h and l, using Equation. (2.33) is

$$\delta h = \delta l\sin\alpha + l\cos\alpha\delta\alpha \tag{2.35}$$

and the corresponding variation in θ of Equation.(2.34) is

$$\delta\theta = \frac{1}{R}(\delta l\cos\alpha - l\sin\alpha\delta\alpha - \delta R\theta) \tag{2.36}$$

The corresponding variations in the components of curvature and twist are

$$\delta\kappa_h = 0 \quad \text{and} \quad \delta\kappa_h' = \frac{2\cos\alpha\sin\alpha}{R}\delta\alpha - \frac{\cos^2\alpha}{R^2}\delta R \tag{2.37}$$

and

$$\delta\varphi_h = \frac{\cos^2\alpha - \sin^2\alpha}{R}\delta\alpha - \frac{\sin\alpha\cos\alpha}{R^2}\delta R \tag{2.38}$$

The axial strains of the strand and the helical wire are $\varepsilon = \delta h/h$ and $\varepsilon_h = \delta l/l$ respectively. Equations (2.33) and (2.35) relate these strains as

$$\varepsilon = \varepsilon_h + \frac{\delta\alpha}{\tan\alpha} \tag{2.39}$$

The strand's twist per unit length is $\phi = \delta\theta/h$, and Equations (2.33), (2.34), and (2.36) are combined to yield

$$\phi = \frac{1}{R}\left(\frac{\varepsilon_h}{\tan\alpha} - \delta\alpha - \frac{\delta R}{R\tan\alpha}\right). \tag{2.40}$$

If the strand's axial strain (ε) and twist per unit length (ϕ) are known, Equations (2.39) and (2.40) provide the helical wire axial strain (ε_h), the change in helix angle ($\delta\alpha$), and the change in helix radius (δR). A third equation can be obtained by relating δR to Poisson's effect in the wires as follows:

$$\nu_h r_h \varepsilon_h + \delta R = -\nu_c r_c \varepsilon \tag{2.41}$$

where ν is the Poisson's ratio. By using equations (2.39) to (2.41), ε_h, $\delta\alpha$ and δR can be determined. Meanwhile, equations (2.37) and (2.38) are used to find $\delta\kappa_h$, $\delta\kappa'_h$, and $\delta\varphi_h$. The resulting bending moment components, M_n^h, M_b^h, and torque, M_t^h, on a cross section of a helical wire in response to these changes are

$$M_n^h = 0 \quad \text{and} \quad M_b^h = \frac{\pi E_h r_h^4}{4}\delta\kappa'_h \tag{2.42}$$

$$M_t^h = \frac{\pi E_h r_h^4}{4(1+\nu_h)}\delta\varphi_h . \tag{2.43}$$

The shear force components, N_b^h, N_n^h, the tension, P_h, and the external force components per unit length, X_h, Y_h, Z_h, maintain the helical wire in equilibrium, where

$$N_n^h = 0, \quad N_b^h = M_t^h \frac{\cos^2\alpha}{R} - M_b^h \frac{\sin\alpha\cos\alpha}{R}, \quad \text{and} \quad P_h = E_h A_h \varepsilon_h \tag{2.44}$$

$$X_h = N_n^h \frac{\sin\alpha\cos\alpha}{R} - P_h \frac{\cos^2\alpha}{R}, \quad Y_h=0, \quad \text{and} \quad Z_h=0. \tag{2.45}$$

The strand axial force, P, and the torque, M_t, required for the specified value of strand axial strain and twist per unit length, are found by summing the response of the m helical wires and the center wire, as follows:

$$P = \pi r_c^2 E_c \varepsilon + m(P_h \sin\alpha + N_b^h \cos\alpha) \tag{2.46}$$

$$M_t = \frac{\pi r_c^4 E_c}{4(1+\nu_c)}\phi + m(M_t^h \sin\alpha + M_b^h \cos\alpha + P_h R\cos\alpha - N_b^h R\sin\alpha) \tag{2.47}$$

Figure 2.9 shows the cross section of a wire rope with a compliant layer of thickness t_c. Neglecting contact deformations, this layer also affects the change in helix radius by its Poisson contraction and Equation. (2.41) can be rewritten as

$$\nu_h r_h \varepsilon_h + \delta R = -\varepsilon(\nu_c r_c + \bar{\nu}_c t_c) \tag{2.48}$$

where $\bar{\nu}_c$ is the Poisson's ratio of the compliant layer.

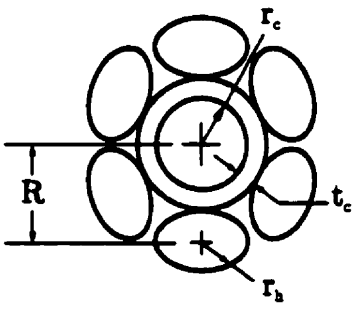

Figure 2.9 Cross section of a simple strand with compliant layer

In order to consider the contribution of contact forces, LeClaire added to Equation. (2.48) a term proportional to the contact force per unit length between the helical wires and the compliant layer as follows:

$$\nu_h r_h \varepsilon_h + \delta R = -\varepsilon(\nu_c r_c + \bar{\nu}_c t_c) + C_h F_{hc} \tag{2.49}$$

where C_h is the contact compliance between the helical wires and the compliant layer, and F_{hc} is the contact force exerted by the compliant layer on a helical wire. If the modulus of elasticity of the compliant layer is significantly less than the wire modulus, the effect of contact deformation on the change of the helix radius will be significant. Adding another layer of helical wires to the simple strand cross section (see Figure 2.10) makes it a complex strand.

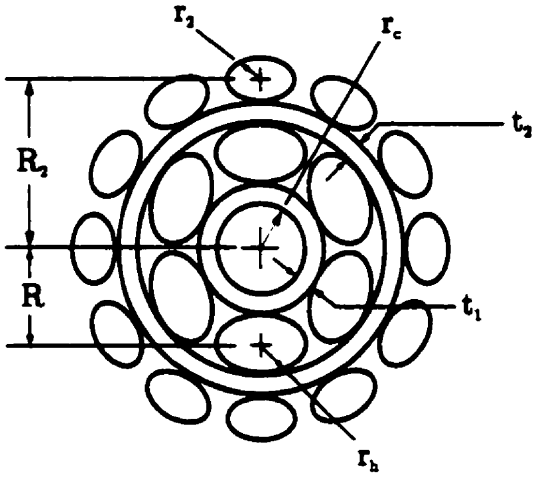

Figure 2.10 Cross section of a two-layer strand with two compliant layers

Contact forces between wires result in deformations that reduce the helix radius of the wires in the strand and consequently reduce the equilibrium contact force per unit length and tension in the wires. The deformations due to contact

between wires of multi-layered metallic strands are expected to be small, but should not be neglected. Moreover, multi-layered cables used for signal transmission often consist of several non-metallic components and are subjected to unavoidable imposed strains. The deformations due to contact between the non-metallic components may be significant and possibly beneficial due to the reduction in contact load and tension.

The results obtained by LeClaire indicate that the presence of a compliant layer between wire layers reduces the tension experienced by the wires in the strand by at least one order of magnitude over the case in which the deformation is neglected or the compliant layer is absent. This effect is desirable in instrumental cables such as optical cables to preserve signal quality. Numerical results for three and ten-layer metallic strands indicate that neglecting contact deformations predicts greater wire tension and equilibrium contact force by only 3% and 11% for the three and ten-layer strands, respectively.

2.1.4 Friction effects in wires

The effect of dry friction and interwire slip in an axially loaded cable is addressed in the work of Huang and Vinogradov (1992). They defined the inter-wire slip as a local displacement of the wire surface with respect to the core or other wires. The cable is composed of a core and m wires wound around it in such a way that each wire, in the first row, interfaces two adjacent wires and the core along the helix. Huang and Vinogradov asserted that inter-wire slippage could occur due to the twisting and bending of the wires. There were two types of contact between the wires: parallel contact between the wires of a same layer, and cross contact between the wires of different layers (see Figure 2.11). They stated that the distributed friction torque, m_f, is related to the contact force, F_c, between the wires in different layers, as

$$m_f = \mu F_c \tag{2.50}$$

where μ is the coefficient of static friction between the surface in contact.

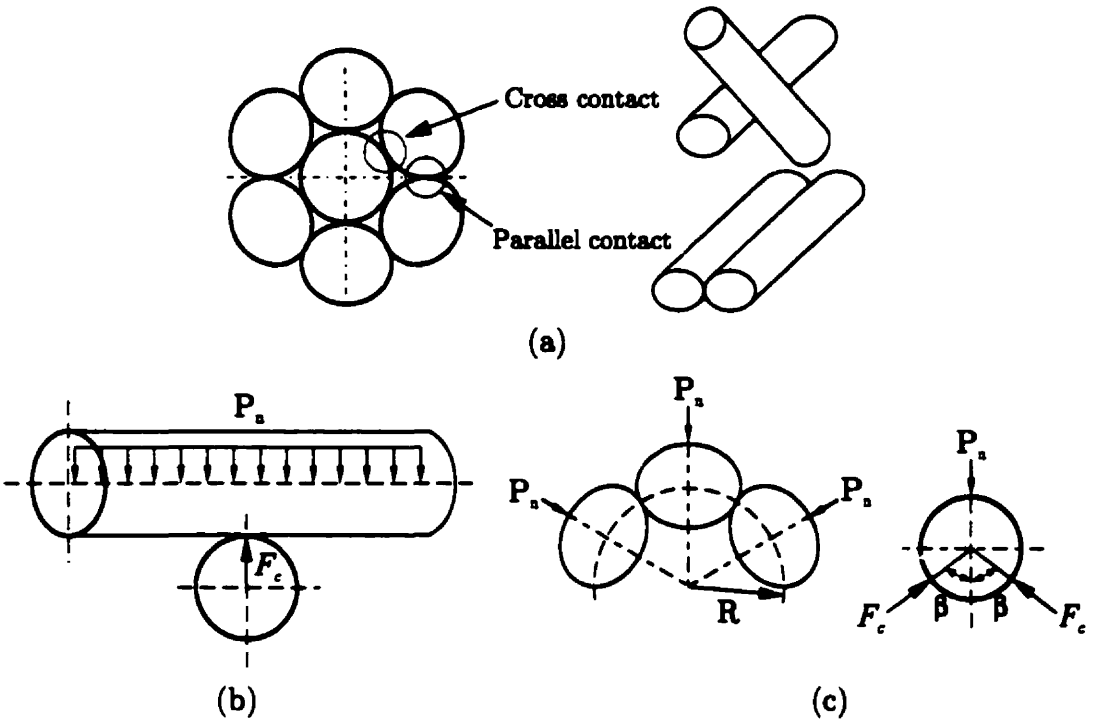

Figure 2.11 (a) Interwire contact, (b) Contact forces in cross touching, and (c) Contact forces in parallel touching

In case of cross contact, F_c was calculated from the equilibrium condition, as shown in Figure 2.11, as

$$F_c = -P_n = \frac{P}{RK_n} E_h A_h \sin^4 \alpha \tag{2.51}$$

where P_n is the inter-wire distributed force in the normal direction and can be presented approximately, using Love's (1944) equation of equilibrium, as

$$P_n = \frac{F_n \sin^2 \alpha}{R} \tag{2.52}$$

in which F_n is the axial component of the resultant force in a wire cross section and is found from the geometry of the developed helix as,

$$F_n = \frac{P}{K_n} E_h A_h \sin^2 \alpha \tag{2.53}$$

and K_n is the cable axial rigidity in non slipping parts and is equal to

$$K_n = E_c A_c + m \frac{E_h A_h}{\sin \alpha}. \tag{2.54}$$

For the parallel type of contact, the contact pressure is

$$F_c = -\frac{P_n}{2\sin\beta} = \frac{PE_hA_h\sin^4\alpha}{2RK_n\cos\beta} \tag{2.55}$$

where β is the contact angle as evaluated by Costello and Phillips (1974),

$$\cos\beta = \frac{1}{\cos\alpha}\sqrt{1+\frac{1}{\tan^2(\frac{\pi}{m})\sin^2\alpha}-\frac{1}{\tan^2(\frac{\pi}{m})}\left(1+\frac{1}{\tan^2\alpha\sin^2(\frac{\pi}{m})\left[\sin^2\alpha+\cot an^2(\frac{\pi}{m})\right]}\right)+\sin^4\alpha} \tag{2.56}$$

As expected, the contact forces are proportional to the axial load for both types of contact. Huang and Vinogradov (1994) also examined a cable as a system of helical wires and a core with distributed dry friction forces at the interfaces. In the analysis of the cable under a uniform bending moment, they found that there was a critical bending curvature when slip occurred between the wire and the core. They assumed small deformations theory and elastic material, and Poisson's effect in the wire was also neglected and only friction forces between the wires and the core were considered. The equations of a rod element derived by Love (1944) were used for the wires. Huang and Vinogradov claimed that slippage between wires was unlikely to occur when the bending deformation of the cable was small. This means that the inter-wire friction force is sufficient to hold the wires together and the cable behaves like a solid beam. In such a case, the corresponding bending rigidity was calculated using the sum of the second moments of area of all the individual wires of the cross section of the cable. They noted that with a large helix angle, the wires wound around the core had a nearly elliptical cross section. By increasing bending, the inter-wire traction force increases and when it is equal to or larger than the friction force, slippage occurs. They concluded that with increasing bending, the slip spreads symmetrically from the neutral plane over the entire area of the cross section of the cable.

2.2 OPGW

2.2.1 Introduction

Optical fibers are widely used in telecommunication network systems. The low-loss and high-bandwidth transmission characteristics of optical fibers make them ideal for transmitting voice, data and video images. An optical fiber is composed of two main parts: an inner cylinder of glass, which is called the core, and a cylindrical shell of glass or plastic of lower refractive index called the cladding (Cherin, 1983). The core is typically made of a high-silica-content or multi-

component glass. The cladding of the fiber is also made of a high-silica-content, multi-component glass, or plastic.

2.2.2 Mechanics of optical fibers

The study of the mechanical behavior of optical fibers is a specialty of optical fibers engineering. The number of studies related to the mechanics of fiber optics is small compared to other areas such as materials and manufacturing, but the proper modeling of the mechanical behavior of optical fibers is important in order to design fibers of optimal mechanical and optical performance. Suhir (1993) showed that the nonlinear stress-strain tensile response of optical fibers is also valid for compression and bending deformations, provided that the axial strains are not exceeding 5%. The stress-strain curve in optical fibers subjected to uni-axial tension (+) or compression (-) can be described as

$$\sigma = E_o \varepsilon (1 \pm \eta \varepsilon / 2) \qquad \varepsilon \leq 5\% \qquad (2.57)$$

where σ and ε are the stress and strain in the fiber, E_o is the initial modulus of elasticity of the fiber (i.e. in the region of very small strain), and η is the parameter of non-linearity. For most optical fibers the Young's modulus is E_o=72 GPa and the non-linearity parameter is η=6 .

2.2.3 Mechanics of OPGW

Russ et al. (1986) investigated the optical and mechanical characteristics of an OPGW. Several experiments were performed to assess such characteristics as attenuation changes due to heat cycling at low and high temperatures, creep, tensional behavior, and performance in simulated short-circuit tests. The OPGW tested was composed of an optical fiber unit surrounded by an aluminum tube covered with one or more layers of aluminum-clad steel strands (Figure 2.12).

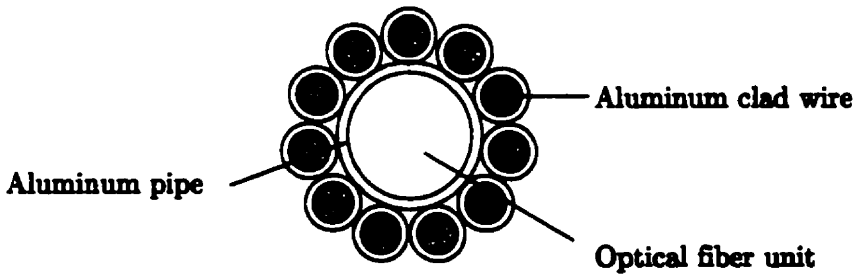

Figure 2.12 Cross section of the OPGW tested by Russ et al.

The fibers are tightened with a filling compound which restraints fiber movements, micro-bending, and local pressure against the fibers under various loads. Two typical constructions were tested; namely the loose tube construction and the tight tube construction. For the loose construction, Russ et al. verified that under the uniaxial tension test, no attenuation was generated when the cable extension remained below the initial fiber over length. However, the attenuation increased drastically for extensions exceeding the over length because the fibers are then unrestrained. As expected, no attenuation loss was measured in the tight construction before the cable failure.

2.2.4 Detailed study of OPGW analysis

The only detailed three-dimensional finite element modeling study of an OPGW reported in the literature is the work of Abé et al. (1989), which was restricted to the study of a grooved aluminum spacer (slotted rod) as illustrated in Figure 2.13 and summarized below. The optical fiber unit was a loose-type and was composed of 600 optical fibers arranged in a ribbon structure. The forces and bending moments in the slotted rod were determined using Love's equilibrium equations (Love, 1944). The deformations of the slotted rod subjected to these forces and bending moments were then obtained using a three-dimensional finite element model. The results showed that for the particular cable studied, the deformations of the slotted rod were very small: it was concluded that for an extensional strain of 0.1% and a bending curvature of 1/1100 mm^{-1}, the clearance between the fibers and the lateral wall of the slot was sufficient to meet the design criteria. It should be emphasized that this study was limited to an isolated slotted rod without considering the other components of the optical fiber cable, i.e., neither the external metallic envelope nor the optical fibers inserted in the slots.

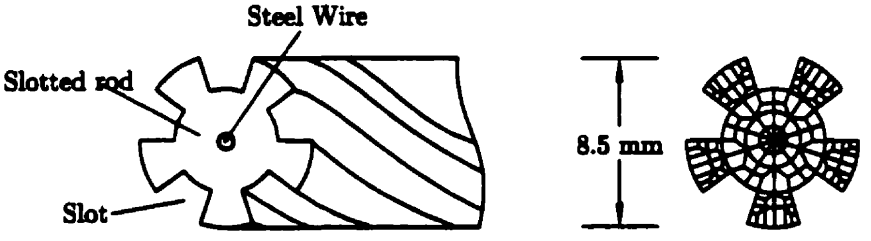

Figure 2.13 Cross section of aluminum spacer (slotted rod) adapted from Abé et al.

A very recent finite element study on stress analysis of helical wires is the work of Jiang et al. (1999). Their finite element model (using ANSYS, a commercial software) was able to take into account the effects of tension, shear, bending, torsion, and contact. Due to limitations in computer resources, precise boundary conditions were developed on only a fraction of a simple seven-wire rope strand slice (Figure 2.7). This slice of 1/12 of the strand section called "basic sector", is modeled with only one element along the axial direction (5% of core wire radius). Constraint equations were applied on the basic sector to include the helical configuration of the wires, rotation and displacement of the strand. Their results show agreement with the elastic theory of Costello (1997) and with experimental data of Utting and Jones (1984). The end effects are also discussed in the study of Jiang and Henshal (1999) for the same model and a 0.2 pitch length of the strand. The axial force-strain relationship of the wires in the linear range agrees with that of Costello.

The concise finite element model of Jiang et al. (1999) seems to have its own limitations. The constraint equations of a more complicated cross section, such as the OPGW in this study, with two layers of wires and a central tube, will be very complicated to apply if not impossible. Hence, considering that there is no direct symmetry in the cross section, the longitudinal helical effects and the effects of contact with the neighboring wires make the application of the boundary conditions too complex. However, their model seems to be capable of predicting the stress and strain for a simple strand when no contact occurs between adjacent wires and for small deformations only.

3

ANALYTICAL SOLUTIONS

3.1 Introduction

In this chapter, two important analytical solutions predicting the static response of a general strand are presented for the OPGW: the theoretical solutions of Machida and Durélli (1973) and Costello (1997) are modified by the author in order to take into account the complex geometry of the OPGW. The main difference between these analytical solutions and the present problem is the central tube (which is a central wire in the original solutions). This is modified in both solutions by using the appropriate radius of the central tube and Poisson's effect.

3.2 Machida and Durelli

Explicit expressions for the determination of the axial force, bending and twisting moments in a helical wire and also in a central core of a seven-wire strand are given by Machida and Durelli (1973). Although they are limited to only two layers of wires (central tube and inner wires), the analysis is used for the OPGW

and appropriate changes are carried out taking into account the geometry and properties of the different components of the OPGW. The axial force F_1 acting on the central tube when undergoing an axial strain (ε) is

$$F_1 = A_1 E_1 \varepsilon \tag{3.1}$$

and the corresponding stress is

$$\sigma_1 = E_1 \varepsilon . \tag{3.2}$$

The axial force and resultant bending and twisting moments of the inner and outer wires are;

$$F_2^h = A_2 E_2 (\varepsilon \sin^2 \alpha_2 + \gamma \cos^2 \alpha_2) \tag{3.3}$$

$$F_3^h = A_3 E_3 (\varepsilon \sin^2 \alpha_3 + \gamma \cos^2 \alpha_3) \tag{3.4}$$

$$M_2 = \frac{2E_2 I_2}{R_2} (\varepsilon - \gamma) \sin^2 \alpha_2 \cos^2 \alpha_2 \tag{3.5}$$

$$M_3 = \frac{2E_3 I_3}{R_3} (\varepsilon - \gamma) \sin^2 \alpha_3 \cos^2 \alpha_3 \tag{3.6}$$

$$M_2^t = \frac{G_2 J_2}{4R_2} (\gamma - \varepsilon) \sin 4\alpha_2 \tag{3.7}$$

$$M_3^t = \frac{G_3 J_3}{4R_3} (\gamma - \varepsilon) \sin 4\alpha_3 \tag{3.8}$$

where the subscripts 2 and 3 stand for the inner and outer wires, and R_2 and R_3 are the radii of the circles measured from the center of the OPGW to the center of an inner and an outer wire respectively, as shown in Figure 3.1.

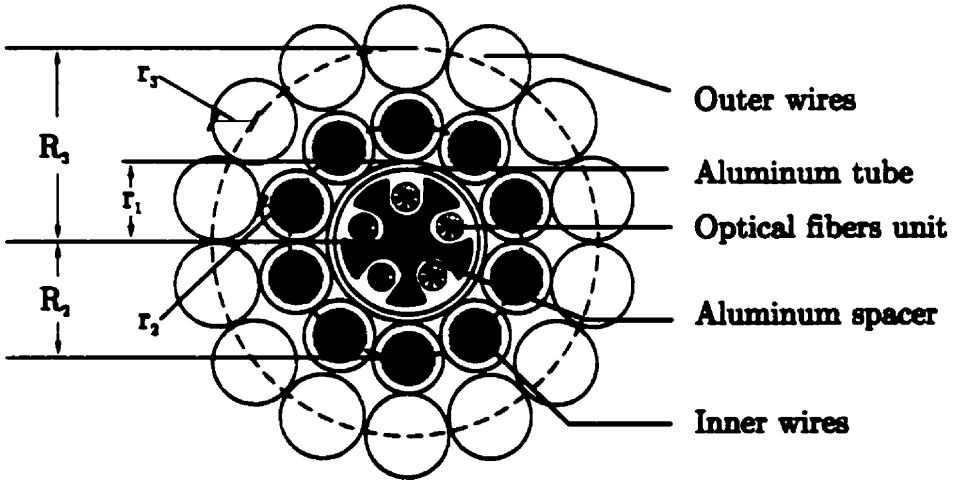

Figure 3.1 Geometry of the OPGW cross section

The contact force per unit length is calculated using

$$F_c = \frac{F_2^h}{\rho'} \approx \frac{F_2^h}{\rho} \tag{3.9}$$

in which the radii of curvature of the undeformed and deformed helix are

$$\rho = R_2 + \left(\frac{p_\ell}{2\pi}\right)^2 \frac{1}{R_2}, \text{ and } \rho' = R_2 + \left(\frac{p'_\ell}{2\pi}\right)^2 \frac{1}{R_2} \tag{3.10}$$

respectively, and p_ℓ and p'_ℓ are the deformed and undeformed pitch lengths of the inner wire (see Figure 2.3). The total axial load and torque acting on the OPGW are

$$F = F_1 + m_2 F_2 + m_3 F_3 \tag{3.11}$$

$$M_t = M_{Tube}^t + M_{t2} - M_{t3} \tag{3.12}$$

where m_2 and m_3 are the number of inner (second layer) and outer (third layer) wires, F_2, F_3, M_{t2}, and M_{t3} are the components of the axial forces and torques along the OPGW axis for the inner and outer wires respectively. The negative sign of the resultant torque on the outer wires (M_{t2}) is due to the opposite direction of the helix angle of the outer wires (Z shape) with respect to the inner wires (S shape).

In the experiments performed by IREQ (1994, see Appendix II), an 83.5 kN tensile force induced an elongation of 0.61% in the OPGW with fixed ends i.e., the unwinding rotation was restricted (γ=0). The axial force and stress in the central tube using Equations (3.1) and (3.2) are

$$F_1 = 635{,}388 \times 0.0061 = 3.88 \text{ kN}$$

$$\sigma_1 = 61{,}803 \times 0.0061 = 377 \text{ MPa.}$$

The OPGW used in transmission lines is assumed to be under axial load only and both ends are restricted such that no rotation is allowed ($\gamma = 0$). Using Equations (3.3) and (3.4), the axial loads acting along the inner and outer wires are

$$F_2^h = 6.38 \times 162{,}000 \times (0.0061 \times 0.988 + 0) = 6.23 \text{ kN}$$

$$F_3^h = 8.92 \times 63{,}765 \times (0.0061 \times 0.945 + 0) = 3.28 \text{ kN}$$

and consequently, the axial loads along the OPGW axis in the inner and outer wires are

$$F_2 = F_2^h \sin\alpha_2 = 6.23 \times 0.994 = 6.19 \text{ kN}$$

$$F_3 = F_3^h \sin\alpha_3 = 3.28 \times 0.972 = 3.19 \text{ kN}.$$

The bending and twisting moments are determined using Equations (3.5) to (3.8),

$$M_2 = \frac{2 \times 162{,}000 \times 3.24}{4.675}(0.0061 - 0) \times 0.012 = 16.40 \text{ N.mm}$$

$$M_3 = \frac{2 \times 63{,}765 \times 6.33}{7.785}(0.0061 - 0) \times 0.0523 = 33.10 \text{ N.mm}$$

$$M_2^t = \frac{162{,}000 \times 3.24}{4 \times 4.675(1 + 0.33)}(0 - 0.0061) \times 0.427 = -54.96 \text{ N.mm}$$

$$M_3^t = \frac{63{,}765 \times 6.33}{4 \times 7.785(1 + 0.33)}(0 - 0.0061) \times 0.814 = -48.37 \text{ N.mm}.$$

The total bending moments acting on the inner and outer wires are

$$M_{b2} = M_2 \sin\alpha_2 + M_2^t \cos\alpha_2 = 16.40 \times 0.994 - 54.96 \times 0.110 = 10.25 \text{ N.mm}$$

$$M_{b3} = M_3 \sin\alpha_3 + M_2^t \cos\alpha_3 = 33.10 \times 0.972 - 48.37 \times 0.235 = 20.79 \text{ N.mm}.$$

The average normal and maximum bending stresses along the helix of the inner and outer wires are

$$\sigma_2^F = \frac{F_2^h}{A_2} = \frac{6.23}{6.38} = 976.48 \text{ MPa}$$

$$\sigma_3^F = \frac{F_3^h}{A_3} = \frac{3.19}{8.92} = 357.63 \text{ MPa}$$

$$\sigma_2^b = \frac{M_2 r_2}{I_2} = \frac{16.40 \times 1.425}{3.24} = \pm 7.21 \text{ MPa}$$

$$\sigma_3^b = \frac{M_3 r_3}{I_3} = \frac{33.10 \times 1.685}{6.33} = \pm 8.81 \text{ MPa}$$

and the stresses along their helix axes are:

$$\sigma_2^h = \sigma_2^F \pm \sigma_2^b = 976.48 \pm 7.21 = \begin{cases} 983.7 \\ 969.3 \end{cases} \text{ MPa}$$

$$\sigma_3^h = \sigma_3^F \pm \sigma_3^b = 357.63 \pm 8.81 = \begin{cases} 366.4 \\ 348.8 \end{cases} \text{ MPa}.$$

The maximum shear stresses of the inner and outer wires along their helical axis due to the resisting torque are,

$$\tau_2^h = \frac{M_2^t r_2}{J_2} = -12.09 \text{ MPa}$$

$$\tau_3^h = \frac{M_3^t r_3}{J_3} = -6.44 \text{ MPa}.$$

To obtain the axial and shear stresses of the wires along the cable axis, the above stresses (normal and shear stresses along helix) are transformed as follows

$$\sigma_2 = \frac{\sigma_2^h}{2} + \frac{\sigma_2^h}{2}\cos 2\theta_2 + \tau_2^h \sin 2\theta_2 = \begin{cases} 969 \\ 955 \end{cases} \text{ MPa}$$

and

$$\tau_2 = -\frac{\sigma_2^h}{2}\sin 2\theta_2 + \tau_2^h \cos 2\theta_2 = \begin{cases} -119 \\ -118 \end{cases} \text{ MPa}$$

where

$$\theta_2 = \frac{\pi}{2} - \alpha_2 = 6.32^\circ.$$

The corresponding maximum shear and principal stresses in the inner wires are calculated using the following formula

$$\tau_{2\max} = \sqrt{\left(\frac{\sigma_2^h}{2}\right)^2 + \left(\tau_2^h\right)^2} = \begin{cases} 492 \\ 485 \end{cases} \text{ MPa}$$

$$\sigma_{2P1} = \frac{\sigma_2^h}{2} + \tau_{2\max} = \begin{cases} 984 \\ 969 \end{cases} \text{ MPa}$$

and the same calculations for the outer wires (third layer) as

$$\theta_3 = \frac{\pi}{2} - \alpha_3 = 13.61^\circ$$

$$\sigma_3 = \frac{\sigma_3^h}{2} + \frac{\sigma_3^h}{2}\cos 2\theta_3 + \tau_3^h \sin 2\theta_3 = \begin{cases} 343 \\ 327 \end{cases} \text{ MPa}$$

and the corresponding shear stresses along the cable axis are

$$\tau_3 = -\frac{\sigma_3^h}{2}\sin 2\theta_3 + \tau_3^h \cos 2\theta_3 = \begin{cases} -90 \\ -86 \end{cases} \text{ MPa}.$$

The corresponding maximum shear and principal stresses in outer wires are

$$\tau_{3\max} = \sqrt{\left(\frac{\sigma_3^h}{2}\right)^2 + \left(\tau_3^h\right)^2} = \begin{matrix}183\\175\end{matrix} \text{ MPa}$$

$$\sigma_{3P1} = \frac{\sigma_3^h}{2} + \tau_{3\max} = \begin{matrix}367\\349\end{matrix} \text{ MPa.}$$

The deformed radius of the curvature and contact forces of the inner and outer wires are

$$\rho_2' = 4.675 + \left(\frac{265.16 \times 1.0061}{2\pi}\right)^2 \frac{1}{4.675} = 390 \text{ mm}$$

$$F_{2c} = \frac{6{,}228}{390} = 15.97 \text{ N/mm.}$$

$$\rho_3' = 142 \text{ and } F_{3c} = 3280/142 = 23.07 \text{ N/mm.}$$

The total twisting moments resulting from the axial force and bending in the plane of the OPGW in the inner and outer wires are determined as follows

$$M_{t2} = m_2(M_2^t \sin\alpha_2 - M_2 \cos\alpha_2 + F_2^h R_2 \cos\alpha_2) \tag{3.13}$$

$$M_{t3} = m_3(M_3^t \sin\alpha_3 - M_3 \cos\alpha_3 + F_3^h R_3 \cos\alpha_3). \tag{3.14}$$

Since the unwinding motion is restricted (γ=0), the twisting moment in the tube ($M_{Tube}^t = 2\pi GJ\gamma / \rho = 0$) is zero and the equilibrium equation of the internal twisting moments using Equation. (3.2) becomes

$$M_t = M_{t2} - M_{t3}$$

where M_t is the reaction torque at the support. Using Equations (3.13) and (3.14)

$M_{t2} = 10(-54.96 \times 0.994 - 16.40 \times 0.110 + 6{,}228 \times 4.675 \times 0.110) = 31.5$ kN.mm

$M_{t3} = 14(-48.37 \times 0.972 - 33.10 \times 0.235 + 3{,}277 \times 7.785 \times 0.235) = -83.3$ kN.mm

and the reaction torque is

$$M_t = -51.8 \text{ kN.mm.}$$

As shown in Figure 3.1, the helical aluminum spacer is inserted in the central tube to house the optical fiber units. Assuming a stress-free state for the optical

fibers and neglecting the helical effects of the aluminum spacer, the axial tension and stress of the aluminum spacer under a 0.61% elongation are

$$F_{Al.spacer} = E_{as} A_{as} \varepsilon = 63{,}765 \times 10.17 \times 0.0061 = 3.96 \text{ kN} \quad (3.15)$$

$$\sigma_{Al.spacer} = 63{,}765 \times 0.0061 = 389 \text{ MPa}$$

where the stress distribution is considered uniform over the cross section of the aluminum spacer. As it will be seen later in the discussion of results from the finite element model, the stress distribution is non-uniform at the cross section of the aluminum spacer due to its geometry.

The total axial force acting on the OPGW using Equations (3.11) and (3.15) is

$$F = 3.96 + 3.88 + 10 \times 6.19 + 14 \times 3.19 = 114.3 \cong 114 \text{ kN}$$

The interpretation of this result is that the linearized theory of Machida and Durelli predicts that an axial load of 114 kN is required to induce a cable elongation of 0.61%. However, in the laboratory tests only 83.5 kN could produce such an elongation measured on the external layer of wires.

3.3 Costello

3.3.1 Response of the OPGW to centric axial load

The geometry of a helical wire with resultant forces is shown in Figure 3.2.

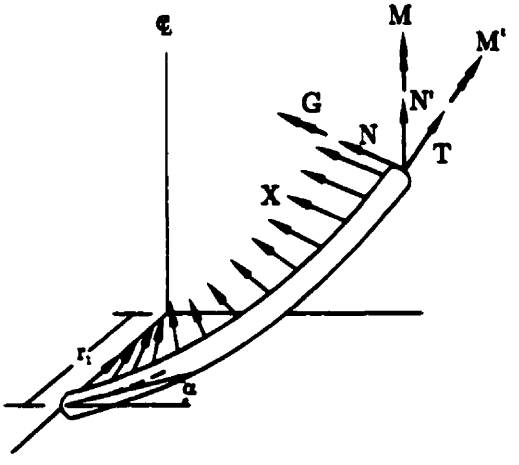

Figure 3.2 Resultant forces and moments on a helical wire

Using the theory of the wire rope presented by Costello for multi-layered strands (1997), for the inner wires (the second layer of the wires denoted with subscript 2), it can be written;

$$R_2 = r_1 + r_2 \tag{3.16}$$

$$\tan\alpha_2 = \frac{p_2}{2\pi R_2} \tag{3.17}$$

$$R_2' = r_1(1 - \nu\varepsilon_1) + r_2(1 - \nu\varepsilon_2) \tag{3.18}$$

$$\frac{R_2}{R_2'} = 1 + \nu\frac{(r_1\varepsilon_1 + r_2\varepsilon_2)}{R_2} \tag{3.19}$$

$$\varepsilon_1 = \varepsilon_2 + \frac{\Delta\alpha_2}{\tan\alpha_2} = \varepsilon \tag{3.20}$$

$$\beta_2 = R_2\varphi_s = \frac{\varepsilon_2}{\tan\alpha_2} - \Delta\alpha_2 + \nu\frac{(r_1\varepsilon_1 + r_2\varepsilon_2)}{R_2\tan\alpha_2} \tag{3.21}$$

$$r_2\Delta\kappa_2' = -\frac{2\sin\alpha_2\cos\alpha_2}{R_2/r_2}\Delta\alpha_2 + \nu\frac{(r_1\varepsilon_1 + r_2\varepsilon_2)\cos^2\alpha_2}{R_2R_2/r_2} \tag{3.22}$$

$$r_2\Delta\varphi_2 = \frac{(1 - 2\sin^2\alpha_2)}{R_2/r_2}\Delta\alpha_2 + \nu\frac{(r_1\varepsilon_1 + r_2\varepsilon_2)\sin\alpha_2\cos^2\alpha_2}{R_2R_2/r_2} \tag{3.23}$$

$$\frac{M_2}{Er_2^3} = \frac{\pi}{4}r_2\Delta\kappa_2' \tag{3.24}$$

$$\frac{M_2^t}{Er_2^3} = \frac{\pi}{4(1+\nu)}r_2\Delta\varphi_2 \tag{3.25}$$

$$\frac{N_2'}{Er_2^2} = \frac{M_2^t}{Er_2^3}\frac{\cos^2\alpha_2}{R_2/r_2} - \frac{M_2}{Er_2^3}\frac{\sin\alpha_2\cos\alpha_2}{R_2/r_2} \tag{3.26}$$

$$\frac{T_2}{Er_2^2} = \pi\varepsilon_2 \tag{3.27}$$

$$\frac{X_2}{Er_2} = \frac{N_2'}{Er_2^2}\frac{\sin\alpha_2\cos\alpha_2}{R_2/r_2} - \frac{T_2}{Er_2^2}\frac{\cos^2\alpha_2}{R_2/r_2} \tag{3.28}$$

$$\frac{F_2}{Er_2^2} = m_2\left[\frac{T_2}{Er_2^2}\sin\alpha_2 + \frac{N_2}{Er_2^2}\cos\alpha_2\right] \tag{3.29}$$

and

$$\frac{M_{2t}}{Er_2^3} = m_2\left[\frac{M_2^h}{Er_2^3}\sin\alpha_2 + \frac{M_2}{Er_2^3}\cos\alpha_2 + \frac{T_2}{Er_2^2}\frac{R_2}{r_2}\cos\alpha_2 - \frac{N_2'}{Er_2^2}\frac{R_2}{r_2}\sin\alpha_2\right] \tag{3.30}$$

$$\frac{F_1}{(EA)_{Tube}} = \varepsilon_1 = \varepsilon \tag{3.31}$$

$$\frac{M_1}{(GJ)_{Tube}} = \tau_s \tag{3.32}$$

$$M_{b2} = M_2 \sin\alpha_2 + M_2^t \cos\alpha_2 \tag{3.33}$$

where;

F_2 total axial force in the OPGW acting on $m_2 = 10$ inner wires

M_2 component of the bending moment (see Figure 3.2)

M_{2b} bending moment in the plane of cable cross section

M_2^t twisting moment in inner wire

M_{2t} total twisting moment acting on inner wires

N_2' component of the shearing force on inner wire (see Figure 3.2)

p_2 initial pitch length of the inner wire

R_2 initial helical radius of the inner wire

R_2' final helical radius of the inner wire

r_1 outside radius of the aluminum tube

r_2 radius of the inner (second layer) wire

T_2 axial tension in inner wire

X_2 component of the external line load per unit length of the centerline of inner wire in the x direction (see Figure 3.2)

$\Delta\alpha_2$ change in the helix angle of an inner wire (between undeformed and deformed geometry)

$\Delta\varphi_2$ change in twist per unit length of inner wire

$\Delta\kappa'_2$ change in curvature of inner wire

α_2 initial helix angle of the inner wire

β_2 rotational strain of inner wire

ε_1 axial strain in the central tube ($\varepsilon_1 = \varepsilon$)

ε_2 axial strain of inner wire

φ_s angle of twist per unit length

and the outer (third) layer of the OPGW ;

$$R_3 = r_1 + 2r_2 + r_3 \tag{3.34}$$

$$\varepsilon_1 = \varepsilon_3 + \frac{\Delta\alpha_3}{\tan\alpha_3} \tag{3.35}$$

$$\beta_3 = R_3\varphi_s = \frac{\varepsilon_3}{\tan\alpha_3} - \Delta\alpha_3 + \nu\frac{(r_1\varepsilon_1 + 2r_2\varepsilon_2 + r_3\varepsilon_3)}{R_3\tan\alpha_3} \tag{3.36}$$

$$r_3\Delta\kappa_3' = -\frac{2\sin\alpha_3\cos\alpha_3}{R_3/r_3}\Delta\alpha_3 + \nu\frac{(r_1\varepsilon_1 + 2r_2\varepsilon_2 + r_3\varepsilon_3)\cos^2\alpha_3}{R_3R_3/r_3} \tag{3.37}$$

$$r_3\Delta\varphi_3 = \frac{(1-2\sin^2\alpha_3)}{R_3/r_3}\Delta\alpha_3 + \nu\frac{(r_1\varepsilon_1 + 2r_2\varepsilon_2 + r_3\varepsilon_3)\sin\alpha_3\cos^2\alpha_3}{R_3R_3/r_3} \tag{3.38}$$

$$\frac{M_3}{Er_3^3} = \frac{\pi}{4}r_3\Delta\kappa_3' \tag{3.39}$$

$$\frac{M_3^t}{Er_3^3} = \frac{\pi}{4(1+\nu)}r_3\Delta\varphi_3 \tag{3.40}$$

$$\frac{N_3'}{Er_3^2} = \frac{M_3^t}{Er_3^3}\frac{\cos^2\alpha_3}{R_3/r_3} - \frac{M_{b3}}{Er_3^3}\frac{\sin\alpha_3\cos\alpha_3}{R_3/r_3} \tag{3.41}$$

$$\frac{T_3}{Er_3^2} = \pi\varepsilon_3 \tag{3.42}$$

$$\frac{X_3}{Er_3} = \frac{N_3'}{Er_3^2}\frac{\sin\alpha_3\cos\alpha_3}{R_3/r_3} - \frac{T_3}{Er_3^2}\frac{\cos^2\alpha_3}{R_3/r_3} \tag{3.43}$$

$$\frac{F_3}{Er_3^2} = m_3\left[\frac{T_3}{Er_3^2}\sin\alpha_3 + \frac{N_3}{Er_3^2}\cos\alpha_3\right] \tag{3.44}$$

and

$$\frac{M_{3t}}{Er_3^3} = m_3\left[\frac{M_3^t}{Er_3^3}\sin\alpha_3 + \frac{M_3}{Er_3^3}\cos\alpha_3 + \frac{T_3}{Er_3^2}\frac{R_3}{r_3}\cos\alpha_3 - \frac{N_3'}{Er_3^2}\frac{R_3}{r_3}\sin\alpha_3\right] \tag{3.45}$$

where the subscript 3 indicates the same quantities of the inner wires but for the outer (third layer) wires.

Now considering the OPGW, r_1=3.25 mm, r_2=1.425 mm, and r_3=1.875 mm, p_2= 265.16 mm right lay, p_3= 202.16 mm left lay, m_2=10, and m_3=14. Equations (3.16) and (3.34) yield,

$$R_2 = 3.25 + 1.425 = 4.675 \text{ mm}$$

and $R_3 = 3.25 + 2 \times 1.425 + 1.685 = 7.785$ mm.

The helix angles of the inner and outer wires can be determined by Equation (3.17),

$$\tan \alpha_2 = \frac{265.16}{2\pi \times 4.675} = 9.03$$

$$\tan \alpha_3 = -\frac{202}{2\pi \times 7.785} = -4.13,$$

which correspond to $\alpha_2 = 83.7^\circ$ and $\alpha_3 = -76.4^\circ$. The negative sign is due to the opposite directions of helix for the inner and outer wires.

If the inner wires are not touching each other in the no-load configuration, the radius of the inner wire helix should be smaller than r_1+r_2 as;

$$r_2\sqrt{1+\frac{\tan^2(\pi/2-\pi/m_2)}{\sin^2\alpha_2}} = 4.637 \text{ mm} < 4.675 = r_1 + r_2$$

and therefore, the internal wires do not touch each other. To find out if the outer wires are touching each other, the radius of the outer wire helix should be smaller than R_3;

$$r_3\sqrt{1+\frac{\tan^2(\pi/2-\pi/m_3)}{\sin^2\alpha_3}} = 7.7805 \text{ mm} < 7.785 = r_1 + 2r_2 + r_3$$

and therefore, the outer wires do not touch each other either in the undeformed cable.

Detailed calculations of internal forces and moments acting on the four OPGW components, using the equations derived above, are presented in Appendix I. The final results of these calculations are given here for a cable strain of $\varepsilon = 0.61\%$. The total axial load and twisting moment acting on the OPGW when $\varepsilon = 0.61\%$ are:

$$F_{\text{Al.spacer}} + F_{\text{Tube}} + F_{\text{Inner}} + F_{\text{Outer}} + = 3{,}956 + 3{,}876 + 10 \times 6{,}179 + 14 \times 3{,}148 = 106 \text{ kN}$$

$$M^t_{\text{Tube}} + M^t_{\text{Inner}} + M^t_{\text{Outer}} = 0 + 31{,}186 - 81{,}541 = -50 \text{ kN.mm}$$

3.3.2 Stress determination of the OPGW

In the previous section, the internal forces and moments in the OPGW were calculated under axial loading and the rotation of the OPGW was restricted ($\beta = 0$). The stress caused by these calculated forces is now investigated in this section. The axial stress of the central tube due to axial load is

$$\sigma_{Tube} = (F / A)_{Tube} = 377 \text{ MPa.}$$

It is evident that the stresses in the tube exceed the maximum allowable stress (162 MPa). In other words, the aluminum tube yields and undergoes some permanent deformation that is not considered in the above analysis. Consequently, one can conclude that the deformation of the tube is greater than 0.61%, while the stresses are smaller. The shearing stress in the central tube remains zero, since no twisting moment is induced in the tube. The stresses due to contact between the tube and the internal wires will be discussed in the next section.

The inner and outer wires are subjected to axial, bending and torsional effects in addition to the shearing resultants N_2' and N_3' due to the axial strain in the OPGW. The stresses caused by shearing are in general very small compared to the other stresses and can be neglected. The normal stresses due to axial loads T_2 and T_3 are

$$\sigma_{F2} = \frac{T_2}{\pi r_2^2} = 975 \quad \text{MPa}$$

$$\sigma_{F3} = \frac{T_3}{\pi r_3^2} = 363 \quad \text{MPa}$$

whereas the maximum normal stresses due to bending moments M_2 and M_3 are

$$\sigma_2^b = \frac{4M_2}{\pi r_2^3} = \pm 7.64 \quad \text{MPa}$$

$$\sigma_3^b = \frac{4M_3}{\pi r_3^3} = \pm 9.59 \quad \text{MPa}.$$

The maximum shearing stresses on the inner and outer wires due to the twisting moment (torsion) are

$$\tau_2^h = \frac{2M_2^t}{\pi r_2^3} = -11.98 \quad \text{MPa}$$

$$\tau_3^h = \frac{2M_3^t}{\pi r_3^3} = -6.24 \quad \text{MPa}.$$

The shearing forces N_2' and N_3' are only 0.3 N and 0.7 N. To obtain the axial and shear stresses of the wires along the cable axis, the above stresses (normal and shear stresses along helix) are transformed such as

$$\theta_2' = \frac{\pi}{2} - \alpha_2' = 90 - 83.72 = 6.28°$$

and

$$\sigma_2^h = \sigma_2^F \pm \sigma_2^b = 974.61 \pm 7.64 = \begin{cases} 982.3 \\ 967.0 \end{cases} \text{MPa}.$$

Therefore,

$$\sigma_2 = \frac{\sigma_2^h}{2} + \frac{\sigma_2^h}{2}\cos 2\theta_2' + \tau_2^h \sin 2\theta_2' = \begin{cases} 968 \\ 953 \end{cases} \text{MPa}$$

and the corresponding shear stresses along the cable axis are

$$\tau_2 = -\frac{\sigma_2^h}{2}\sin 2\theta_2 + \tau_2^h \cos 2\theta_2 = \begin{cases} -118 \\ -117 \end{cases} \text{MPa}.$$

The corresponding maximum shear and principal stresses are calculated using the following formula

$$\tau_{2\max} = \sqrt{\left(\frac{\sigma_2^h}{2}\right)^2 + \left(\tau_2^h\right)^2} = \begin{cases} 491 \\ 483 \end{cases} \text{MPa}$$

$$\sigma_{2P1} = \frac{\sigma_2^h}{2} + \tau_{2\max} = \begin{cases} 982 \\ 967 \end{cases} \text{MPa}.$$

Performing the same calculations for the outer wires:

$$\theta_3' = \frac{\pi}{2} - \alpha_3' = 90 - 76.48 = 13.52°$$

$$\sigma_3^h = \sigma_3^F \pm \sigma_3^b = 362.92 \pm 9.59 = \begin{cases} 372.6 \\ 353.4 \end{cases} \text{MPa}$$

$$\sigma_3 = \frac{\sigma_3^h}{2} + \frac{\sigma_3^h}{2}\cos 2\theta_3' + \tau_3^h \sin 2\theta_3' = \begin{cases} 349 \\ 331 \end{cases} \text{MPa}.$$

The corresponding shear stresses along the cable axis are

$$\tau_3 = -\frac{\sigma_3^h}{2}\sin 2\theta_3' + \tau_3^h \cos 2\theta_3' = \begin{cases} -90.2 \\ -85.9 \end{cases} \text{ MPa.}$$

The corresponding maximum shear and principal stresses are calculated as follows

$$\tau_{3\,max} = \sqrt{\left(\frac{\sigma_3^h}{2}\right)^2 + \left(\tau_3^h\right)^2} = \begin{cases} 186 \\ 177 \end{cases} \text{ MPa}$$

and

$$\sigma_{3P1} = \frac{\sigma_3^h}{2} + \tau_{3\,max} = \begin{cases} 373 \\ 353 \end{cases} \text{ MPa.}$$

It is worth noting that the increase or decrease in axial strain (ε) when the rotation is restricted (φ_z=0) will affect the stresses in the tube, and the inner and outer wires in the same proportion, due to the linearity of the equations. However, the contact stresses are nonlinear and will be discussed later.

3.3.3 Contact stresses

To estimate the contact stresses, the contact force per unit length must be known. The line of contact between the inner wires and the central tube in the OPGW is a helix of radius r_1 (3.25 mm). The approximate equation suggested by Costello (1997) to determine the resultant force per unit length X_2 is

$$X_c\sqrt{p_2^2 + (2\pi r_1)^2} = -X_2\sqrt{p_2^2 + \left[2\pi(r_1 + r_2)\right]^2} \tag{3.46}$$

where X_c is the contact force per unit length acting along the line of contact. Figure 3.3 shows a point along the line of contact between the central tube and a wire, whereas the cross section of the internal wire is shown circular and the central tube is elliptical. The radius of curvature of the surface of the central tube at the point of contact is ρ_1, where

$$\rho_1 = \frac{r_1}{\sin^2 \alpha_2} \tag{3.47}$$

and the maximum contact stress σ_c is given by

$$\sigma_c = -\frac{b}{\Omega} \tag{3.48}$$

where

$$\Omega = -\frac{4(1-\nu^2)}{\left(\frac{1}{\rho_1}+\frac{1}{R_2}\right)E} \tag{3.49}$$

and

$$b = \sqrt{\frac{2X_c\Omega}{\pi}}\,. \tag{3.50}$$

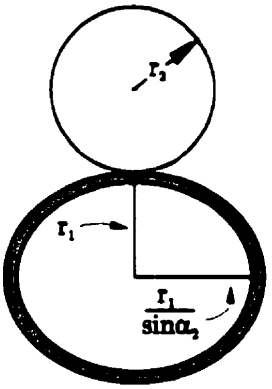

Figure 3.3 Contact between the central tube and an inner wire

Considering the OPGW and applying Equation (3.28),

$$X_2 = -6.98E - 5 \times 162{,}000 \times 1.425 = -22.97 \cong -23 \text{ N/mm.}$$

and Equation (3.46) yields

$$X_c = 23\frac{\sqrt{(265.16)^2 + (2\pi \times 4.675)^2}}{\sqrt{(265.16)^2 + (2\pi \times 3.250)^2}} = 23.0 \text{ N/mm}$$

and Equation (4.47) results in

$$\rho_1 = \frac{3.250}{0.988} = 3.29 \text{ mm.}$$

The maximum contact stress σ_c using Equation (3.48) is

$$\sigma_c = -\frac{214 \times 10^{-2}}{3.12 \times 10^{-5}} = -685 \text{ MPa}$$

and for the third layer (outer wires)

$$X_3 = -2.14E - 4 \times 63{,}765 \times 1.685 = -23.01 \approx -23 \text{ N/mm}$$

$$X_c = 23\frac{\sqrt{(202)^2 + (2\pi \times 7.785)^2}}{\sqrt{(202)^2 + (2\pi \times 6.1)^2}} = 23.25 \text{ N/mm}$$

and applying Equations (3.48 to 3.50)

$$\sigma_c = -\frac{3.32 \times 10^{-3}}{7.43 \times 10^{-5}} = -446 \text{ MPa.}$$

The above contact stress is calculated assuming linear stress-strain laws for the central tube and the inner wires.

3.4 Summary of the analytical solutions

Table 3.1 summarizes the forces and moments obtained by the two above solutions and the corresponding stresses are presented in Table 3.2.

Table 3.1 Resultant forces and moments on the OPGW components

	Aluminum tube	Inner wires			Outer wires			OPGW	
	F_c (kN)	F_2 (kN)	M_{2b} (N.mm)	M_{2t} (N.m)	F_3 (kN)	M_{3b} (N.mm)	M_{3t} (N.m)	F_t (kN)	M_t (N.m)
Machida & Durelli	4.04	6.2	10.3	31.5	3.2	20.8	83.3	114	51.8
Costello	4.04	6.2	11.0	31.2	3.2	24.0	81.5	106	50.3

Table 3.2 Stresses on the OPGW components

	Aluminum tube	Inner wires			Outer wires		
	σ_c (MPa)	σ_2 (MPa)	τ_2 (MPa)	X_c (kN/m)	σ_3 (MPa)	τ_3 (MPa)	X_c (kN/m)
Machida & Durelli	377	969	119	16	367	90	23
Costello	377	968	118	23	349	90	23.25

A comparison between the two analytical solutions shows that there is almost no difference in the stress predictions of the different components of the OPGW. However, the contact line forces between the central tube and the inner wires are smaller in Machida and Durelli's work. The normal and shear stresses are transformed stresses along the cable axis. These analytical solutions will be compared with the finite element numerical model. In general, the differences in the analytical solutions are due to the fact that the solution of Machida and Durelli is based on the undeformed geometry (no Poisson's effect), and Costello's is based on deformed geometry (including Poisson's effect).

4

NUMERICAL MODELING

4.1 Introduction

A numerical or mathematical model is a simplified and approximated model of a real physical problem. The physical problem typically involves an actual structure or a component of it. An actual problem is almost impossible to model exactly as it is in reality. However, an ideal mathematical model should retain the most important characteristics of the actual physical problem. Nevertheless, it is important to realize that the numerical solution can never give more information than that contained in the mathematical model.

4.2 Finite element analysis

The finite element method is a numerical procedure to analyze continua. It is very useful when the problem is too complex to be solved satisfactorily by classical analytical methods. The method is commonly employed to solve physical problems in engineering analysis and design. In other words, ***the idealized mathematical model of a physical problem is solved by finite element analysis.***

Certain assumptions are required for the idealization of a physical problem to a mathematical model, and it is important to choose a mathematical model, which is reliable and effective. An effective model is one that yields the required response with a reasonable accuracy and least cost, and is considered reliable if the predicted response is within the accuracy of the response of a very comprehensive mathematical model (Bathe 1996). Results are rarely exact, however, errors are decreased by processing more equations, and accuracy of the results is obtainable at reasonable cost for engineering purposes (Cook et al., 1989)

In this study, the finite element analysis software **ADINA** (1999), AUTOMATIC DYNAMIC INCREMENTAL NONLINEAR ANALYSIS is utilized, which has been proved in many previous studies of complex mechanical problems (Roshan Fekr et. al., 1999, Bathe et. al., 1999). Two important features of finite element analysis are crucial to this study and discussed in the next sections. They are:

- Nonlinear analysis (kinematics and material nonlinearities)
- Contact analysis

4.2.1 Nonlinear analysis

The finite element set of equilibrium equations for linear static analysis is

$$\mathbf{KU} = \mathbf{R} \tag{4.1}$$

where, **K** is the structure stiffness matrix, **U** is a vector of the system global displacements and **R** is a vector of loads acting in the direction of these displacements. In Equation (4.1), the displacement response **U** is a linear function of the applied load vector **R**. In linear analysis, the displacements must be small since all integrations are performed over the original volume of the finite elements in the evaluation of the stiffness matrix **K** and load vector **R**, and the strain-displacement matrix **B** of each element is assumed to be constant and independent of the element displacements. Besides, the material is considered linear elastic in the use of a constant stress-strain matrix **C**, and the boundary conditions remain unchanged in reflecting of constant constraint relations for the complete response. When **U** is not a linear function of **R**, then a nonlinear analysis is performed. Generally, the nonlinearities arise either from material behavior, large kinematics and/or change in boundary conditions. In materially nonlinear analysis, the stress-strain relation is nonlinear, and in large kinematics,

the displacements and rotations are large, however, the axial and rotational strains can be small, moderate, or large. In the latter, either the Total Lagrangian or Updated Lagrangian formulation is used. The *second Piola-Kirchhoff stress* and the *Green-Lagrange strain* are measured in Total Lagrangian while the *Cauchy stress* and the *Almansi strain* are calculated in the Updated Lagrangian formulation. In the Total Lagrangian solution scheme all static and kinematic variables are referred to the initial configuration but in the Updated Lagrangian they are referred to the last calculated configuration. Both formulations include all kinematic nonlinear effects, but whether the large strain behavior is modeled appropriately depends on the constitutive relations specified.

In this study, the nonlinearities arise from the material law, kinematics, and the contact problem. The stress-strain relation is nonlinear for the aluminum tube and spacer but stays linear for the steel wires. The kinematics are large (moderately large displacements with small or large strain), while the boundary conditions change during the motion of the body due to contact between components of the OPGW.

4.2.2 Nonlinear static analysis

In a nonlinear analysis, the problem is to find the state of equilibrium of a body corresponding to the applied loads. Assuming that the external applied loads are a function of time, the equilibrium conditions of a system of finite elements representing the body can be expressed as

$$^{t}\mathbf{R} - {}^{t}\mathbf{F} = \mathbf{0} \tag{4.2}$$

where $^{t}\mathbf{R}$ is the vector of external nodal loads in the configuration at time t and $^{t}\mathbf{F}$ is the nodal point forces that correspond to the element stresses in this configuration.

$$^{t}\mathbf{F} = \sum_{m} \int_{^{t}V^{(m)}} {}^{t}\mathbf{B}^{(m)T} \; {}^{t}\boldsymbol{\tau}^{(m)} \; {}^{t}dV^{(m)} \tag{4.3}$$

In Equation (4.3), $^{t}\mathbf{B}^{(m)}$ is the strain-displacement matrix, $^{t}\boldsymbol{\tau}^{(m)}$ is the stress matrix, which is integrated over the volume $^{t}V^{(m)}$ at time t. The equilibrium relation in Equation (4.2) must be satisfied and solved throughout the complete history of load application when the analysis includes path-dependent nonlinear

geometric or material conditions. The analysis is effectively carried out using a step-by-step incremental solution, which is reduced to one-step if in a static solution the total load is applied all at once and only one final configuration is calculated.

For an incremental step-by-step analysis the solution for discrete time $t + \Delta t$ is required while it is known for the discrete time t, where Δt is a chosen time increment. Hence, Equation (4.2) at time $t + \Delta t$ becomes

$$^{t+\Delta t}\mathbf{R} - {}^{t+\Delta t}\mathbf{F} = \mathbf{0} \tag{4.4}$$

assuming that $^{t+\Delta t}\mathbf{R}$ is independent of the deformations, and since the solution is known at time t,

$$^{t+\Delta t}\mathbf{F} = {}^{t}\mathbf{F} + \mathbf{F} \tag{4.5}$$

where $\mathbf{F}$ is the increment in nodal forces corresponding to the increment in element displacements and stresses from time t to $t + \Delta t$. The approximate solution of $\mathbf{F}$ using a tangent stiffness matrix $^{t}\mathbf{K}$ at time t is

$$\mathbf{F} \approx {}^{t}\mathbf{K}\mathbf{U} \tag{4.6}$$

where $\mathbf{U}$ is the incremental nodal point displacement vector and

$$^{t}\mathbf{K} = \frac{\partial {}^{t}\mathbf{F}}{\partial {}^{t}\mathbf{U}}. \tag{4.7}$$

Applying Equations (4.6) and (4.5) into (4.4),

$$^{t}\mathbf{K}\mathbf{U} = {}^{t+\Delta t}\mathbf{R} - {}^{t}\mathbf{F} \tag{4.8}$$

and then solving for $\mathbf{U}$ yields an approximation of the displacement at time $t + \Delta t$, as

$$^{t+\Delta t}\mathbf{U} \approx {}^{t}\mathbf{U} + \mathbf{U}. \tag{4.9}$$

This is an approximation to nodal point displacements since Equation (4.6) is used. The approximated stresses and corresponding nodal point forces at time $t + \Delta t$ can now be evaluated before proceeding to the next time step. The errors may be significant depending on the time or load step size. Therefore, to obtain a satisfactory accuracy, an iterative solution is used in solving Equation (4.4).

To solve the incremental nonlinear static equations using the classical Newton-Raphson iteration technique, the equations are, for $i = 1, 2, 3, \ldots$

$$
\begin{aligned}
{}^{t+\Delta t}\mathbf{K}^{(i-1)}\Delta\mathbf{U}^{(i)} &= {}^{t+\Delta t}\mathbf{R} - {}^{t+\Delta t}\mathbf{F}^{(i-1)} \\
{}^{t+\Delta t}\mathbf{U}^{(i)} &= {}^{t+\Delta t}\mathbf{U}^{(i-1)} + \Delta\mathbf{U}^{(i)}
\end{aligned}
\tag{4.10}
$$

with the initial conditions

$$
{}^{t+\Delta t}\mathbf{U}^{(0)} = {}^{t}\mathbf{U}; \qquad {}^{t+\Delta t}\mathbf{K}^{(0)} = {}^{t}\mathbf{K}; \qquad {}^{t+\Delta t}\mathbf{F}^{(0)} = {}^{t}\mathbf{F}. \tag{4.11}
$$

The out-of-balance load vector ${}^{t+\Delta t}\mathbf{R} - {}^{t+\Delta t}\mathbf{F}^{(i-1)}$ corresponds to a load vector that is not yet balanced by element stress resultants, and hence an increment in the nodal point displacements is required. This updating of the nodal point displacements is continued until the out-of-balance loads and incremental displacements are small. An additional equation is applied in the full Newton iteration when the algorithms employ line searches, as

$$
{}^{t+\Delta t}\mathbf{U}^{(i)} = {}^{t+\Delta t}\mathbf{U}^{(i-1)} + \beta^{(i)}\Delta\mathbf{U}^{(i)} \tag{4.12}
$$

where $\beta^{(i)}$is an acceleration factor obtained from a line search in the direction $\Delta\mathbf{U}^{(i)}$ such that

$$
\Delta\mathbf{U}^{(i)^T}\left({}^{t+\Delta t}\mathbf{R} - {}^{t+\Delta t}\mathbf{F}^{(i)}\right) \le \text{STOL} \quad \Delta\mathbf{U}^{(i)^T}\left({}^{t+\Delta t}\mathbf{R} - {}^{t+\Delta t}\mathbf{F}^{(i-1)}\right) \tag{4.13}
$$

where STOL is the user-input line search convergence tolerance and ${}^{t+\Delta t}\mathbf{F}^{(i)}$ is calculated using the total displacement vector ${}^{t+\Delta t}\mathbf{U}^{(i)}$.

In any incremental solution based on iterative methods, a realistic criterion should be imposed to terminate the iteration. A suitable predefined tolerance is used as a check at the end of each iterations to see whether it has converged within that tolerance or it is diverging. Too loose a tolerance can result in inaccurate results while a too stringent one may be costly. Different convergence criteria can be used in ADINA, such as energy, energy and force/moment, translation/rotation, etc. The internal energy convergence criterion is more attractive in our problem since it contains both forces and displacements. In this criterion, the amount of work done by the out-of-balance loads on the displacement increment is compared to the initial internal energy increment. Convergence is assumed to be reached when

$$
\Delta\mathbf{U}^{(i)^T}\left({}^{t+\Delta t}\mathbf{R} - {}^{t+\Delta t}\mathbf{F}^{(i-1)}\right) \le \varepsilon_E\left(\Delta\mathbf{U}^{(1)^T}\left({}^{t+\Delta t}\mathbf{R} - {}^{t}\mathbf{F}\right)\right) \tag{4.14}
$$

where $\varepsilon_E$is a preset energy tolerance .

In ADINA if the user-predefined time or load steps are possibly too large, the solution will not converge after a defined number of iterations when Full Newton iteration is used. The automatic-time-stepping (ATS) method can then be used to obtain a converged solution. If no convergence is reached after the defined number of iterations, the program automatically subdivides the total load step increment to reach convergence, while the maximum number of subdivisions can be controlled by the user.

4.2.3 Contact analysis

Contact problems can be either frictionless or with friction. The concept of contact effects is illustrated schematically in Figure 4.1. The virtual work done by contact tractions can be written as

$$\int_{S^{IJ}} \delta u_i^I \; {}^t f_i^{IJ} \; dS^{IJ} + \int_{S^{JI}} \delta u_i^J \; {}^t f_i^{JI} \; dS^{JI} = \int_{S^{IJ}} \delta u_i^{IJ} \; {}^t f_i^{IJ} \; dS^{IJ} \qquad (4.15)$$

where I and J denote the two bodies in contact, δu^I_i and δu^J_i are the components of the virtual displacements on the contact surfaces of bodies I and J, respectively, and

$$\delta u_i^{IJ} = \delta u_i^I - \delta u_i^J \,. \qquad (4.16)$$

The two contact surfaces S^{IJ} and S^{JI} are called a *contact surface pair*. These surfaces are not necessarily equal and at time t, the actual area of contact for bodies I and J is ${}^tS_c$ of bodies I and J. In a contact surface pair, usually the stiffer surface is called the *target surface* and the other *contactor surface*.

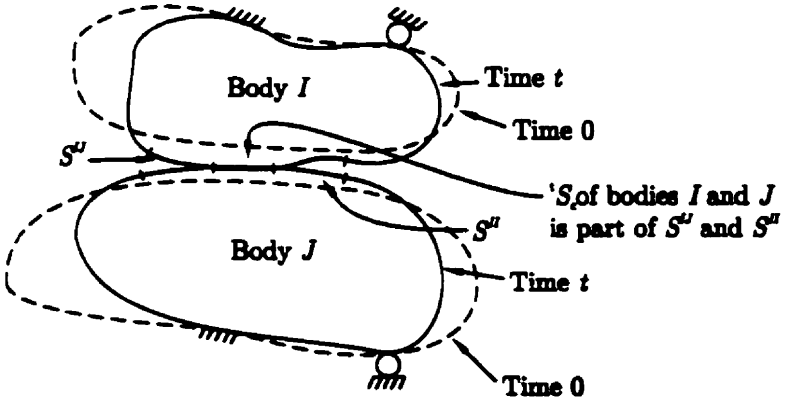

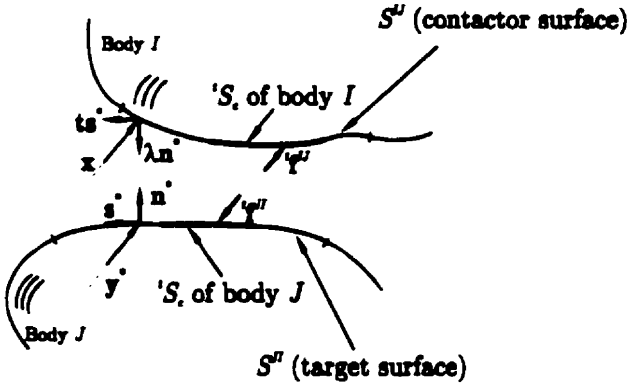

Figure 4.1 Contact between two bodies at time t

In calculating the right-hand-side of Equation (4.15), the contact traction $^t\mathbf{f}^{IJ}$ acting on S^{IJ} can be decomposed into normal and tangential components corresponding to $\mathbf{n}$ and $\mathbf{s}$ on S^{JI}

$$^t\mathbf{f}^{IJ} = \lambda\mathbf{n} + t\mathbf{s} \tag{4.17}$$

where λ and t are the normal and tangential traction components. Now consider a generic point $\mathbf{x}$ on S^{IJ} and let $\mathbf{y}^*(\mathbf{x},t)$ be the point on S^{JI} satisfying

$$\left\|\mathbf{x} - \mathbf{y}^*(\mathbf{x},t)\right\|_2 = \min_{\mathbf{y}\in S^{JI}}\left\{\left\|\mathbf{x} - \mathbf{y}\right\|_2\right\} \tag{4.18}$$

the distance (gap) from $\mathbf{x}$ to S^{JI} is given by

$$g(\mathbf{x},t) = (\mathbf{x} - \mathbf{y}^*)^T\mathbf{n}^* \tag{4.19}$$

where $\mathbf{n}^*$ is the unit normal vector that is used at $\mathbf{y}^*(\mathbf{x},t)$, and $\mathbf{n}^*$, $\mathbf{s}^*$ are used in Equation (4.17) corresponding to point $\mathbf{x}$. The conditions for normal contact can be written as

$$g \geq 0; \qquad \lambda \geq 0; \qquad g\lambda = 0 \tag{4.20}$$

and when $g > 0$, then $\lambda = 0$, and vice versa.

In order to add the frictional conditions, the nondimensional variable τ can be given as

$$\tau = \frac{t}{\mu\lambda} \tag{4.21}$$

where μ is the coefficient of static friction and $\mu\lambda$ is the *frictional resistance*. The magnitude of the relative tangential velocity is

$$\dot{u}(\mathbf{x},t) = (\dot{\mathbf{u}}^J\big|_{\mathbf{y}^*(\mathbf{x},t)} - \dot{\mathbf{u}}^I\big|_{(\mathbf{x},t)}).\mathbf{s}^* \tag{4.22}$$

corresponding to the unit tangential vectors $\mathbf{s}$ at $\mathbf{y}^*(\mathbf{x},t)$. Consequently, $\dot{u}(\mathbf{x},t)\mathbf{s}^*$ is the tangential velocity at time t of the material point at $\mathbf{y}^*$ relative to the material point at $\mathbf{x}$. Hence, the Coulomb's law of friction states

$$|\tau| \le 1$$

and $$|\tau| < 1 \text{ implies } \dot{u} = 0 \tag{4.23}$$

while $$|\tau| = 1 \text{ implies sign } (\dot{u}) = \text{sign } (\tau)$$

Assuming w and v are two functions such that the solutions of $w(g,\lambda) = 0$ and $v(\dot{u},\tau) = 0$ satisfy the conditions (4.20) and (4.23), the contact conditions are

$$w(g,\lambda) = 0 \tag{4.24}$$

$$v(\dot{u},\tau) = 0 \tag{4.25}$$

These two conditions can be imposed on the principle of virtual work equation using either a penalty approach or the Lagrange multiplier method (Bathe, 1996). The variables λ and τ can be considered Lagrange multipliers, therefore multiplying (4.24) by $\delta\lambda$ and (4.25) by $\delta\tau$ and integrating over S^{IJ}, the constraint equation becomes

$$\int_{S^{IJ}} [\delta\lambda w(g,\lambda) + \delta\tau v(\dot{u},\tau)]\, dS^{IJ} = 0 \tag{4.26}$$

The finite element solution for the governing continuum mechanics equations is now obtained by discretizing the contact condition along with the discretization procedures for the principle of virtual work. ADINA offers two contact solution algorithms; 1) constraint function and 2) segment method. The latter uses Lagrange multipliers to enforce the contact conditions in which the kinematic conditions are enforced at the contactor nodes, and the frictional conditions are enforced over the contact segments (ADINA, 1999).

The following constraint function is used in ADINA for the constraint function algorithm:

$$w(g,\lambda) = \frac{g+\lambda}{2} - \sqrt{\left(\frac{g-\lambda}{2}\right)^2 + \varepsilon_N} \tag{4.27}$$

where ε_N is a very small positive parameter. The frictional constraint function is an out-of-plane extension of the relationship

$$\tau = \frac{2}{\pi}\arctan\left(\frac{\dot{u}}{\varepsilon_T}\right) \tag{4.28}$$

where ε_T is a small numerical parameter that can provide some "elasticity" to the Coulomb friction law.

4.3 Modeling

In the ADINA system of finite element analysis programs (ADINA R & D, Inc., 1999), the model is defined using the pre-processor ADINA-IN, and analyzed using the structural analysis program ADINA (for stresses and displacements), and finally the results are displayed using the post-processor ADINA-PLOT.

In ADINA-IN, it is necessary to completely describe the model including its geometry, material properties, boundary conditions and loads. By defining the geometry of the model and using an appropriate mesh the model is discretized into finite elements. When the finite element model is constructed, data files containing the model definition are created by ADINA-IN and are used as input to ADINA to be run for the stress and displacement analysis. The solution program runs in the background and produces "porthole" files containing all details of the model definition and response. The porthole file is loaded in ADINA-PLOT where the results can be displayed and examined. In the next sections, only the particular features of finite element analysis, which are used in the analysis of the OPGW will be presented.

4.3.1 Geometry of OPGW

The geometry of the OPGW is shown in Figure 4.2. It is seen that the outer wires are helically twisted over the inner wires, which are also helically twisted around the central aluminum tube but in the opposite direction of the outer wires. The pitch lengths of the outer and inner wires are 202.0 and 265.2 mm, corresponding to 76.4 and 83.7 degree helix angles, respectively.

A cylindrical coordinate system is used to define the geometry of the helical wires. The shape of a helical wire can be generated by extruding a circular

surface along a helix. However, extruding cannot be done along a curvilinear line in ADINA-IN (1999).

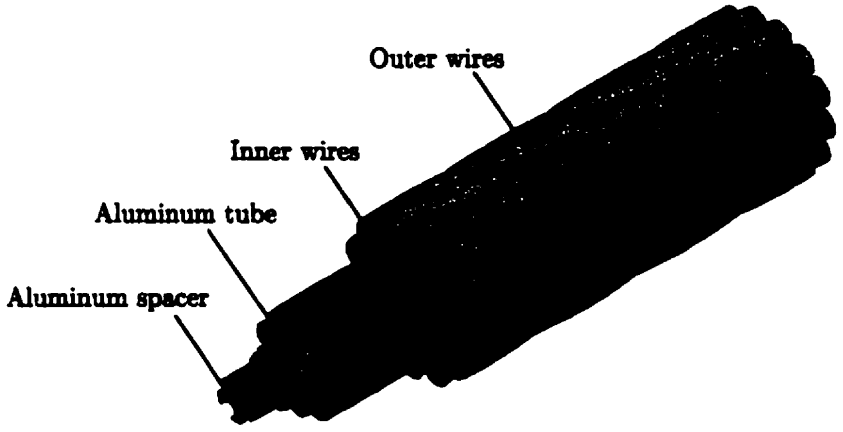

Figure 4.2 Geometry of OPGW

The volume generated by revolving a rectangular surface around its side is a cylinder, but revolving a surface delimited by two curvilinear lines and two straight lines around its curvilinear axis does not generate a helical shape. To obtain the correct helical shape, a circular surface must be explicitly defined along the axis of the helix. To this end, four quarters of a circular surface normal to the longitudinal axis of the strand (X-axis) were created at every quarter of pitch length. One quarter of a helical wire was formed by defining a volume with these surfaces and the curvilinear lines connecting the vertices of each quarter of the circle as shown in Figure 4.3. The result is a quarter of a helical wire where both end surfaces are circular and normal to the X-axis. This is not exactly the cross section of a helical wire when a plane with normal in the X-direction cuts the wire: the exact cross-section is elliptical. The other three-quarters of the helical wire are generated the same way and are combined. Consequently, only the cross sections of the wire ends are slightly approximated. Since the results of both ends are affected by end effects, it is assumed that this approximation has no influence on the results in the middle of the wire (Roshan Fekr et al. 1999).

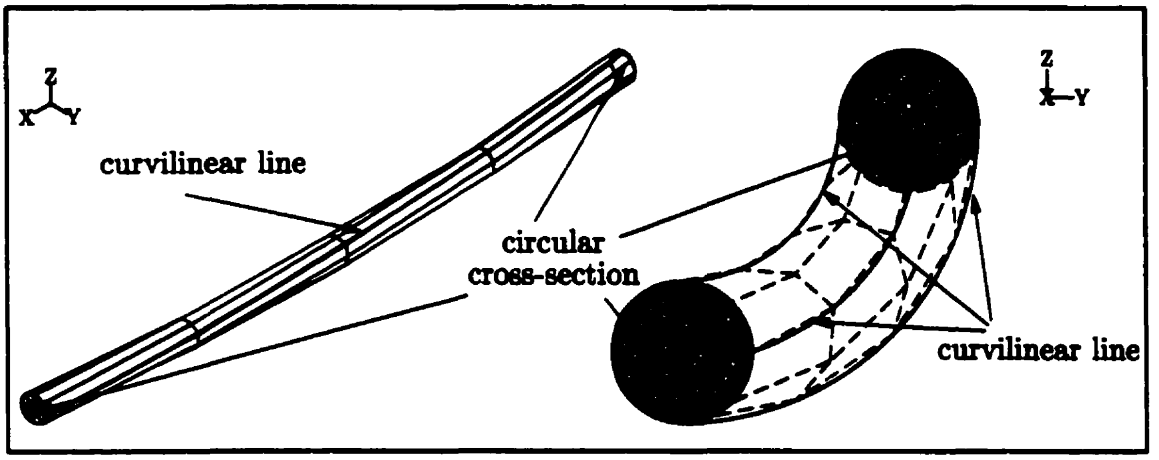

Figure 4.3 Defining of the geometry of helical wires using curvilinear lines and circular cross sections

The total length of the OPGW model is based on the longest pitch length of the different components. As the pitch length of the inner wires is greater than that of the outer wires (265.2 mm vs. 202.0 mm), the geometry of the model is generated for a length of 265.16 mm, which is almost 1.31 times the pitch length of the outer wires and 1.77 times the pitch length of the aluminum spacer.

Different pitch lengths were also modeled to find out the effect of pitch length and to determine the best length of the OPGW. Only two and three pitch lengths of the inner wires were modeled due to high computational cost and limitations of the platform.

The geometry of the central tube is simply created by translating a circle along the X-axis. The radius of the circle is 2.975 mm corresponding to mid surface radius of the central aluminum tube. It is worth noting that in ADINA-IN, the contact problem of a thin shell element is formulated on mid surface of the shell whereas in reality the contact occurs on its external and/or internal surfaces.

The geometry of the aluminum spacer is based on its exact cross section. Once the exact cross-sectional area of the aluminum spacer is created at one end, it is rotated by 90° at a quarter of its pitch length and the vertices of the two cross sections are connected by curvilinear lines to form a volume of helical shape which is twisted about its helix angle.

The full-length geometry of the OPGW (265.2 mm) is shown in Figure 4.4. The overall ratio of the length (265.2 mm) to diameter (19 mm) of the model is 14.

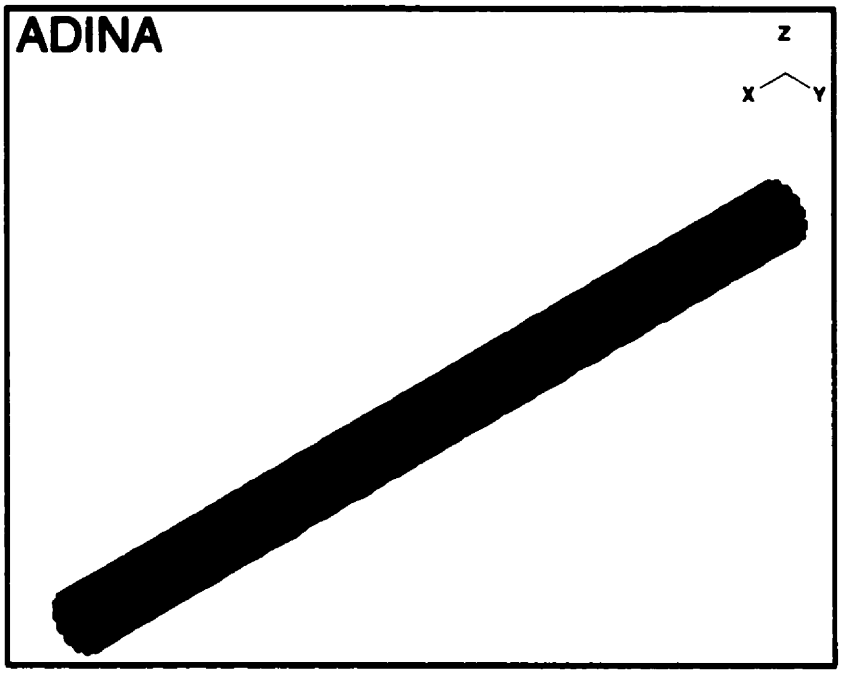

Figure 4.4 Full length geometry of the OPGW model

4.3.2 Finite element model

4.3.2.1 Outer and inner helical wires

The helical wires are modeled either with 8- or 20-node three-dimensional solid elements. The 20-node element is the most efficient among all available 3-D solid elements in ADINA, however its use can be extremely costly. On the other hand, the 8-node element is efficient for the contact analysis and when bending effects are not significant (ADINA 1999, Bathe 1996). The 20-node 3-D solid elements were only used to check the results obtained with the 8-node elements, but the additional running time seemed not justified since the increase in accuracy was not significant. The Gauss integration orders are 2×2×2 for the 8-node and 3×3×3 for the 20-node solid elements.

Each wire finally consists of a total of 384 3-D 8-node solid elements. As it is seen in Figure 4.5, the mesh is finer at both ends as 128 elements are used in the first and the last quarters, and 64 elements for the second and third quarter lengths. The large deformation/small strain formulation is used such that the outputs are

Cauchy stresses and Green-Lagrange strains. The material is assumed linear elastic both for the inner and outer wires. The modulus of elasticity of the inner aluminum-clad steel wires is 162 GPa, with a tensile strength of 1474 MPa and an allowable tensile stress of 1250 MPa. The modulus of elasticity for the outer aluminum alloy wires is 64 GPa and the maximum tensile strength is limited to 336 MPa. The finite element model of the inner and outer wires is shown in Figure 4.5.

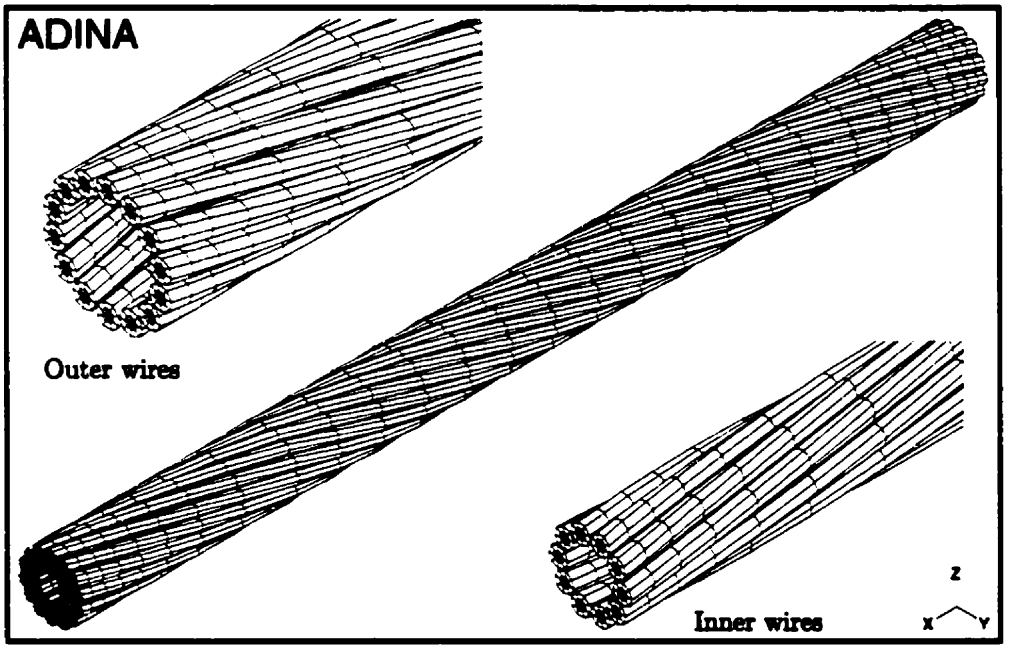

Figure 4.5 Finite element model of the inner and outer wires

4.3.2.2 Central aluminum tube

The central aluminum tube is modeled with 256 4-node shell elements (16 circumferential by 16 longitudinal) with 0.55 mm thickness. In a finer mesh, 512 elements corresponding to 32 longitudinal and 16 circumferential segments are used. The former mesh can be considered a coarse mesh for contact analysis but the gain in accuracy obtained with the latter was almost negligible considering the extra computational effort of the finer mesh. The tube material is first assumed Hookean with a Young's modulus of 61.8 GPa and a Poisson's ratio of 0.33. The maximum tensile stress is 168 MPa. In the initial stage of the research, yielding of the tube was predicted due to the large displacements induced in the cable for an equivalent tensile load. Therefore, axial tension tests were performed

to obtain a more exact stress-strain curve for the aluminum tube. The results of these characterization tests are presented in Appendix II.

The material nonlinearity of the aluminum tube is modeled as a multilinear stress-strain behavior in ADINA. This stress-strain curve is plotted in Figure 4.6, where for the linear part, the modulus of elasticity of the tube of 61.8 GPa is used.

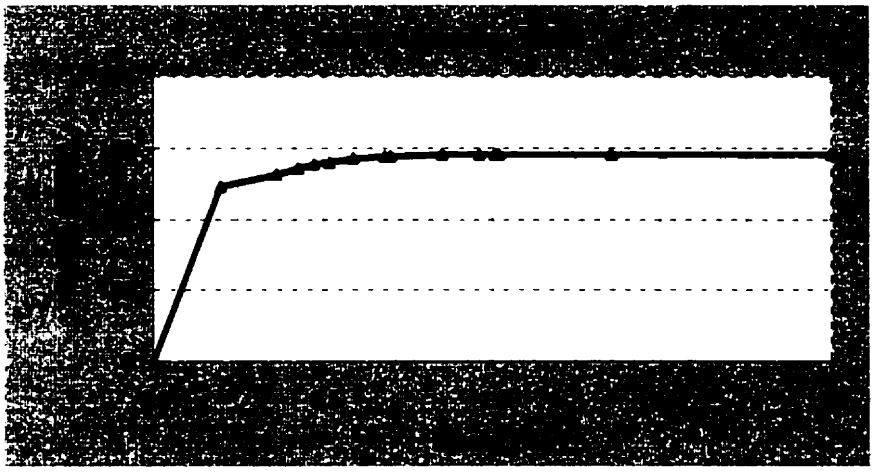

Figure 4.6 Multilinear plastic material behavior of the aluminum tube

4.3.2.3 Aluminum spacer

The geometry of the aluminum spacer is shown in Figure 4.7. It is made of Aluminum 6201, with modulus of elasticity of 64 GPa. The spacer (slotted rod) is helically twisted (*S* pattern) with a 150 mm pitch length (helix angle of 84°). The maximum and allowable stresses are 218 and 200 MPa, respectively. As it is shown in Figure 4.7, the outside diameter of the aluminum spacer is 5.15 mm, which is slightly smaller than the inside diameter of the aluminum tube (5.40 mm), and therefore, it is not touching the tube in the initial configuration. Since both the tube and the spacer are made of aluminum, it seems unlikely that they become in contact when analyzed for equal elongation. Consequently, the aluminum spacer can be analyzed separately as there is no interaction with the other components of the OPGW, provided that the maximum applied load or elongation remains equal or smaller than the load used in the analysis. For other types of loading, such as transversal loading, bending, and thermal effects, the aluminum spacer may be in contact with the central tube. In those cases, the outer surfaces of the aluminum spacer must be defined as contact surfaces while

the tube is defined as a double sided contact surface since it will be in contact from inside with aluminum spacer and from outside with the inner wires. For the prescribed displacement loading in this study, the double-sided contact surface for the tube is modeled, however, the tube and spacer surfaces had no contact during the analysis.

Although, including the aluminum spacer in the model increases the number of elements and equations in the model, however, it is modeled with no contact surface since during the analysis no contact occurred with other components of the OPGW. It is subjected to the compatible axial elongation of 1.62 mm (like the outer and inner wires and the aluminum tube) at its free surface while the other end is fixed.

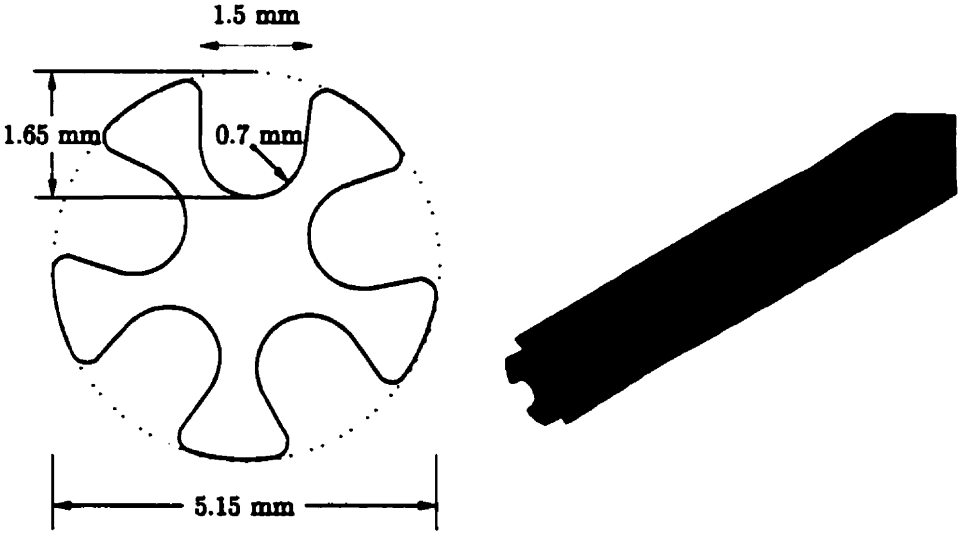

Figure 4.7 Geometry of the aluminum spacer

The material law of the aluminum spacer is modeled as a multilinear stress-strain behavior in ADINA. The stress-strain curve of aluminum spacer (Figure 4.8) is obtained by uniaxial test (see Appendix I), where for the linear part, the modulus of elasticity of the spacer is 63.8 GPa.

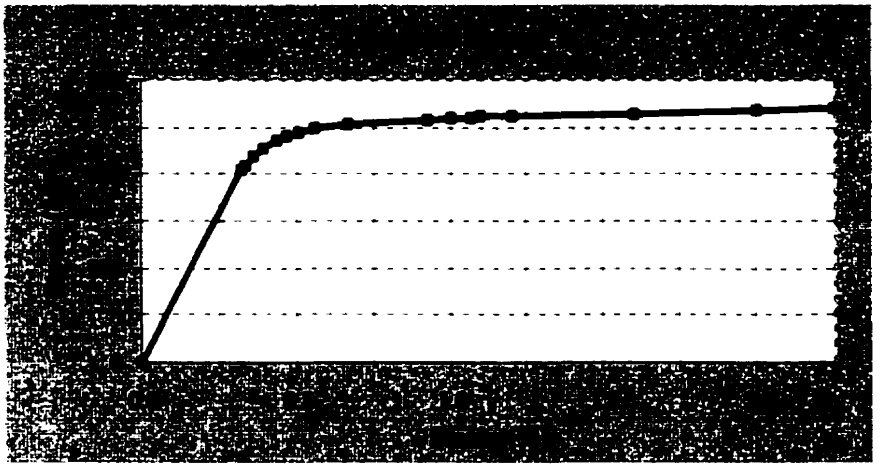

Figure 4.8 Multilinear plastic material behavior of the aluminum spacer

4.3.2.4 Boundary conditions and loading

The exact details of the attachment of the OPGW to the transmission line tower may vary with the tower type. Inasmuch as possible, continuity of the cable is assured and the OPGW is gripped in a suspension clamp. The stress-state in the cable is very complex in the vicinity of these attachment points and would require an analysis that is beyond the scope of this project. Far from the ends, however, the cable can be assumed under uniform tension. To model these conditions, one end of the cable is fixed in all translational and rotational degrees of freedom, while only the translational degrees of freedom of the loading end are free along the loading axis, letting the wires elongate freely. The other two in-plane translational degrees of freedom are fixed to prevent unwinding of the wires. For a free-end loading, these DOFs can be released. All six degrees of freedom are free for all the other nodes of the mesh. ADINA automatically restrains those degrees of freedom that are redundant.

For a length of one pitch, the stress-state is found almost invariant in a cross-section located at half pitch of the cable. End effects are discussed in more details in chapter 5. The end effects are essentially due to the fact that full contact of all the components is prevented at the fixed end where the undeformed geometry of the cross-section is prescribed. At both fixed and loading ends, spurious stresses are due to the shape of the solid model generated for the helical wire, which

forces a circular cross section for all the wires along the cable axis, whereas a cutting plane in a real cable would reveal elliptical sections.

Considering compatibility between the different components of a short segment of straight cable, it is assumed that all components (the outer, inner helical wires, the tube, and the aluminum spacer) stretch equally along the cable axis. Different types of loadings were investigated in order to achieve this condition. The load-control approach, with a uniform distributed load on each wire or a concentrated load at the center of each wire cannot achieve the compatible equal elongation in the outer and inner wires due to the effects of contact, material differences, and the helical geometry. In other words, the object of the study is to find the exact axial force applied to each component of the OPGW that is necessary to induce equal stretch. The load-control approach also resulted in convergence problems in the contact analysis, and it was found that the problem was better behaved whenever a prescribed displacement approach was used.

There are different ways to prescribe the displacements at the free end: the control can be done only at the central node of each helical wire or at all the interior nodes of the wire cross section. Prescribed displacements are not allowed on the nodes located at the perimeter of the wire cross section, since those nodes belong to contact surfaces that must be unrestricted in all degrees of freedom. Applying an axial displacement only at the central node of the wires lets the wires deform more freely along the cable axis, and consequently less stresses are induced compared to the second method where equal displacements are prescribed at all the internal nodes. Both types of loading were tested and compared with analytical and experimental solutions. Results are discussed in details in Chapter 5.

The longitudinal cable axis in the model is the global X-axis and consequently the in-plane axes are Y and Z. The equivalent elongation due to 0.61% strain of the cable is 1.617 mm ($\Delta l = \varepsilon l = 0.61\% \times 265.16 = 1.62$ mm), which is applied to all the inner and outer wires, central aluminum tube, and the aluminum spacer. As mentioned earlier, no prescribed deformations can be applied to the contact surfaces if considered contactor in defining the contact pair surfaces. For this reason, the aluminum tube is considered as target surface in contact pairs with the inner wire surfaces. Therefore, 1.62 mm elongation is applied on the

circumference of the tube and the free end surface of the aluminum spacer. This prescribed displacement will be applied to all interior nodes of the aluminum spacer.

4.3.2.5 Contact surfaces and pairs

Contact surfaces of a body are defined as surfaces that are either initially in contact or are anticipated to come into contact during the analysis. Three-dimensional contact surfaces formed of 4-node quadrilateral segments are used in the contact analysis of the OPGW. The inner and outer wires and the aluminum tube are separate entities, which are not initially in contact, but are expected to come into contact during the response solution. In general, contact between the different components of the OPGW is as following:

- contact between outer wires
- contact between inner wires
- contact between outer and inner wires
- contact between inner wires and the central tube
- contact between the central tube and the aluminum spacer.

The last contact is not observed during the response solution, as the gap between the inside diameter of the central tube and the aluminum spacer is large enough to keep both surfaces separated. The contact between the outer wires can be prescribed as self-contact, and consequently all the circumferential surfaces of the 3-D solid elements describing the outer wires is modeled as one contact surface. The same applies to the inner wires. Therefore, three 3-D contact surfaces are defined in ADINA as;

contact surface 1 : surface of the central aluminum tube,
contact surface 2 : all the circumferential surfaces of the inner wires, and
contact surface 3 : all the circumferential surfaces of the outer wires.

The contact surfaces that are expected to come into contact during analysis must be defined as *contact surface pairs*, where one surface is defined as the *contactor surface* and the other as the *target surface*. It is preferable to define the stiffer surface as the target surface (ADINA R&D 1999). As a result, the contact surface pairs are;

Table 4.1 Contact surfaces and pairs

Contact surface pairs	*Contactor surface*	*Target surface*
1	2	1
2*	2	2
3*	3	3
4	3	2

* self contact

Contact analysis is solved for frictionless contact ($\mu = 0$) and with Coulomb friction ($\mu > 0$). The static friction coefficient of 0.33 is used between all the contact surfaces (Davis 1994, Rabinowicz 1995). This value is based on the contact between aluminum surfaces. The inner wires are made of aluminum-clad steel, i.e. they are coated with a very thin layer of aluminum (0.191 mm). Therefore, the contact between the inner wires, and between the inner wires and the aluminum tube, and between the outer wires is essentially contact between aluminum surfaces. The thickness of the aluminum coating of the inner wires is too small to be modeled and its effect is only considered for the coefficient of the friction. The purposes of the cladding are to protect the steel wires against corrosion and to maximize the cable conductivity.

In general, a better mesh is obtained when the segment length on the contactor and the target surfaces are approximately equal. This is also considered in the mesh of the contact surfaces, as there are multiple contact surface pairs.

4.3.2.6 Model information

The information of the complete OPGW model (coarse mesh) including the aluminum spacer is;

Number of elements: 12,672 three-D solid and 256 shell elements
Number nodes: 15,087
Number of equations including contact: 59,128
Number of contact equations: 15,744

4.4 Stress analysis

4.4.1 Static displacement and stress analysis

The sparse matrix solver algorithms are used to solve the equilibrium equation of the system. ADINA 7.3 (1999) features sparse solvers in addition to *direct* and *iterative* solvers. However, the sparse solvers have been proven to yield drastic reduction in solution times, being almost twice as fast as direct solver, and with the least overall memory. The stiffness updates are based on a Full-Newton scheme with and without line search, with a set limit of ten iterations per load increment. It was found that using the Full-Newton iteration method without line search was less costly. An energy-based convergence tolerance (Eq. 4.14) is used (ETOL=0.001). The convergence line search tolerance (STOL) of 0.1 is also considered (Eq. 4.13) whenever applicable. The total number of steps necessary for convergence varied between 35 and 50 steps, depending on the model and loading conditions. Automatic-Time-Stepping (ATS) is used to obtain a converged solution whenever the predefined time steps are too large. Using this method, the program automatically subdivides the total load step increment so as to reach convergence. The maximum number of subdivisions is set to 512. The number of time steps is selected in such a way that ATS is only used for one or two steps.

As mentioned previously, the contact analysis is based on constraint functions (Algorithm 1 in ADINA, 1999). In Algorithm 1, only the contact states at the contactor nodes are considered, while in Algorithm 2 (Lagrange multipliers), the actions on the contactor segments are used to determine the states of the contactor nodes. Algorithm 1 is used in contact analysis since the convergence rate is usually better for frictionless contact compared to Algorithm 2, as recommended in ADINA (1999). The parameters ε_N (Eq. 4.27) and ε_T (Eq. 4.28) are set to 10^{-8} and 0.1, respectively, when friction is included. The convergence tolerance for the contact forces is RCTOL = 0.1 (Eq. 4.29) and NSUPPRESS which indicates the number of iterations for target segments in order to suppress oscillation between adjacent segments is set to 5 (Bathe 1996). Such oscillation can occur when a contactor node approaches the junction between two adjacent target segment. Using NSUPPRESS allows for such oscillation to be detected and eliminated (ADINA 1999).

$$\text{RCTOL} \geq \frac{\text{CFORCE}}{\max(\text{CFNORM}, \text{RCONSM})} = \frac{\left\| \mathbf{R}_c^{(i-1)} - \mathbf{R}_c^{(i-2)} \right\|_2}{\max\left(\left\| \mathbf{R}_c^{(i-1)} \right\|_2, \text{RCONSM} \right)} \qquad (4.29)$$

where the parameter CFORCE is the norm of the contact force increment between two iterations ($\mathbf{R}_c^{(i-1)}$ is the contact force vector), CFNORM is the norm of contact force vector, and RCONSM is a pre-set reference contact force level (0.01) used to prevent possible division by zero.

4.4.2 Pitch length effect on the wires

The finite element model of the OPGW needs to be reliable and accurate. In finite element analysis, it is very efficient and economical to use symmetry of the structure wherever possible. Generally, using geometrical symmetry and limiting the size of the model significantly reduce the analysis time, and yields good accuracy provided appropriate boundary conditions are applied. The helical shape and the composite cross section of the OPGW make it impossible to apply any symmetry in order to reduce the size of the model. However, along the cable axis, the model can be restricted to one, two, or three pitch lengths. In order to verify the effect of pitch length on the response, a model was studied that consisted of the central tube and only one inner wire for the three different pitch lengths (one, two and three) as discussed in chapter 5.

The above model is incapable of predicting the real behavior of the cable as the inner wire is not restricted by the other inner and outer wires. However, it can be used to verify the influence of the pitch length on the response. It is worth noting that the pitch length effect was impossible to verify with all the components of the OPGW or even with the inner wires alone as the computational facilities available to conduct this research were insufficient. To this end, the above one-wire-and-tube model is analyzed by ADINA, where the boundary conditions of the loading end are fixed for in-plane degrees of freedom. The results are discussed in the next chapter.

4.4.3 Inner wires and the aluminum tube

The modeling of the OPGW is very complex and requires a great computational effort. As a first step of any finite element analysis, it is better to analyze some parts of the model and then improve it until a more complete model is obtained. Therefore, the first step to model the whole cable was to model the aluminum tube with the inner wires only. The results of this one-pitch model with different boundary conditions and loadings are compared with analytical solutions. This model can be considered as a benchmark for the OPGW modeling. Two boundary

conditions at the free (loading) ends are modeled; the in-plane translations are fixed to prevent any unwinding rotation, and the end is free to allow the wires to unwind. The former boundary conditions is more realistic of transmission lines applications, however, the latter is modeled to verify results and compare the unwinding motion calculated with the analytical solutions by Machida and Durelli (1973) and Phillips and Costello (1973). The finite element model of the inner wires and the aluminum tube for one pitch length (265.16 mm) is shown in Figure 4.9. A detailed discussion of the results is presented in the next chapter.

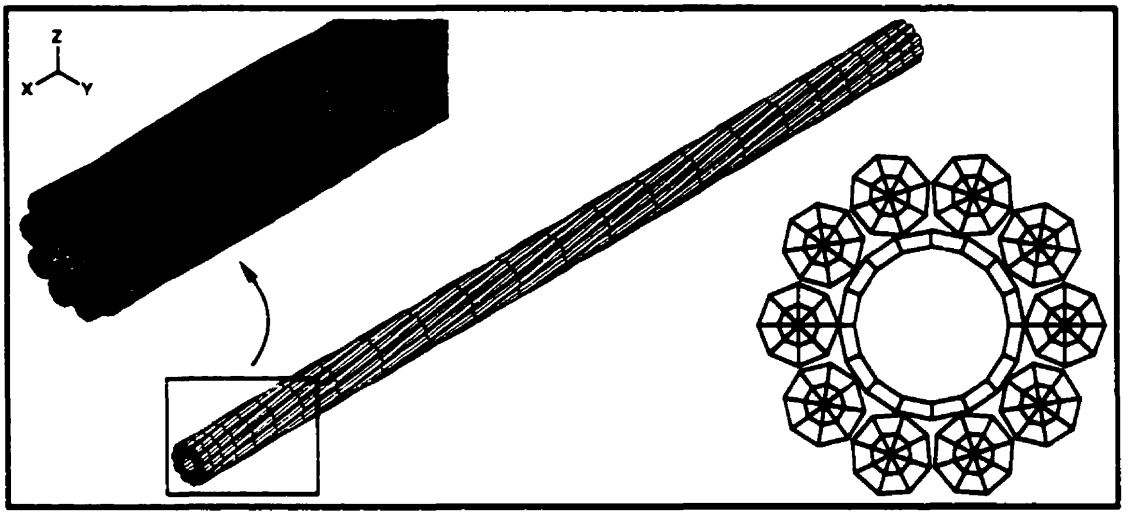

Figure 4.9 Finite element mesh of the inner wires and the central tube (one-pitch length)

4.4.4 OPGW

The OPGW model consists of all the components of the cable excluding the optical fibers unit. The response of the optical fiber units is considered as being identical as that of the aluminum spacer plus the excess length. The optical fiber units are impossible to include in the model since their cross section is too small (0.0123 mm^2) to be efficiently modeled in 3-D contact with the aluminum spacer. The outer wires are modeled like the inner wires with finer mesh at the ends; since their pitch length (202 mm) is smaller than that of the inner wires (265.2 mm), an additional length is modeled in order to reach the same length as the inner wires. The opposite helix directions of the outer wires and the inner wires are also considered. The finite element model of the inner and outer wires is shown in Figure 4.5. The finite element mesh of the aluminum spacer is shown in Figure 4.10. Its pitch length is 150 mm (S pattern).

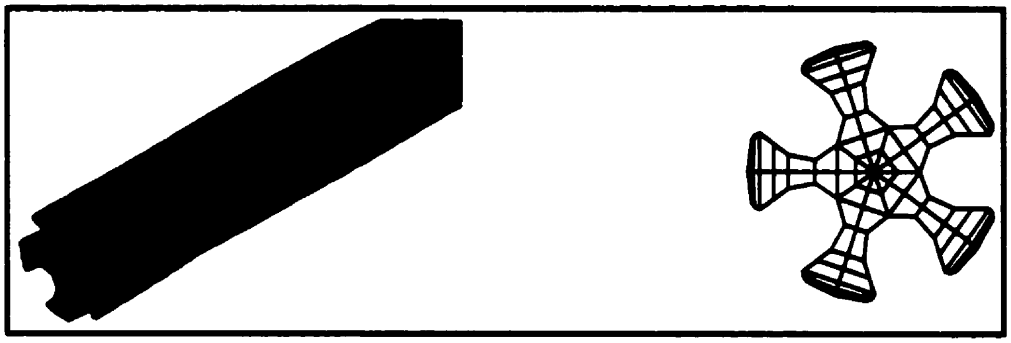

Figure 4.10 Finite element mesh of the aluminum spacer

4.5 Post-processing of results

Results of the finite element stress analysis are stored in a porthole file that can be accessed by ADINA-PLOT. Detailed results and discussions of the different models are presented in the next chapter. It is necessary to describe some of the special features that are used in ADINA-PLOT to present the results of the numerical model.

The results computed by ADINA are stresses, forces, reaction forces/moments, and segment tractions or forces for contact surfaces. Results can be obtained at nodes, element sections or layers, and on contact segments. There are different approaches to evaluate the results. If an element/layer variable such as a stress is requested within an element at a point; the variable is interpolated as follows;

- *RST interpolation* : the variable is interpolated using the nearest integration points and bilinear interpolation.
- *Face interpolation* : the results at the nearest element face are used.
- *Centroid interpolation* : the results at the element centroid are used.
- *Integration point interpolation* : the results at the nearest integration point are used.

Besides different interpolation schemes, the element section results can be smoothed, i.e. made continuous between adjacent elements. Hence, the contributions of each element are combined into a single result, as specified by the type of smoothing. In this study, the *averaged* smoothed results are obtained.

5

RESULTS AND DISCUSSION

5.1 Pitch length effects

Detailed state-of-the-art finite element modeling of the OPGW demands very high capacity and powerful computing facilities. In order to minimize the size of the model and its computational cost, the optimum length of the cable model needs to be assessed. The optimum ratio of the diameter to the length of the cable (called aspect ratio) is undefined in the literature and the theoretical aspect ratio for beams or shells is inapplicable for the OPGW due to its helical shape and composition. To study this parameter, three lengths of one, two, and three pitch lengths for a model comprising only one inner wire and the tube are studied. In the absence of the other inner wires, the single wire rotates around the tube as there is no restriction from contact with adjacent wires, which results in asymmetric response in the central tube. It is noteworthy that the actual behavior of the OPGW is completely different from that of these one-wire-and-tube models, however, the optimum length of the model can be assessed with this simplification. All degrees of freedom of the aluminum tube and the wire cross

sections are fixed at one end, while only the in-plane translational degrees of freedom (Y and Z) are fixed for the tube at the loading end. This fixity is applied to reflect the overall symmetric behavior of the tube in the presence of all the wires.

5.1.1 One inner wire - one-pitch length

Figure 5.1 shows the model of one inner wire for one-pitch length (265.16 mm). The aluminum tube and the wire (all interior nodes) are subjected to an axial elongation of 1.62 mm, equivalent to a 0.61% cable axial strain, assuming linearity between the strain and the stretch, and neglecting three-dimensional effects.

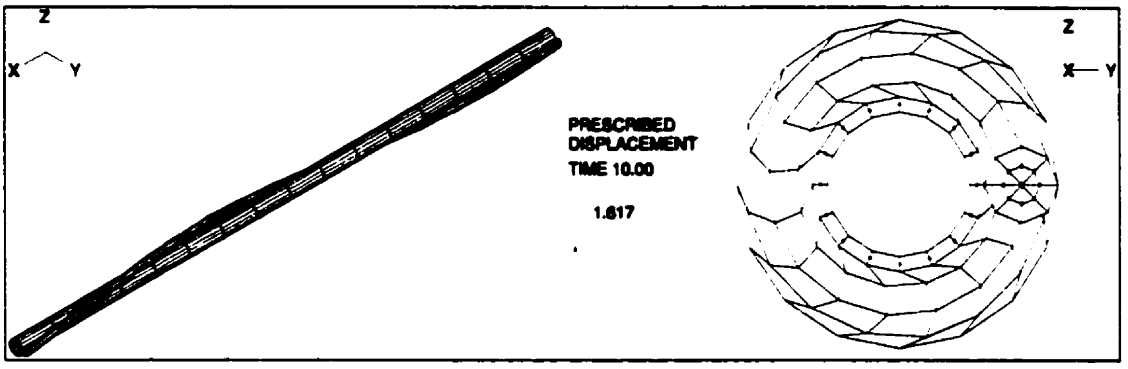

Figure 5.1 One-pitch single wire and the aluminum tube model

The axial stress (σ_{xx}), strain (ε_{xx}), and displacement (δ_{xx}) distributions over the cross section located at half pitch length, i.e., at 132.58 mm from the fixed end, are presented in Figure 5.2, together with the x-displacements of the complete model.

The results indicate that the normal stress in the X-direction varies within the wire cross-section, which results from combined axial tension and bending due to the helical geometry. The stresses and strains plotted are smoothed values (average values with linear interpolation). The extreme values of stresses are 766 MPa and 353 MPa, respectively, corresponding to an average tensile stress of 560 MPa and maximum bending stresses of ±206 MPa. The average strain at the center of the wire is 0.34%, corresponding to a 0.8 mm elongation.

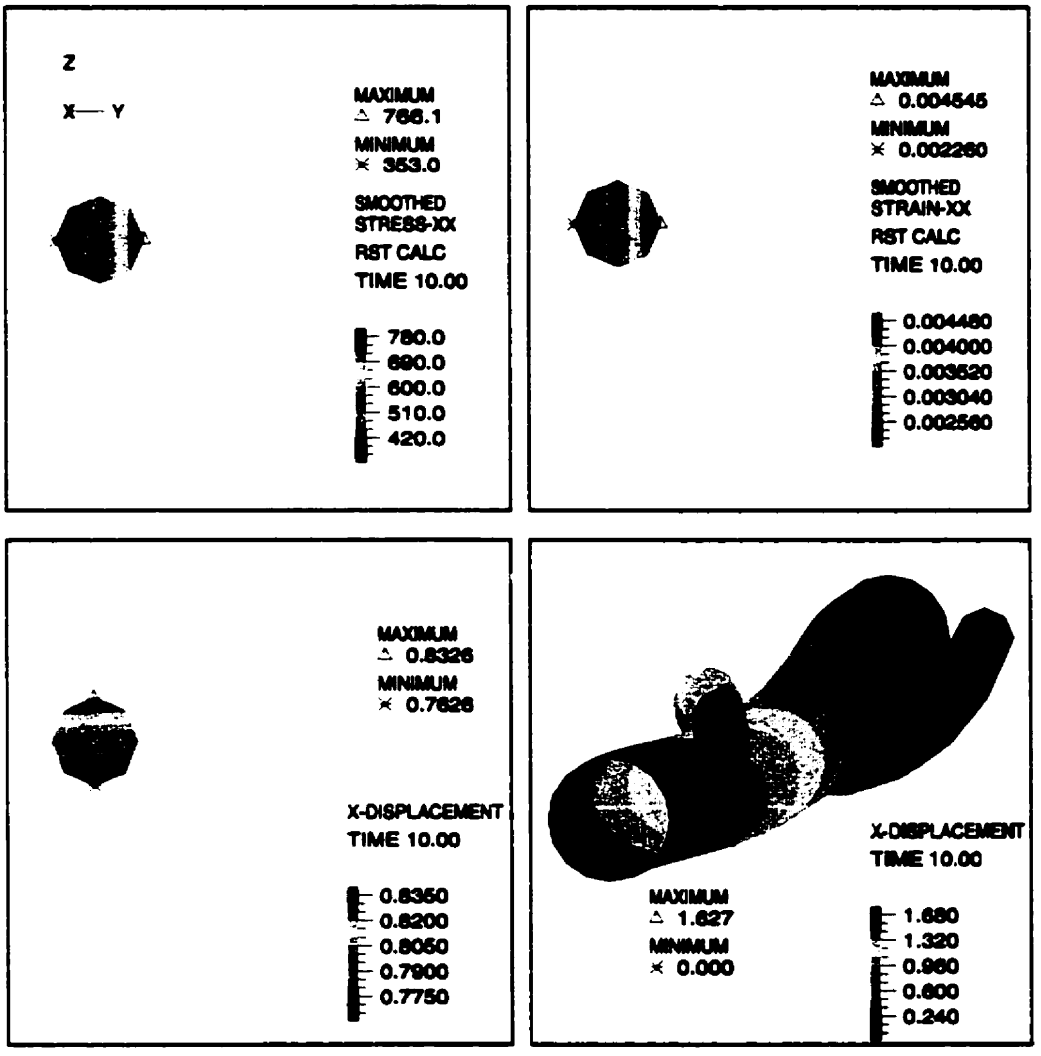

Figure 5.2 Stresses, strains, and displacements of a wire at half pitch length (one-pitch model)

If a linear strain-displacement relation ($\varepsilon=\Delta l/l$) is assumed, then the strain is 0.6% (0.8/132.58). The results confirm the nonlinear behavior of strain vs. displacement. As a result, for a maximum strain of 0.45%, which is 74% of the prescribed cable strain (0.61%), the maximum normal stress (766 MPa) is 79% of the stress (970 MPa) predicted by Machida and Durelli (1973), and Phillips and Costello (1973).

Figure 5.3 illustrates the nonlinearity of the longitudinal strain versus displacement for the center of the wire at half-pitch length. The calculated strain (0.34%) is about 56% of the assumed linear strain of 0.61%.

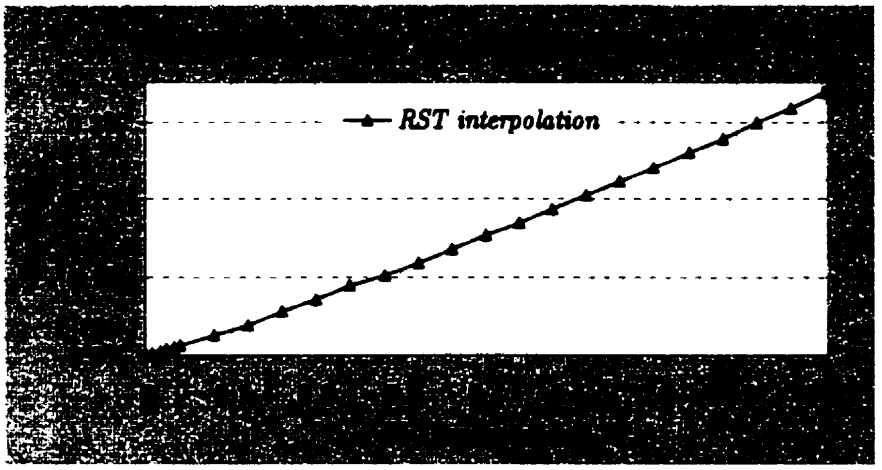

Figure 5.3 Nonlinear response of a wire at half-pitch length (one-pitch model)

The end effects on the calculated stresses are illustrated in Figure 5.4. The stress along the wire axis is plotted for the center node. It is seen that the end effects are limited to only a few end elements, and the stress is almost constant along the wire.

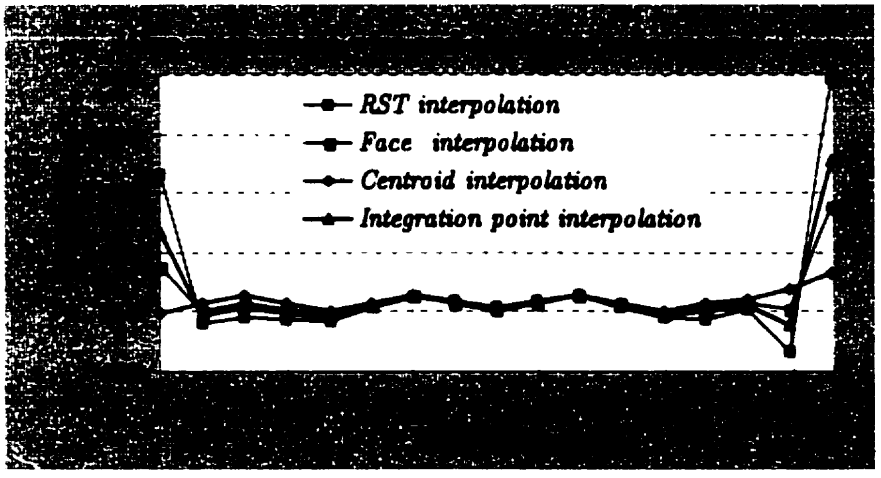

Figure 5.4 End effect and stress distribution along a wire (one-pitch model)

The stress graphs plotted in Figure 5.4 are calculated using different schemes in ADINA-PLOT as discussed in section 5.4. It is observed that the calculated normal stresses (σ_{xx}) are identical at half pitch length using all evaluation techniques (RST, face, centroid, and integration point interpolation). The results also indicate that the end effects are minimal when using the results at the element centroid (centroid interpolation). In general the RST interpolation scheme is used in which

the variable is interpolated or extrapolated using the nearest integration points and bilinear interpolation.

The strain versus displacement of the center of the wire is plotted in Figure 5.5. It is seen that the strain is varying between 0.3% and 0.4%, neglecting the end effects. This range is far from the one-dimensional cable strain of 0.61%, which means that the three-dimensional effects (Poisson's effects and helical geometry) are significant and should not be ignored.

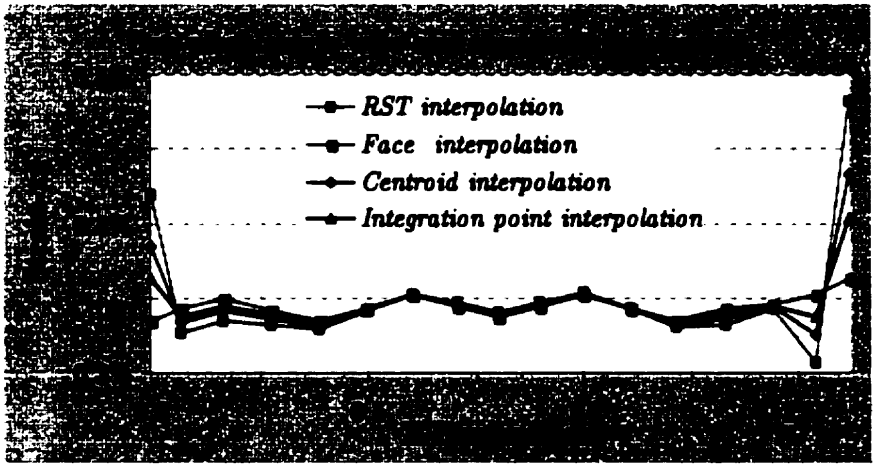

Figure 5.5 Strain-displacement relation along the center of the wire

The aluminum tube is also subjected to a prescribed axial elongation of 1.62 mm. The surface of the tube is considered the target surface here, and the outer surface of the wire is the contactor since only its interior nodes are subjected to the prescribed displacements.

It is observed that the aluminum tube yields under such a deformation. Consequently, the nonlinear stress-strain curve obtained from a uniaxial tensile test is used to define the material properties of the aluminum tube (see Figure II.1, Appendix II).

The total reaction force at the loading end of the tube needed to induce a 1.62 mm elongation is 2162 N.

5.1.2 One inner wire - two-pitch length

The model of one inner wire for a two-pitch length (530.32 mm) is shown in Figure 5.6.The aluminum tube and the wire (all interior nodes) are subjected to an axial elongation of 3.24 mm, equivalent to a 0.61% cable axial strain.

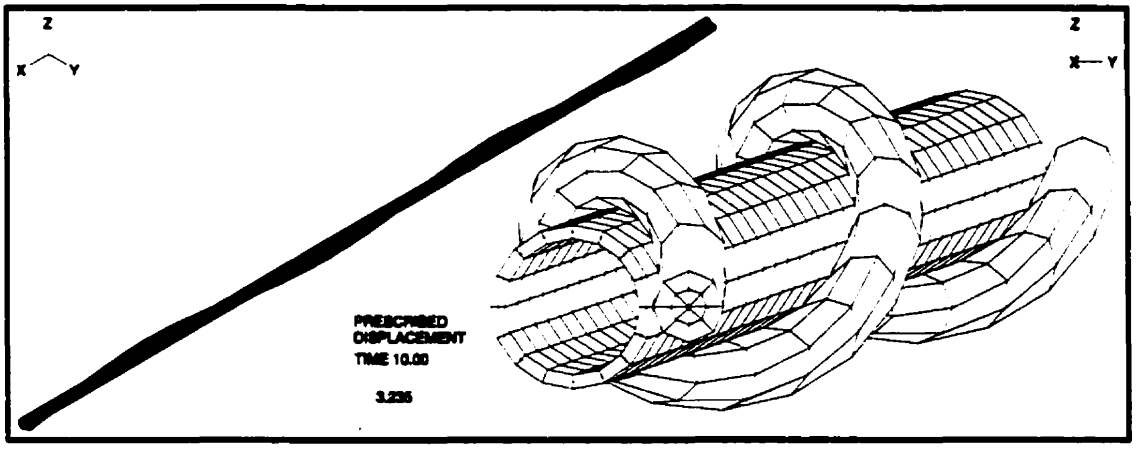

Figure 5.6 Two-pitch single wire and aluminum tube model

The axial stress (σ_{xx}), strain (ε_{xx}), and displacement (δ_{xx}) distributions are presented in Figure 5.7 over the cross sections located at half-pitch and at one-pitch, i.e., at distances of 132.58 mm, 265.16 mm, and 397.74 mm from the fixed end. These cross-sections are selected for comparison with the results of the one- and three-pitch length models.

As expected, the maximum normal stress in the X-direction at different pitch lengths is almost the same. The extreme values for half and one-and-half pitch lengths are 715 MPa and 317 MPa, corresponding to the average tensile stress of 516 MPa and maximum bending stresses of ±199 MPa. At one-pitch length, these values are almost the same as the average tensile stress is 514 MPa and the maximum bending stress ±198 MPa. In fact, no significant variations are observed in the stresses at different cross sections located far from the ends. The average strain (0.31%) is exactly the same at the different cross sections considered.

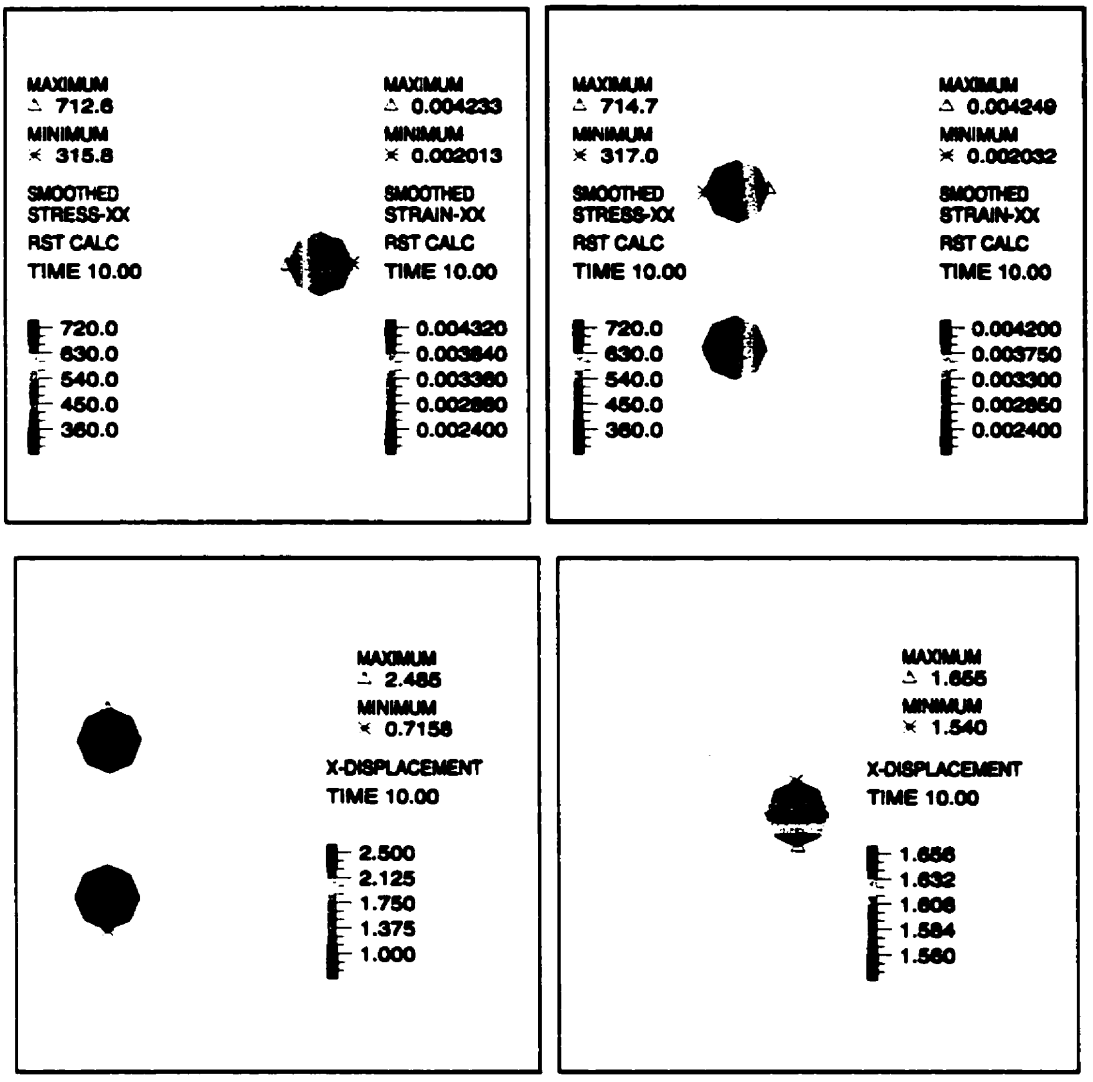

Figure 5.7 Stresses, strains, and displacements in two-pitch one-wire model at half-, one-, and one-and-half pitch lengths

The consistent contact force and normal stress in the aluminum tube is presented in Figure 5.8, where the asymmetric deformation of the tube is due to the presence of only one wire.

The viewpoint in Figure 5.8 exaggerates the deformed shape. Ignoring the end effects, the normal stress in the tube varies from 130 MPa to 155 MPa. The maximum contact force is 30 N, and is acting along the contact line between the wire and the tube. In the presence of all the wires, the contact force reduces the normal tensile stress in the tube.

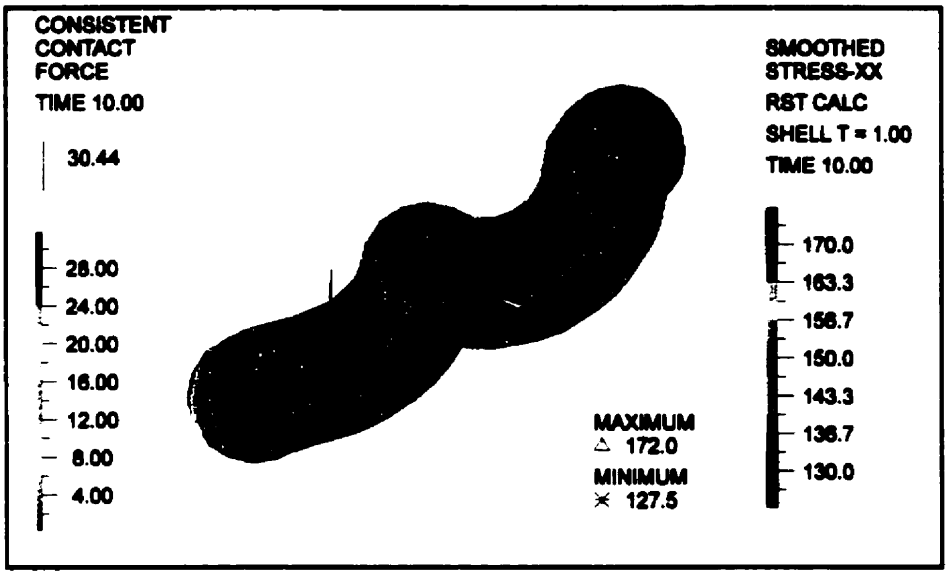

Figure 5.8 Normal stress and contact force in the tube (two-pitch model)

5.1.3 One inner wire - three-pitch length

The three-pitch length of a helical wire and the central tube model is illustrated in Figure 5.9.

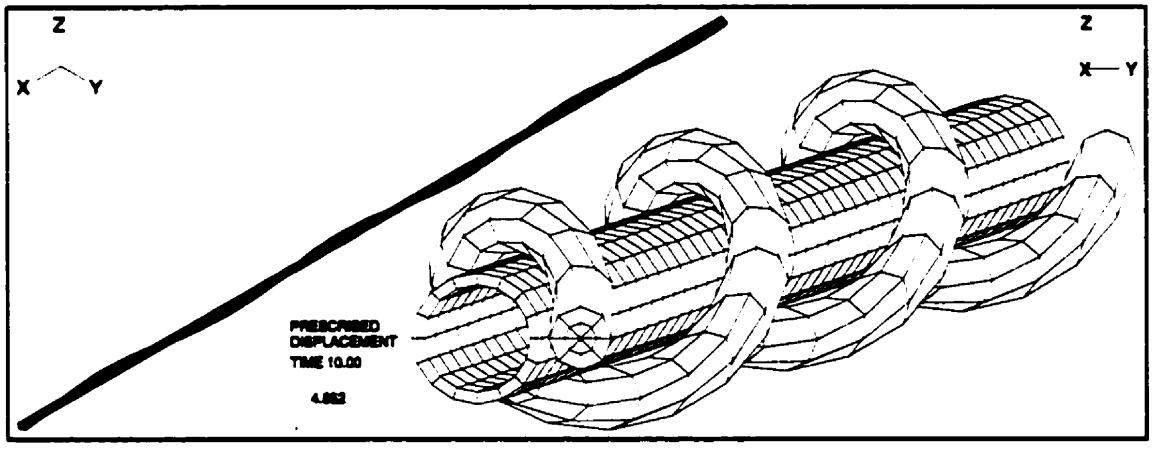

Figure 5.9 Three-pitch single wire and aluminum tube model

It is noted that the aspect ratio of the wire in this model is about 280 and the tube is more than 120. The aluminum tube and the wire are subjected to an axial stretch of 4.85 mm, corresponding to a 0.61% axial cable strain (4.85/795.78). All properties of the model remained the same as for the one- and two-pitch length models. The response of the wire at different cross sections along the three-pitch-length model is presented in Figures 5.10 and 5.11.

The stress and strain distributions are practically the same at all cross sections of the wire with negligible variations far from the ends. The maximum and minimum normal stresses are 697 MPa and 278 MPa, respectively, corresponding to an average tensile stress of 492 MPa, and maximum bending stresses of ±205 MPa. The average axial strain is of only 0.3%.

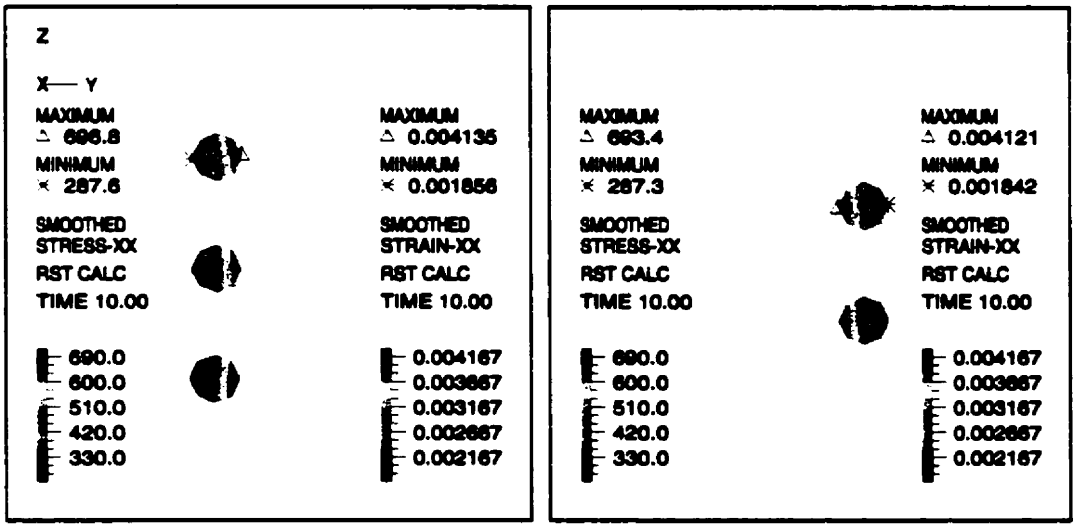

Figure 5.10 Axial response of the three pitch length model of an inner wire

Figure 5.11 shows the contact force acting along the wire axis. The maximum concentrated contact force is 28 N, and the maximum stress in the aluminum tube exceeds the maximum allowable stress (146 MPa).

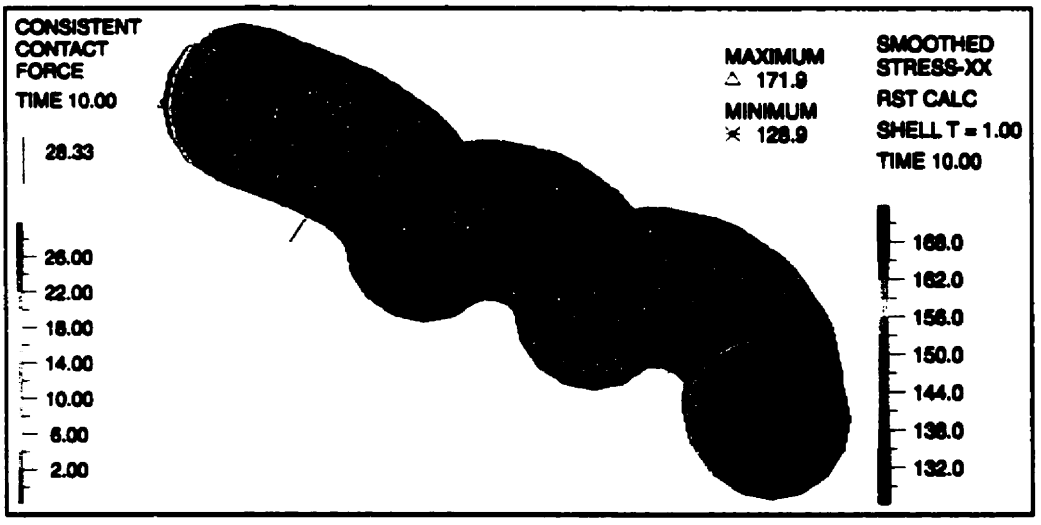

Figure 5.11 Normal stress and contact force in three-pitch length model

The axial stress at the contact surface between the wire surface and the tube is reduced to about 140 MPa. It is noted that the above series of analyses (including those for one- and two-pitch models) were carried out for frictionless contact ($\mu = 0$), which allowed the wire to slide over the tube surface

5.1.4 Comparison of the results of the three models

The stresses and strains at the center of the wire along the cable axis are plotted in Figure 5.12, excluding the end effects that are limited to only one element length at each end.

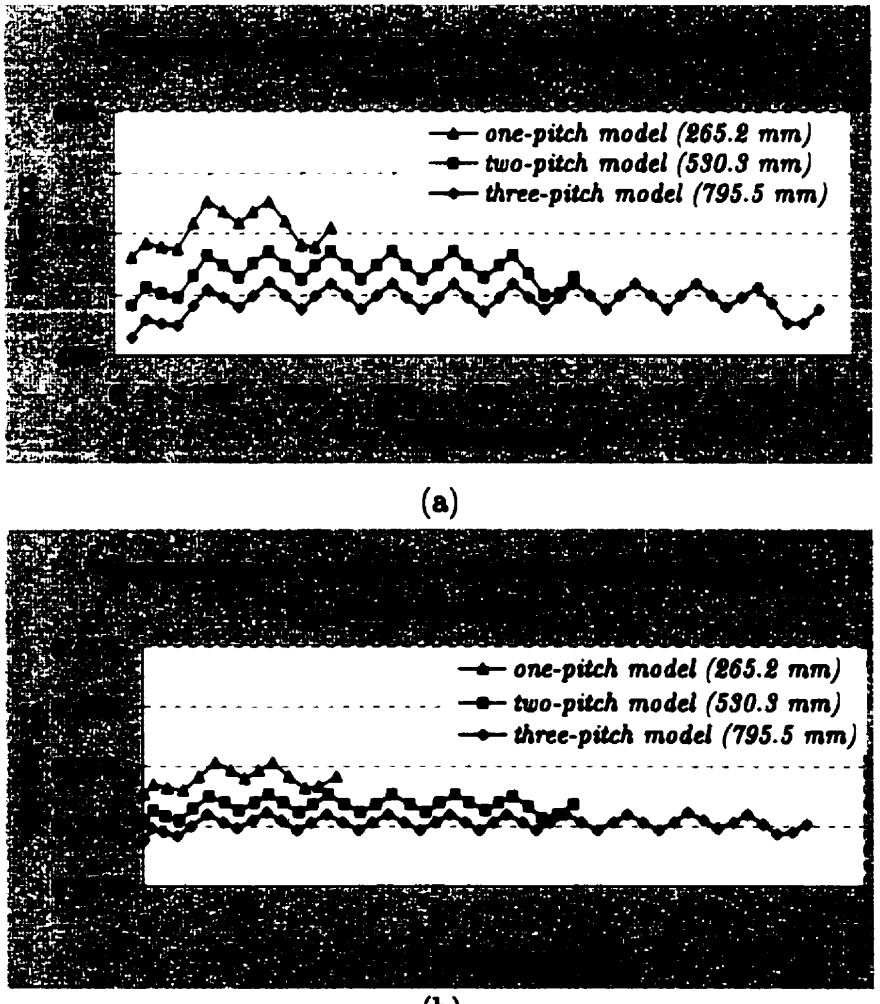

Figure 5.12 (a) σ_{xx}, and (b) ε_{xx} of the three different pitch length models

The results of the above three models are summarized in Table 5.1.

Table 5.1 Summary of stress-xx and strain-xx of three models

Model	Min. and Max. of σ_{xx} (MPa)				
	half-pitch	full-pitch	1 1/2-pitch	two-pitch	2 1/2-pitch
One-pitch	353-766	—	—	—	—
Two-pitch	318-711	316-713	317-715	—	—
Three-pitch	289-692	287-692	290-687	287-693	288-697

Model	Min. and Max. of ε_{xx} (%)				
	half-pitch	full-pitch	1 1/2-pitch	two-pitch	2 1/2-pitch
One-pitch	2.2-4.5	—	—	—	—
Two-pitch	2.0-4.2	2.0-4.2	2.0--4.2	—	—
Three-pitch	1.9-4.1	1.8-4.1	1.9-4.1	1.8-4.1	1.9-4.1

As it can be seen, the maximum and minimum normal stress and strain along the cable axis decrease when the pitch length increases. However, the maximum difference in the results is less than 10%. For the longer models, the influence of the stiff boundary conditions at the fixed end is less and overall strain energy dissipation is greater than for the shorter models. Despite the larger stresses and strains of the one-pitch model, the comparison shows that the one-pitch model is sufficiently accurate and reliable for the OPGW model. The accuracy obtained by increasing the model length is not significant if compared to the computational effort. As a result, the minimum and optimum length of the model is considered to be the *one-pitch length*.

5.2 Inner wires and aluminum tube model

The next step in modeling the OPGW is to consider all the inner wires around the central tube. The finite element mesh of this model is presented in Figure 5.13, for a full-pitch length (265.16 mm). Ten aluminum-clad steel wires of 2.85 mm in diameter are helically twisted (83.7° helix angle) around the aluminum tube. The steel wires are subjected to a prescribed axial displacement of 1.62 mm, either at all the internal nodes of their free cross section, or only at their central node. The latter is an alternative to impose the stretch on the wires with less restriction on the deformed cross-sectional shape of the wires than with the former loading procedure. In general, these two different loading procedures produce the same overall response of the cable. The in-plane degrees of freedom of the wires and the tube at the loading end are either fixed or free. The free-end boundary

conditions let the wires unwind due to the effect of the helical shape, therefore, the reaction torque at the free end is zero. Conversely, when the in-plane degrees of freedom are fixed, theoretically no unwinding occurs due to the resistant torque. It is noted on Figure 5.13 that the finite elements mesh of the inner wires is finer near the ends.

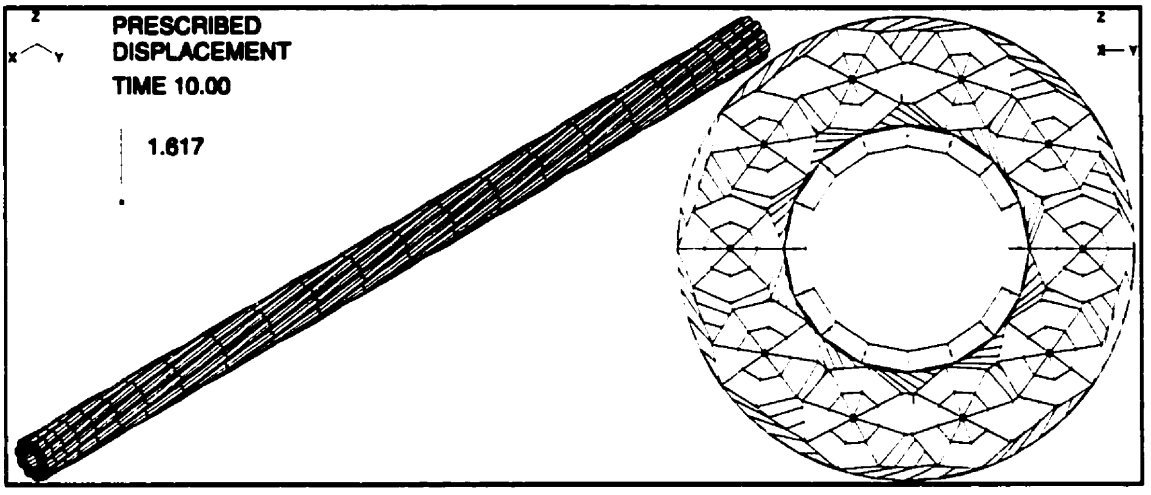

Figure 5.13 Ten-wire and aluminum tube model

5.2.1 Inner wires and aluminum tube - only wires are loaded

In the analysis of the cable, the inner wires are elongated under the applied loads. However, the actual behavior of the central tube is uncertain when the OPGW is subjected to a given tensile load either in a suspension catenary or in the laboratory experiments performed at IREQ (see Appendix II). Nevertheless, the elongation of the optical fibers in the helical aluminum spacer is observed. Since the aluminum spacer and the optical fibers are located inside the tube, it can be postulated that the tube also elongates in compatibility with the wires. This assumption needs to be verified numerically, and it is important to understand how the inner wires can affect the elongation of the tube, with or without friction effects. Consequently, in the inner wires and tube model, only the wires are loaded (1.62 mm prescribed elongation) and no load is applied to the tube. The results for the contact with friction (μ=0.33) and frictionless contact (μ=0) are presented in Figures 5.14 and 5.15, respectively. It should be noted that the results of the wires are not reported along their axis of symmetry (helix) but along the cable axis (or tube), therefore non-symmetric results are expected. Numerical inaccuracies inherent to nonlinear analysis are also inevitable, which may add to the slight non-symmetry of the results.

The presence of friction in contact between the cable components is inevitable and its effect seems to be significant as the aluminum tube elongates by as much as 0.32 mm, while the elongation is negligible (0.05 mm) without friction. The maximum stress in the tube is 163 MPa in the presence of friction corresponding to a 0.2% axial strain, which indicates that the tube is yielded even without being subjected to any direct tensile load. The finite element effective stress at the integration points of the tube is 134 MPa, and it is seen that the tube is plastified.

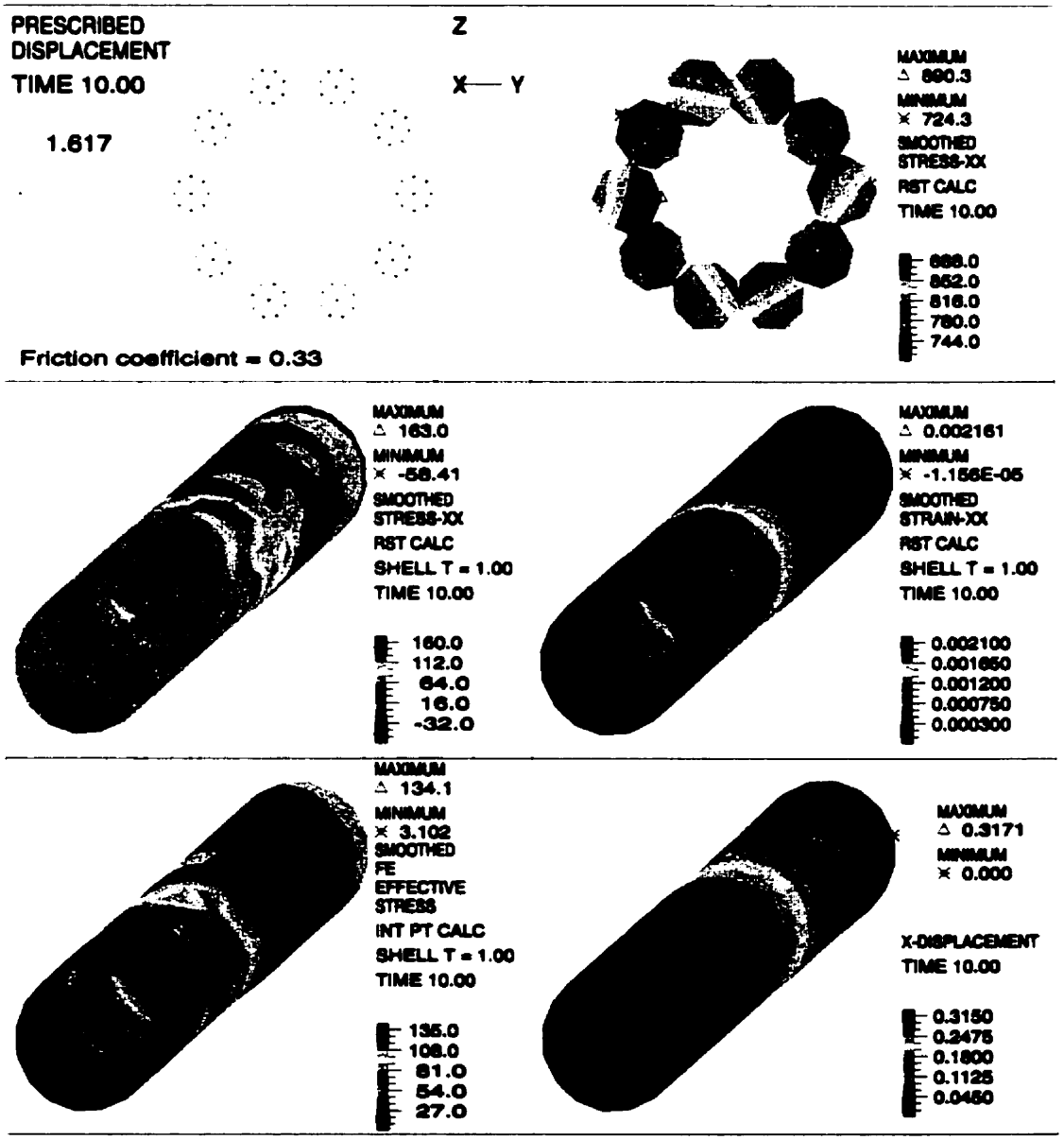

Figure 5.14 Inner wires and central tube responses (with friction μ=0.33)

The average strain in the cable is only 0.1%, which means that the plastic elongation of the tube exceeds the excess length (0.018%) of the optical fibers. The maximum normal stress in the wire cross sections located at half pitch length (132.6 mm) is 890 MPa, which corresponds to an 855 MPa average tensile stress and ±35 MPa bending stresses. The bending stress is as high as 50 MPa in the other wires.

In the frictionless analysis, the maximum values of σ_{xx} and ε_{xx} in the aluminum tube are 91 MPa and 0.03%, respectively (see Figure 5.15). The effect of friction between the wires and the tube are therefore significant and cannot be ignored. To verify the sensitivity of the analysis to the coefficient of friction, different coefficients (0.25, 0.3, and 0.4) were considered but the differences in the results were found negligible.

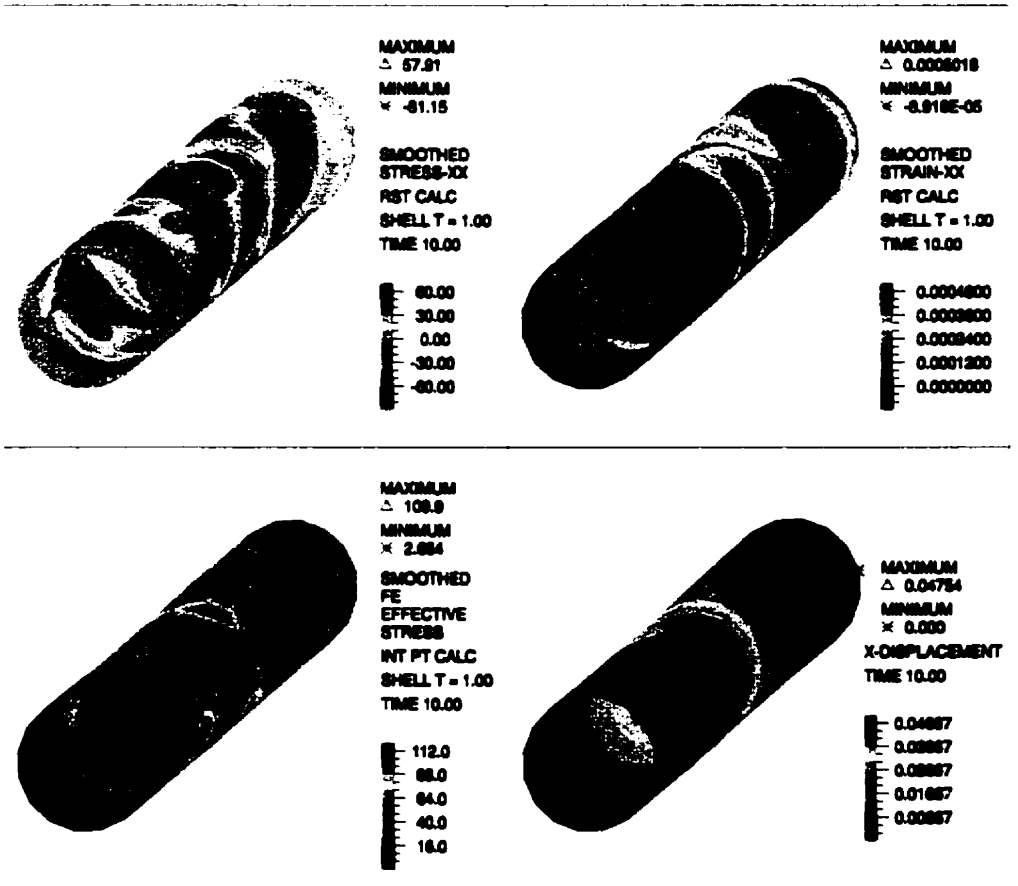

Figure 5.15 Central tube response in frictionless contact (μ=0) (only inner wires are loaded)

There is almost no difference in axial stress in the wires in a frictionless and a friction contact analysis. The maximum normal stress in the cable (not shown here) is 885 MPa, equivalent to an 845 MPa average stress and ±40 MPa in bending stresses. As a result, the friction between the inner wire surfaces is negligible compared to the friction between the tube and the wires. These analyses were also carried out for the loading (prescribed displacement) applied only at the center of the inner wires, and the behavior of the tube was found to be the same. Therefore, the results are not presented here.

5.2.2 Inner wires and aluminum tube model - compatible displacements

As mentioned before, the optical ground wires used in transmission lines are either clamped to towers at both ends of a span, and/or continuous over the tower suspension joint. In either case, the rotation of the OPGW is restricted against unwinding. In the model, the in-plane degrees of freedom (Y and Z) are fixed at the loading end cross section of all the wires and stretching of the cable is allowed along the X-axis. Two loading cases are analyzed: prescribed displacement at the center of each wire, and prescribed displacement at all the interior nodes of each wire cross section. These cases are also considered in frictionless and with friction analysis.

The displacement-control approach is used for both the tube and the wires, in which the exterior surface of the tube is considered as a target surface in contact pair with the wires as contactor surfaces. A prescribed displacement of 1.62 mm is applied to both the inner wires and the central tube. All degrees of freedom at the loading end of the central tube are free. The results of the case when all interior nodes are prescribed an equal displacement in a friction analysis are presented in the next section. The numerical results of the other cases are summarized in Table 5.2.

It can be assumed that the tube elongates as much as the inner wires due to displacement compatibility. The experiments have also revealed that after the fiber excess length has been stretched some elongation is induced in the optical fibers inside the central tube.

5.2.2.1 Stresses and displacements

Figure 5.16 shows the loading end cross section and X-displacement of the inner wires at half pitch length. The displacements of the wires along the cable axis are practically constant over the cross section. The average displacement is 0.8 mm which is exactly half of the prescribed displacement at the full pitch length. Therefore, the displacement of the wires along the cable axis is linear.

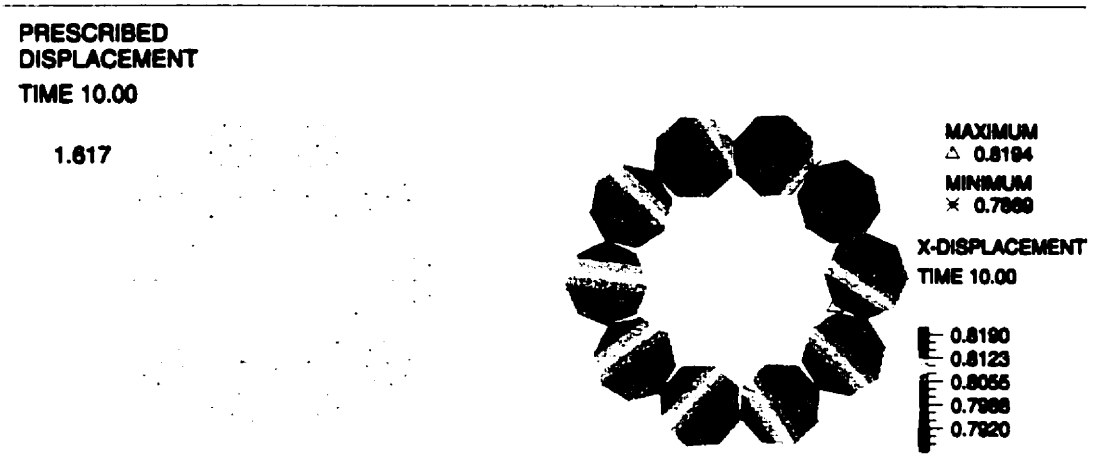

Figure 5.16 Loading section and displacements of the wires along the cable axis (contact analysis with friction, μ=0.33)

The averaged smoothed stress and strain of the inner wires are presented in Figure 5.17.

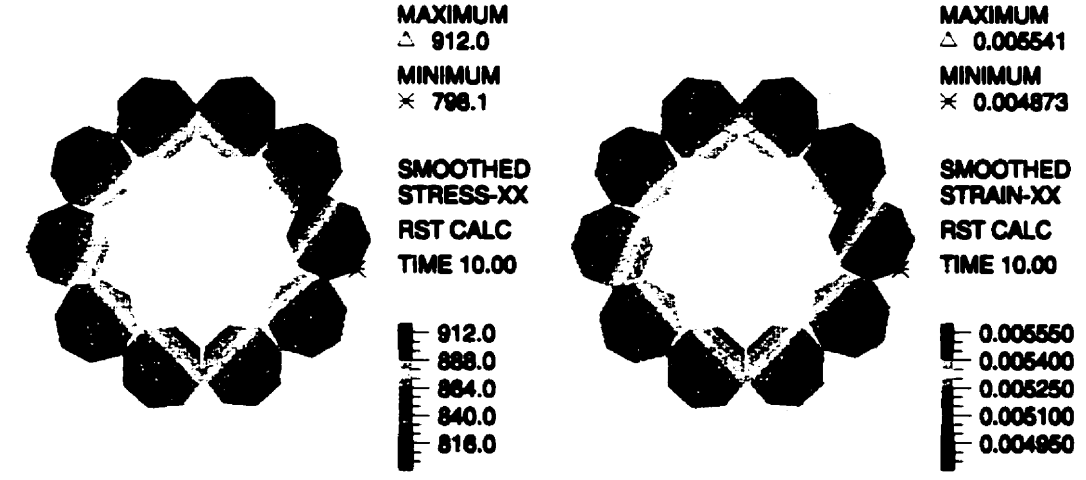

Figure 5.17 Smoothed stresses and strains in the wires along the cable axis

The extreme values are located on one wire, while the response of all wires is similar. The normal stresses in the wires vary between 798 and 912 MPa, corresponding to an 855 MPa average normal stress and ±57 MPa of bending stresses. The average strain is 0.52%, which is less than the prescribed strain (0.61%), and consequently indicates a nonlinear behavior with the displacement. The interior edges of the wires are more strained, and as a result, more stress is induced towards the center of the cable.

The axial strain and displacement distributions in the central tube are shown in Figure 5.18. The maximum strain in the tube has reached 0.88%, which is 44% higher than the linear prescribed strain of 0.61%. This behavior is expected due to the material nonlinearity of the tube. It is worth noting that the minimum strain in the tube is 0.37%, at the fixed end, and the maximum strain is found almost at the middle length of the tube where plastification starts.

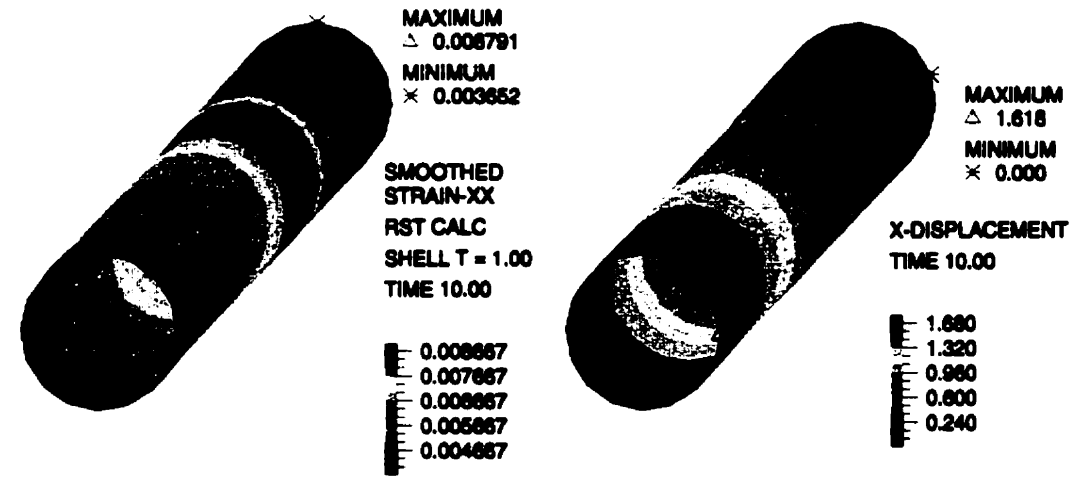

Figure 5.18 Axial strain and displacement of the central tube

The smoothed axial stress of the tube using RST interpolation with finite element effective stresses at the integration points is presented in Figure 5.19. The maximum stress of the tube in defining the stress-strain curve is limited to 145 MPa. The finite element effective stress is the effective stress directly taken from the solution program and obtained from the following formula.

$$\sigma_e = \sqrt{\frac{1}{2}\left[(\sigma_{xx} - \sigma_{yy})^2 + (\sigma_{xx} - \sigma_{zz})^2 + (\sigma_{yy} - \sigma_{zz})^2 + 6(\tau_{xy}^2 + \tau_{xz}^2 + \tau_{yz}^2)\right]} \quad (5.1)$$

The maximum value of the effective finite element stress is limited to the maximum stress defined in the multilinear inelastic material law. However, the axial stress (σ_{xx}) is the stress along the cable axis and since the RST interpolation has been used, its maximum value can be found larger than the maximum stress of the cable defined in the stress-strain curve. However, in reality, the maximum stress is limited to 145 MPa as shown on the right portion of Figure 5.19. The effects of the contact forces on the tube from the inner wires are more evident in the axial stress of the tube, decreasing the stress down to 98 MPa. It is noted that all the results of the central tube are calculated at the top surface of the shell, to include the direct effects of the contact force.

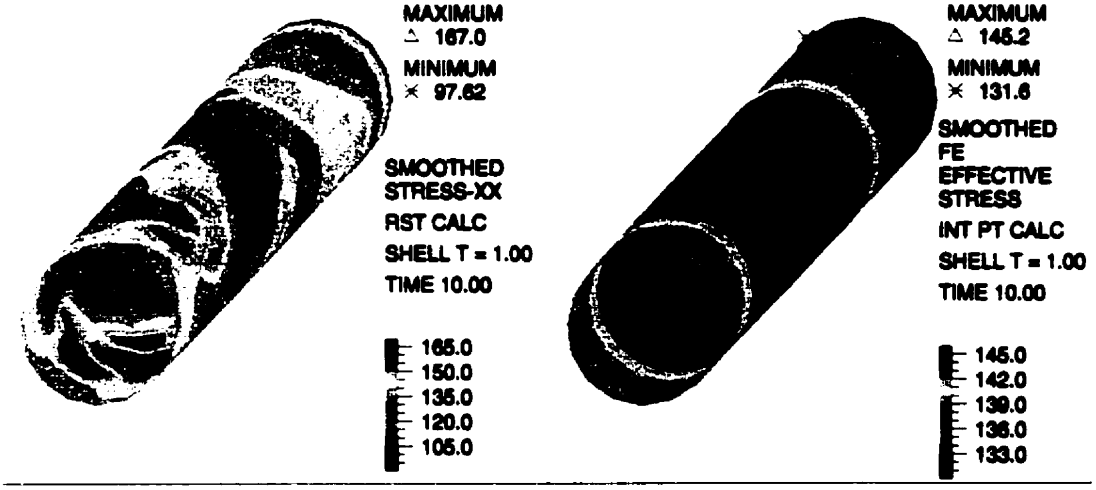

Figure 5.19 Smoothed axial stress (RST calculation) and finite element effective stress (integration points calculation) of the central tube

The consistent contact forces directly exerted on the tube by the inner wires and the smoothed plastic strains are shown in Figure 5.20.

It can be seen that the contact forces are concentrated within the half middle length of the tube, and no contact force is generated from the inner wires at the ends. This is due to the in-plane fixity of the wires at the ends, which prevents the wires to be in contact with the tube. The maximum concentrated contact force is 203 N, and decreases the axial stress of the tube at that point. In general, the overall effects of the contact forces are to decrease the axial stress of the

tube. Due to large axial elongation of the tube, no net compression is induced in any part of the central tube.

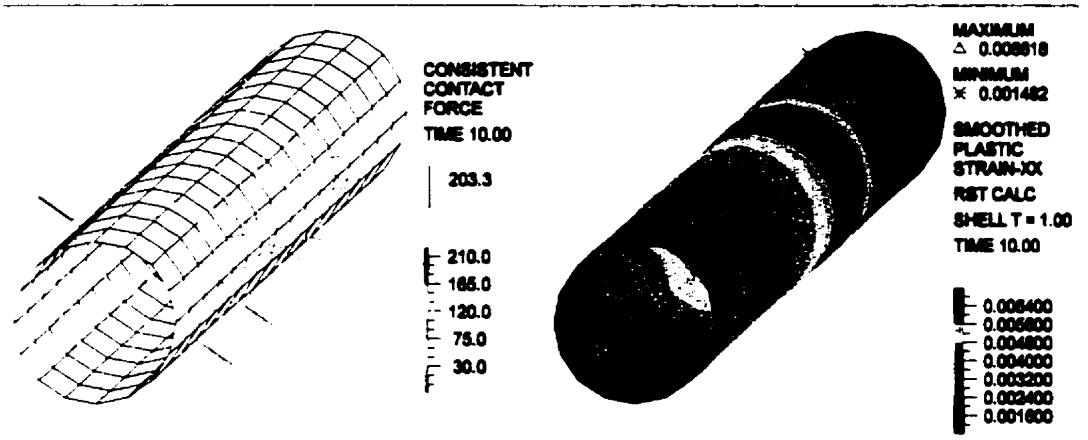

Figure 5.20 Consistent contact forces and plastic strains in the tube

The plastic strain in the tube varies between 0.15% and 0.66%. The maximum plastic deformation occurs only for about 1/8 length of the tube, and most of the tube has an average of 0.4% plastic deformation. Such a plastic deformation of the tube was expected but it seems very large as it is exceeding the excess length of the optical fibers inserted in the spacer. More discussion of this observation is presented in the OPGW model section (5.3).

5.2.2.2 Reaction forces at loading end

The results of the two loading cases with friction effects are summarized in Table 5.2. Comparisons of the results with and without friction (not shown in Table 5.2) show that the friction effects are significant on the axial strain and reaction of the tube but negligible on the response of the wires. The interaction of the tube and the wires is most affected by friction. When friction is included, a total axial tension of 1357 N (or 1340 N) is required to induce an elongation of 1.62 mm in the tube whereas this tension is reduced to 1306 N when friction effects are neglected.

5.2.2.3 Comparison with analytical solutions

The inner wire and tube model is analyzed for four load combinations, with prescribed displacement at either all the interior nodes of the wires or only at the central node, and with or without friction.

Only the results of contact analysis with friction and all interior nodes loaded are presented in section 5.2.2. However, the results of the other cases with the analytical solutions of Machida and Durelli (1973) and Phillips and Costello (1973), are also summarized in Table 5.2. In the analytical solutions, the axial load and stresses on the tube and the wires are calculated based on a 0.61% cable axial strain.

Table 5.2 Stresses and displacements of inner-wire-and-tube model

Response / Model		Total axial load (kN)		Max. Stress-XX (MPa)		Max. Strain-XX (%)	
		μ=0	μ=0.33	μ=0	μ=0.33	μ=0	μ=0.33
Wires (**all interior nodes are loaded**)		46.12	46.12	903	912	0.549	0.554
Central tube		1.31	1.36	171	167	0.984	0.879
Wires (**only central node is loaded**)		45.28	45.24	897	904	0.545	0.549
Central tube		1.31	1.34	171	170	0.976	0.710
Machida & Durelli (1973)	Inner wires	61.89		969		0.61	
	Tube	3.88		377		0.61	
Phillips & Costello (1973)	Inner wires	61.80		971		0.61	
	Tube	3.88		377		0.61	

The total axial load of the model is calculated by adding the reaction force induced at the loading end due to the prescribed displacements. It is recalled that friction effects are neglected in the analytical solutions of Machida and Durelli (1973) and Phillips and Costello (1973).

The total axial stress resultant of the wires is 62 kN in both analytical solutions. The values obtained by the model are of 45-46 kN, for the different loading scenarios, which is 74% of the theoretical value. However, due to the nonlinear behavior of the model, less strain is induced in the cable (0.55%), compared to the linear strain of 0.61% used in the analytical solutions.

The axial stresses and strains of the aluminum tube cannot be compared since a linear material law is used in the analytical solutions and the numerical model uses a nonlinear law. It is further noted that the aluminum tube is yielding under

all the scenarios studied. In conclusion, the calculated total axial force needed to elongate the cable by 1.62 mm, is 66 kN and 47 kN, using theoretical and finite element analysis, respectively. Consequently, the analytical solutions overestimate the stiffness of the cable.

5.2.2.4 Loading effects - displacement approach

As mentioned before, two types of loading were applied to the inner wires. The prescribed displacement was applied to either all the interior nodes of the wire cross section or only to the central node. The results indicate that slightly more stresses (903 and 912 MPa) are induced when all interior nodes have a prescribed displacement than when only the central wire node is constrained (897 and 904 MPa). However, the differences in stresses and strains are insignificant (less than 1%). The effect of these two loading conditions is also minimal on the aluminum tube stresses.

However, the maximum axial strain of the tube is more affected when friction is considered. This is explained by the fact that when only the central wire node is constrained the exterior surface of the wire is allowed to deform and produce more contact with tube compared to the other loading scenario (displacement prescribed at all interior nodes). This increases the wire strain in the no friction case (0.976% to 0.984%) and decreases it in the contact with friction case (from 0.88% to 0.71%). The loading effects on axial reaction forces are discussed in section 5.2.2.6.

5.2.2.5 Friction effects

The results indicate that friction has negligible effects on the wire response. Since the aluminum tube is yielded in all analyses, no changes occur in its maximum stress. However, the effect of friction is considerable on the axial strain of the tube. The maximum effective stress of the tube (at integration points) is limited to 145.6. However, in the calculation of the stresses using different interpolation schemes and smoothing, the maximum stress in the tube is more than 145.6 MPa (167 MPa). As mentioned in the previous section, the maximum axial strain of the tube decreases when friction is considered between the wires and the tube, especially when only the central nodes of the wires are loaded.

5.2.2.6 Reaction forces at loading end

A prescribed displacement approach is used in modeling the tube for a 0.61% elongation. Whenever a nodal point is constrained, a reaction force is obtained at the same point, which is required to induce the prescribed displacement. The reaction force shown in Table 5.2 is the summation of all the nodal reaction forces either on the wire cross section or on the circumference of the aluminum tube. These reaction forces versus prescribed displacement are plotted is Figures 5.21 and 5.22, for the aluminum tube and the inner wires, respectively.

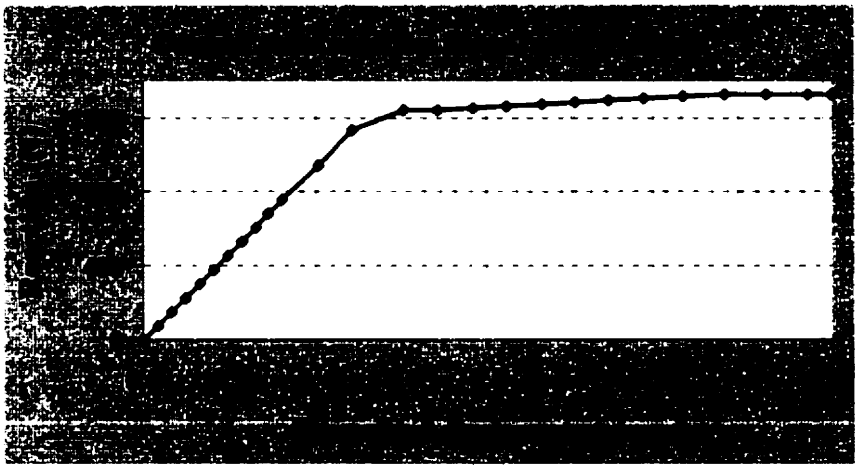

Figure 5.21 Axial reaction force acting on the tube (μ=0.33)

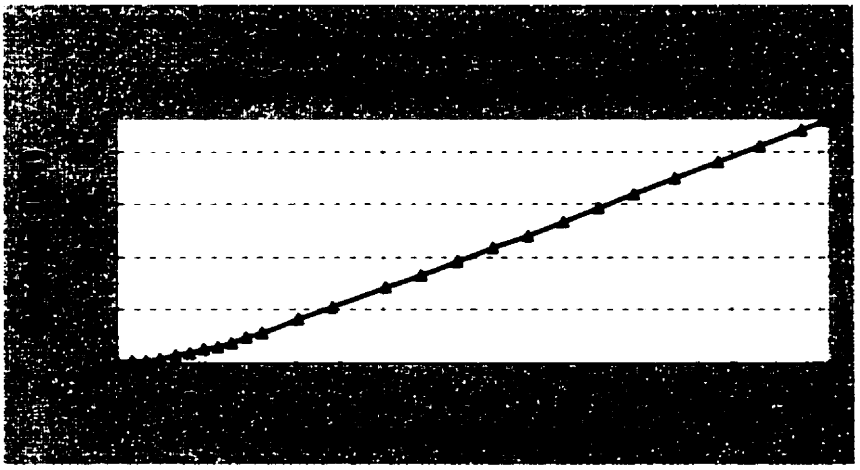

Figure 5.22 Axial reaction force acting at all central nodes of inner wires

The axial stress resultant at the loading end of the tube that induces a 1.62 mm elongation is slightly affected by friction. This reaction force varies from 1306 N to 1357 N, in contact analysis with and without friction, respectively.

5.2.3 Inner wires and aluminum tube model - free loading end

In this model (inner-wires-and-tube), all the interior nodes of the wires are subjected to a prescribed displacement and the loading end is free to rotate. The analysis is considered with friction effects. The inner wires are expected to unwind (rotate against their helix direction) when subjected to an elongation along the cable axis. The purpose of this analysis is to verify if the model is adequate under free end conditions and also to compare its results with analytical solutions. The detailed results are summarized in Table 5.3.

Initially there is a small gap between the wires and between the tube and the wires. Upon loading, the wires first wind until touching each other and then unwinding occurs due to the helical configuration. The maximum and minimum stresses along the cable axis (σ_{xx}) are 788 MPa and 562 MPa, corresponding to an average normal stress of 675 MPa and ±113 MPa of bending stresses (Figure 5.23), at the half-length cross section.

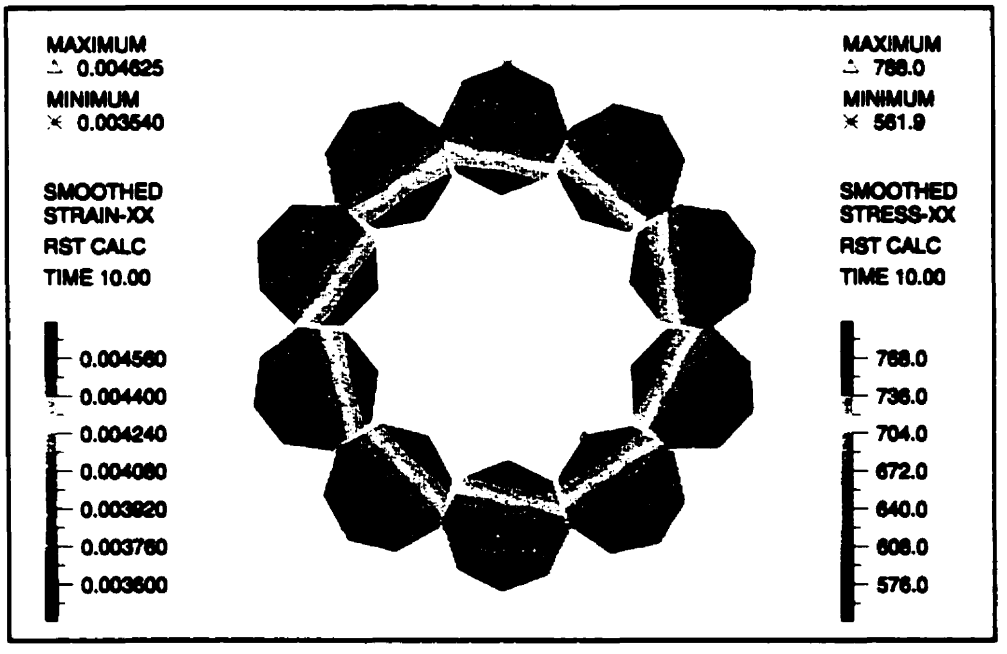

Figure 5.23 Stress and strain distribution on inner wires (unwinding allowed)

It is seen that the stress and strain distributions have a symmetric response in all the wires. This is due to the free ends of both the wires and the tube which allow them to deform freely and to expand because of unwinding. Therefore, individual wires are less restricted by each other, and behave more independently. The

maximum stress and strain in the wires occur toward the center and the bending directions in the individual wires (perpendicular to the bending axes) are aligned toward the center. Consequently, the individual wires are not twisted.

The average strain is about 0.41%, which is 67% of the prescribed linear strain (0.61%). Therefore, less axial force is expected compared to that obtained by the analytical solutions based on the 0.61% axial strain.

The maximum principal stresses in the wires vary from 568 MPa to 867 MPa, and the maximum shear stresses are 297 MPa to 448 MPa. The maximum effective stress in the wires is 870 MPa (see Equation 5.1).

The total axial reactions of the wires and the tube are 35.8 kN, and 1.37 kN, respectively. Therefore, the total reaction is 37.2 kN, which is 78% of the value obtained by Machida and Durelli (47.5 kN) and 80% of that using Phillips and Costello's (46.4 kN). The results are summarized in Table 5.3.

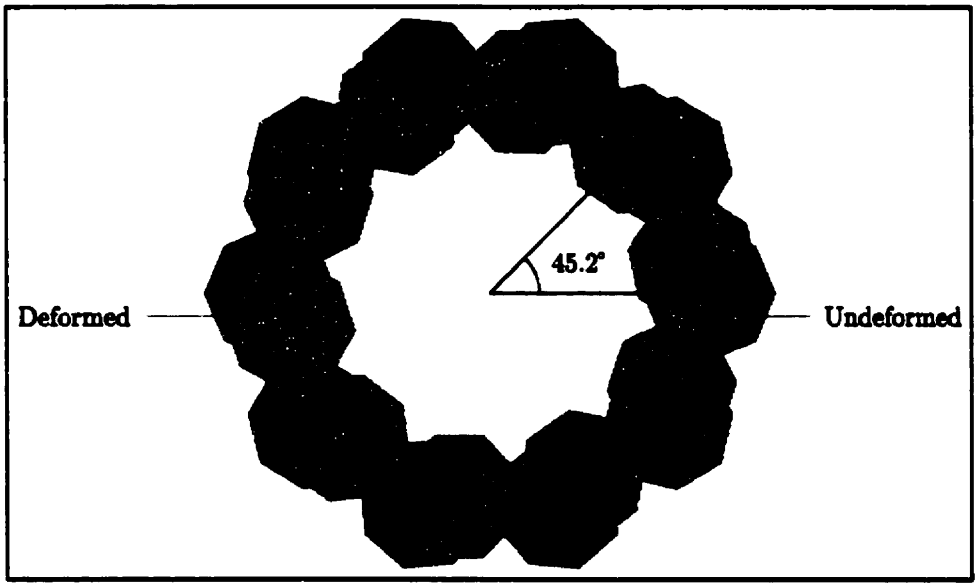

Figure 5.24 Unwinding displacement of inner wire cross section at free end

The deformed section of the wires at the loading end is shown in Figure 5.24. As indicated, the total unwinding rotation is 45.2 degrees at the free end and is about 17.4 degrees at half-pitch length (not shown here). This result indicates that the unwinding motion is not linear along the wire axis, contrary to what is

assumed in the analytical solutions. The unwinding rotations at the loading end calculated using the analytical solutions by Machida and Durelli (1973) and Phillips and Costello (1973) are 52.9 and 48.1 degrees, respectively.

The maximum stress of the wire along the cable axis (788 MPa) is practically the same as the value obtained by the analytical solution of Machida and Durelli, and is 96% of that of Phillips and Costello. The bending stress (113 MPa) is less than 10% different from those predicted by Machida and Durelli, and Phillips and Costello.

Table 5.3 Inner wires stresses and forces (unwinding allowed)

	Unwinding rotation	Max. Stress-xx (MPa)	Strain-xx (%)	Bending stress (MPa)	Total axial force (kN)
Finite element model	45.2	788	0.46	±113	37.2
Machida & Durelli (1973)	54.6	786	0.61	±117	46.9
Phillips &Costello (1973)	49.6	821	0.61	±103	49.9

The total axial force of the finite element model is 75% to 80% of that predicted by the analytical solutions. This is expected, as the axial strain in the wires is also 57% to 75% of that of Machida and Durelli (1973) and Phillips and Costello (1973). In summary, the axial stiffness of the model is smaller than that of the analytical solutions. Therefore, the cable finite element model is likely to simulate more elongation than the analytical models if being subjected to the same axial force. Meanwhile, the unwinding rotations of the wires differ by 9.7% and 20.8% with those of Phillips and Costello (1973) and Machida and Durelli (1973), respectively. In the experiments performed by Utting and Jones (1989 II), differences in unwinding rotations predicted by the analytical solutions of Phillips and Costello (1973) were of 9.0% to 15.7%. In fact, the unwinding rotation predicted by the finite element model (45.2°) is closer to what can be expected from experiments.

5.3 OPGW model

5.3.1 Central nodes of the wires are loaded

The next step in modeling the OPGW is to add the outer wires and the aluminum spacer to the previous model. It has been mentioned earlier that the gap between the aluminum spacer and the central tube is too large for contact to develop for equal elongation. Therefore, no contact surfaces are defined for the aluminum spacer, which implies that the aluminum spacer can also be modeled separately. However, for completeness, it is included here along with the outer wires, the inner wires, and the aluminum tube. The outer wires are modeled like the inner wires with their specifications. Results obtained for the different components are presented in details in the next sections. The results for the 3-D solid elements (the outer and inner wires, and the aluminum spacer) are for the cross section located at half-length of the cable model (132.58 mm). To be precise, the exact half-length of the deformed shape is 133.39 mm, where half of the axial elongation of the cable is added to the half-length of the undeformed shape. The finite element mesh and the prescribed displacement at the center of each wire and in the aluminum tube and spacer are shown in Figure 5.25.

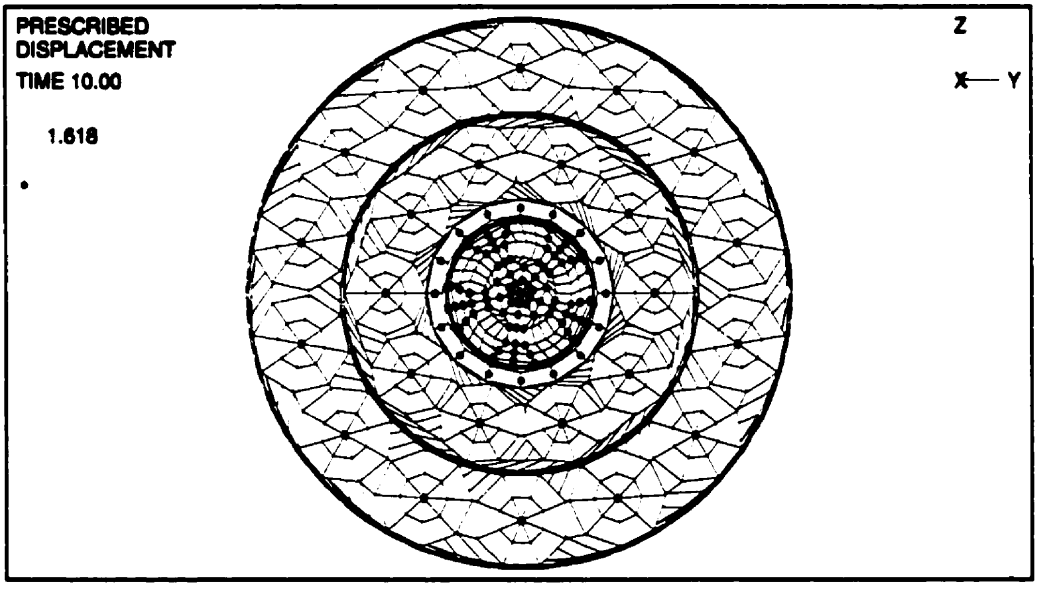

Figure 5.25 Finite element mesh and loading on the OPGW (μ=0.33)

5.3.1.1 OPGW response

The overall deformed shape of the OPGW at the loading end is presented in Figure 5.26. Since the in-plane displacements of the wires are fixed, the

unwinding rotation is restricted and the wires deform towards the center of the OPGW. However, the central tube is free to twist and the aluminum spacer does unwind as shown in the figure.

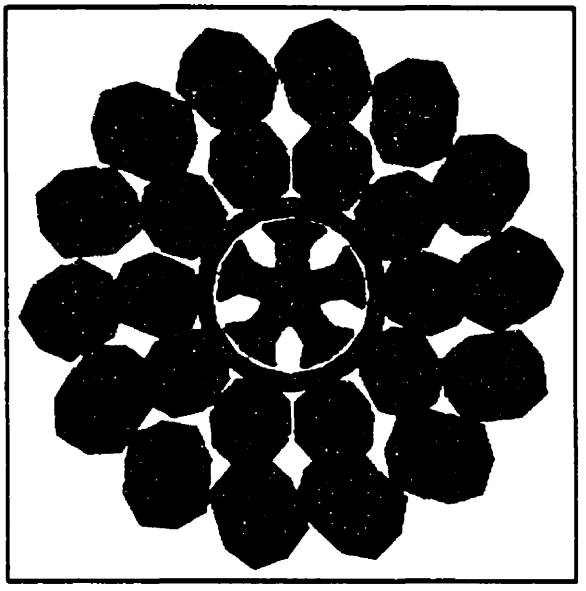

Figure 5.26 Deformed (cyan) and undeformed (blue) geometry of the OPGW (central nodes are loaded and μ=0.33)

The X-displacement distribution in Figure 5.27 is for the cross section located at half-length of the cable. Although the axial displacements of the different components are very close, it is seen that the components on the periphery have larger axial displacements than the components near the core.

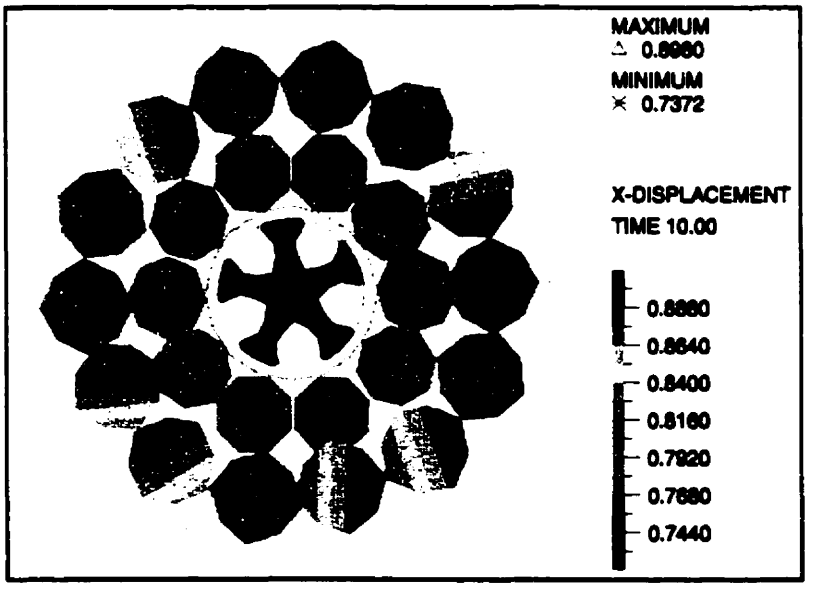

Figure 5.27 Axial displacement (X-DISPLACEMENT) of the OPGW components at half length (X=132.6 mm)

Figure 5.28 shows the axial stresses and strains in the cable. The maximum axial stress occurs in the steel inner wires, which are considered the main load-bearing part of the cable. Due to nonlinear stress-strain behavior of the aluminum spacer and the tube, their stress level cannot be compared with that of the other components. The maximum stress in the cable occurs in the inner wires (920 MPa) and the minimum in the outer aluminum wires (38 MPa).

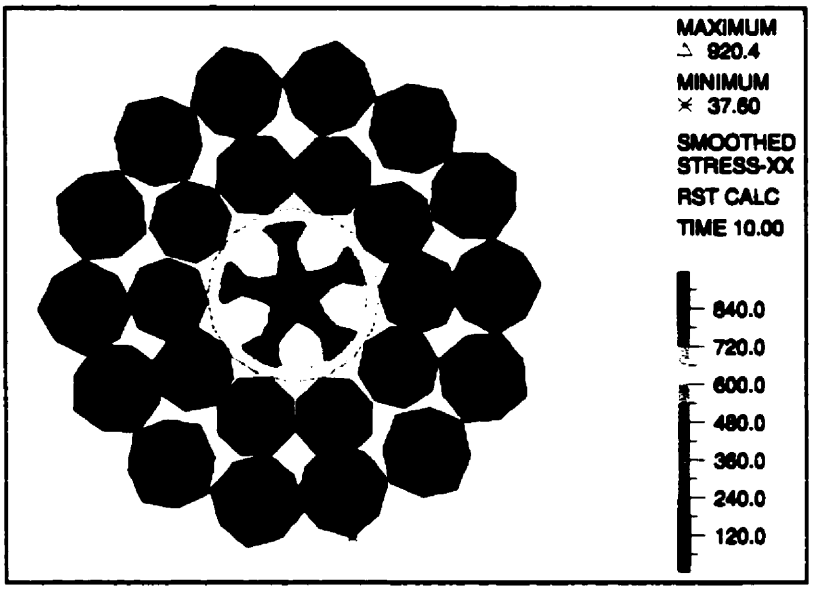

(a) STRESS-XX

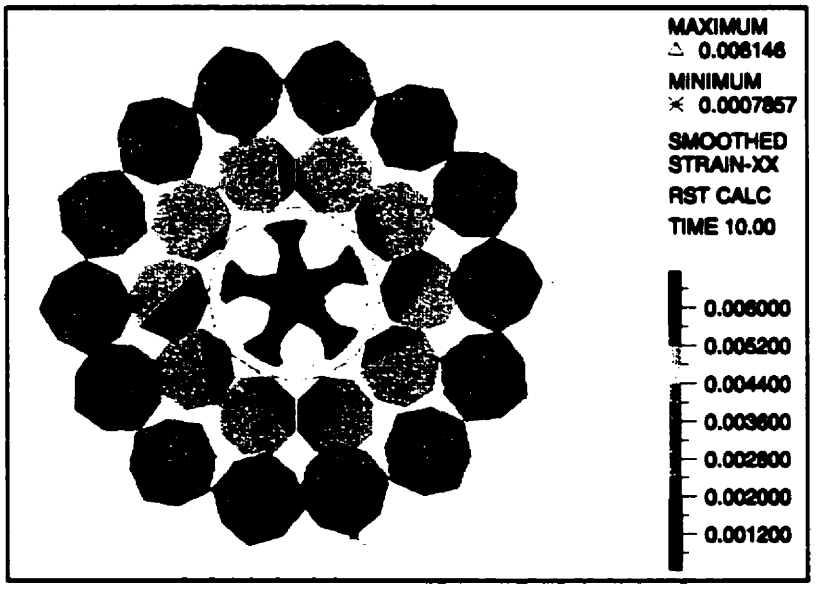

(b) STRAIN-XX

Figure 5.28 (a) Axial stress (σ_{xx}) and (b) axial strain (ε_{xx}) in OPGW

The axial strain (ε_{xx}) distribution in the OPGW is clearly non-uniform and indicates that the farther the component from the center of the cable, the less strain is induced in the component. The maximum strain occurs in the center of the cable where it is exactly equal to prescribed strain (0.61%) when the linear relationship of displacement versus strain is assumed. It is noted that the strain decreases as low as 0.08% at the external fibers.

5.3.1.2 Outer wires

Fourteen aluminum wires with a 3.37 mm diameter are helically twisted around the layer of inner wires with a pitch length of 202 mm. Their helix angle (76.4°) is in opposite direction to that of the inner wires so as to reduce the internal axial twisting moment of the cable. The displacement-control approach is used for the two cases in which either the central nodes or all the interior nodes are subjected to an axial elongation of 1.62 mm, equivalent to a 0.61% axial cable strain. The friction effects in contact are also verified, where friction is assumed between all the outer wires and between the outer and the inner wires. The results of the different loadings, with and without friction are presented below.

The averaged smoothed axial stress in the outer wires is shown in Figure 5.29, and is interpolated using the nearest integration points and bilinear interpolation (RST CALC).

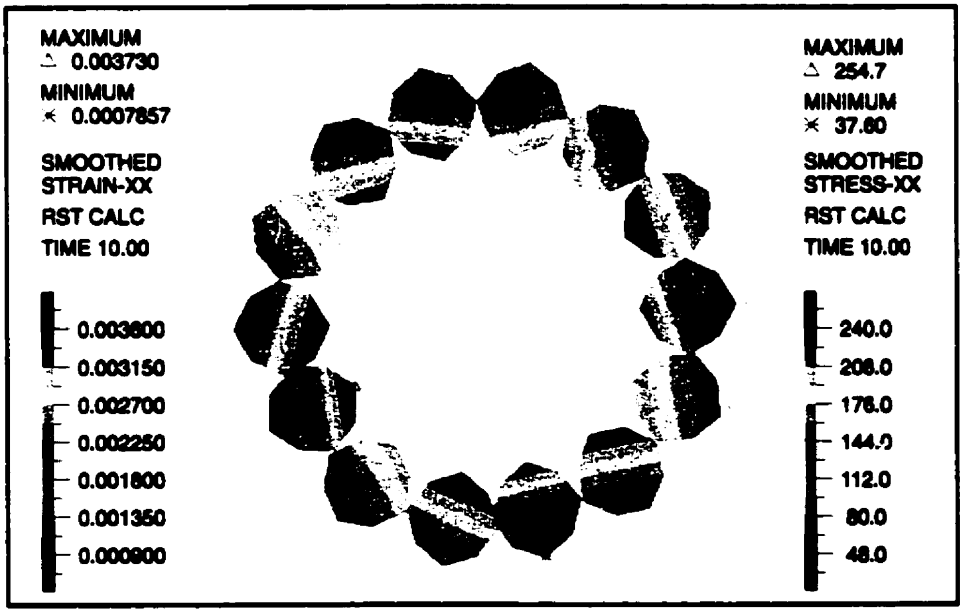

Figure 5.29 Smoothed axial stress (σ_{xx}) and strain (ε_{xx}) in outer wires

The outer wire stresses along the cable axis are varying almost linearly within the cross section and are increasing towards the center of the cable.

The maximum and minimum values are 255 MPa and 38 MPa, which are equivalent to superimposing a 146 MPa average normal stress and a ±109 MPa bending stress. As it can be seen, the extreme values occur at one particular cross section of the outer wires. The maximum stress is less than the allowable value in the aluminum wires (336 MPa), which are still in the linear range. Therefore, the Hookean material law is valid for the applied load.

As expected, the axial strain variation is identical to that of the axial stress. The average normal strain is about 0.23%; the maximum strain occurs on the inner side of the strand and the minimum at external fibers. The average displacement (see Figure 5.30) is 0.823 mm, corresponding to a 0.62% (0.823/132.58) axial strain, assuming a linear strain-displacement relationship. It is slightly more than half of the total elongation of the wires (0.81 mm), and is linear along the cable axis.

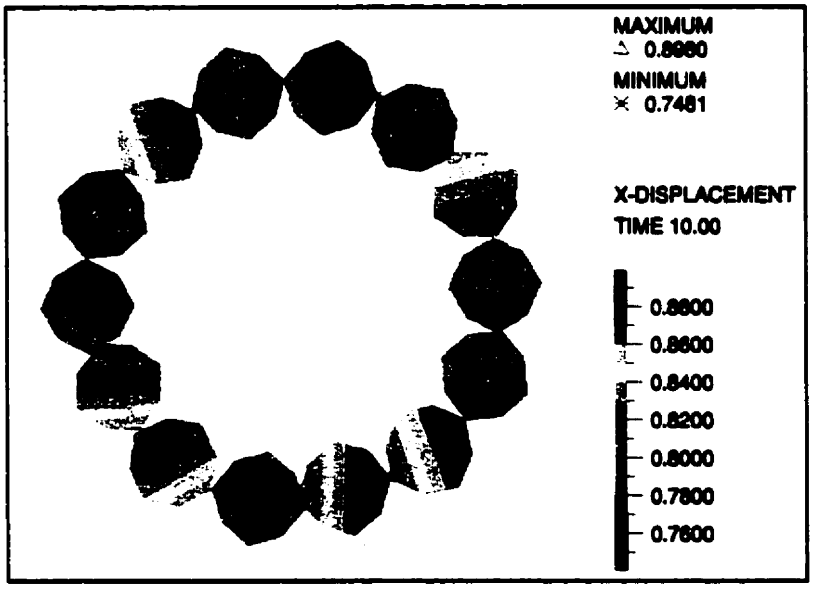

Figure 5.30 Axial displacement of the outer wires (X-DISPLACEMENT)

It is seen that the three-dimensional effects (Poisson's effects, contact, and helical geometry) significantly affect the axial strains of the outer wires, and consequently the axial stresses. The axial displacement in the cable is not therefore a good indicator of the strain in the wires. It may be used to specify the overall strain of the cable but it does not correspond to the strain level in the

individual components. Consequently, the stress in the wires cannot be calculated directly from the global strain using the axial displacement. More discussion on this important topic is presented in section 5.3.5.

It is seen in Figure 5.30 that the X-displacement of the individual wire cross section is increasing counterclockwise, i.e. opposite to the helix direction. Although the change in displacement is relatively small, it shows the non-symmetric behavior of the response due to the helical configuration of the wires.

Figure 5.31 shows the maximum principal stress (σ_{P1}) in the outer wires. Its distribution is similar to that of the axial stress (Figure 5.29), with a maximum stress of 280 MPa, which is still less than the allowable stress (336 MPa).

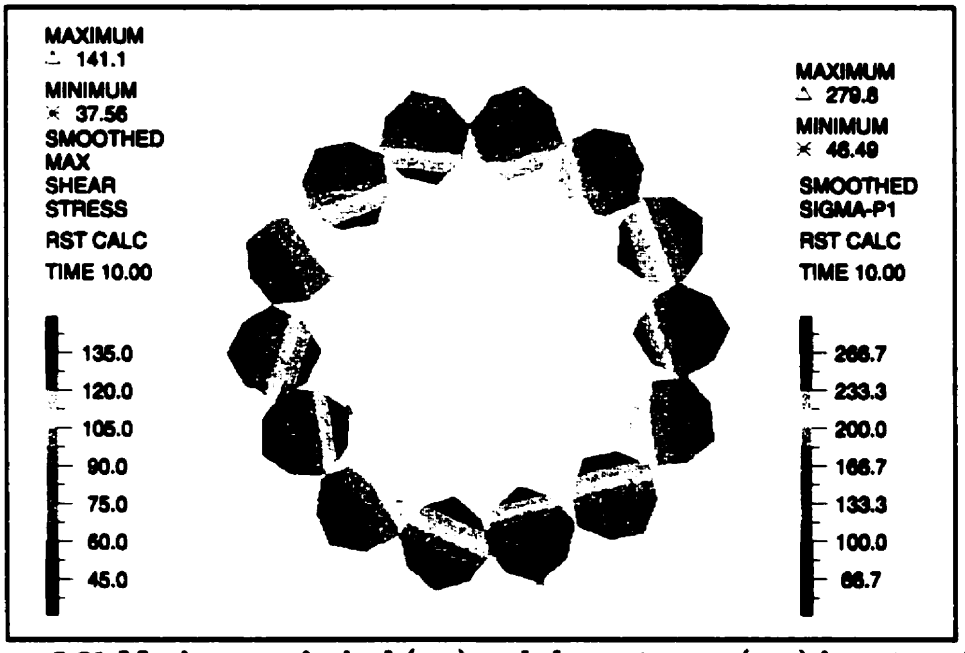

Figure 5.31 Maximum principal (σ_{P1}) and shear stresses (τ_{max}) in outer wires

The maximum shear stress (τ_{max}) is one-half the difference between the maximum and minimum principal stresses. Its distribution is identical to the maximum principal stresses, which indicates that the maximum values occur towards the center of the cable.

The in-plane displacements (Y and Z) of the inner wires (not shown here) confirm that the wires tend to move towards the center of the cable (see Figure 5.24).

The in-plane displacements are anti-symmetric in pairs located on the same diameter inwards the center of the cable. The maximum displacement is 0.7 mm, which corresponds to a decrease of 1.4 mm in the cable diameter.

5.3.1.3 Inner wires

The inner wire responses are calculated when only the central nodes of the wires are subjected to a prescribed axial displacement with friction in contact analysis. The axial stress in Figure 5.32 indicates that the maximum and minimum stresses induced in the wires are 920 MPa and 772 MPa. These extreme values occur in two different wires for which the average normal stresses are 855 and 826 MPa, and the maximum bending stresses of ±65 and ±54 MPa, respectively. It is noted that the maximum normal stress is less than the allowable stress in the inner wire (1250 MPa).

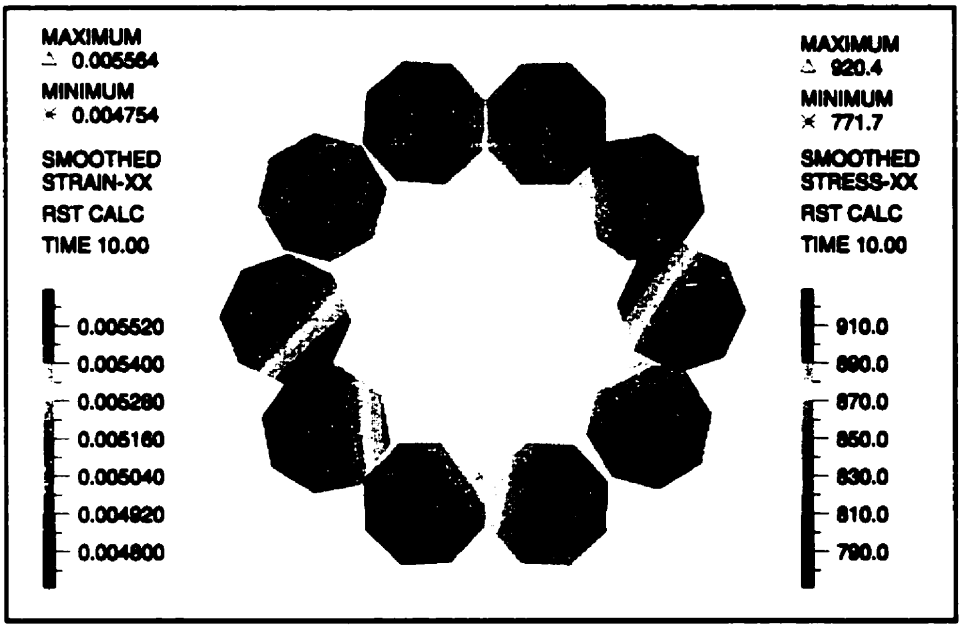

Figure 5.32 Stress-xx and strain-xx distribution in inner wires (μ=0.33, central nodes loaded)

The axial strain distribution in the inner wires is similar to the stress distribution. The maximum strain (0.56%) is slightly less than the prescribed axial strain of the cable (0.61%), and the average strain is 0.52%, which is 85% of the prescribed strain.

The maximum shear stress (τ_{max}) in the inner wires is 466 MPa and occurs on the interior side of the wire. The variation of the maximum shear stress over the cross section is small (in the order of 10%), which indicates that the differences between the maximum and minimum principal stresses (σ_{P1} and σ_{P3}) are small. The distribution of the maximum principal stresses is similar to that of the maximum shear stresses (Figure 5.33). The extreme value is 935 MPa, which is slightly larger than the normal axial stress and is 75% of the maximum allowable stress in the wires.

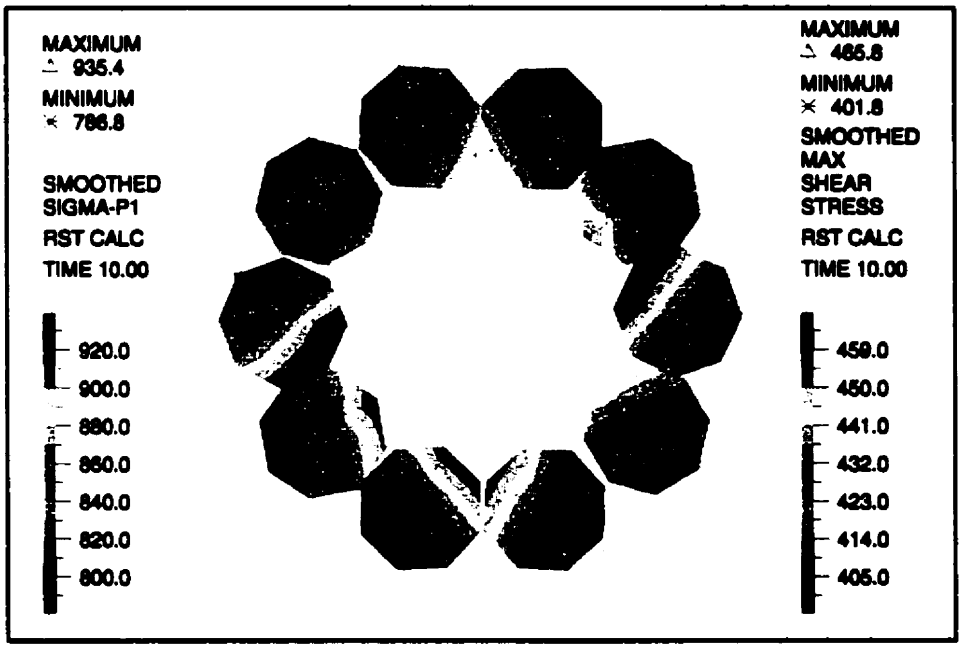

Figure 5.33 Maximum shear and principal stresses of inner wires (μ=0.33, central nodes loaded)

The variation of the displacements of the inner wires along the cable axis is presented in Figure 5.34. The maximum displacement (0.81) corresponds exactly to the applied strain (0.61%) at full pitch length.

The variation of the displacement over a wire cross section is very small and corresponds to the direction of the helix (increase in clockwise direction). The displacement should be uniform at the cross sections normal to the helical axis of the wires. It is noted that when only the central nodes of the wires are constrained, the cross sections deform more freely than when all the interior nodes are constrained.

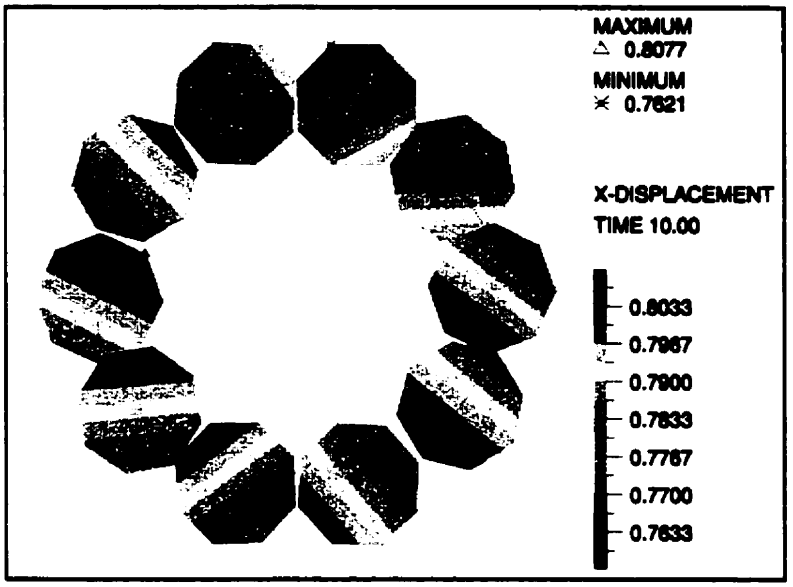

Figure 5.34 X-displacement of inner wires (μ=0.33, central nodes are loaded)

5.3.2 All interior nodes of the wires are loaded

In the next sections, the results of the OPGW analysis are presented for the case when all the interior nodes of the wires and the central tube are prescribed a 1.62 mm elongation along the cable axis.

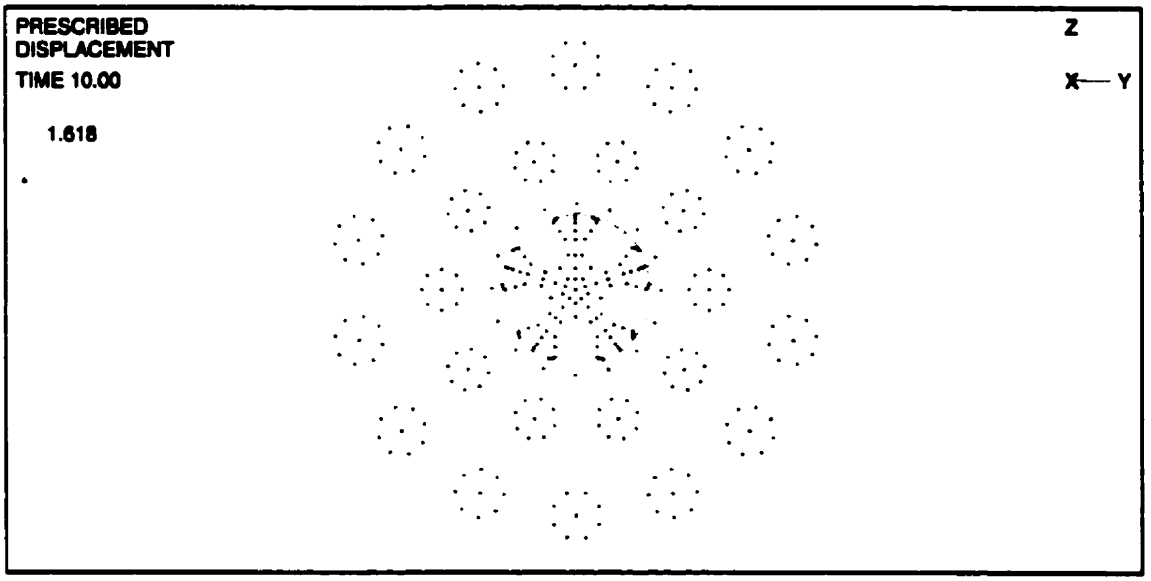

Figure 5.35 Finite element mesh of OPGW - all interior nodes are loaded

This loading case is analyzed with and without friction effects. However, only the results of the model with friction are illustrated, and the results of all the other

cases being only summarized in Tables 5.3 and 5.4. The overall behavior of the wires (inner and outer) and the central tube is expected to show only moderate variations compared to the central node loading case.

5.3.2.1 OPGW response

The deformed configuration of the OPGW cross section at mid length is shown in Figure 5.36.

The wires are restricted to any in-plane displacement, such that unwinding of the wires is prevented. Nevertheless, the aluminum spacer is allowed to unwind as its loading end is free to rotate.

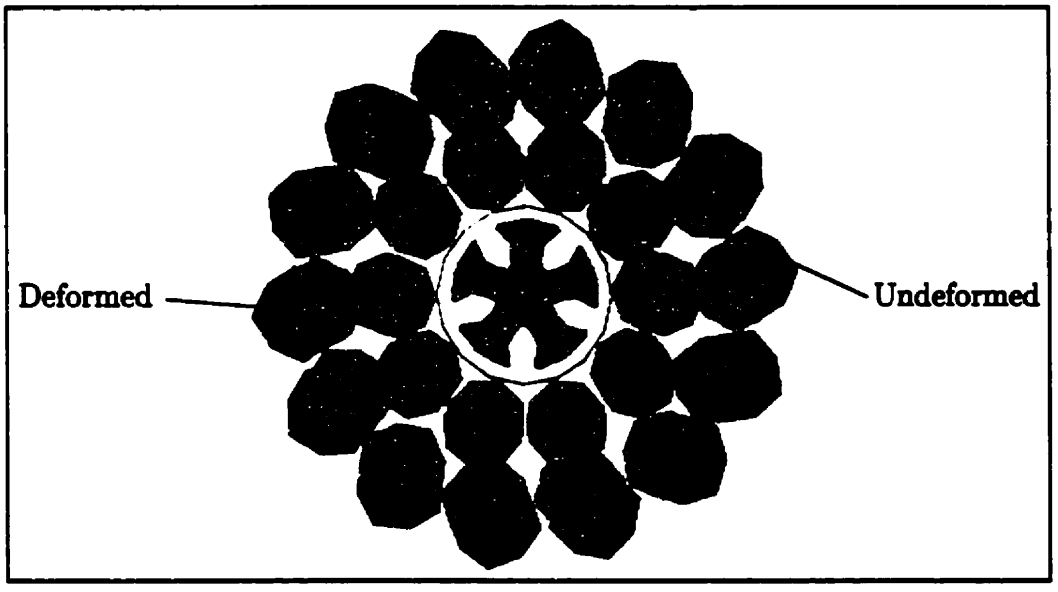

Figure 5.36 Deformed (cyan) and undeformed (blue) configurations of OPGW (with friction μ=0.33)

As expected and observed in the previous case (Figure 5.24), the wires displace towards the center of the cable where the inner wires are restricted by the central tube. The stress and strain distributions along the cable axis of the OPGW cross section at mid length are shown in Figures 5.37(a) and (b).

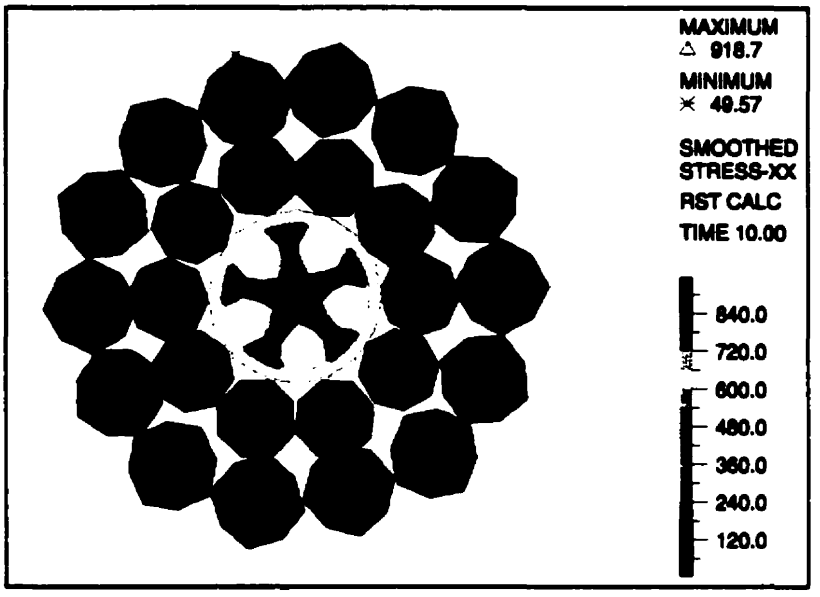

(a)

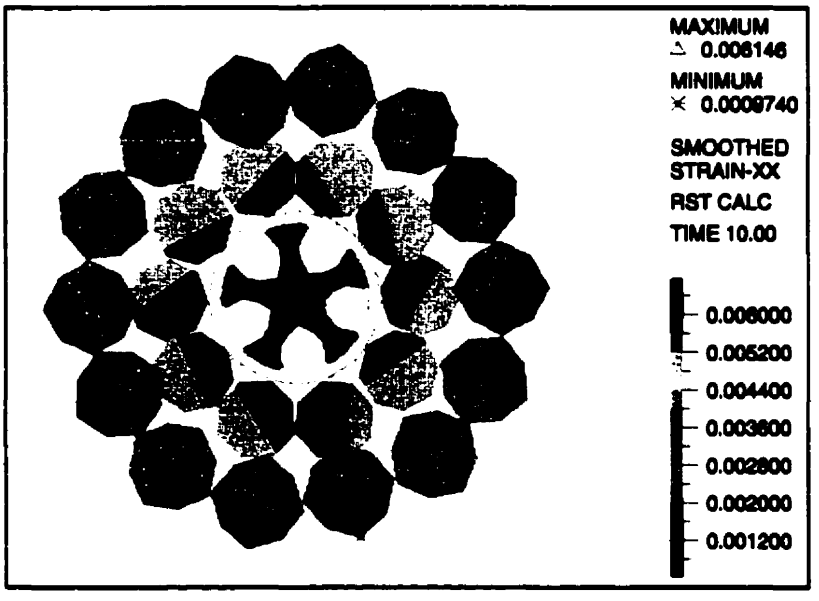

(b)

Figure 5.37 (a) Stress-xx and (b) Strain-xx distribution at mid length

The axial stress and strain response of the cable is similar to the other loading case (Figure 5.27). However, the minimum stress and strain in the outer wires are slightly higher than in the previous loading case (50>38 MPa, and $1\times10^{-3}>8\times10^{-4}$). The maximum effective stress (calculated using Equation 5.1) in the OPGW (Figure 5.38) is 938 MPa, and occurs in the inner wires. This is the largest stress induced in the wires, but is still less than the allowable stress (1250 MPa).

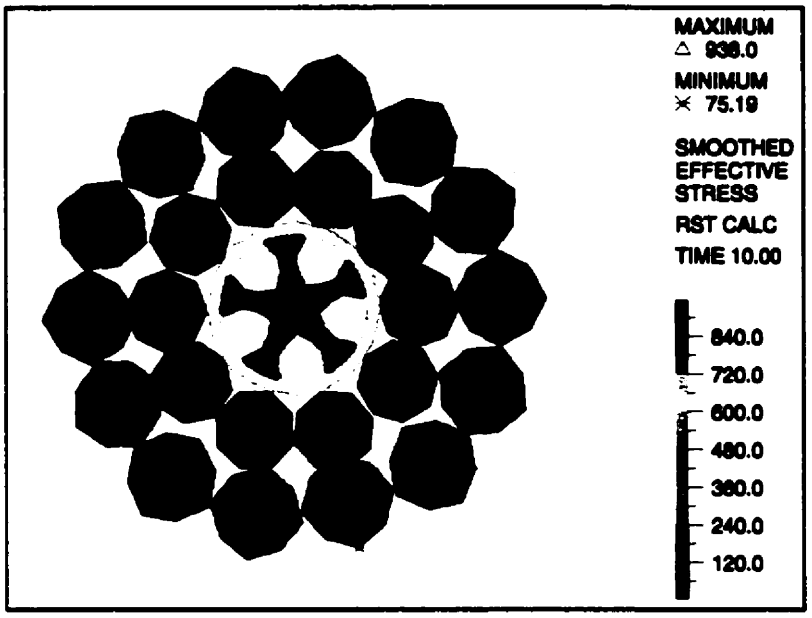

Figure 5.38 Effective stress in OPGW

5.3.2.2 Outer Wires

The stress and strain distributions of the outer wires are shown in Figure 5.39. The maximum and minimum stresses are 258 MPa and 50 MPa, corresponding to 0.38% and 0.1% axial strains, respectively, which occur on different wires.

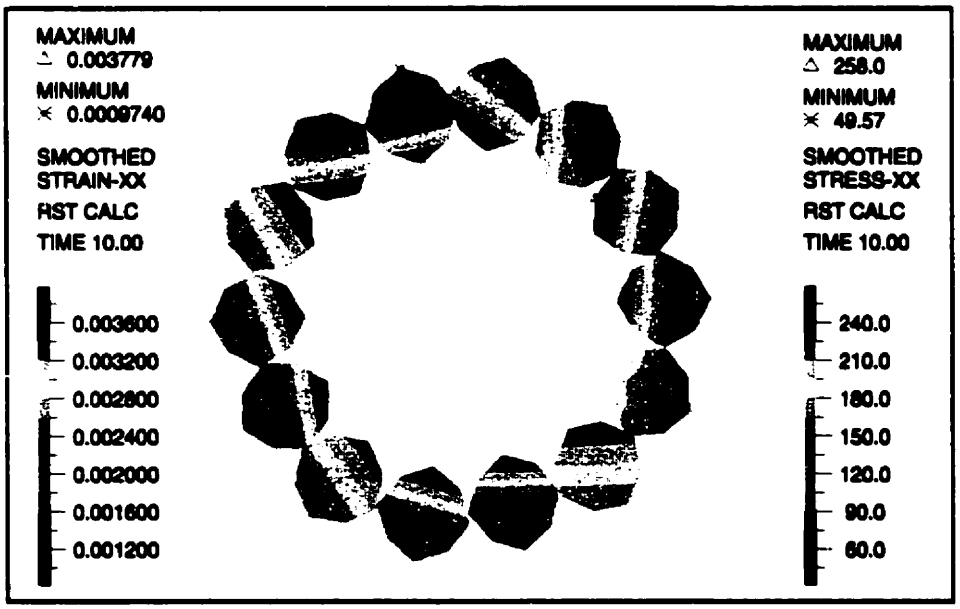

Figure 5.39 Stress-XX (σ_{xx}) Strain (ε_{xx}) in the outer wires (μ=0.33)

The average tensile and bending stresses are about 150 and ±100 MPa, for the wire where the minimum stress occurs, and they are 180 and ±78 MPa, for the wire where the maximum stress is induced. All other wire stresses are in that range. The maximum stress (258 MPa) is 77% of the strength of the outer wires (336 MPa). The maximum stresses calculated using the analytical solutions are 349 MPa and 367 MPa, which are about 35% larger than the stresses obtained by the model. The maximum strain (0.38%) is only 62% of the prescribed linear strain of the cable (0.61%). As it is seen in Figure 5.39 the larger strains are induced close to the center of the cable.

The maximum principal and shear stresses are presented in Figure 5.40 and 5.40. The extreme values of the normal and shear stress are 292 and 157 MPa, respectively. The maximum principal stress is 87% of the wire strength.

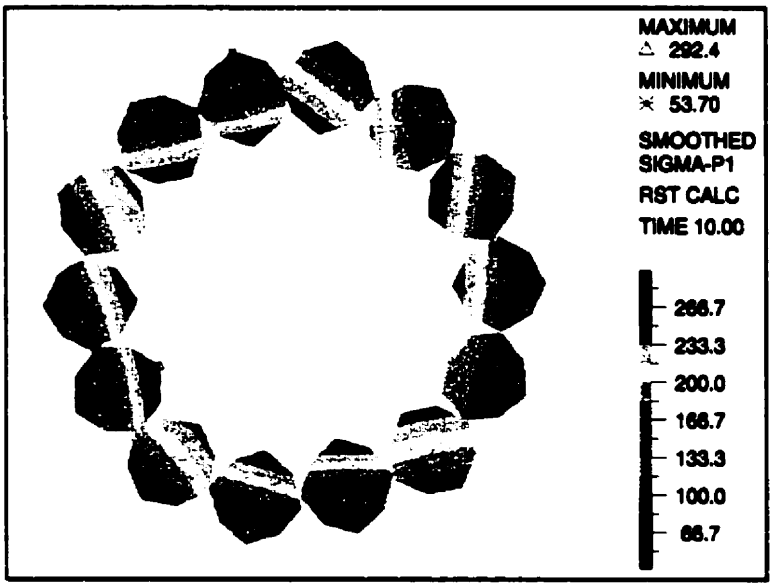

Figure 5.40 Maximum principal stress (σ_{P1}) of outer wires (μ=0.33)

The maximum shear stresses obtained by the analytical solutions are 183 MPa and 186 MPa, which are about 85% of the maximum shear stress in the wire. The maximum in-plane shear stresses (τ_{xy} and τ_{xz}) are 73 (-86) and 66 (-103) MPa (not shown here). It is worth noting that the design of a wire is based on its maximum tensile strength only, as it fails in tension.

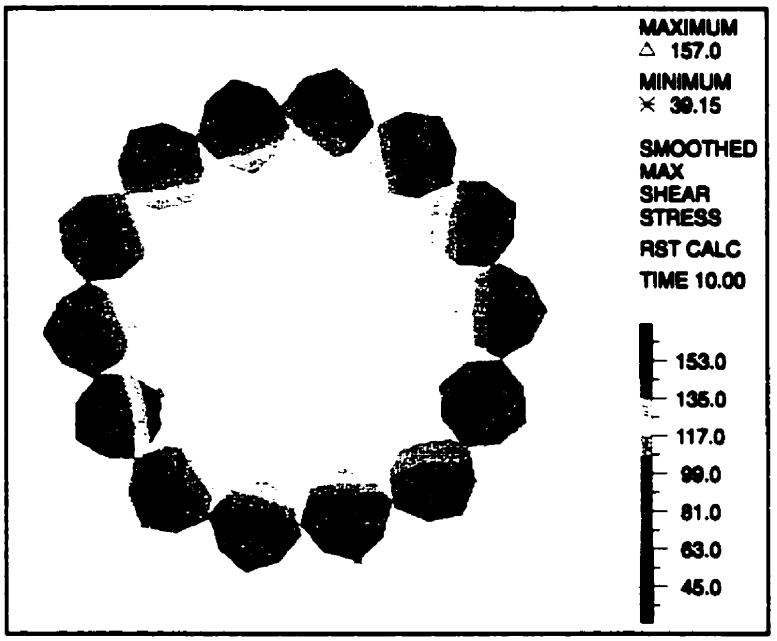

Figure 5.41 Maximum shear stress (τ_{max}) of outer wires (μ=0.33)

Reactions of outer wires

The total reaction force induced at all the nodes along the cable axis is 17.0 kN. This reaction force versus the applied load (prescribed displacement) is plotted in Figure 5.42. The behavior of the reaction force is nonlinear with respect to the prescribed displacement when the latter is small. However, it is linear after a 0.8 mm displacement (half of the load). This nonlinearity is due to the increase in contact surfaces and 3-D helical effects. This behavior is also observed in the experimental work of Utting and Jones (1989), where for a small axial load, the elongation was nonlinear with respect to tension.

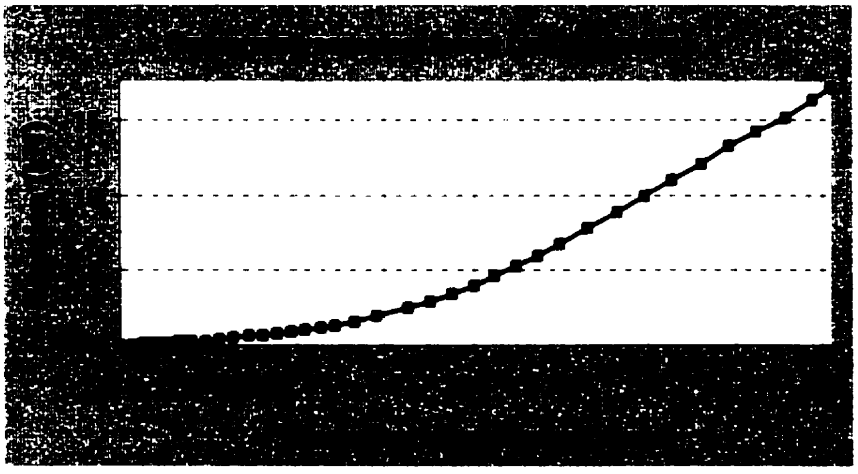

Figure 5.42 Reaction force of outer wires

In the analytical solutions of Machida and Durelli (1973) and Phillips and Costello (1973), the axial force in the inner wires necessary to induce a 0.61% strain is 44.6 and 44.0 kN, respectively. However, the finite element results show that only 17.0 kN is required to induce an average strain of 0.25% (maximum of 0.38%) in the outer wires. In all cases, the elongation of the cable is prescribed at 1.62 mm. As a result, the axial displacement cannot be used to predict the true strain in the wires and the linear displacement-strain relation ($\varepsilon=\Delta l/l$), valid for uniaxial loading, is invalid here because the three-dimensional effects are significant in the behavior of the outer wires.

The total twisting moment reaction of the outer wires is 17.04 kN.mm at the loading end. Its response versus loading (prescribed displacement) is plotted in Figure 5.43.

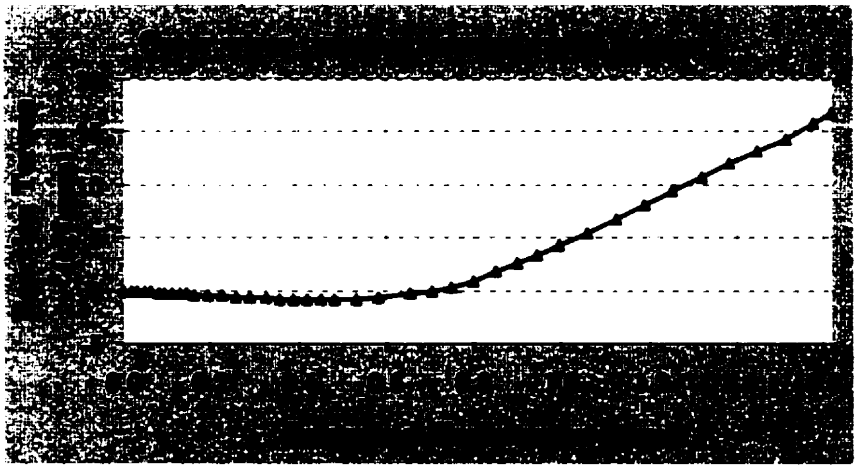

Figure 5.43 Reaction torque of outer wires

Using the analytical solutions, the axial twisting moment acting on the outer wires is 83.3 kN.mm according to Machida and Durelli (1973), and 81.5 kN.mm according to Phillips and Costello (1973). The reaction torque obtained by finite element analysis is significantly smaller than those of theoretical values. The results are summarized in Table 5.4 and more discussion is presented in the next sections.

5.3.2.3 Inner wires

The axial stress of the inner wires along the cable axis is presented in Figure 5.44. The average normal and bending stresses are 850 and ±70 MPa, respectively. The minimum stress generally occurs on the exterior side of the wire cross section, but due to the rotation of the individual wires, the maximum stresses occur at the interior side but slightly rotated from the center of the cable. This is mostly due to the contact between the wires and to the presence of the outer wires, which have a helical direction opposite to that of the inner wires. In the analysis of the inner wires only (inner wires-and-tube model), this phenomenon is not observed.

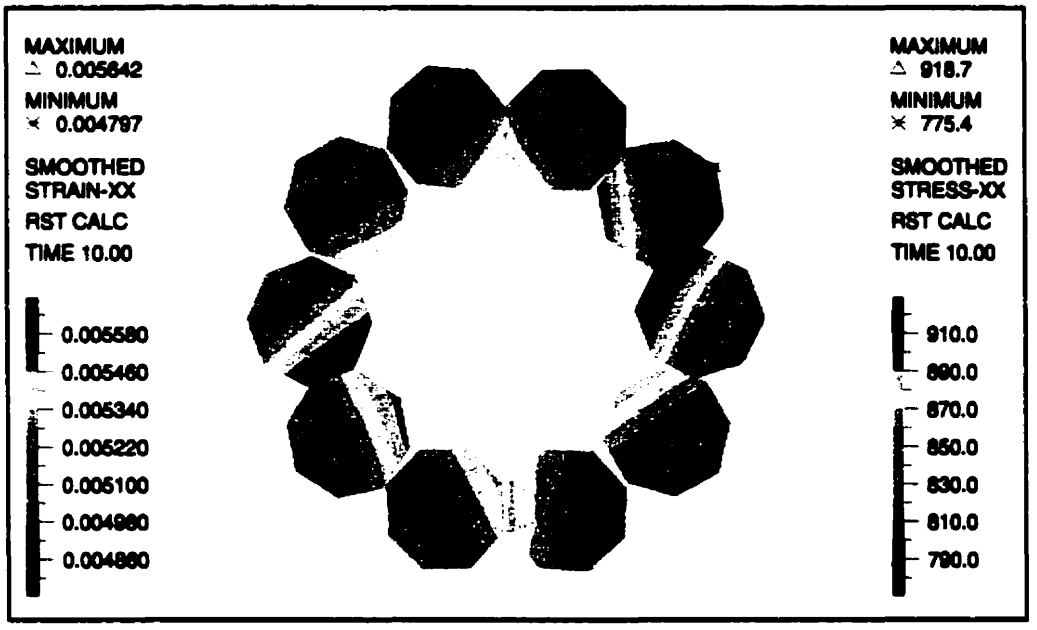

Figure 5.44 Axial stress-XX and strain-XX of inner wires (μ=0.33)

The strain distribution in the inner wires along the cable axis is similar the corresponding stress. The extreme values are 0.56% and 0.48%, corresponding to an average strain of 0.52%. The maximum strain is 92% of the linear applied axial cable strain (0.61%).

The maximum axial displacement (Figure 5.45) in the inner wires is 0.81 mm. It is also seen on the figure that the maximum displacement on the cross section occurs in the helical axis direction.

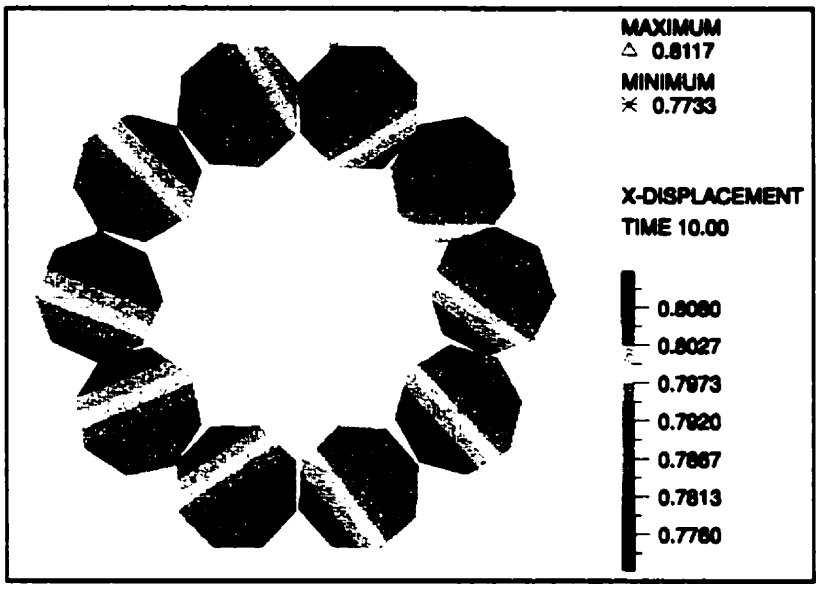

Figure 5.45 X-Displacement in inner wires (μ=0.33)

The in-plane (Y and Z) displacement distributions of the inner wires (not shown here) indicate almost a symmetric movement of the inner wires towards the center. The diameter of the cylinder on which the centerlines of the inner wires lie is shortened by about 1.0 mm.

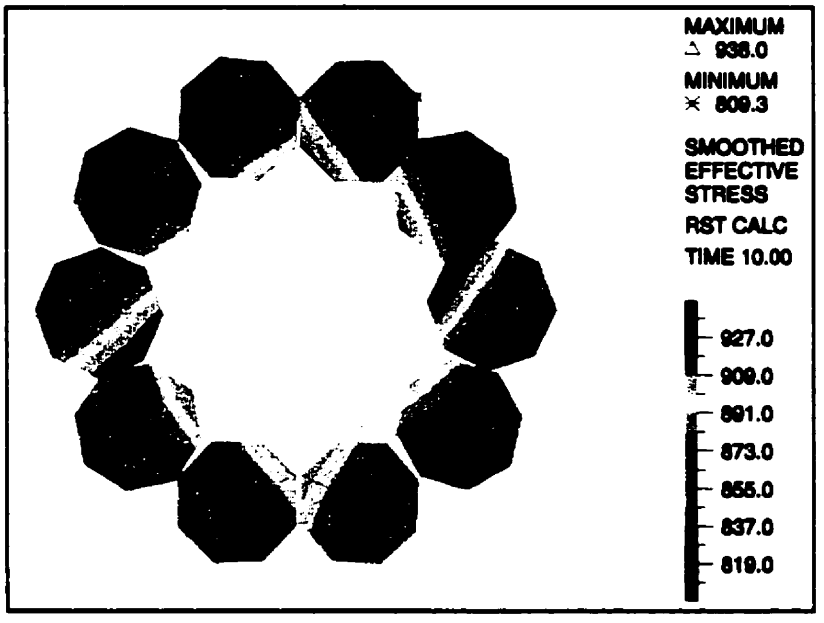

Figure 5.46 Effective stress of inner wires (μ=0.33)

The smoothed effective stresses of the inner wires are illustrated in Figure 5.46. The effective stress is the maximum stress induced in the wires. For the inner wires, the extreme value is 938 MPa, which corresponds to 75% of the allowable stress (1250 MPa) and 64% of the wire strength (1474 MPa).

The maximum shear stress (one-half the difference between the maximum and minimum principal stress) is 473 MPa. Its distribution is shown in Figure 5.47 and is somewhat similar to that of the effective stress.

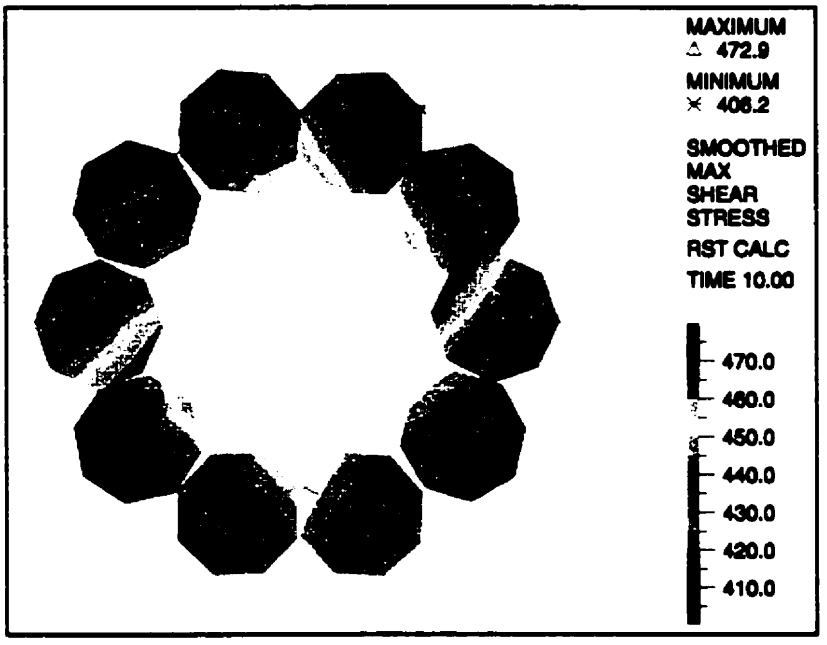

Figure 5.47 Maximum shear stress of inner wires (μ=0.33)

5.3.2.4 Central aluminum tube

The stresses and displacements of the aluminum central tube are presented in the following sections. The axial displacement is linear along the tube axis and its maximum is 1.62 mm (prescribed displacement).

The finite element effective stress calculated at the integration points is limited to 145.6 MPa (Figure 5.48), the maximum value in the stress-strain curve. This maximum stress is reached in an important portion of the tube length.

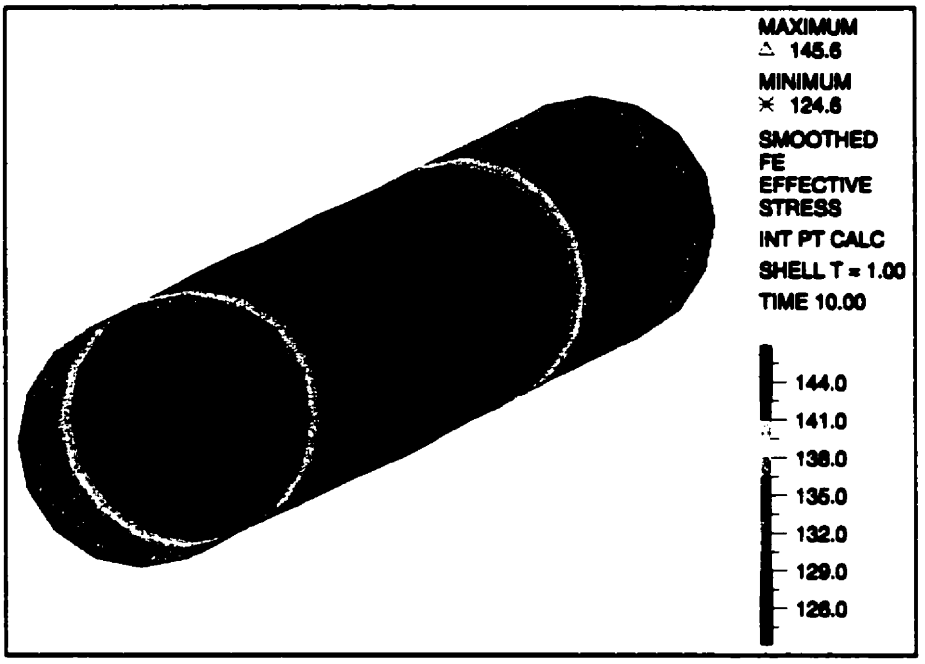

Figure 5.48 Effective stress of the tube (integration point interpolation, μ=0.33)

The maximum axial stress in the tube is 203 MPa (smoothed value on Figure 5.49). This value is larger than the maximum allowable stress in the tube (145.6 MPa), and is based on *RST* calculation (using nearest integration points and bilinear interpolation).

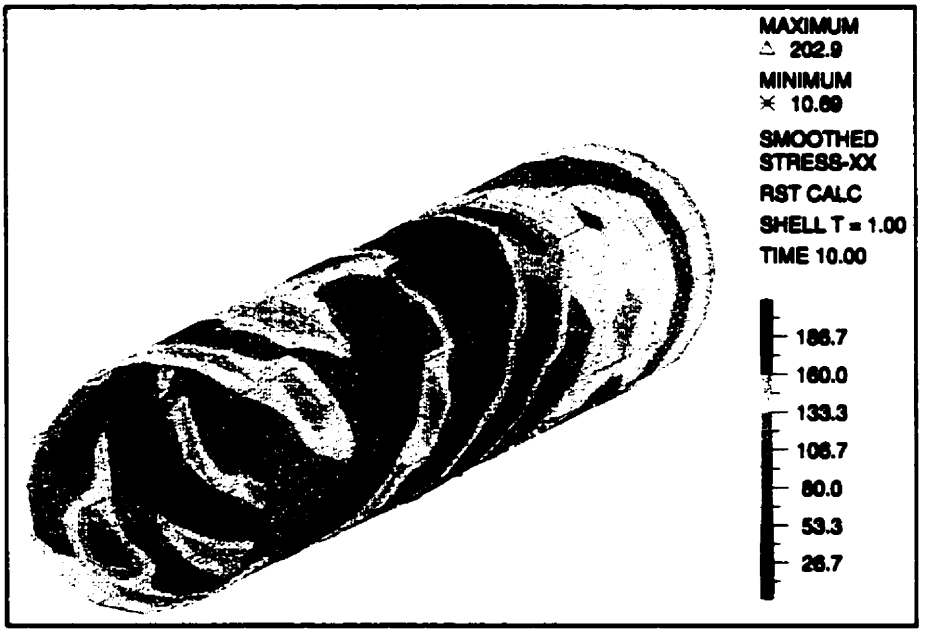

Figure 5.49 Axial stress in the central tube

The contact forces exerted from the inner wires on the tube locally decrease the axial tension; there are consistent contact forces on the portions of the tube with smaller stress. All the values are calculated at the top surface of the tube. As expected, stresses at mid-surface of the tube are less affected by the contact forces.

The corresponding axial strain in the tube is shown in Figure 5.50. Its extreme values vary from 0.33% at the ends to 0.87% at the middle. It is completely in the plastic range as the minimum strain exceeds the strain at the proportionality limit (0.2%). Figure 5.51 shows the smoothed plastic strain generated in the tube.

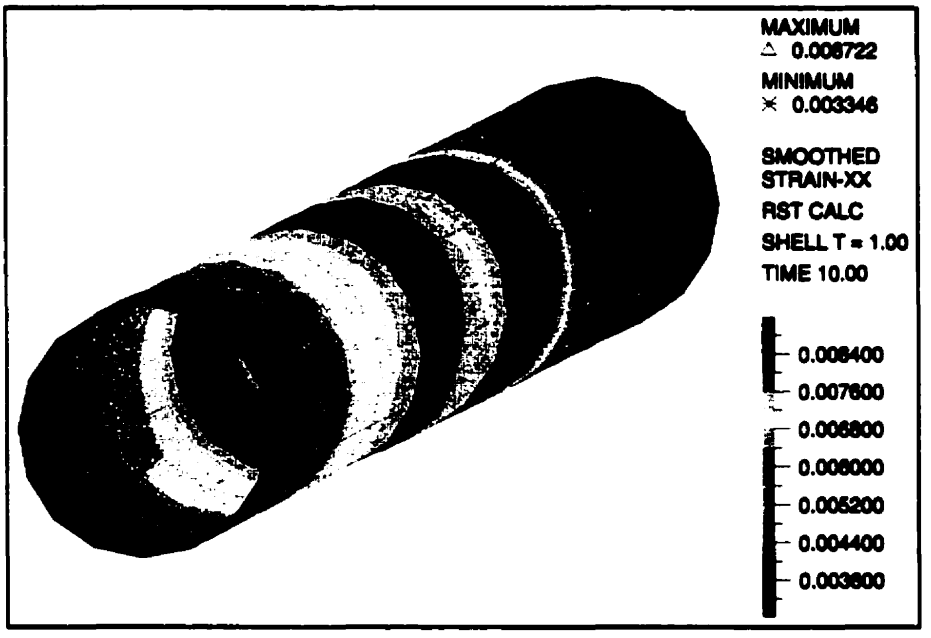

Figure 5.50 Smoothed axial strain of the tube

Since the tube is fully plastified, the effect of the contact forces from the inner wires on the stress and strain distributions cannot be observed. It means that the 1.62 mm prescribed displacement is large enough to induce permanent deformations in the tube.

The distribution of smoothed yield stress (not shown) indicates that the tube is yielded and the maximum value (145.6 MPa) is equal to the ultimate strength of the tube used in the stress-strain curve. Since no failure criterion for the tube is defined in the model, the calculated strains can be very large without the tube being failed. However, in reality (such as in the IREQ and McGill University

experiments) the tube is failed after reaching a maximum plastic deformation (of about 1 to 1.5%). In fact, the design criterion is based on the linear range of the stress-strain curve (maximum strain of 0.2%) and tube is considered failed beyond that.

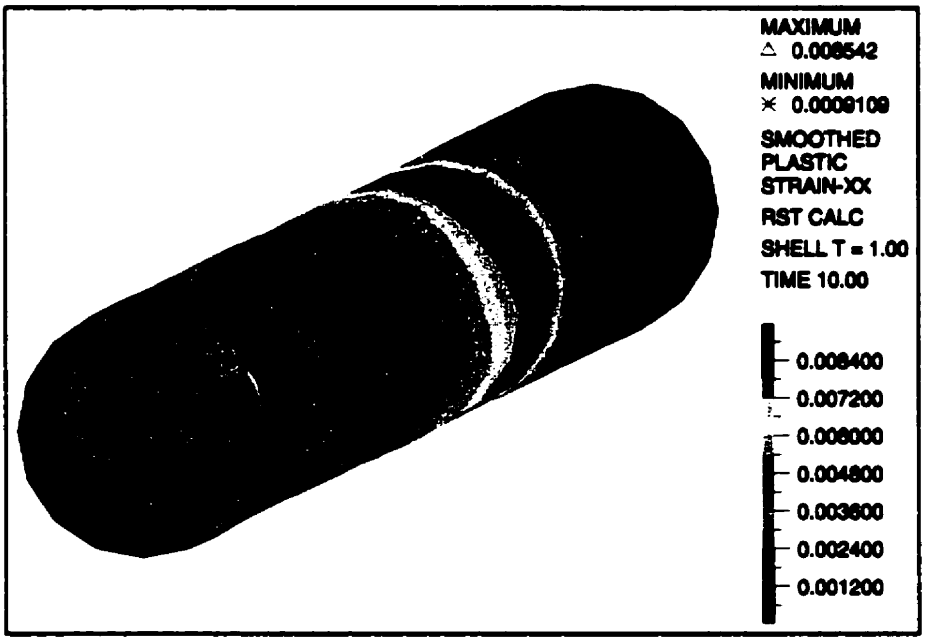

Figure 5.51 Plastic strain distribution in the tube

5.3.3 Aluminum spacer

The 5-groove aluminum spacer is at the core of the OPGW that houses the optical fiber units. The cross-sectional area at the loading end is subjected to a 1.62 mm elongation at all the interior nodes. Due to the spacer's cross-sectional and helical configurations, a non-uniform stress distribution is expected. Furthermore, there is no interaction with the other components of the OPGW and the stress and strain distributions are expected to be symmetric. Figure 5.52 shows the axial stress distribution on a cross section located at half of the cable length (132.58 mm). The maximum stress of 254.4 MPa occurs exactly at the center of the aluminum spacer and decreases gradually to its sides where the minimum of 238.3 MPa occurs. This small variation of the stress will diminish using a finer mesh, as the prescribed displacement will be more uniform over the cross section. Since no significant bending stresses are induced in the spacer, the average stress can be taken as 246 MPa, which is 88% of the ultimate tensile strength of the aluminum spacer (280.6 MPa) and is also in the inelastic range. The ultimate

strength of the aluminum spacer found in the experiments is 275 MPa (see Appendix II).

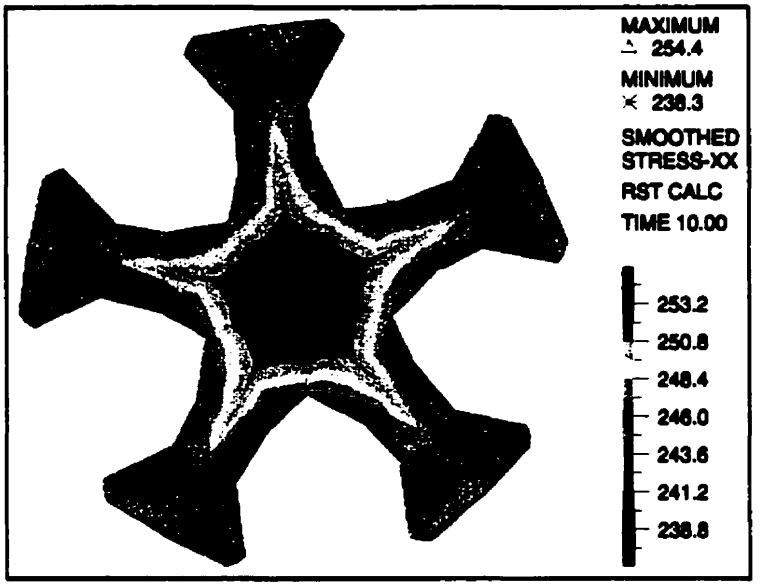

Figure 5.52 Normal stress (σ_{xx}) of the aluminum spacer at X=132.6 mm

The effective stress distribution is shown in Figure 5.53. The maximum effective stress (Equation 5.1) of the aluminum spacer is 258 MPa and its distribution is also considered uniform.

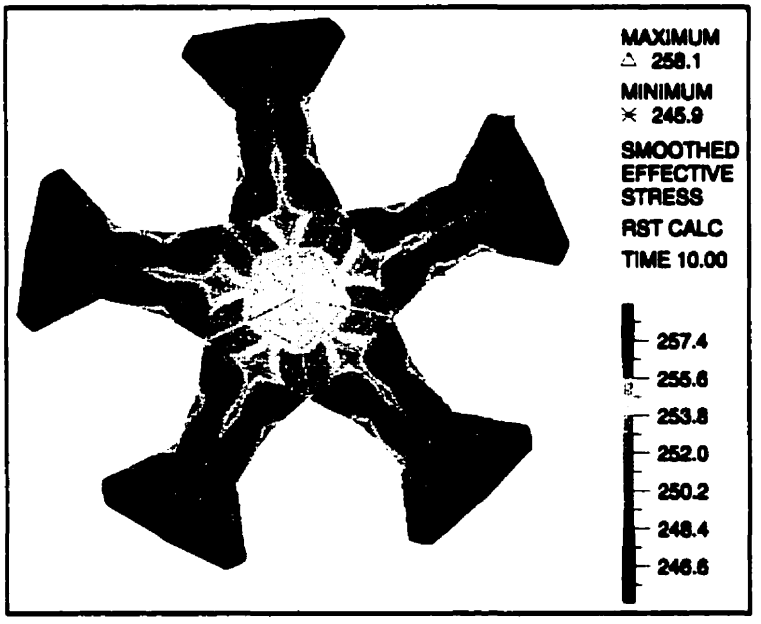

Figure 5.53 Distribution of the effective stress in the aluminum spacer

The axial strain distribution in the spacer (Figure 5.54) is different than that of the normal stresses due to the non-linearity of the material law. The maximum strains occur in the grooves and are equal to the prescribed strain (0.61%). The minimum strain (0.54%) occurs at the outer edges of the spacer, which are plastified.

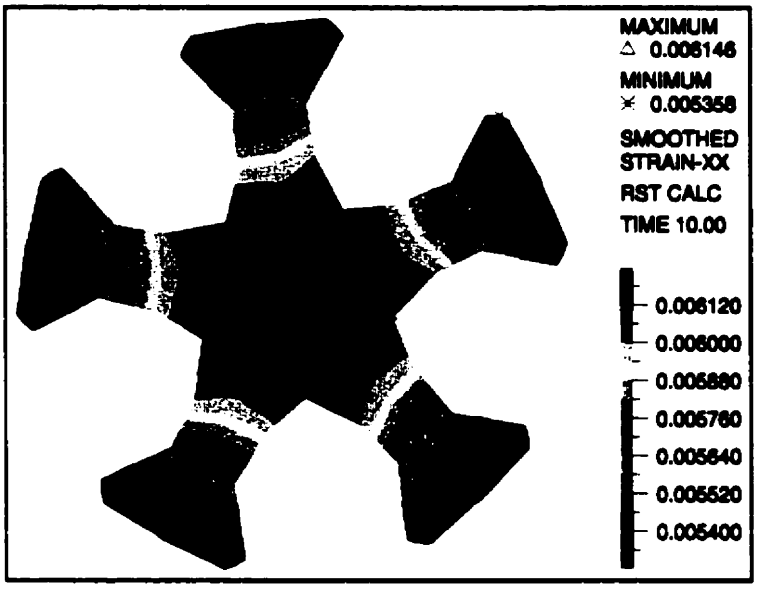

Figure 5.54 Axial strain (ε_{xx}) in the aluminum spacer

The distribution of the smoothed plastic strain-xx of the aluminum spacer is shown in Figure 5.55. The maximum is 0.24% which is significantly more than the excess length (0.018%) of the optical fibers inserted in the grooves. Considering an overall average plastic strain of 0.20%, it is expected that stresses are induced in the optical fibers, assuming the spacer elongates as much as the cable.

Experimental results (IREQ 1994) indicate that the measured maximum elongation of optical fibers are 0.52% and 0.48% for the 6-fiber and the 8-fiber groups, respectively. It is seen that these maximum elongations are less than the measured elongation of the external envelope of 0.61%, which is expected. However the difference is of 0.09% and 0.13% and exceed by the nominal fiber excess length of 0.018%. This is an important observation and it is discussed in details in the next sections.

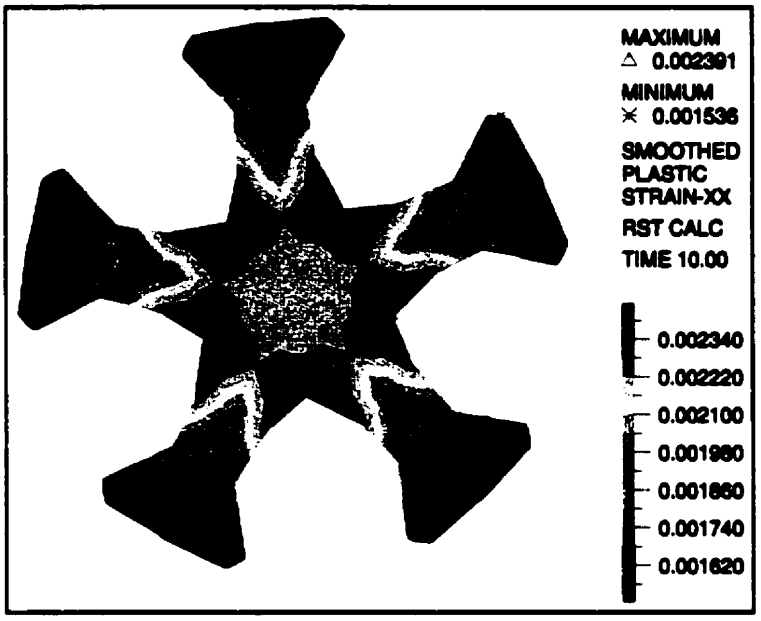

Figure 5.55 Smoothed plastic strain of the aluminum spacer

The maximum principal and shear stresses of the aluminum spacer are presented in Figures 5.56 and 5.57. The maximum values are 258.3 MPa and 132.5 MPa, respectively. It is seen that the variation of the distribution on the cross section is very small.

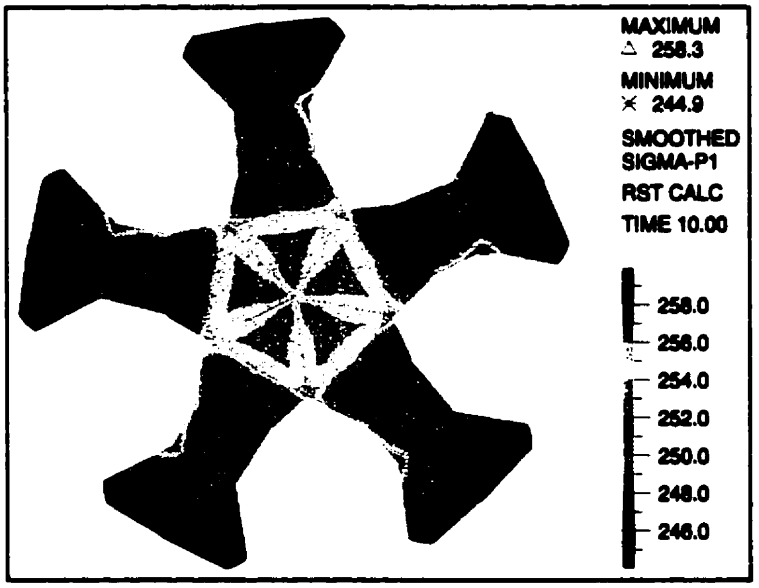

Figure 5.56 Maximum principal stress of the aluminum spacer

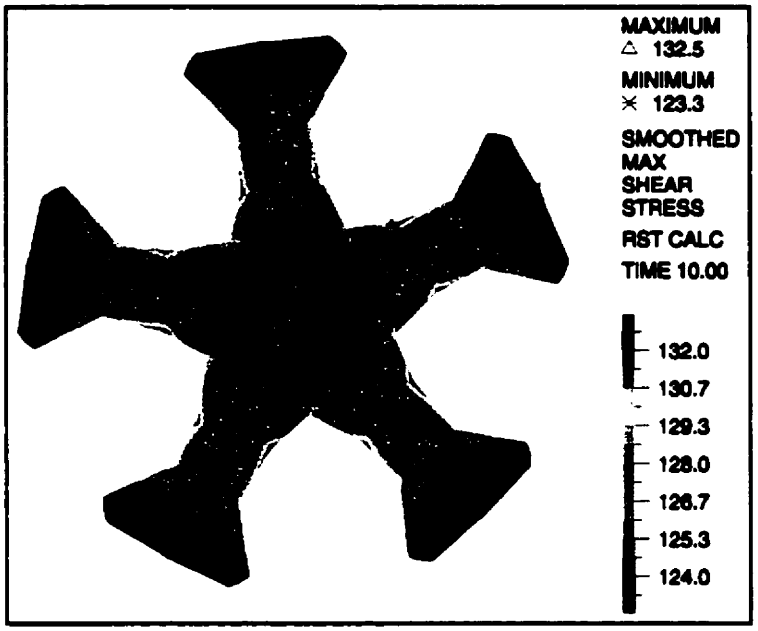

Figure 5.57 Maximum shear stress, $0.5(\sigma_{p1}-\sigma_{p3})$, of the aluminum spacer

The maximum axial displacement of the aluminum spacer at half-length of the cable is 0.75 mm (see Figure 5.58). Its distribution is practically uniform with an average of 0.74 mm, which is less than half of the prescribed displacement at the loading end (0.81 mm). This is consistent with the nonlinear material behavior. As mentioned in Chapter 4, the loading end of the aluminum spacer is free to rotate. Therefore, no reaction torque is induced at the free end.

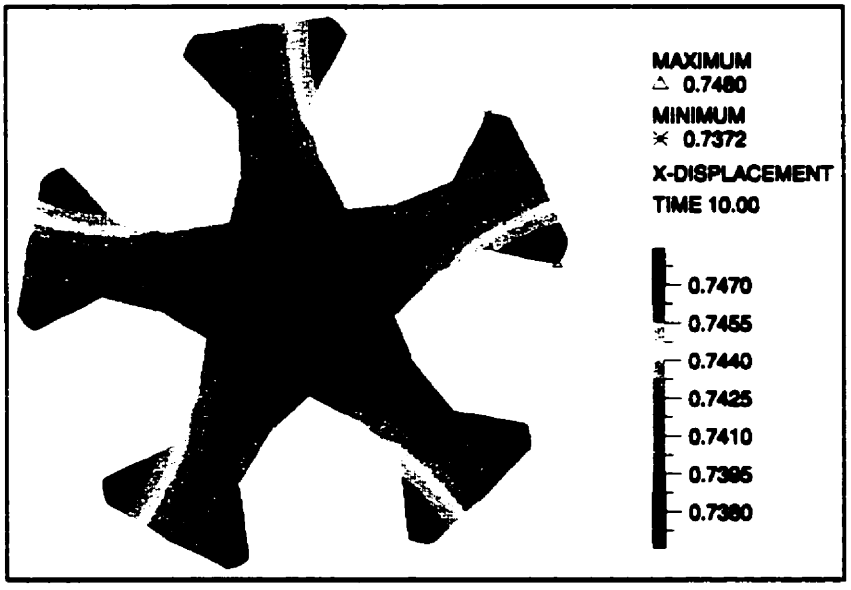

Figure 5.58 Axial displacement of the aluminum spacer at cable half length

Due to its helical geometry, the aluminum spacer tends to unwind when stretched. The unwinding rotation shown in Figure 5.59 is 42 degrees at the free end (full length of the cable) corresponding to 1.77 times of the spacer's pitch length (150 mm). Assuming a linear variation of this rotation, it amounts to 24 degrees per pitch length of the spacer.

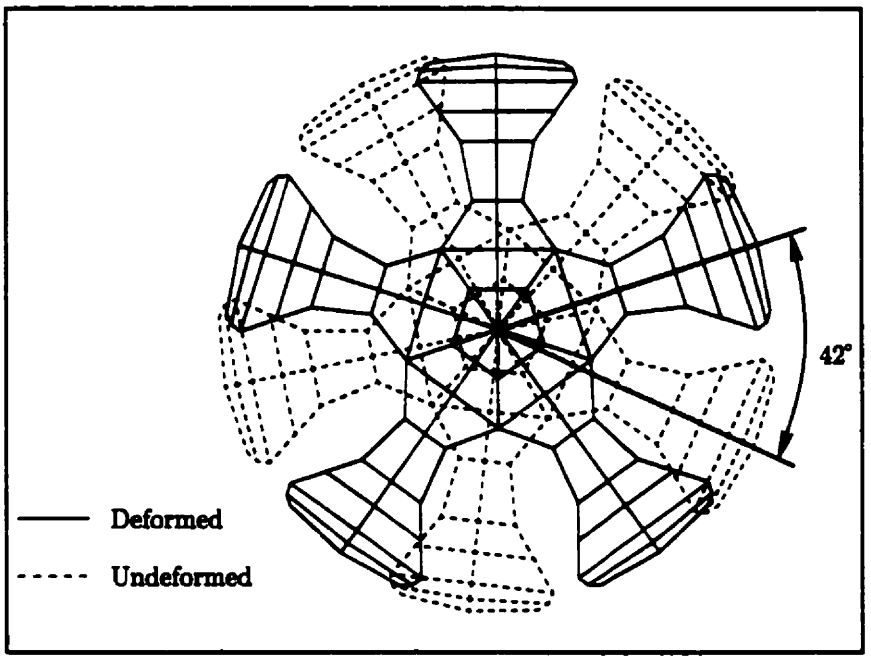

Figure 5.59 Unwinding displacement of the aluminum spacer at loading end

5.3.4 OPGW response

5.3.4.1 Torque and force reactions

In the finite element model, the torque reaction (*MOMENT-REACTION-X*) is calculated by summation of the multiplication of the Z- and Y-REACTION of each constraint node by its corresponding Y- and Z-LEVER.

The torque reaction at the loading (free) and the support (fixed) ends of the outer and inner wires and the tube versus load increments are shown in Figure 5.60. The central tube is free to rotate at the loading end, therefore no torque is generated at free end and only the fixed end torque reaction is plotted.

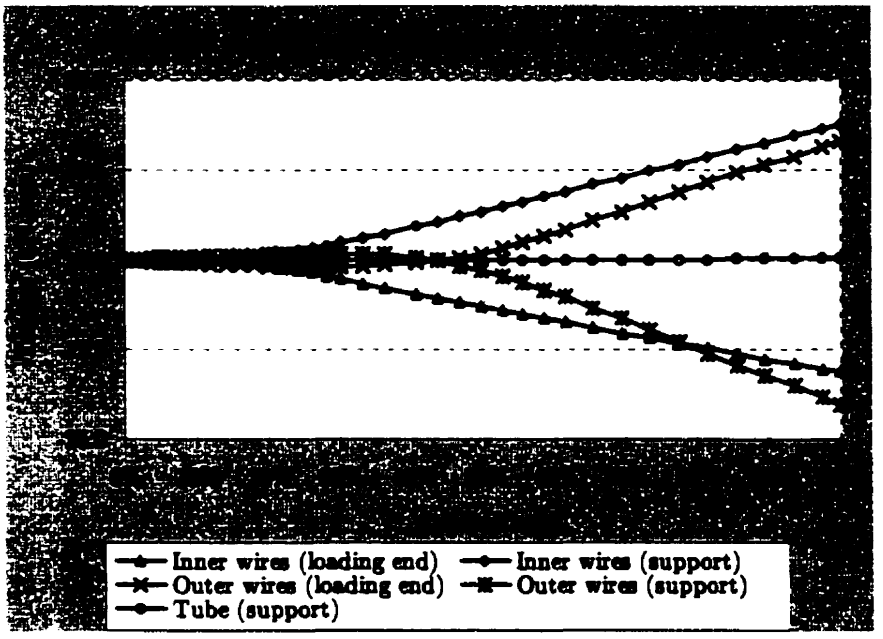

Figure 5.60 Torque reaction of the OPGW components

The directions of the torque reaction at the free end of the outer wires and inner wires are opposite with respect to each other. The torque reactions at the loading end of the inner and outer wires are -15.6 and 16.7 kN.mm, respectively. These values are smaller than the torque reactions at the support (19.0 and -20.3 kN.mm). The history of the loading shows that up to 50% of the load the response is non-linear but then becomes almost linear up to the full load for both the outer and inner wires. The results indicate that the opposite helix of the outer and inner wires significantly reduces the resultant torque at both ends. The contribution of the central tube in torque resistance is negligible compared to that of the wires.

The reaction force in the X-direction at ends (fixed and free) is presented in Figure 5.61. The aluminum spacer reaction is not shown here since its response is independent of the tube and wires.

The loading history of the reaction force shows that the inner wire contribution is the most important one. The reaction forces of the inner wires at the free end and at the support are 45.85 and -45.69 kN, respectively. The difference (160 N) is the resultant friction force exerted by the outer wires and the central tube. The reaction forces of the outer wires at the loading end and at the support are 17.04

and -17.17 kN, respectively. Therefore, the resultant friction force between the outer wires and inner wires is 130 N. It can be concluded that the effect of the friction force is negligible on the response in axial load. The results for the other loading case when only the central node is loaded is similar to the above and is presented in Tables 5.4 to 5.6.

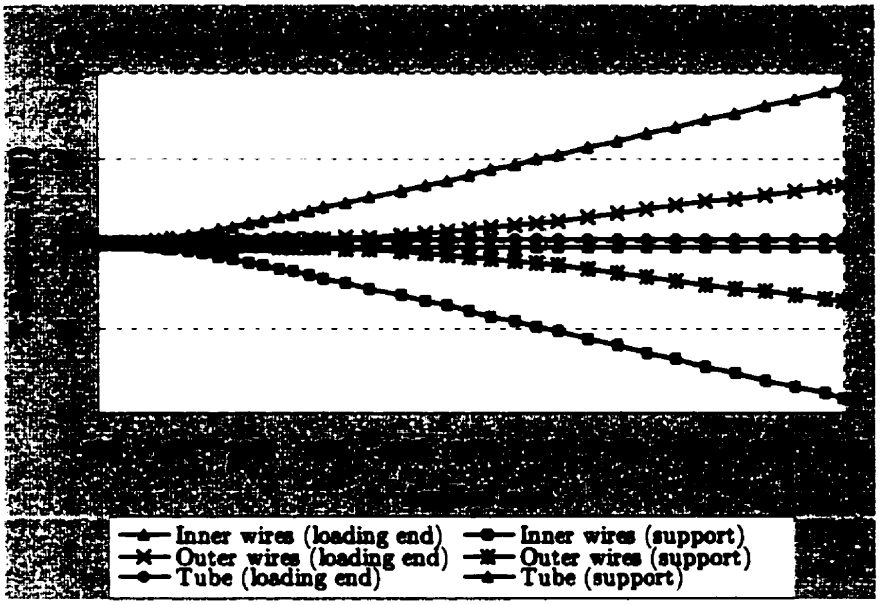

Figure 5.61 Cable axial reaction force of the OPGW components

5.3.4.2 Stresses and strains

The strain and displacement (along the cable axis) of a central node of the inner and outer wires at the free end are plotted in Figure 5.62 with the results obtained by the analytical solution of Phillips and Costello (1973). This solution is based on the one-dimensional linear strain-displacement relation ($\varepsilon = \Delta l / l$). The numerical response of the inner wires for small displacements is close to that obtained from the analytical solution, however, the difference is increasing for larger displacements. Nevertheless, the strain-displacement relation is almost linear.

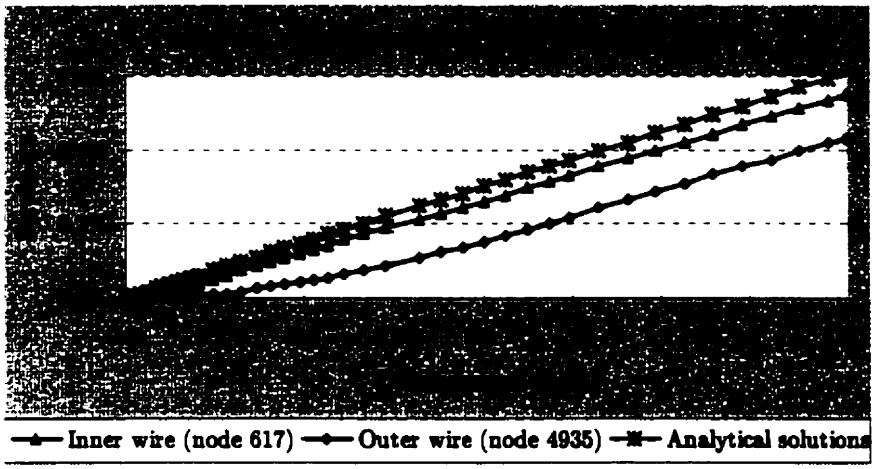

Figure 5.62 Loading end response of the wires (all interior nodes are loaded)

The central nodes of the inner and outer wires (Nodes 518 and 4770 selected here) are located almost at the mid-length of the cable. The strain versus displacement relation of those nodes is plotted in Figure 5.63. The linear analytical solution predicts the same response for the inner wires for small displacements (up to 0.26 mm) but underestimates the strains for large displacements.

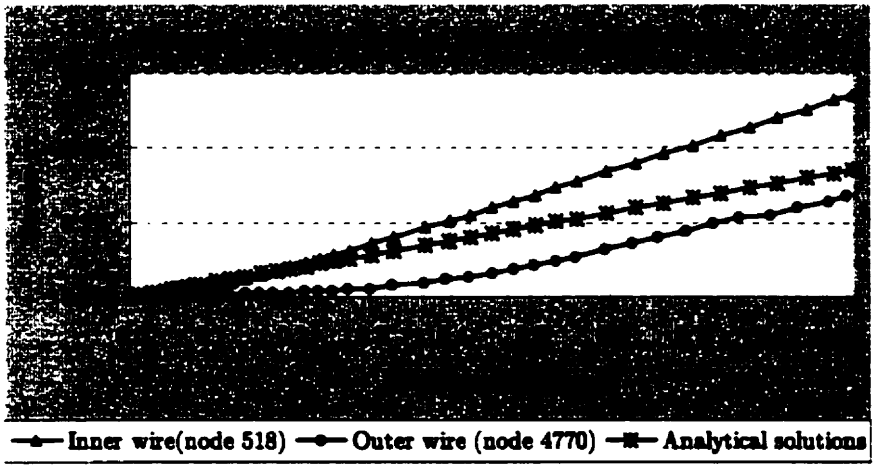

Figure 5.63 Mid-length response of the wires (all interior nodes are loaded)

The numerical response of the outer wires is smaller than that predicted by the analytical solutions and is nonlinear throughout the loading history. The numerical strains plotted are a smoothed average using bilinear interpolation between integration points.

5.3.4.3 End effects

Figure 5.64 shows an inner wire's stresses along the cable axis for the two cases studied. There is almost no variation in stress far from the ends. It is seen that end effects are limited to few elements and the stress is very high at the loading end when the displacement is prescribed only at the central node. As mentioned earlier, the end effects vanish when using the centroid interpolation scheme. The results in Figure 5.64 are extrapolated using the results at the nearest integration points and bilinear interpolation (RST) for a floating-point. The stresses vary between 820 to 890 MPa, neglecting the end effects.

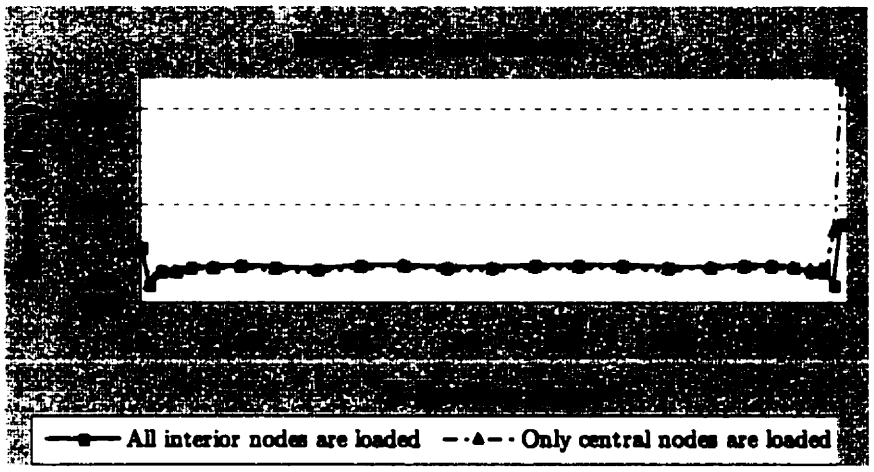

Figure 5.64 Stress end effects in an inner wire

The stresses and strains of an outer wire versus its position (final coordinate) are plotted in Figures 5.65 and 5.66, respectively.

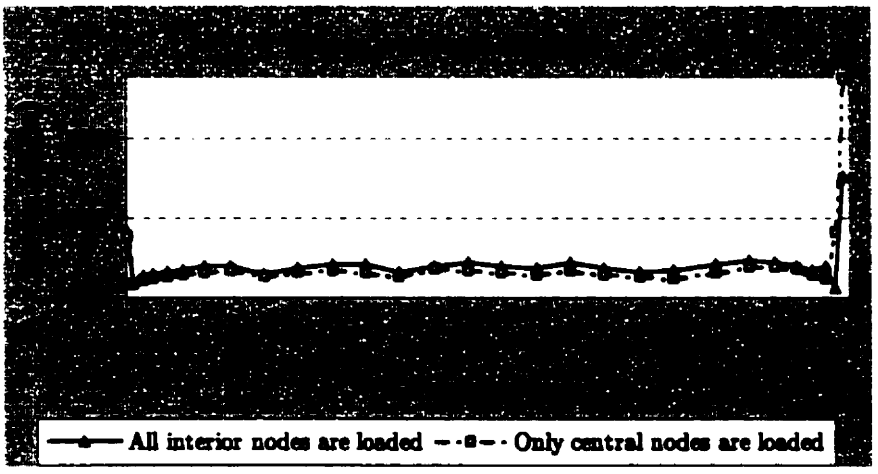

Figure 5.65 Stress end effects in an outer wire

The overall response is similar to that of the inner wire, however, the difference between the two the loading cases is more evident for the outer wires. The stresses vary between 150 to 190 MPa when the end effects are neglected.

The strain variation along the cable axis in an outer wire is almost periodic. Its period is almost a quarter of pitch length (202 mm) which consists of five cycles for the full length of the model (265.16 mm). The strain varies between 2.3 and 3.0%, and it is larger when all the interior nodes of the loading cross section are loaded.

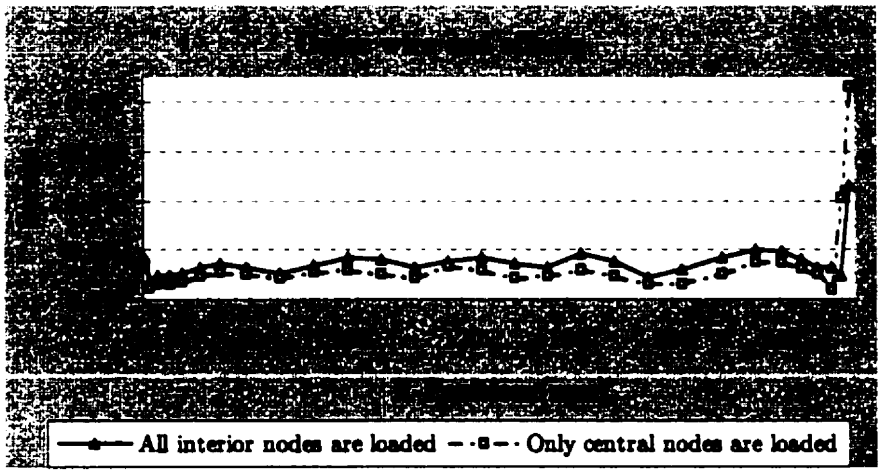

Figure 5.66 Strain end effects in an outer wire

5.3.4.4 Displacements

The displacements of the central node of an inner and an outer wire are plotted in Figures 5.67 and 5.68 along the cable axis.

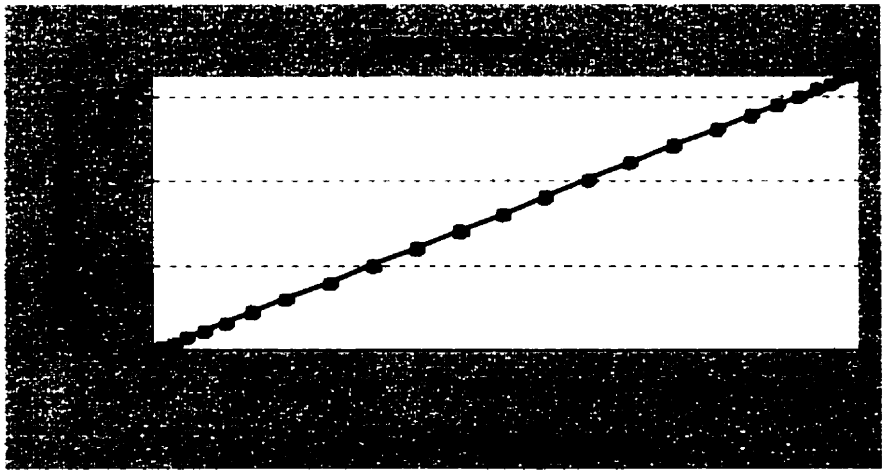

Figure 5.67 Inner wires displacement along cable axis

The solid lines represent the linear strain (0.61%).

The graph shows the elongation of an outer wire along the cable length (Figure 5.68) and the linear theoretical displacement (solid line) indicates that the behavior of the outer wires are slightly nonlinear for some part of the cable. It is noted that in a region where the displacement is prescribed (free end), the relation is linear.

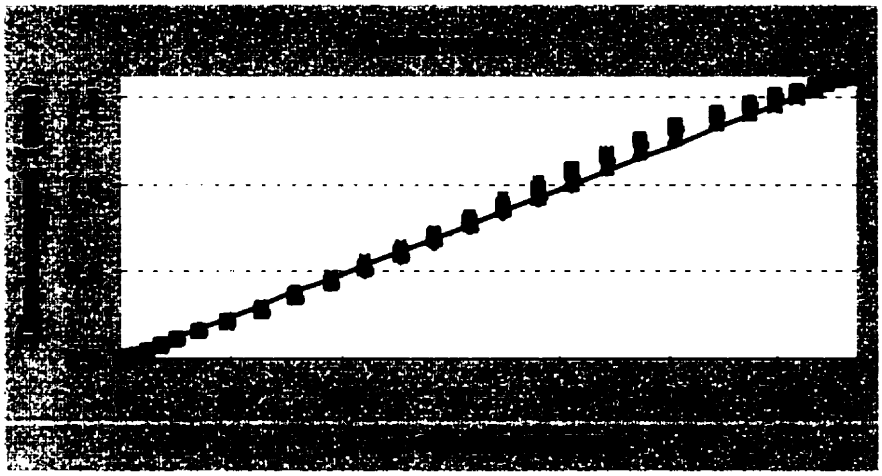

Figure 5.68 Outer wires displacement along cable axis

As it is seen, the axial displacement of the wires along the cable length is, in general, linear with respect to the cable length. However, the true strain in the wires cannot be extrapolated using the linear strain-displacement relation.

5.4 Summary of the results

The results of the OPGW finite element model for the two cases presented in the sections 5.2 and 5.3 are summarized in Tables 5.4 to 5.6.

These results are compared with those of the two analytical solutions by Machida and Durelli (1973), and Phillips and Costello (1973). Results listed for the inner and outer wires and the aluminum spacer are at the cross section located at mid length of the cable model. The central aluminum tube results are those calculated over its entire length.

Table 5.4 Responses of OPGW - Finite element models and analytical solutions

Model \ Response	Total axial load (kN)		Stress-XX (MPa)	Strain-XX (%)
	Fixed-end	Free-end		
Outer wires (all interior nodes are loaded)	-17.17	17.04	50 - 258	0.097 - 0.378
Inner wires (all interior nodes are loaded)	-45.69	45.85	775 - 919	0.480 - 0.564
Tube	-1.34	1.30	4 - 193	0.311 - 0.940
Outer wires (only central node are loaded)	-16.75	16.70	38 - 255	0.079 - 0.373
Inner wires (only central node are loaded)	-45.10	45.12	772 - 920	0.475 - 0.556
Tube	-1.35	1.27	11 - 203	0.303 - 1.024
Aluminum spacer (FE model)	2.5		238 - 254	0.536 - 0.615
Machida & Durelli (1973)				
Outer wires	44.7		349 - 367	0.560
Inner wires	61.9		955 - 969	0.599
Tube	3.9		377	0.610
Phillips & Costello (1973)				
Outer wires	44.1		331 - 349	0.569
Inner wires	61.8		953 - 968	0.602
Tube	3.9		377	0.610
Aluminum spacer (Analytical)	4.0		389	0.610

5.4.1 Comparison of two loading cases in the finite element analysis

The two finite element models only differ in the application of the loading, with either the displacement prescribed at the central nodes or at all the interior nodes of the wires. The results indicate that the two models are similar and the differences in the calculated responses in the outer and inner wires are negligible. However, in general, the overall responses of the model with more restrictions (when all interior nodes are loaded) show slightly higher stresses and strains. The axial strain and stress of the central aluminum tube is mostly affected. The maximum axial strain in the tube increases by about 9% when the central nodes are loaded. This is due to the increased contact of the inner wires with the tube since the wires have more freedom to move compared to the other loading case. Therefore, the axial stress is slightly higher too. In reality, the applied axial load

on the OPGW is almost uniform and the deformation of the wires at the loading end are expected to lie in between those obtained in the above two loading cases.

The study reveals that the effect of the two loading modes are insignificant on the overall response of the OPGW, and only the by using displacement-control approach allows that compatible displacements be induced in the OPGW components.

5.4.2 Comparison with analytical solutions

The analytical solutions of Machida and Durelli (1973) and Phillips and Costello (1973) are calculated based on a 0.61% axial elongation of the cable (OPGW) without friction effects. It is recalled that the calculations of the finite element model are based on a prescribed displacement of 1.62 mm subjected to all components of the OPGW (inner and outer wires, aluminum tube and spacer), which is equivalent to a 0.61% elongation, assuming a *linear* strain-displacement relationship. An axial load of 114 kN or 106 kN is required to induce an elongation of 0.61% using the analytical solutions of Machida and Durelli or Costello. However only 67 kN is needed to stretch a 265.2 mm length cable segment as much as 1.62 mm. The exact displacement is used here as a reference, since the axial strain induced in the model differs from 0.61%, and varies in components.

The equivalent secant modulus of elasticity of the finite element OPGW model based on the 0.61% elongation is 57.5 GPa. A theoretical calculation considering full compatibility of all the cable components elongation yields an initial tangent modulus of 93 GPa. This comparison reveals that the finite element OPGW model is more flexible than that of the analytical solutions. More discussion is presented in the next section in the transmission line application of the OPGW.

The resultant torque at the fixed end is almost zero, which means that the induced torques in the outer and inner wires are almost equal but in opposite directions. The net torque reaction is about 50 kN.mm using the analytical solutions. The outer wires reaction torque (-82 kN.mm) is significantly larger than that of the finite element model (-20 kN.mm). In fact, the opposite direction and the angle of the helix of the outer and inner wires are optimal.

Table 5.5 Responses of OPGW models and analytical solutions

Model \ Response	Torque (kN.mm)		Max. Principal Stress (MPa)	Max. Shear Stress (MPa)
Outer wires (all interior nodes are loaded)	Fixed end: -20.3	Free end: 16.7	54 – 292	39 – 157
Inner wires (all interior nodes are loaded)	19.0	-15.7	790 – 932	406 – 473
Tube	0.29	0.0	5 – 194	65 – 98
Outer wires (only central node are loaded)	-19.5	17.8	47 – 280	38 – 141
Inner wires (only central node are loaded)	18.2	-16.7	787 – 935	402 – 466
Tube	0.17	0.0	12 – 205	64 – 104
Aluminum spacer	0.0		245 – 258	123 – 133
Machida & Durelli (1973)				
Outer wires	-83.3		349 – 367	175 – 183
Inner wires	31.5		969 – 984	485 – 492
Tube	0.0		—	—
Phillips & Costello (1973)				
Outer wires	-81.5		353 – 373	177 – 186
Inner wires	31.2		967 – 982	483 – 491
Tube	0.0		—	—

5.4.3 Comparison with experimental results

In the experiments performed by IREQ (see APPENDIX II), an 83.5 kN axial force induces an elongation of 0.61%, including the creep effects. The reaction force obtained by the finite element model (67 kN) is only 80% of that obtained in the experiments. It is worth noting that the elongation measured in the experiment is of the external envelope of the cable (outer wires) and the behavior of the other components (inner wires, aluminum spacer and the tube) cannot be observed. The elongation of the optical fibers inserted in the aluminum spacer grooves is 0.52%, considering the excess length of the fibers (0.018%). Assuming compatible displacements for all the OPGW components, the optical fibers must extend up to 0.59%. Therefore, it can be inferred that the elongation of the optical fibers unit and consequently the aluminum spacer is incompatible with the measured elongation of the external wires (0.61%). As an approximation, one would predict that the elongation of the aluminum spacer is equal to the measured fiber

elongation (0.52%) plus the actual fiber excess length (nominal value of 0.018%), which amounts to only 0.54%.

5.4.4 Unloading cycle

In order to verify the final configuration and stresses of the OPGW, the cable model is unloaded. In the process of unloading, the prescribed displacement (1.62 mm) is gradually decreased (in 40 steps) to zero displacement. It is noted that due to the presence of plastic deformations in the aluminum tube and spacer, the zero displacement state will not correspond to a stress-free state. Figure 5.69 shows the loading history of the free end of the central tube. The tube is unloaded after reaching a 1.62 mm displacement. The figure shows that at 1.07 mm the reaction force is zero and the free end of the tube is in a stress-free state. In other words, a permanent displacement of 1.07 mm, equivalent to 0.4% axial strain, is induced in the tube. This permanent deformation is at the free end of the tube, and it varies along the cable.

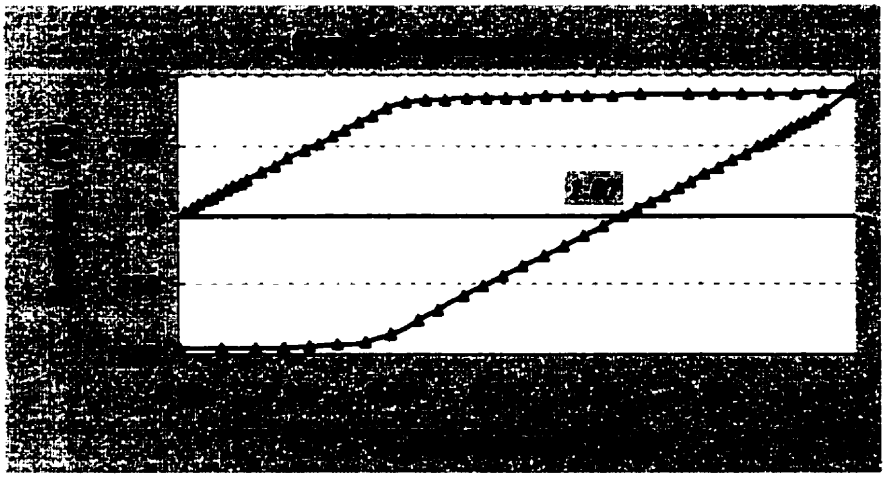

Figure 5.69 Load cycle in the central tube

Figure 5.70 shows the history of loading in the aluminum spacer. Due to the non-linear material behavior of the spacer, the spacer yields after an elongation of almost 0.9 mm. The total reaction force reaches 2.5 kN. The response indicates that during unloading to zero displacement, the reaction force becomes zero for a 0.55 mm deformation. As a result, the permanent plastic deformation of the aluminum spacer is 0.55 mm. The graph also shows a linear response in the unloading cycle.

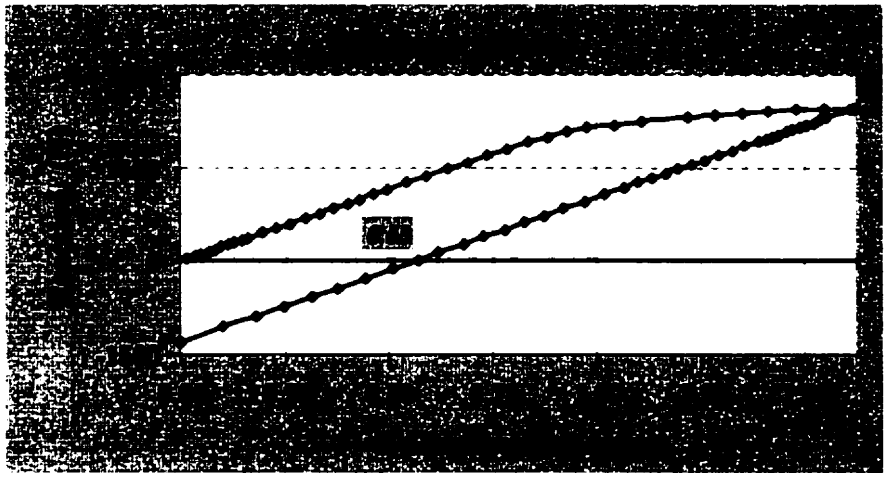

Figure 5.70 Load cycle in the aluminum spacer

The permanent deformation of the aluminum spacer (0.55 mm) is about half of that of the central tube (1.07 mm). Since the optical fiber units are housed in the spacer's grooves, compatible deformations can be assumed between the fibers and the spacer, excluding the excess length of the fibers. For the length of the model (265.16 mm), the excess length of the fibers is 0.05 mm (0.018%), therefore, the optical fiber units are expected to undergo a 0.5 mm elongation (0.19%) after the cable is unloaded. This deformation can be the cause of the permanent signal attenuation observed in the IREQ experiment (IREQ 1994), although the report is not specific about it.

Due to the linear material law of the inner and outer wires, no permanent deformations are left after the wires are unloaded. In a typical transmission line span which the total cable length is large (300 m-450 m), the effect of the accumulated plastic deformations of the aluminum tube and spacer will be redistributed in the inner and outer wires.

5.4.5 Extreme loading case

As mentioned before, the response of the inner and outer wires in the finite element model is linear. In order to verify the strength of the cable prior to wire yielding, an extreme loading scenario is considered. The prescribed displacement in the OPGW model is increased by 20% to 1.94 mm, which is equivalent to a 0.73% axial elongation. It is applied to all the interior nodes of the wires and friction effects are included. The results indicate that this threshold is almost the maximum loading for which the wires remain linear. The responses of the wires

and the tube are similar to that obtained for the 1.62 mm prescribed displacement, and therefore only the numerical results are presented here.

The maximum stress (σ_{xx}) in the outer and inner wires are 319 and 1126 MPa, corresponding to 214 and 1061 MPa average stresses and ±105 and ±65 MPa bending stresses, respectively. Results indicate a large bending stress in the outer wires compared to the inner wires. The maximum strains are 0.47% and 0.68% in outer and inner wires, respectively. However, the average strains in the outer wires are 0.35% and 0.63% in inner wires. All the results are obtained at the cross section located at half-length of the model.

The axial reaction forces induced at the loading end are 24 and 56 kN in the outer and inner wires, respectively. Adding the aluminum spacer and tube reaction forces to those of the wires, the total axial reaction of the cable is 84 kN. This is almost equal to the axial tension force used in the experiment (83.5 kN)(IREQ 1996). Despite the loading (prescribed displacement) is increased by 20%, the total axial force is increased by 27%. This confirms the nonlinear relation of the axial deformation and the tensile force of the cable

The reaction torque at the fixed and the loading ends of the outer wires are -31 and 28 kN.mm. These values for the inner wires are -21 and 23 kN.mm, respectively. The resultant torque of the inner and outer wires is about 7 kN.mm. This indicates that increasing the axial displacement increases the resultant torque. The reaction torque in the wires shows an increase of 23% to 50%, compared to the reference loading case. The response of the aluminum tube and spacer remains almost the same as in the reference loading case, but the plastic deformations are increased due to the additional loading.

5.5 Mesh refinement

In order to verify the accuracy of the finite element model, a finer mesh is generated for the outer and inner wires. Figure 5.71 shows the cross section of the OPGW with a finer mesh compared to the previous model. In this fine mesh model, the number of elements in the wire cross sections is doubled of that the previous mesh, while the number of longitudinal elements is the same. The finer mesh of the cross section is selected to simulate more contact with neighboring wires and the tube in comparison with the previous coarser mesh.

In order to compare the two models, the prescribed displacement is applied to the same nodes as in the previous model, and not to all the interior nodes of the wires cross section. All other characteristics of the model are kept the same as those of the previous model. Due to the increased number of elements and the limitations of the computing platform, the aluminum spacer is excluded from the model.

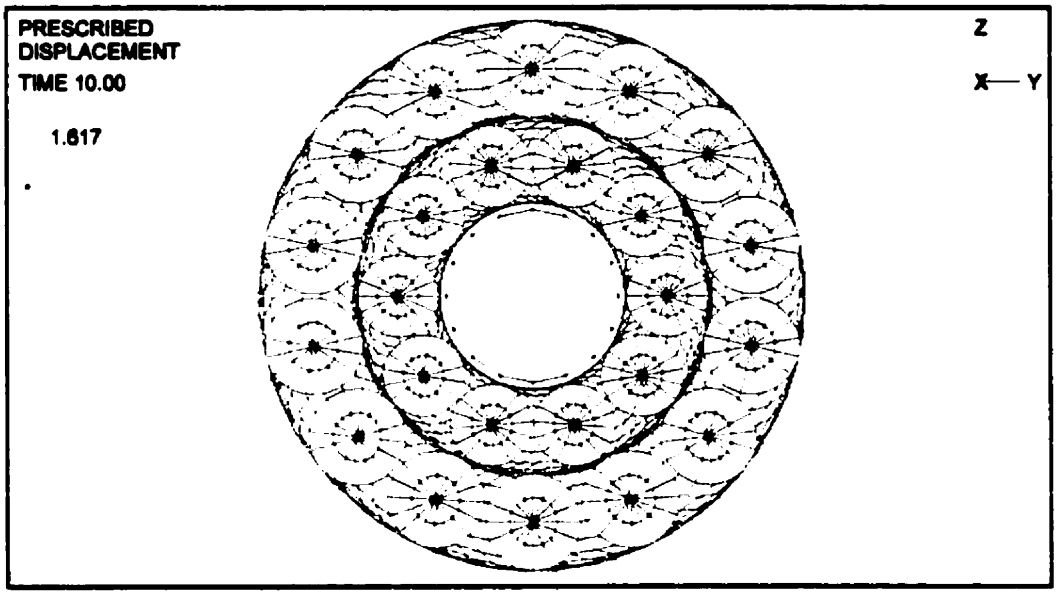

Figure 5.71 Fine mesh of the OPGW

Contrary to the coarse mesh where the wires touch each other only in the third load step, the wires are in contact from the first load step since the gaps between the wires are small. Selected results of this model are presented in the next section for comparison with the previous model.

5.5.1 Outer wire response - fine mesh

The strains and stresses of the outer wires cross-section at mid-length of the cable are presented in Figure 5.72. Comparison of the results with the same loading scenario of the coarser mesh reveals that the strains and consequently stresses are higher using a finer mesh. The maximum stress (294 MPa) is almost 12% larger than that of the coarser mesh (258 MPa). In general the bending effect is more evident in the coarse mesh and is smaller in the fine mesh. The overall trends of the stresses and strains are similar to the previous model and contrary to the inner wire response, no local contact stresses are observed.

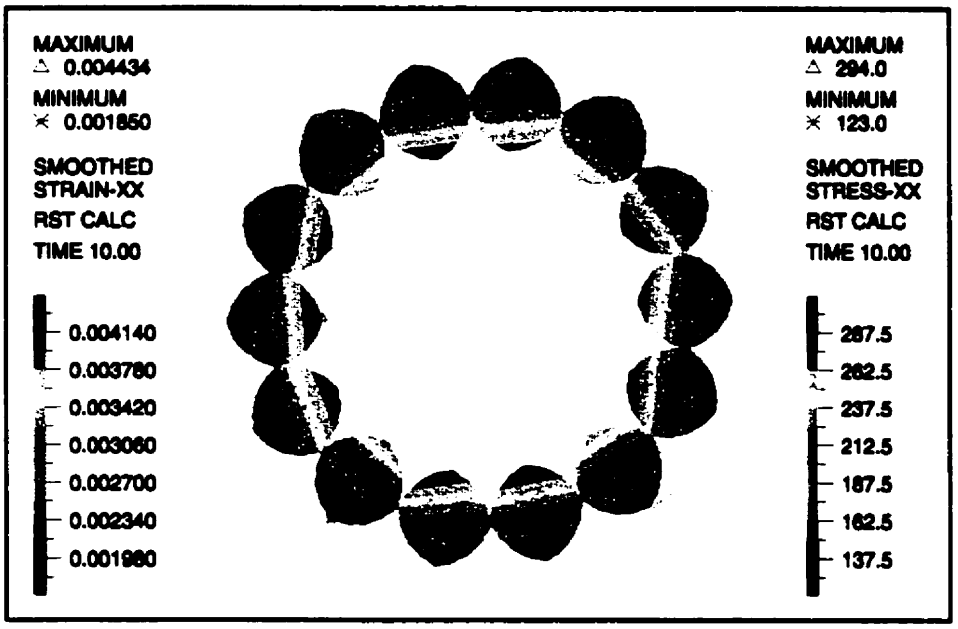

Figure 5.72 Stress and strain distribution in outer wires - fine mesh model

The maximum principal and shear stresses are 319 and 162 MPa, respectively. These values are only 8% and 3% larger than those of the previous model. The distribution of the shear and principal stresses are the same in the fine mesh as the bending effects are minimal compared to the previous model.

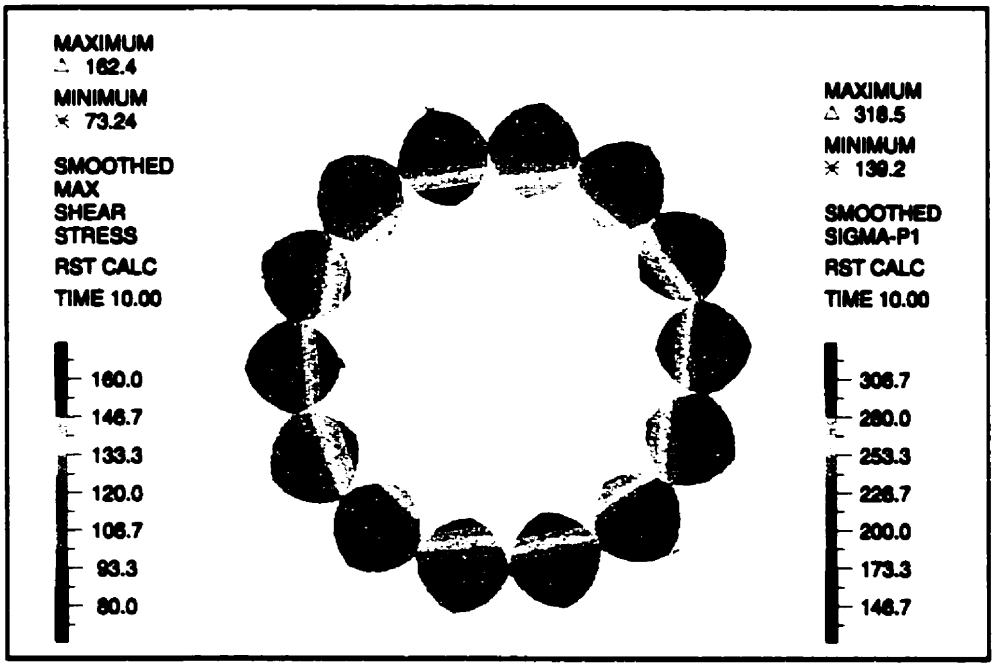

Figure 5.73 Principal and maximum shear stresses of outer wires

5.5.2 Inner wires response - fine mesh

The smoothed principal and XX-stresses of the inner wires along the cable axis are illustrated in Figure 5.74. The compression due to the contact forces between neighboring wires decreases the stresses along the cable axis. Although this effect is globally insignificant, however, the local effects can be seen clearly.

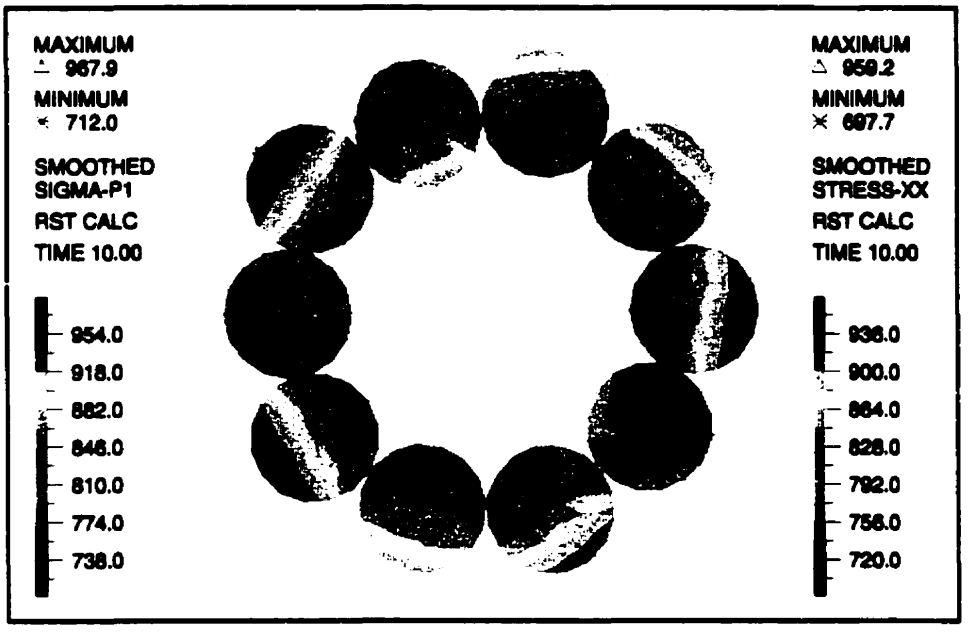

Figure 5.74 Principal and normal stresses of inner wires along cable axis

The maximum stress (959 MPa) is only 4% larger than the value found in the previous model and the minimum (698 MPa) is 1% smaller. The changes in normal stresses are very small and using a finer mesh does not seem to be efficient. However, the distribution of the stresses is very affected by the use of a fine mesh. It is observed that after applying half of the load, due to excess contact between the adjacent inner wires, the stress distribution changed gradually such that, at the end the maximum stresses occur at the outer fibers in four wires, whereas the maximum stresses occurred at the inner fibers in the coarse mesh model. The stress distribution is no longer uniform, but the extreme values are not much affected.

The maximum shear stress distribution is presented in Figure 5.75. The maximum value (525 MPa) is about 10% larger than that of the coarser mesh (473 MPa). However, this maximum is limited to the contact point of the wires, which is not a good indicator for comparison. The average shear stress is only

about 5% more than that of the previous model. In general, the distribution of the stresses is more uniform using the finer mesh, neglecting the concentrated contact force effects.

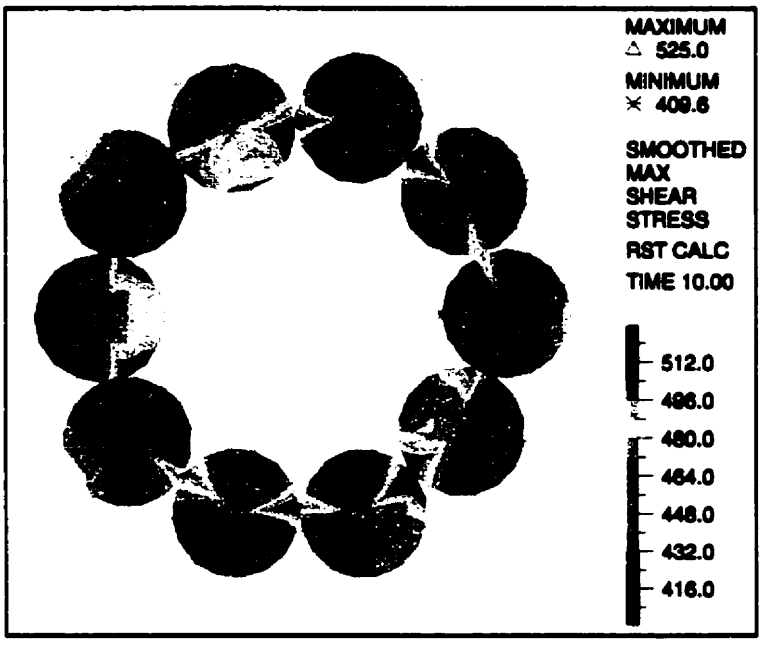

Figure 5.75 Maximum shear stress of inner wires along cable axis

The stress distributions are affected by the contact forces but the strain is not, such that the strain distribution (Figure 5.76) being different than the stress distribution.

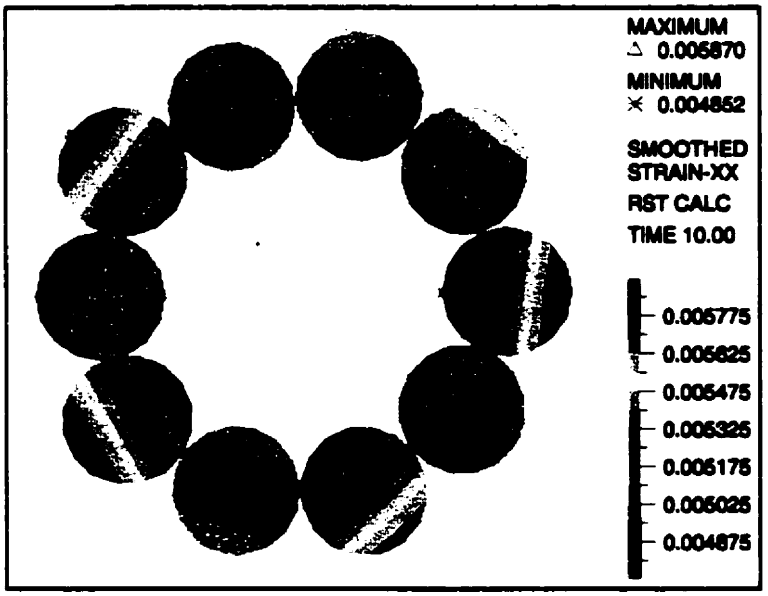

Figure 5.76 Strain distribution of inner wires - fine mesh model

Again, here the maximum strain occurs at the outer fibers where the stress is maximal. The maximum strain (0.59%) is only about 4% larger than that of the coarse mesh (0.56%)

Using a finer mesh for the inner wires increases the contact between the wires and the tube. Figure 5.77 shows the axial stress distribution in the central tube using the fine mesh model. Stresses and strains (Figure 5.78) in the tube are slightly larger than those of the previous model. However, since the tube in both model yields, the overall effects are not significant. Due to more contact from the inner wires, the stress distribution is more uniform in the tube compared to the previous model where concentrated contact forces decreased the axial stress locally.

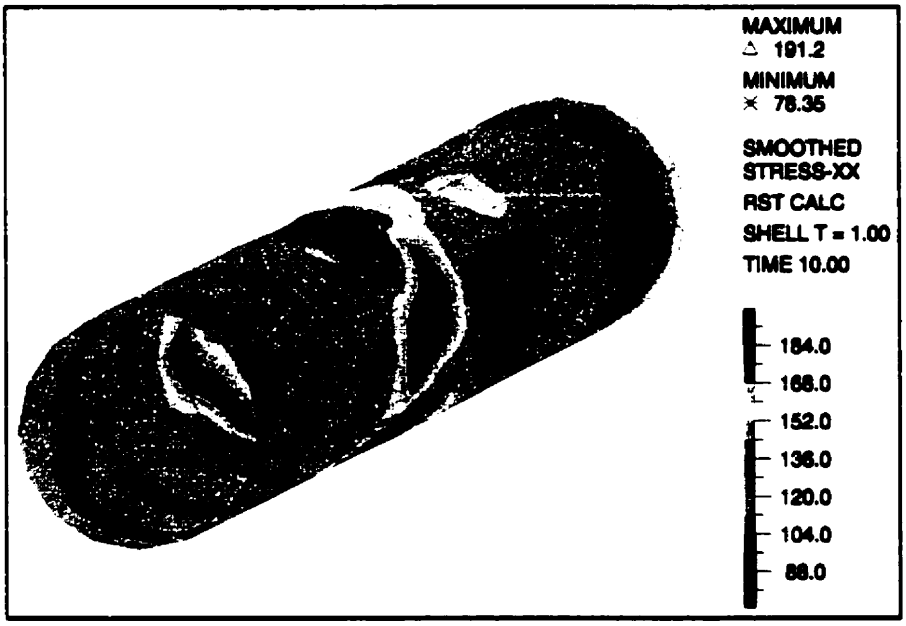

Figure 5.77 Stress distribution in central tube

The maximum axial stress (191 MPa) is about 6% lower than that obtained in the coarse mesh model (203 MPa), while the minimum (78 MPa) is 86% larger due to localized contact effects. The changes in the average stress and strain values are insignificant.

The maximum and minimum axial strains in the tube (0.91% and 0.41%) are about 6 and 19% larger using a finer mesh. Again, the localized contact forces explain the reason of larger difference in minimum strain. However, the changes

in average strain are insignificant. The average smoothed plastic strain in the tube (0.44%) is about 6.7% smaller using the finer mesh model.

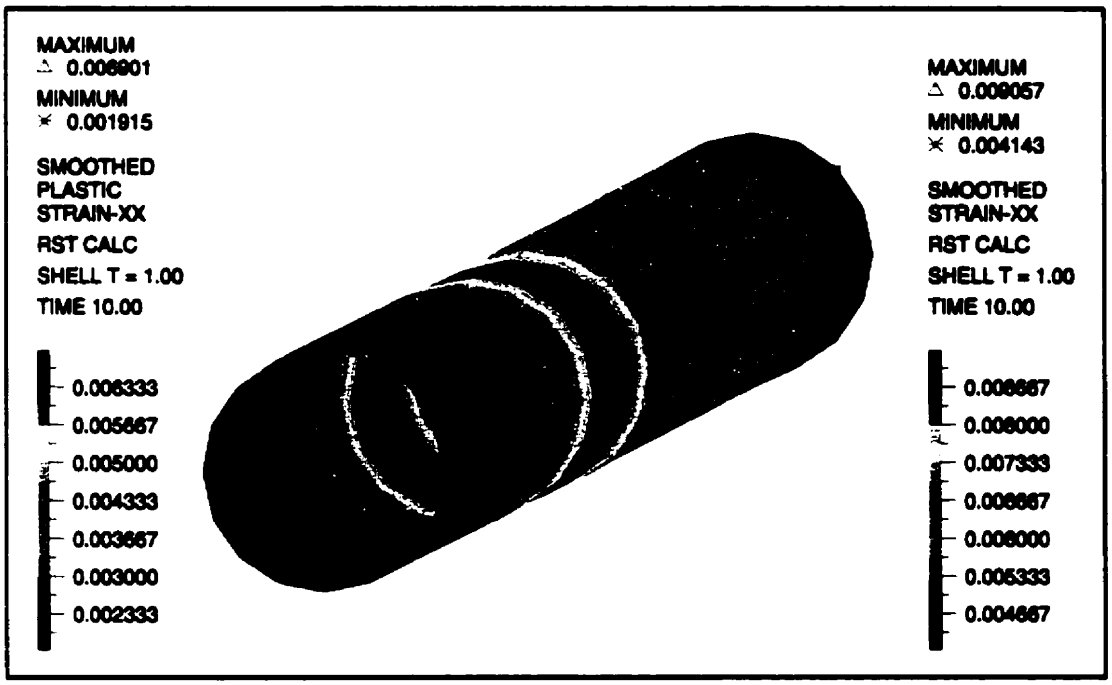

Figure 5.78 Strain distribution in aluminum tube - fine mesh model

5.6 Behavior of the OPGW in transmission lines

The OPGW analyzed in this study is used in Hydro-Québec's transmission lines. The cable elastic extension, δS_e, due to horizontal tension, H, in the catenary configuration can be obtained by

$$\delta S_e = \frac{H^2}{wAE}\left[\frac{1}{2}\left(\frac{X}{H/w}\right)+\frac{1}{2}\sinh\left(\frac{X}{H/w}\right)\cosh\left(\frac{X}{H/w}\right)\right] \qquad (5.2)$$

where;

w : weight per unit length (uniform)

A : cable cross-sectional area

E : Young's modulus of cable (effective)

X : nodal coordinate of the cable with respect to the absolute origin

The lowest point of the cable in a level suspension span is usually controlled by the horizontal tension. In practical cable stringing operations, the maximum sag is controlled which corresponds to a calculated tension.

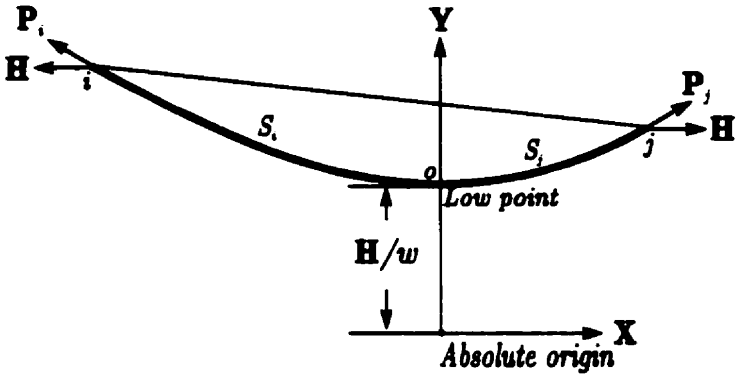

Figure 5.79 Catenary configuration of a cable

Equation (5.2) is based on the effective axial rigidity, EA, of the cable. When an additional gravity load is applied to the cable (such as accumulated ice), the cable elongates due to the increase in horizontal tension. The elongation of an elastic catenary cable when horizontal tension changes from H_1 to H_2 is

$$\Delta S = S_2 - S_1 = \frac{H_1}{w_1}\left(\frac{H_2 - H_1}{AE}\right)\left[\frac{1}{2}\left(\frac{X}{H_1/w_1}\right) + \frac{1}{2}\sinh\left(\frac{X}{H_1/w_1}\right)\cosh\left(\frac{X}{H_1/w_1}\right)\right] \quad (5.3)$$

where w_1 and w_2 are the loads per unit length in the initial and final states. In equations (5.2) and (5.3), A and E are nominal values of the cross-sectional area and effective modulus of elasticity of the cable. The theoretical values of A and E calculated for the OPGW of this study are 209 mm^2 and 93 GPa, respectively, based on the total cross-sectional area and compatibility of strains and displacements of all components.

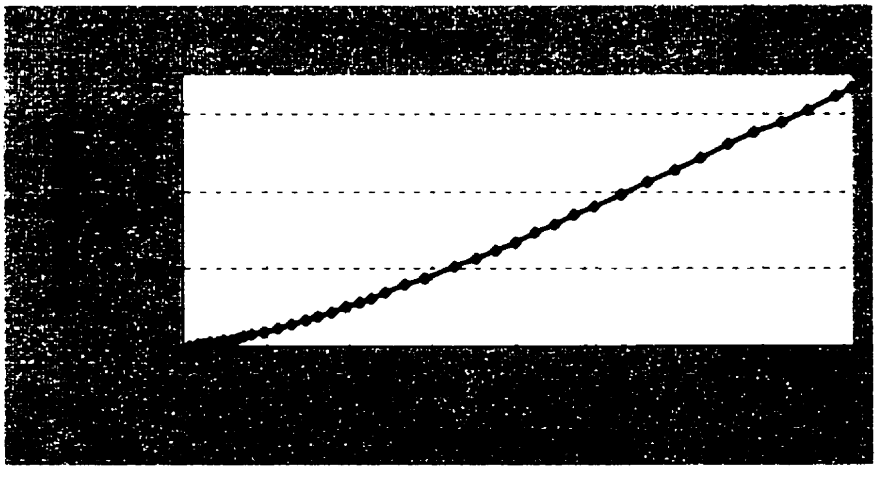

Figure 5.80 Cable response - elongation vs. axial force

The total reaction force of the OPGW versus elongation is plotted in Figure 5.80. An axial force of 67 kN is required to induce a 1.62 mm elongation in the OPGW.

The effective modulus of elasticity of the cable can be calculated as follows,

$$E_{effective} = \frac{P_t l}{A_t \delta_x} \tag{5.4}$$

where, P_t is the total reaction force (variable), A_t is the total cross-sectional area of the cable model (190 mm^2), δ_x is the cable axial displacement (variable) and l is the cable model length (265.16 mm). Since the ratio of the axial force over displacement is variable (Figure 5.80), the effective modulus of elasticity also varies with reaction force or displacement. Figure 5.81 shows the effective modulus of elasticity of the OPGW with respect to the axial displacement. As it can be seen the modulus of elasticity is increasing with displacement, and the maximum modulus is 57.5 GPa. This behavior is due to material linearity of the inner wires, which dominates the overall modulus of elasticity of the cable. However, the moduli of elasticity of the aluminum tube and spacer are constant in the linear range and then decreasing when plastification occurs.

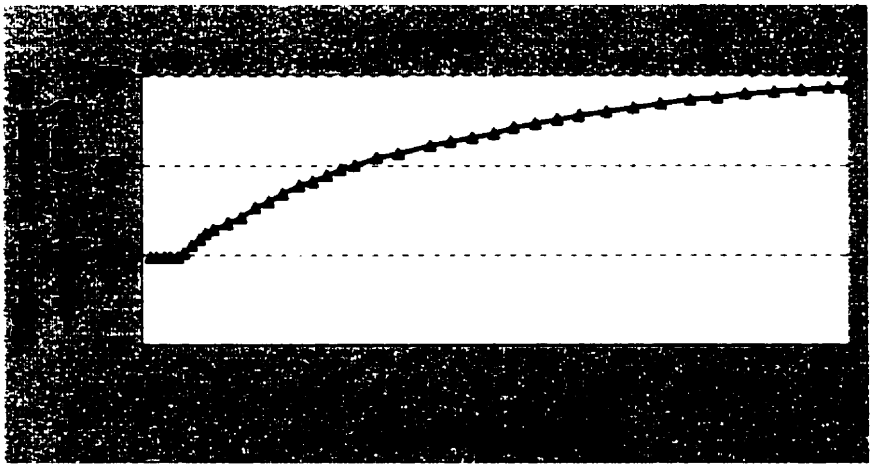

Figure 5.81 Effective modulus of elasticity of the OPGW

Considering the effective modulus of elasticity (Figure 5.81) of the OPGW and using the reaction force (Figure 5.80) as the horizontal tension in Equation (5.2), the elastic elongation of a 200 m span of cable versus the horizontal tension is plotted in Figure 5.82. For comparison purposes, the theoretical modulus of

elasticity (93 GPa), calculated based on compatible elongation of all the cable components, is also used as shown in the figure. It is worth noting that this modulus of elasticity is kept constant for varying tensions.

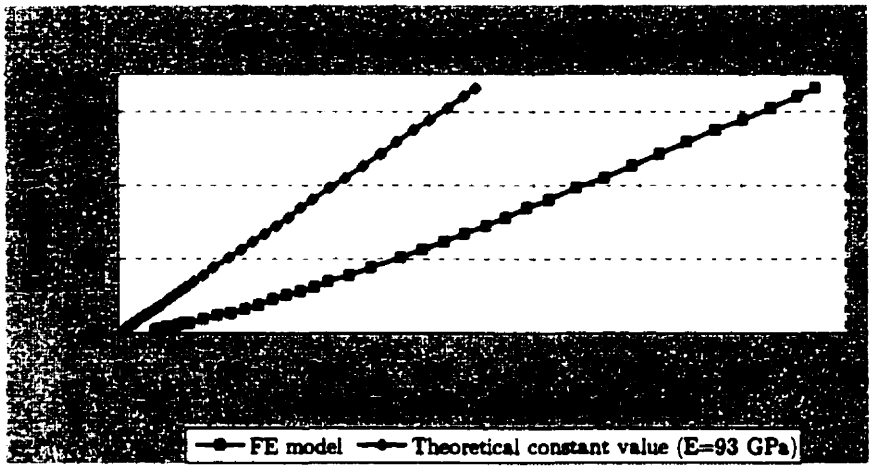

Figure 5.82 Elongation of catenary cable under horizontal tension

The graph shows that for a span of 200 m, the cable elongation is larger using the effective modulus of elasticity obtained from the finite element model. For example, for a horizontal tension of 67 kN, the finite element cable model is stretched by 670 mm, compared to a prediction of only 342 mm using the theoretical value. This means that under the same horizontal tension, the maximum sag predicted using the cable effective properties obtained from the finite element model is larger than that using the constant theoretical value of the modulus of elasticity. It is noted that in practice, sag and tension calculations take into account the nonlinear variation of the cable axial rigidity.

6

CONCLUSIONS

6.1 OPGW finite element model

The constructed finite element model is proven to be capable of predicting stresses and displacements in the OPGW components. The following are the main conclusions of the research.

6.1.1 Three-dimensional modeling

The detailed analysis of the OPGW is possible only with a three-dimensional model due to its complex cross section, helical configuration of the wires in different directions, and their contact effects. Three-dimensional solid elements were used in modeling the wires and aluminum spacer, and shell elements for the central aluminum tube. Both types of elements are designed to take the three-dimensional contact effects.

6.1.2 Optimum length for computations

The optimum length of the model is *one-pitch* corresponding to the longest pitch length of all the OPGW components. This is also the minimum length of a helically shaped member that is feasible to model. The shorter the length of the model, the less reliable the results are in terms of inducing contact forces with other parts of the cable, especially near the ends. However, the longer models can be used for added accuracy but it drastically increases the computational cost (time and capabilities of computing facilities).

6.1.3 End effects

All degrees of freedom of the OPGW model are fixed at one end (fixed-end support). At the loading end, however, only the axial translational degree of freedom of the wires is free, while all degrees of freedom of the central tube are free. At both ends of the helical wires, due to the nature of the loading or fixity, very large stresses are induced. This behavior is only limited to one length of elements at each end. It is observed that end effects are minimized using different schemes of interpolation in stress calculations. Negligible end effects are induced using the *centroid interpolation* calculation. However, the effects are maximum using *RST interpolation*. Consequently, average stresses and displacements are calculated at the cross section located at half-pitch length of the cable, which is deemed more representative of reality, and using *RST interpolation*.

6.1.4 Loading modes

The displacement-control approaches perform better than the load-control in the finite element model. For compatible displacements of the different components, the prescribed elongation approach is the only one that can be used. Applying direct tensile forces is possible, however compatibility in the extensions of the components cannot be achieved due to the helical configurations of the outer and inner wires and the nonlinear behavior of the aluminum tube and spacer. In general, due to the helical shape of the wires and the contact forces between them, the load-control approaches create difficulties in convergence.

6.1.5 Friction effects

The friction effects between the outer wires, the inner wires and the two layers of wires are insignificant. The changes in stresses and displacements of the outer and inner wires with and without friction effects are negligible (less than 1%).

However, friction effects are substantial on the displacements and stresses of the central tube. In the inner-wires-and-tube model, when only the wires are loaded, the displacement of the tube is more than 6 times larger with friction than without friction (0.32 mm vs. 0.047 mm). The stresses and strains are also 2.8 and 4.3 times larger with friction than those obtained without friction. In reality, the presence of the friction is inevitable, and its effects are significant in the response of the tube. Inter-wire friction is also an important source of damping in flexural vibration.

6.1.6 Nonlinear response

The axial strain along the cable axis in the wires is nonlinear with respect to the corresponding displacements. In other words, the uniaxial strain-displacement relation ($\varepsilon = \Delta l/l$) is no longer valid in predicting the strain in the three-dimensional model (axial strain in the wires and in the tube). However, it can be used to predict the strain in the aluminum spacer, which is located at the center of the cable and has little interaction with the other cable components. Consequently, the overall elongation of the cable can be considered 0.61%, but not the strain in individual components of the cable.

6.1.7 The differences in stresses and strains

The axial stresses of the inner and outer wires of the coarse mesh are in the range of ±10% different than those obtained by the analytical solutions (Machida and Durelli and Phillips and Costello). However, the axial strains are smaller in the finite element model. Using a finer mesh, the strains and stresses of the inner wires are almost identical to those of the analytical solutions (1%), although the responses of the outer wires are smaller (9%). The responses of the aluminum tube and spacer cannot be compared with the materially linear analytical solutions due to plastification.

6.1.8 Reactions

The reaction force obtained at the loading end is equivalent to the axial tension that can be induced by the prescribed displacement in the components. The axial forces induced in the outer and inner wires are 17 and 45 kN, which are 27% and 73% of those obtained using the analytical solutions of Machida and Durelli (1973) and Phillips and Costello (1973). These reactions are 49 and 63 kN if the

wires are considered straight. The comparison reveals that the finite element model is significantly more flexible than the theoretical models. It also seems that the analytical solutions are less accurate to predict the response of the outer wires than that of the inner wires, mainly due to the fact that the analytical solutions neglect the mechanical interaction between the different layers. The total axial reaction force of the OPGW coarse mesh is 67 kN, and it is increased to 77 kN using the finer mesh. These reaction forces are 80% and 92% of the axial force (83.5 kN) used in the experiment at IREQ (IREQ 1994) to induce the 0.61% elongation. The difference in the forces is due to the smaller cross-sectional area of the coarse and fine mesh models, which is less than 10% and 2.6% of the actual cross-sectional area of the cable, respectively. The 0.61% elongation measured in the experiment is the extension of the external envelope (outer wires); it is noted that strains or displacements of the internal components of the OPGW are not measured.

The axial reaction forces of the finite element coarse and fine meshes are 80% and 92% of the maximum tensile force used in the experiments, respectively. It is noted that the improved accuracy of the finer mesh model is essentially due to its better approximation of the actual cross sectional area of the wires, as explained above.

The effective modulus of elasticity of the finite element coarse and fine mesh models at maximum elongation are 58 and 65 GPa, respectively, while the theoretical value, considering a composite cross section, is 93 GPa, neglecting all three-dimensional effects. The smaller effective modulus of the finite element model results in a larger elongation in the cable than that of the theoretical one under the same axial tension.

6.1.9 Load cycle

The aluminum spacer and the tube are yielded under the prescribed displacement. In the unloading cycle, it is observed that the permanent plastic deformations of the aluminum tube and spacer are 1.07 and 0.55 mm, respectively. Assuming compatible elongation of the spacer and the optical fiber units (which are inserted in the spacer's grooves), and taking into account the fibers' excess length of 0.018% with respect to the spacer, a 0.5 mm (0.19%) elongation remains in the optical fibers after the removal of the load. This

elongation will cause permanent signal attenuation. This is a very important finding since no long-term attenuation is permissible according to the design criteria. In case of repeated cycles of loading, the permanent deformation of the aluminum tube and the spacer will accumulate in each cycle. Periodic ice shedding from transmission lines are examples of repeated load cycles.

6.1.10 Extreme loading case

The inner and outer wire responses stay in the linear range up to a 20% increase above the maximum tension in normal operation (0.73% elongation). In such a case, the total axial force of the cable is increased by 27%, and the torque reaction in the outer and inner wires increase by 23 to 50%, respectively. The outer and inner wire stresses are almost equal to their maximum tensile strength in this extreme loading case. Beyond this extreme loading, the responses of the outer and inner wires are becoming nonlinear.

6.1.11 Transmission line behavior

Due to the smaller effective modulus of elasticity of the finite element model compared to the nominal values, the elongation of the cable will be larger and consequently the maximum sag of a suspended cable span is larger for a given horizontal tension.

6.2 Summary of conclusions

The study shows that the finite element modeling of the OPGW is reliable and efficient in predicting the detailed response of its different components. The central aluminum tube and spacer are yielded after only 36% and 62% of the load level corresponding to the maximum tension in normal operation, respectively. In a transmission line, the plastic deformations of the tube and spacer will be accumulated under periodic loading-unloading cycles, and the optical fibers are eventually under stress. The response of the optical fibers is even more complicated since the tube plastification occurs prior to that of the spacer. Therefore, permanent signal attenuation due to induced stresses in the fibers will occur.

The friction effects between the outer wires, the inner wires and the two layers of wires are insignificant. However, friction effects are substantial between the central tube and the aluminum spacer.

The effective modulus of elasticity of the finite element model is smaller than that of the analytical solutions and its effect induces a larger elongation and sag in a suspended cable than that of the theoretical prediction under the same horizontal tension.

In general, the results of the finite element model agree with the experiments and the analytical solutions. However, neither the experiments nor the analytical solutions can predict the detailed response of the OPGW resulting from the complex interactions between the components.

6.3 Recommendations for future work

Following are recommendations for future research on the numerical modeling of helical wires:

- Compatible prescribed displacement is considered as the loading condition for the OPGW components in this study. Combinations of prescribed displacements or forces acting on the various components of the OPGW can be studied such that represent more realistic behavior of the cable in transmission lines. In reality, only the external envelope is usually clamped at the ends and the axial tension is distributed among the cable components due to contact and friction.
- Investigation of load cycling effects;
- Verification of pitch length effects on the accuracy of the full model;
- Optimization of cable design, considering other types of cables with extra layers, different materials, helix angles and directions;
- Detailed stress analysis of the attached ends of OPGW in clamps or special sleeves;
- Analysis of cable subjected to external torque, bending moments, and complex loadings.

BIBLIOGRAPHY

Abé, H., Kusumi, Y., Saka, M. 1989. "Deformation of slot rods in a slot-type optical fiber cable," *Nippon Kikai Gakkai Ronbunshu*, Vol. 55, No. 514, pp. 1462-1468. (Paper in Japanese with abstract in English).

ADINA, R & D, Inc., 1999. *ADINA - A Finite Element Program for Dynamic Incremental Nonlinear Analysis, Theory and Modeling Guide,* Report ARD 99-7, Watertown, MA.

Boresi, A. P., Achmidt, R. J. and Sidebottom, O. M. 1993. "Advance mechanics of materials," *John Wiley & sons, Inc.*.

Bacon, F. and Maklad, M. S. 1994. "Long-term mechanical reliability of single mode optical fibers," *Proceedings of SPIE-The International Society for Optical Engineering,* Society of Photo-optical Instrumentation Engineers, Bellingham, WA, USA. Vol. 2292, pp. 340-352.

Barnoski, M. K. 1981. "Fundamentals of optical fiber communications," *Academic Press Inc.*

Blau, P. J. 1996. "Friction science and technology," *Marcel Dekker, Inc.*

Bathe, K. J. 1996. "Finite element procedures," *Prentice-Hall, Inc.* New Jersey, USA.

Bathe, K. J., Walczak, J., Guillermin, O., Bouzinov, P., and Chen, H. 1999. "Advances in crush analysis," *Computers and structures*, USA. Vol. 72, pp. 31-47.

Cherin, A. H. 1983. "An introduction to optical fibers," *McGraw-Hill Book Company.*

Cook, R. D., Malkus, D. S., and Plesha, M. E. 1989. "Concepts of application of finite element analysis," *John Wiley & sons, Inc.*

Costello, G. A. 1997. "Theory of wire rope," *Mechanical Engineering series, Second edition, Springer-Verlag, New York, Inc.* New York, NY, USA.

Costello, G. A. 1978. "Analytical investigation of wire rope," *Applied Mechanics Review*, Vol. 31, No. 7, pp. 897-900.

Costello, G. A. 1983. "Stresses in Multilayered Cables," *Journal of Energy Resources Technology,* Vol. 105, pp. 337-340.

Costello, G. A. and Phillips, J. M. 1974. "A more exact theory for twisted wire cable," *Journal of the Engineering Mechanics Division, ASCE,* Vol. 100, pp. 1096-1099.

Davis, J. R. 1994. "Aluminum and aluminum alloys," *ASM Specialty Handbook,* Davis & Associates.

Drucker, D. C. and Tachau, H. 1945. "A new design criterion for wire rope," *Journal of Applied Mechanics, Transactions, American Society of Mechanical Engineering.* 67, pp. A-33 - A-38.

Fee, J. M. 1994. "Pulling tension calculation program which allows coefficient of friction to vary continuously with cable sidewall pressure," *Proceedings of the IEEE Power Engineering Society Transmission and Distribution Conference.* pp. 314-316.

Fee, J. M. and Quist, D. J. 1992. "A new cable pulling friction measurement method and results," *IEEE Transactions on Power Delivery.* Vol. 7, No. 2, pp. 681-686.

Fee, J. M. and Solheid, D. P. 1994. "Coefficient of friction effects of polymers, silicone oil, and mini-rollers in cable pulling," *Proceedings of the IEEE Power Engineering Society Transmission and Distribution Conference. Published by IEEE, IEEE Service Center, Piscataway,* NJ, USA. pp. 317-322.

Hall, H. M. 1951. "Stresses in small wire Ropes," *Wire and Wire Products,* Vol. 26, pp. 228, 257-259.

Hatano, S., Katsuyama, Y., Kokubun, T., and Hogari, K. 1986. "Multi-hundred-fiber cable composed of optical fiber ribbons inserted tightly into slots," *Proceedings of 35th International Wire and Cable Symposium,* Published by US Army Communications-Electronics Command, Fort Monmouth, NJ, USA. pp. 17-23.

Hayata, K., Koshiba, M., and Suzuki, M. 1987. "Stress-applied optical fiber having inhomogeneous core," *Electronics and Communications in Japan, Part2: Electronics,* Vol. 70, No. 9, pp. 74-81.

Hruska, F. H. 1951. "Calculation of stresses in wire ropes," *Wire and Wire Products,* Vol. 26, pp. 766-767, 799-801.

Hruska, F. H. 1952. "Radial forces in wire ropes," *Wire and Wire Products,* Vol. 27, No. 5, pp. 459-463.

Hruska, F. H. 1953. "Tangential forces in wire ropes," *Wire and Wire Products,* Vol. 28, No. 5, pp. 455-460.

Huang, X. and Vinogradov, O. 1992. "Interwire slip and its influence on the dynamic properties of tension cables," *Proceedings of the Second*

International Offshore and Polar Engineering Conference San Francisco, USA, pp. 392-396.

Huang, X. and Vinogradov, O. 1994. "Analysis of dry friction hysteresis in a cable under uniform bending," *Structural Engineering and Mechanics*, Vol. 2, No. 1, pp. 63-80.

Huang, X. and Vinogradov, O. 1996. "Extension of a cable in the presence of dry friction," *Structural Engineering and Mechanics,* Vol. 4, No. 3, pp. 313-329.

Huang, X. and Vinogradov, O. 1996. "Dry friction losses in axially loaded cables," *Structural Engineering and Mechanics,* Vol. 4, No. 3, pp. 330-344.

Jiang, W. G. and Henshall, J. L. 1999. "The analysis of termination effects in wire strand using the finite element method," *Journal of Strain analysis,* Vol. 34, No. 1, pp. 31-38.

Jiang, W. G., Yao, M. S., and Walton, J. M. 1999. "A consise finite element model for simple straight wire rope strand," *International Journal of Mechanical sciences,* No. 41, pp. 143-161.

IREQ, Laboratoire Grande Puissance. 1994. "96 Hours traction test on 19 mm OPGW," *Institut de recherche d'Hydro-Québec,* Test report #84274B.

Knapp, R. H. 1979. "Derivation of a new stiffness matrix for helically armoured cables considering tension and torsion," *International Journal for Numerical Methods in Engineering,* Vol. 14, pp. 515-529.

Knapp, R. H. 1988. "Helical wire stresses in bent cables," *Journal of Offshore Mechanics and Arctic Engineering,* Vol. 110, No. 1, pp. 55-61.

Leissa, A. W. 1959. "Contact stresses in wire ropes," *Wire and Wire Products*, Vol. 34, No. 3, pp. 307-314, 372-373.

LeClaire, R. A. 1989. "Upper bound to mechanical power transmission losses in wire rope," *Journal of Engineering Mechanics-ASCE.* Vol. 115, No. 9, pp. 2011-2019.

LeClaire, R. A. 1991. "Axial response of multilayered strands with compliant layers," *Journal of Engineering Mechanics-ASCE.* Vol. 117, No. 12, pp. 2884-2903.

Love, A. E. H. 1944. "A treatise on the mathematical theory of elasticity," *Dover Publications Inc.*, New York.

Machida, S. and Durelli. A. J. 1973. "Response of a strand to axial and torsional displacements," *Journal of Mechanical Engineering Science,* Vol. 15, No. 4, pp. 241-251.

Miller, S. E., and Chynoweth, A. G. 1979. "Optical fiber telecommunications," *Academic Press Inc.*

Ogai, M., Hiramatsu, H., Oda, M., Kamata, Y., Miajima, Y., and Ieshigo, M. 1985. "Long-term reliability of optical fiber composite ground wire," *Proceedings of International Wire and Cable Symposium 34th.* Published by US Army, Fort Monmouth, NJ, USA. pp. 92-96.

Park, Y. B., Yoon, J. H., and Yang, D. Y. 1994. "Finite element analysis of steady-state three-dimensional helical extrusion of twisted sections using recurrent boundary conditions," *International Journal of Mechanical Science,* Vol. 36, No. 2, pp. 137-148.

Phillips, J. W. and Costello, G. A. 1973. "Contact stresses in twisted wire cables," *Journal of the Engineering Mechanics Division, Proceedings of the American Society of Civil Engineers.* Div. 99, pp. 331-341.

Ramsey, H. 1990. "Analysis of interwire friction in multilayered cables under uniform extension and twisting," *International Journal of Mechanical Science,* Vol. 32, No. 8, pp. 709-716.

Raoof, M. 1991. "Wire recovery length in a helical strand under axial-fatigue loading," *International Journal of Fatigue,* Vol. 13, No. 2, pp. 127-132.

Raoof, M. and Hobbes, R., E. 1988. "Analysis of Multilayered Structural Strands," *Journal of Engineering Mechanics,* Vol. 114, No. 7, pp. 1166-1182.

Raoof, M. and Huang, Y., P. 1992. "Wire stress calculations in helical strands undergoing bending," *Journal of Offshore Mechanics and Arctic Engineering,* Vol. 114, No. 3, pp. 212-219.

Raoof, M. and Kraincanic, I. 1994. "Critical examination of various approaches used for analyzing helical cables," *Journal of Strain Analysis for Engineering Design,* Vol. 29, No. 1, pp. 43-55.

Raoof, M. and Kraincanic, I. 1995. "Simple derivation of the stiffness matrix for axial/torsional coupling of spiral strands," *Computers and Structures,* Vol. 55, No. 4, pp. 589-600.

Rabinowicz, E. 1995. "Friction and wear of materials," *John Wiley & Sons, Inc.*

Roshan Fekr, M. 1998. "A survey of publications on stress analysis of helical wires, optical fibers and optical ground wires," Department of Civil Engineering and Applied Mechanics, McGill University, *Structural Engineering report,* No. 97-12, 32p.

Roshan Fekr, M., McClure, G., and Farzaneh, M. 1999. "Application of ADINA to stress analysis of an optical ground wire," *Computers and structures*, USA. Vol. 72, pp. 301-316.

Russ, C. R., Misono, N. Okazato, A. and Kobayashi, T. 1986. "Composite ground wire with optical fibers," *Proceedings of 35th International Wire and Cable Symposium,* Published by US Army Communications-Electronics Command, Fort Monmouth, NJ, USA. pp. 484-489.

Sathikh, S. 1989. "Effect of interwire friction on transverse vibration of helically stranded cable," *American Society of Mechanical Engineers, Design Engineering Division.* Published by ASME, New York, Vol. 18-4, pp. 147-153.

Savadjiev, K. and McComber, P. 1995. "Mechanical behavior of ice loaded optical ground wires," *Arctic/Polar Technology ASME.* Vol. IV, OMAE, pp. 107-113.

Schneider, H. W., Schobert, A., and Staudt A. 1987. "Influence of drawing conditions on the tensile strength of fluoride glass optical fibers," *Glastechnische Berichte,* Vol. 60, No. 6, pp. 205-210.

Singh, H. and Sirkis, J. S. 1993. "Strain analysis of thick and thin composites with embedded optical fibers under compression," *Experiments in Smart Materials and Structures, American Society of mechanical Engineers, Applied Mechanics division, AMD.* Published by ASME, New York, Vol. 181, pp. 39-46.

Suhir, E. 1993. "The effect of the nonlinear stress-strain relationship on the mechanical behavior of optical glass fibers," *International Journal of Solids and Structures.* Vol. 30, No. 7, pp. 947-961.

Suhir, E. 1995. "Fiber optics structural mechanics," *Proceedings of the Electronic Components and Technology Conference, IEEE, Piscataway,* NJ, USA, 95CH35820, pp. 937-948.

Szentesi, O. I. 1986. "Reliability of optical fibers, cables, and splices," *IEEE Journal on Selected Areas in Communications.* No. 9, pp. 1502-1508.

Velinsky, S. A., Anderson, G. L. and Costello, A. G. 1984. "Wire rope with complex cross-sections," *Journal of the Engineering Mechanics Division, Proceedings of the American Society of Civil Engineers.* Div. 110, pp. 380-391.

Uttings, W. S. and Jones, N. 1987. "The response of wire rope strands to axial tensile loads-Part I. Experimental results and theoretical predictions," *International Journal of Mechanical Science*, Vol. 29, No. 9, pp. 605-619.

Uttings, W. S. and Jones, N. 1987. "The response of wire rope strands to axial tensile loads-Part II. Comparison of experimental results and theoretical predictions," *International Journal of Mechanical Science*, Vol. 29, No. 9, pp. 621-636.

Ura, A., Nakashima, A., Yamamoto, Y., Kawazoe, T. 1991. "Friction properties of a wire rope for a cable puller," *International Conference on Wear of Materials,* Published by ASME, New York, NY, USA. Vol. 2, pp. 651-654.

APPENDIX I

DETAILED ANALYTICAL SOLUTIONS

The detailed theoretical solutions by Machida and Durelli (1973), and Costello (1997) are presented in the following sections. The subscripts 1, 2, and 3 refer to the central aluminum tube (first layer), the inner wires (second layer) and the outer wires (third layer), respectively. The solutions are carried out for two cases: 1) when the in-plane degrees of freedom of the loading end are fixed (unwinding of the wires is prevented), and 2) when the loading end is free, which means the wires are unwinding. The geometrical properties of the OPGW are as follows:

m_2	10		number of inner wires
m_3	14		number of outer wires
p_2	265.16	mm	initial pitch length of inner wire, right lay
p_3	202.00	mm	initial pitch length of outer wire, left lay
r_1	3.25	mm	outside radius of the aluminum tube
r_2	1.425	mm	radius of the inner (second layer) wire
r_3	1.685	mm	radius of the outer (third layer) wire
t_1	0.55	mm	central aluminum tube thickness
A_{Tube}	10.28	mm^2	cross sectional area of central tube
$A_{Al.\ Spacer}$	10.17	mm^2	cross section of the aluminum spacer
R_2	4.675	mm	initial radius of the helix of the inner wire
R_3	7.785	mm	initial radius of the helix of the outer wire
α_2	83.68°		helix angle of the inner wires
α_3	-76.39°		helix angle of outer wires
ε_1	0.61%		axial strain in the central tube ($\varepsilon_1=\varepsilon$)

where α_2, and α_3 are calculated as follows:

$$\tan\alpha_2 = \frac{265.16}{2\pi \times 4.675} = 9.027 \Rightarrow \alpha_2 = 83.68^\circ \qquad \text{(I.1)}$$

$$\tan\alpha_3 = -\frac{202}{2\pi \times 7.785} = -4.1296 \Rightarrow \alpha_3 = -76.39^\circ. \tag{I.2}$$

The geometry of the OPGW cross section is illustrated in Figure I.1.

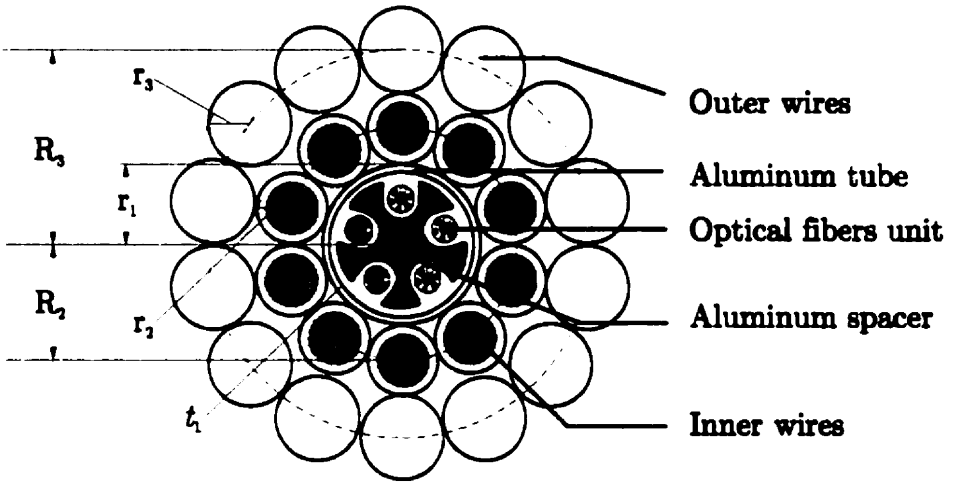

Figure I.1 OPGW cross section

I.1 Machida and Durelli (1973)

$$F_1 = A_1E_1\varepsilon \tag{I.3}$$

$$\sigma_1 = E_1\varepsilon \tag{I.4}$$

$$F_2^h = A_2E_2(\varepsilon\sin^2\alpha_2 + \gamma\cos^2\alpha_2) \tag{I.5}$$

$$F_3^h = A_3E_3(\varepsilon\sin^2\alpha_3 + \gamma\cos^2\alpha_3) \tag{I.6}$$

$$M_2 = \frac{2E_2I_2}{R_2}(\varepsilon - \gamma)\sin^2\alpha_2\cos^2\alpha_2 \tag{I.7}$$

$$M_3 = \frac{2E_3I_3}{R_3}(\varepsilon - \gamma)\sin^2\alpha_3\cos^2\alpha_3 \tag{I.8}$$

$$M_2^t = \frac{G_2J_2}{4R_2}(\gamma - \varepsilon)\sin 4\alpha_2 \tag{I.9}$$

$$M_3^t = \frac{G_3J_3}{4R_3}(\gamma - \varepsilon)\sin 4\alpha_3 \tag{I.10}$$

$$M_{t2} = m_2(M_2^t\sin\alpha_2 - M_2\cos\alpha_2 + F_2^hR_2\cos\alpha_2) \tag{I.11}$$

$$M_{t3} = m_3(M_3^t\sin\alpha_3 - M_3\cos\alpha_3 + F_3^hR_3\cos\alpha_3) \tag{I.12}$$

$$M_{Tube}^t = 2\pi GJ\gamma / p \tag{I.13}$$

$$F_c = \frac{F_2^h}{\rho'} \approx \frac{F_2^h}{\rho} \tag{I.14}$$

$$\rho = R_2 + \left(\frac{p}{2\pi}\right)^2 \frac{1}{R_2} \tag{I.15}$$

$$\rho' = R_2 + \left(\frac{p'}{2\pi}\right)^2 \frac{1}{R_2} \tag{I.16}$$

$$p' = p\frac{1+\varepsilon}{1+\gamma} \tag{I.17}$$

$$F = F_1 + m_2 F_2^h \sin\alpha_2 + m_3 F_3^h \sin\alpha_3 \tag{I.18}$$

$$M_t = M_{Tube}^t + M_{t2} - M_{t3}. \tag{I.19}$$

I.1.1 Unwinding motion is restricted ($\gamma = 0$)

When the in-plane degrees of freedom of the loading end are fixed, the wires are not allowed to unwind and consequently the motion is resisted by twisting moments M_{2t}, M_{3t}, and $M_{Tube}^t = 2\pi GJ\gamma / p = 0$. Using the equations (I.3) to (I.6),

$$F_1 = 635{,}388 \times 0.0061 = 3.88 \text{ kN} \tag{I.20}$$

$$\sigma_1 = 61{,}803 \times 0.0061 = 377 \text{ MPa} \tag{I.21}$$

$$F_2^h = 6.38 \times 162{,}000 \times (0.0061 \times 0.988 + 0) = 6.23 \text{ kN} \tag{I.22}$$

$$F_3^h = 8.92 \times 63{,}765 \times (0.0061 \times 0.945 + 0) = 3.28 \text{ kN} \tag{I.23}$$

and the axial forces along the cable axis are

$$F_2 = F_2^h \sin\alpha_2 = 6.23 \times 0.994 = 6.19 \text{ kN} \tag{I.24}$$

$$F_3 = F_3^h \sin\alpha_3 = 3.28 \times 0.972 = 3.19 \text{ kN}. \tag{I.25}$$

The bending and twisting moments are determined using Equations (I.7) to (I.10),

$$M_2 = \frac{2 \times 162{,}000 \times 3.24}{4.675}(0.0061 - 0) \times 0.012 = 16.40 \text{ N.mm} \tag{I.26}$$

$$M_3 = \frac{2 \times 63{,}765 \times 6.33}{7.785}(0.0061 - 0) \times 0.0523 = 33.10 \text{ N.mm} \tag{I.27}$$

$$M_2^t = \frac{162{,}000 \times 3.24}{4 \times 4.675(1 + 0.33)}(0 - 0.0061) \times 0.427 = -54.96 \text{ N.mm} \quad \text{(I.28)}$$

$$M_3^t = \frac{63{,}765 \times 6.33}{4 \times 7.785(1 + 0.33)}(0 - 0.0061) \times 0.814 = -48.37 \text{ N.mm}. \quad \text{(I.29)}$$

The total bending moments acting on the inner are outer wires in the plane of the cable are:

$$M_{b2} = M_2 \sin\alpha_2 + M_2^t \cos\alpha_2 = 16.40 \times 0.994 - 54.96 \times 0.110 = 10.25 \text{ N.mm} \quad \text{(I.30)}$$

$$M_{b3} = M_3 \sin\alpha_3 + M_2^t \cos\alpha_3 = 33.10 \times 0.972 - 48.37 \times 0.235 = 20.79 \text{ N.mm}. \quad \text{(I.31)}$$

The average normal and bending stresses along the helix of the inner and outer wires are

$$\sigma_2^F = \frac{F_2^h}{A_2} = \frac{6.23}{6.38} = 976.48 \text{ MPa} \quad \text{(I.32)}$$

$$\sigma_3^F = \frac{F_3^h}{A_3} = \frac{3.19}{8.92} = 357.63 \text{ MPa} \quad \text{(I.33)}$$

$$\sigma_2^b = \frac{M_2 r_2}{I_2} = \frac{16.40 \times 1.425}{3.24} = \pm 7.21 \text{ MPa} \quad \text{(I.34)}$$

$$\sigma_3^b = \frac{M_3 r_3}{I_3} = \frac{33.10 \times 1.685}{6.33} = \pm 8.81 \text{ MPa} \quad \text{(I.35)}$$

and the stresses along their helix axis are:

$$\sigma_2^h = \sigma_2^F \pm \sigma_2^b = 976.48 \pm 7.21 = \begin{cases} 983.7 \\ 969.3 \end{cases} \text{ MPa} \quad \text{(I.36)}$$

$$\sigma_3^h = \sigma_3^F \pm \sigma_3^b = 357.63 \pm 8.81 = \begin{cases} 366.4 \\ 348.8 \end{cases} \text{ MPa}. \quad \text{(I.37)}$$

The maximum shear stresses of the inner and outer wires along their helical axis due to the resisting torque are,

$$\tau_2^h = \frac{M_2^t r_2}{J_2} = -12.09 \text{ MPa} \quad \text{(I.38)}$$

$$\tau_3^h = \frac{M_3^t r_3}{J_3} = -6.44 \text{ MPa}. \quad \text{(I.39)}$$

To obtain the axial and shear stresses of the wires along the cable axis, the above stresses (normal and shear stresses along helix) are transformed as follows

$$\sigma_2 = \frac{\sigma_2^h}{2} + \frac{\sigma_2^h}{2}\cos 2\theta_2 + \tau_2^h \sin 2\theta_2 = \begin{Bmatrix} 969 \\ 955 \end{Bmatrix} \text{ MPa} \tag{I.40}$$

and

$$\tau_2 = -\frac{\sigma_2^h}{2}\sin 2\theta_2 + \tau_2^h \cos 2\theta_2 = \begin{Bmatrix} -119 \\ -118 \end{Bmatrix} \text{ MPa} \tag{I.41}$$

where

$$\theta_2 = \frac{\pi}{2} - \alpha_2 = 6.32^\circ . \tag{I.42}$$

The corresponding maximum shear and principal stresses are calculated using the following formula

$$\tau_{2\max} = \sqrt{\left(\frac{\sigma_2^h}{2}\right)^2 + \left(\tau_2^h\right)^2} = \begin{Bmatrix} 492 \\ 485 \end{Bmatrix} \text{ MPa} \tag{I.43}$$

$$\sigma_{2P1} = \frac{\sigma_2^h}{2} + \tau_{2\max} = \begin{Bmatrix} 984 \\ 969 \end{Bmatrix} \text{ MPa.} \tag{I.44}$$

Performing the same calculations for the outer wires:

$$\theta_3 = \frac{\pi}{2} - \alpha_3 = 13.61^\circ \tag{I.45}$$

$$\sigma_3 = \frac{\sigma_3^h}{2} + \frac{\sigma_3^h}{2}\cos 2\theta_3 + \tau_3^h \sin 2\theta_3 = \begin{Bmatrix} 343 \\ 327 \end{Bmatrix} \text{ MPa} \tag{I.46}$$

and the corresponding shear stresses along the cable axis are

$$\tau_3 = -\frac{\sigma_3^h}{2}\sin 2\theta_3 + \tau_3^h \cos 2\theta_3 = \begin{Bmatrix} -90 \\ -86 \end{Bmatrix} \text{ MPa.} \tag{I.47}$$

The corresponding maximum shear and principal stresses are calculated using the following formula

$$\tau_{3\max} = \sqrt{\left(\frac{\sigma_3^h}{2}\right)^2 + \left(\tau_3^h\right)^2} = \begin{Bmatrix} 183 \\ 175 \end{Bmatrix} \text{ MPa} \tag{I.48}$$

$$\sigma_{3P1} = \frac{\sigma_3^h}{2} + \tau_{3\max} = \begin{Bmatrix} 367 \\ 349 \end{Bmatrix} \text{ MPa.} \tag{I.49}$$

The deformed radius of the curvature of the inner wires

$$\rho_2' = 4.675 + \left(\frac{265.16 \times 1.0061}{2\pi}\right)^2 \frac{1}{4.675} = 390 \text{ mm} \tag{I.50}$$

and the contact force

$$F_{2c} = \frac{6228}{390} = 15.97 \text{ N/mm.} \tag{I.51}$$

And for the outer wires

$$\rho_3' = 142 \text{ and } F_{3c} = 3280/142 = 23.07 \text{ N/mm.} \tag{I.52}$$

The total twisting moment resisted by the inner and outer wires at the loading ends are

$$M_{t2} = 10(-54.96 \times 0.994 - 16.40 \times 0.110 + 6{,}228 \times 4.675 \times 0.110) = 31.5 \text{ kN.mm} \tag{I.53}$$

$$M_{t3} = 14(-48.37 \times 0.972 - 33.10 \times 0.235 + 3{,}277 \times 7.785 \times 0.235) = 83.3 \text{ kN.mm} \tag{I.54}$$

and the resultant twisting moment on the cable

$$M_t = -51.8 \text{ kN.mm.} \tag{I.55}$$

The total applied load and normal stress in the aluminum spacer are,

$$F_{Al.spacer} = E_{al} A_{al} \varepsilon = 63{,}765 \times 10.17 \times 0.0061 = 3.96 \text{ kN} \tag{I.56}$$

$$\sigma_{Al.spacer} = 63{,}765 \times 0.0061 = 389 \text{ MPa} \tag{I.57}$$

and the total load applied to the OPGW to induce 0.61% strain is

$$F = 3.96 + 3.88 + 10 \times 6.19 + 14 \times 3.19 = 114.3 \cong 114 \text{ kN} \tag{I.58}$$

I.1.2 Unwinding motion is allowed ($\gamma \neq 0$ and $M_{t2} = 0$)

In this section, the calculations are carried on the cable with only the inner wires and the central tube. In this case, the loading ends of the wires unwind and no torque is generated in the cable. Therefore, the total twisting moment is zero,

$$M_t = M_{Tube}^t + M_{t2} = 0 \tag{I.59}$$

$$M_t = \frac{2\pi GJ\gamma}{p} + m_2(M_2^t \sin\alpha_2 - M_2 \cos\alpha_2 + F_2^h R_2 \cos\alpha_2) = 0 \tag{I.60}$$

Applying Equation (I.60), the rotational strain is obtained as

$$\gamma = -0.152 \tag{I.61}$$

and the unwinding rotation is

$$\Delta = 2\pi\gamma = 0.954 \text{ radian} = 54.63^\circ . \tag{I.62}$$

The axial force of the inner wire is

$$F_2^h = 6.38 \times 162000 \times (0.0061 \times 0.988 - 0.152 \times 0.0121) = 4.33 \text{ kN} \quad \text{(I.63)}$$

$$F_2 = F_2^h \sin\alpha_2 \ = 4.33 \times 0.994 = 4.30 \text{ kN}. \quad \text{(I.64)}$$

The bending and twisting moments are determined using Equations (I.7) to (I.10),

$$M_2 = \frac{2 \times 162000 \times 3.239}{4.675}(0.0061 + 0.152) \times 0.012 = 424.30 \text{ N.mm} \quad \text{(I.65)}$$

$$M_2^t = \frac{162000 \times 3.239}{4 \times 4.675(1 + 0.33)}(-0.152 - 0.0061) \times 0.427 = -1422.23 \text{ N.mm}. \quad \text{(I.66)}$$

The normal and bending stresses along the helix are

$$\sigma_2^F = \frac{F_2^h}{A_2} = \frac{4.33}{6.38} = 678.2 \text{ MPa} \quad \text{(I.67)}$$

$$\sigma_2^b = \frac{M_2 r_2}{I_2} = \frac{424.30 \times 1.425}{3.24} = \pm 186.7 \text{ MPa} \quad \text{(I.68)}$$

and the maximum and minimum normal and shear stresses are:

$$\sigma_2^h = \sigma_2^F \pm \sigma_2^b = 678.7 \pm 186.6 = \begin{cases} 865.3 \\ 492.1 \end{cases} \text{ MPa} \quad \text{(I.69)}$$

and

$$\tau_2^h = \frac{M_2^t r_2}{J_2} = -312.9 \text{ MPa}. \quad \text{(I.70)}$$

To obtain the axial and shear stresses of the wires along the cable axis, the above stresses (normal and shear stresses along helix) are transformed as follows

$$\sigma_2 = \frac{\sigma_2^h}{2} + \frac{\sigma_2^h}{2}\cos 2\theta_2 + \tau_2^h \sin 2\theta_2 = \begin{cases} 786 \\ 417 \end{cases} \text{ MPa}. \quad \text{(I.71)}$$

The corresponding shear stresses along the cable axis are

$$\tau_2 = -\frac{\sigma_2^h}{2}\sin 2\theta_2 + \tau_2^h \cos 2\theta_2 = \begin{cases} -400 \\ -359 \end{cases} \text{ MPa}. \quad \text{(I.72)}$$

The corresponding maximum shear and principal stresses are calculated using the following formula

$$\tau_{2\max} = \sqrt{\left(\frac{\sigma_2^h}{2}\right)^2 + \left(\tau_2^h\right)^2} = \begin{cases}534\\398\end{cases} \text{ MPa} \tag{I.73}$$

and

$$\sigma_{2P1} = \frac{\sigma_2^h}{2} + \tau_{\max 2} = \begin{cases}966\\644\end{cases} \text{ MPa.} \tag{I.74}$$

The total bending moment acting on the inner wires along the cable axis is,

$$M_{b2} = M_2 \sin\alpha_2 + M_2^t \cos\alpha_2 = 424.30 \times 0.994 - 1422.23 \times 0.110 = 265 \text{ N.mm} \tag{I.75}$$

The twisting moment in the tube is

$$M_{Tube}^t = 2\pi GJ\gamma \,/\, p = 2\pi \times 2.41E6 \times 0.152 \,/\, 265.16 = 7667 \text{ N.mm} \tag{I.76}$$

and the total applied load on the inner wires and the tube to induce 0.61% elongation is

$$F = 3.88 + 10 \times 4.30 = 46.88 \cong 47 \text{ kN.} \tag{I.77}$$

I.2 Costello (1997)

I.2.1 Unwinding motion is restricted ($\beta = 0$)

$$R_2 = r_1 + r_2 \tag{I.78}$$

$$\tan\alpha_2 = \frac{p_2}{2\pi R_2} \tag{I.79}$$

$$R_2' = r_1(1 - \nu\varepsilon_1) + r_2(1 - \nu\varepsilon_2) \tag{I.80}$$

$$\frac{R_2}{R_2'} = 1 + \nu\frac{(r_1\varepsilon_1 + r_2\varepsilon_2)}{R_2} \tag{I.81}$$

$$\varepsilon_1 = \varepsilon_2 + \frac{\Delta\alpha_2}{\tan\alpha_2} = \varepsilon \tag{I.82}$$

$$\beta_2 = R_2\varphi_n = \frac{\varepsilon_2}{\tan\alpha_2} - \Delta\alpha_2 + \nu\frac{(r_1\varepsilon_1 + r_2\varepsilon_2)}{R_2\tan\alpha_2} \tag{I.83}$$

$$r_2\Delta\kappa_2' = -\frac{2\sin\alpha_2\cos\alpha_2}{R_2/r_2}\Delta\alpha_2 + \nu\frac{(r_1\varepsilon_1 + r_2\varepsilon_2)\cos^2\alpha_2}{R_2R_2/r_2} \tag{I.84}$$

$$r_2\Delta\varphi_2 = \frac{(1 - 2\sin^2\alpha_2)}{R_2/r_2}\Delta\alpha_2 + \nu\frac{(r_1\varepsilon_1 + r_2\varepsilon_2)\sin\alpha_2\cos^2\alpha_2}{R_2R_2/r_2} \tag{I.85}$$

$$\frac{M_2}{Er_2^3} = \frac{\pi}{4} r_2 \Delta\kappa_2' \tag{I.86}$$

$$\frac{M_2^t}{Er_2^3} = \frac{\pi}{4(1+\nu)} r_2 \Delta\varphi_2 \tag{I.87}$$

$$\frac{N_2'}{Er_2^2} = \frac{M_2^t}{Er_2^3} \frac{\cos^2\alpha_2}{R_2/r_2} - \frac{M_2}{Er_2^3} \frac{\sin\alpha_2 \cos\alpha_2}{R_2/r_2} \tag{I.88}$$

$$\frac{T_2}{Er_2^2} = \pi\varepsilon_2 \tag{I.89}$$

$$\frac{X_2}{Er_2} = \frac{N_2'}{Er_2^2} \frac{\sin\alpha_2 \cos\alpha_2}{R_2/r_2} - \frac{T_2}{Er_2^2} \frac{\cos^2\alpha_2}{R_2/r_2} \tag{I.90}$$

$$\frac{F_2}{Er_2^2} = m_2 \left[\frac{T_2}{Er_2^2} \sin\alpha_2 + \frac{N_2}{Er_2^2} \cos\alpha_2 \right] \tag{I.91}$$

$$\frac{M_{t2}}{Er_2^3} = m_2 \left[\frac{M_2^t}{Er_2^3} \sin\alpha_2 + \frac{M_2}{Er_2^3} \cos\alpha_2 + \frac{T_2}{Er_2^2} \frac{R_2}{r_2} \cos\alpha_2 - \frac{N_2'}{Er_2^2} \frac{R_2}{r_2} \sin\alpha_2 \right] \tag{I.92}$$

$$\frac{F_1}{(EA)_{Tube}} = \varepsilon_1 = \varepsilon \tag{I.93}$$

$$\frac{M_{Tube}^t}{(GJ)_{Tube}} = \varphi_s \tag{I.94}$$

$$M_{b2} = M_2 \sin\alpha_2 + M_2^t \cos\alpha_2 \tag{I.95}$$

where

F_2 total axial force in the OPGW acting on ($m_2 = 10$) inner wires

M_2 bending moment in the inner wire

M_{b2} bending moment in the plane of cable cross section

M_2^t twisting moment in an inner wire

M_{t2} total axial twisting moment acting on inner wires

N_2' component of the shearing force on an inner wire

R_2 initial radius of the helix of the inner wire

R_2' final helical radius of the inner wire

T_2 axial tension in an inner wire

X_2 component of the external line load per unit length of the centerline of an inner wire in the x direction

$\Delta\alpha_2$ changes in the helix angle of an inner wire (between undeformed and deformed geometry)

$\Delta\kappa'_2$ change in curvature of an inner wire

$\Delta\varphi_2$ change in twist per unit length of an inner wire

ε_1 axial strain in the central tube ($\varepsilon_1=\varepsilon$)

ε_2 axial strain in an inner wire

β_2 rotational strain of an inner wire

φ_s angle of twist per unit length

and the outer (third) layer of the OPGW ;

$$R_3 = r_1 + 2r_2 + r_3 \tag{I.96}$$

$$\varepsilon_1 = \varepsilon_3 + \frac{\Delta\alpha_3}{\tan\alpha_3} \tag{I.97}$$

$$\beta_3 = R_3\varphi_s = \frac{\varepsilon_3}{\tan\alpha_3} - \Delta\alpha_3 + \nu\frac{(r_1\varepsilon_1 + 2r_2\varepsilon_2 + r_3\varepsilon_3)}{R_3\tan\alpha_3} \tag{I.98}$$

$$r_3\Delta\kappa'_3 = -\frac{2\sin\alpha_3\cos\alpha_3}{R_3/r_3}\Delta\alpha_3 + \nu\frac{(r_1\varepsilon_1 + 2r_2\varepsilon_2 + r_3\varepsilon_3)\cos^2\alpha_3}{R_3R_3/r_3} \tag{I.99}$$

$$r_3\Delta\varphi_3 = \frac{(1-2\sin^2\alpha_3)}{R_3/r_3}\Delta\alpha_3 + \nu\frac{(r_1\varepsilon_1 + 2r_2\varepsilon_2 + r_3\varepsilon_3)\sin\alpha_3\cos^2\alpha_3}{R_3R_3/r_3} \tag{I.100}$$

$$\frac{M_3}{Er_3^3} = \frac{\pi}{4}r_3\Delta\kappa'_3 \tag{I.101}$$

$$\frac{M_3^t}{Er_3^3} = \frac{\pi}{4(1+\nu)}r_3\Delta\varphi_3 \tag{I.102}$$

$$\frac{N'_3}{Er_3^2} = \frac{M_3^t}{Er_3^3}\frac{\cos^2\alpha_3}{R_3/r_3} - \frac{M_{b3}}{Er_3^3}\frac{\sin\alpha_3\cos\alpha_3}{R_3/r_3} \tag{I.103}$$

$$\frac{T_3}{Er_3^2} = \pi\varepsilon_3 \tag{I.104}$$

$$\frac{X_3}{Er_3} = \frac{N'_3}{Er_3^2}\frac{\sin\alpha_3\cos\alpha_3}{R_3/r_3} - \frac{T_3}{Er_3^2}\frac{\cos^2\alpha_3}{R_3/r_3} \tag{I.105}$$

$$\frac{F_3}{Er_3^2} = m_3\left[\frac{T_3}{Er_3^2}\sin\alpha_3 + \frac{N_3}{Er_3^2}\cos\alpha_3\right] \tag{I.106}$$

$$\frac{M_{t3}}{Er_3^3} = m_3\left[\frac{M_3^t}{Er_3^3}\sin\alpha_3 + \frac{M_3}{Er_3^3}\cos\alpha_3 + \frac{T_3}{Er_3^2}\frac{R_3}{r_3}\cos\alpha_3 - \frac{N_3'}{Er_3^2}\frac{R_3}{r_3}\sin\alpha_3\right] \quad (I.107)$$

$$r_2\sqrt{1+\frac{\tan^2(\pi/2-\pi/m_2)}{\sin^2\alpha_2}} = 4.637 < 4.675\ \text{mm} = r_1 + r_2 \quad (I.108)$$

$$r_3\sqrt{1+\frac{\tan^2(\pi/2-\pi/m_3)}{\sin^2\alpha_3}} = 7.7805 < 7.785\ \text{mm} = r_1 + 2r_2 + r_3 \quad (I.109)$$

$$\varepsilon_1 = \varepsilon = 0.61\%,\ \beta = 0 \quad (I.110)$$

$$0.0061 = \varepsilon_2 + \frac{\Delta\alpha_2}{9.03} \quad (I.111)$$

$$0 = \frac{\varepsilon_2}{9.03} - \Delta\alpha_2 + 0.33\frac{(0.55\times 0.0061 + 1.425\varepsilon_2)}{4.675\times 9.03} \quad (I.112)$$

$$0.0061 = \varepsilon_3 + \frac{\Delta\alpha_3}{-4.13} \quad (I.113)$$

$$0 = \frac{\varepsilon_3}{-4.13} - \Delta\alpha_3 + 0.33\frac{(0.55\times 0.0061 + 1.425\varepsilon_2 + 1.685\varepsilon_3)}{7.785\times -4.13} \quad (I.114)$$

$$\varepsilon_2 = 6.016\text{E-}3 \quad (I.115)$$

$$\Delta\alpha_2 = 7.597\text{E-}4 \quad (I.116)$$

$$\varepsilon_3 = 5.691\text{E-}3 \quad (I.117)$$

$$\Delta\alpha_3 = 1.687\text{E-}3 \quad (I.118)$$

$$r_2\Delta\kappa_2' = -\frac{2\times 0.994\times 0.110\times 7.6\text{E}-4}{3.28} + \frac{0.33(0.55\times 0.0061 + 1.425\times 6.0\text{E}-3)\times 0.0121}{3.28\times 1.425} = -47.57\mu \quad (I.119)$$

$$r_2\Delta\varphi_2 = \frac{(1-2\times 0.988)\times 7.6\text{E}-4}{3.28} + \frac{0.33\times(0.55\times 0.0061 + 1.425\times 6.016\text{E}-3)\times 0.109}{3.28\times 1.425} = -197.86\mu \quad (I.120)$$

$$r_3\Delta\kappa_3' = -\frac{2\times -0.972\times 0.235\times -1.687\text{E}-3}{4.620} + \frac{0.33(0.55\times 0.0061 + 2\times 1.425\times 6.016\text{E}-3 + 1.685\times 5.691\text{E}-3)\times 0.0554}{4.620\times 1.685} = -151.76\mu \quad (I.121)$$

$$r_3\Delta\varphi_3 = \frac{(1-2\times0.945)\times-1.687E-3}{4.620} + \frac{0.33(0.55\times0.0061+2\times1.425\times6.016E-3+1.685\times5.691E-3)\times-0.972\times0.0554}{4.620\times1.685} \quad \text{(I.122)}$$

$$= -261.55$$

$$\frac{M_2}{Er_2^3} = -37.4\mu \quad \text{(I.123)}$$

$$\frac{M_2^t}{Er_2^3} = -116.84\mu \quad \text{(I.124)}$$

$$\frac{N_2'}{Er_2^2} = 0.815\mu \quad \text{(I.125)}$$

$$\frac{T_2}{Er_2^2} = 0.019 \quad \text{(I.126)}$$

$$\frac{X_2}{Er_2} = -69.81\mu \quad \text{(I.127)}$$

$$\frac{F_2}{Er_2^2} = 0.188 \quad \text{(I.128)}$$

$$\frac{M_{2t}}{Er_2^3} = 0.067 \quad \text{(I.129)}$$

$$\frac{F_1}{(EA)_{Tube}} = 0.0061 \quad \text{(I.130)}$$

$$\frac{M_{Tube}^t}{(GJ)_{Tube}} = 0 \quad \text{(I.131)}$$

and for the outer wires (third layer),

$$\frac{M_3}{Er_3^3} = -119.2\mu \quad \text{(I.132)}$$

$$\frac{M_3^t}{Er_3^3} = -154.5\mu \quad \text{(I.133)}$$

$$\frac{N_3'}{Er_3^2} = 4.05\mu \quad \text{(I.134)}$$

$$\frac{T_3}{Er_3^2} = 0.0179 \quad \text{(I.135)}$$

$$\frac{X_3}{Er_3} = -214.16\mu \tag{I.136}$$

$$\frac{F_3}{Er_3^2} = 0.243 \tag{I.137}$$

$$\frac{M_{3t}}{Er_3^3} = 0.269 \tag{I.138}$$

$$F_{Al.spacer} + F_{Tube} + F_{Inner} + F_{Outer} = 3{,}956 + 3{,}876 + 10 \times 6{,}179 + 14 \times 3{,}148 = 106 \text{ kN} \tag{I.139}$$

$$M^t_{Tube} + M^t_{Inner} + M^t_{Outer} = 0 + 31{,}186 - 81{,}541 = -50 \text{ kN.mm} \tag{I.140}$$

The total bending moments acting on the inner and outer wires in the plane of the cable are:

$$M_{b2} = M_2 \sin\alpha'_2 + M^t_2 \cos\alpha'_2 = 17.35 \times 0.994 - 54.46 \times 0.109 = 11.30 \text{ N.mm} \tag{I.141}$$

$$M_{b3} = M_3 \sin\alpha'_3 + M^t_2 \cos\alpha'_3 = 36.05 \times 0.972 - 46.90 \times 0.234 = 24.09 \text{ N.mm}. \tag{I.142}$$

I.2.2 Stress determination of the OPGW

$$\sigma_{Tube} = (F / A)_{Tube} = 377 \text{ MPa} \tag{I.143}$$

$$\sigma^F_2 = \frac{T_2}{\pi r_2^2} = 974.61 \text{ MPa} \tag{I.144}$$

$$\sigma^F_3 = \frac{T_3}{\pi r_3^2} = 362.92 \text{ MPa} \tag{I.145}$$

$$\sigma^b_2 = \frac{4M_2}{\pi r_2^3} = \pm 7.64 \text{ MPa} \tag{I.146}$$

$$\sigma^b_3 = \frac{4M_3}{\pi r_3^3} = \pm 9.59 \text{ MPa} \tag{I.147}$$

$$\tau^h_2 = \frac{2M^t_2}{\pi r_2^3} = -11.98 \text{ MPa} \tag{I.148}$$

$$\tau^h_3 = \frac{2M^t_3}{\pi r_3^3} = -6.24 \text{ MPa} \tag{I.149}$$

As previously mentioned, to obtain the axial and shear stresses of the wires along the cable axis, the above stresses (normal and shear stresses along helix) are transformed along the cable axis where

$$\theta_2' = \frac{\pi}{2} - \alpha_2' = 90 - 83.72 = 6.28^\circ \tag{I.150}$$

and

$$\sigma_2^h = \sigma_2^F \pm \sigma_2^b = 974.61 \pm 7.64 = \begin{cases} 982.3 \\ 967.0 \end{cases} \text{MPa} \tag{I.151}$$

therefore,

$$\sigma_2 = \frac{\sigma_2^h}{2} + \frac{\sigma_2^h}{2}\cos 2\theta_2' + \tau_2^h \sin 2\theta_2' = \begin{cases} 968 \\ 953 \end{cases} \text{MPa} \tag{I.152}$$

and the corresponding shear stresses along the cable axis are

$$\tau_2 = -\frac{\sigma_2^h}{2}\sin 2\theta_2 + \tau_2^h \cos 2\theta_2 = \begin{cases} -118 \\ -117 \end{cases} \text{MPa.} \tag{I.153}$$

The corresponding maximum shear and principal stresses are calculated using the following formula

$$\tau_{2\max} = \sqrt{\left(\frac{\sigma_2^h}{2}\right)^2 + \left(\tau_2^h\right)^2} = \begin{cases} 491 \\ 483 \end{cases} \text{MPa} \tag{I.154}$$

$$\sigma_{2P1} = \frac{\sigma_2^h}{2} + \tau_{2\max} = \begin{cases} 982 \\ 967 \end{cases} \text{MPa.} \tag{I.155}$$

and same calculation for the outer wires (third layer) as

$$\theta_3' = \frac{\pi}{2} - \alpha_3' = 90 - 76.48 = 13.52^\circ \tag{I.156}$$

$$\sigma_3^h = \sigma_3^F \pm \sigma_3^b = 362.92 \pm 9.59 = \begin{cases} 372.6 \\ 353.4 \end{cases} \text{MPa} \tag{I.157}$$

$$\sigma_3 = \frac{\sigma_3^h}{2} + \frac{\sigma_3^h}{2}\cos 2\theta_3' + \tau_3^h \sin 2\theta_3' = \begin{cases} 349 \\ 331 \end{cases} \text{MPa.} \tag{I.158}$$

The corresponding shear stresses along the cable axis are

$$\tau_3 = -\frac{\sigma_3^h}{2}\sin 2\theta_3' + \tau_3^h \cos 2\theta_3' = \begin{cases} -90.2 \\ -85.9 \end{cases} \text{MPa.} \tag{I.159}$$

The corresponding maximum shear and principal stresses are calculated using the following formula

$$\tau_{3\max} = \sqrt{\left(\frac{\sigma_3^h}{2}\right)^2 + \left(\tau_3^h\right)^2} = \begin{cases} 186 \\ 177 \end{cases} \text{MPa} \tag{I.160}$$

and

$$\sigma_{3P1} = \frac{\sigma_3^h}{2} + \tau_{3\,max} = \begin{matrix}373\\353\end{matrix} \text{ MPa.} \tag{I.161}$$

I.2.3 Contact stresses

The approximate equations suggested by Costello (1997) to determine the resultant force per unit length X_2 is

$$X_c\sqrt{p_2^2 + (2\pi r_1)^2} = -X_2\sqrt{p_2^2 + \left[2\pi(r_1 + r_2)\right]^2} \tag{I.162}$$

where X_c is the contact force per unit length acting along the line of contact. The radius of curvature of the surface of the central tube at the point of contact is ρ_1, where

$$\rho_1 = \frac{r_1}{\sin^2\alpha_2} \tag{I.163}$$

and the maximum contact stress σ_c is given by

$$\sigma_c = -\frac{b}{\Omega} \tag{I.164}$$

where $$\Omega = -\frac{4(1-\nu^2)}{\left(\frac{1}{\rho_1} + \frac{1}{R_2}\right)E} \tag{I.165}$$

and $$b = \sqrt{\frac{2X_c\Omega}{\pi}}. \tag{I.166}$$

Considering the OPGW

$$X_2 = \text{-}6.98E - 5 \times 162{,}000 \times 1.425 = -22.97 \cong -23 \text{ N/mm} \tag{I.167}$$

$$X_c = 23\frac{\sqrt{(265.16)^2 + (2\pi \times 4.675)^2}}{\sqrt{(265.16)^2 + (2\pi \times 3.250)^2}} = 23.0 \text{ N/mm} \tag{I.168}$$

and $$\rho_1 = \frac{3.250}{0.988} = 3.29 \text{ mm.} \tag{I.169}$$

The maximum contact stress in the second layer (inner wires) σ_c is

$$\sigma_c = -\frac{214 \times 10^{-2}}{3.12 \times 10^{-5}} = -685 \text{ MPa} \tag{I.170}$$

and for the third layer (outer wires)

$$X_3 = \text{-2.14E - 4} \times 63{,}765 \times 1.685 = -23.01 \approx -23 \text{ N/mm} \tag{I.171}$$

$$X_c = 23\frac{\sqrt{(202)^2 + (2\pi \times 7.785)^2}}{\sqrt{(202)^2 + (2\pi \times 6.1)^2}} = 23.25 \text{ N/mm} \tag{I.172}$$

and $$\sigma_c = -\frac{3.32 \times 10^{-3}}{7.43 \times 10^{-5}} = -446 \text{ MPa.} \tag{I.173}$$

I.2.4 Unwinding motion is free ($\beta \neq 0$ and $M_{t2} = 0$)

As mentioned earlier, the analytical solution when the loading end is free is only demonstrated for the inner wires and the tube model. The total twisting moment acting on the strand is zero, i.e.,

$$M^t_{Tube} + M_{t2} = 0\,. \tag{I.174}$$

Using Equations (I.92), (I.94), and (I.174), the unwinding rotation is $\beta = 0.867$ radian, corresponding to 49.61°. The following results are obtained:

$$M^t_{Tube} = 6957.72 \text{ N.mm} \cong 6.96 \text{ kN.mm} \tag{I.175}$$

and the normal and bending stresses along the helix are

$$\sigma^F_2 = \frac{T_2}{\pi r_2^2} = 724.74 \text{ MPa} \tag{I.176}$$

$$\sigma^b_2 = \frac{4M_2}{\pi r_2^3} = \pm 157.78 \text{ MPa} \tag{I.177}$$

and the maximum and minimum normal and shear stresses are:

$$\sigma^h_2 = \sigma^F_2 \pm \sigma^b_2 = 724.74 \pm 157.78 = \begin{cases} 882.5 \\ 567.0 \end{cases} \text{ MPa} \tag{I.178}$$

$$\tau^h_2 = \frac{2M^t_2}{\pi r_2^3} = -284.74 \text{ MPa.} \tag{I.179}$$

To obtain the axial and shear stresses of the wires along the cable axis, the above stresses (normal and shear stresses along helix) are transformed as follows

$$\sigma_2 = \frac{\sigma_2^h}{2} + \frac{\sigma_2^h}{2}\cos 2\theta_2 + \tau_2^h \sin 2\theta_2 = \begin{Bmatrix} 821 \\ 508 \end{Bmatrix} \text{ MPa} \tag{I.180}$$

and the corresponding shear stresses along the cable axis are

$$\tau_2 = -\frac{\sigma_2^h}{2}\sin 2\theta_2 + \tau_2^h \cos 2\theta_2 = \begin{Bmatrix} -363 \\ -333 \end{Bmatrix} \text{ MPa.} \tag{I.181}$$

The corresponding maximum shear and principal stresses are calculated using the following formula

$$\tau_{2\max} = \sqrt{\left(\frac{\sigma_2^h}{2}\right)^2 + \left(\tau_2^h\right)^2} = \begin{Bmatrix} 525 \\ 402 \end{Bmatrix} \text{ MPa} \tag{I.182}$$

$$\sigma_{2P1} = \frac{\sigma_2^h}{2} + \tau_{2\max} = \begin{Bmatrix} 966 \\ 685 \end{Bmatrix} \text{ MPa.} \tag{I.183}$$

The total bending moment acting on the inner wires along the cable axis is,

$$M_{b2} = M_2 \sin\alpha_2' + M_2^t \cos\alpha_2' = 358.59 \times 0.996 - 1294.24 \times 0.094 = 235 \text{ N.mm} \tag{I.184}$$

and the total applied load on the inner wires and the tube to induce 0.61% elongation is

$$F_{Tube} + F_{Inner} = 3.88 + 10 \times 4.60 = 49.90 \cong 50 \text{ kN} \tag{I.185}$$

I.3 Summary of the results

The stresses that are given in the tables are transformed stresses along the cable axis. The stresses and forces using the analytical solutions of Machida and Durelli (1973) are summarized in the following tables.

Table I.1 Forces and moments using the solution of Machida and Durelli (unwinding rotation is restricted)

	Axial force (kN)	Bending (N.mm)	Torque (kN.mm)	Contact force (N/mm)
Outer wires	3.2	20.8	83	23
Inner wires	6.2	10.3	32	16

Table I.2 Stresses of the wires using the solution of Machida and Durelli (unwinding rotation is restricted)

	Normal stress (σ) (MPa)	Shear stress (τ) (MPa)	Principal stress (σ_{P1}) (MPa)	Maximum shear stress (τ_{max}) (MPa)
Outer wires	349-367	86-90	349-367	175-183
Inner wires	955-969	117-119	969-984	485-492

When the loading end is free, the wires unwind and the stress resultants are summarized below.

Table I.3 Stresses of the wires using the solution of Machida and Durelli (unwinding rotation is allowed)

	Normal stress (σ) (MPa)	Shear stress(τ) (MPa)	Principal stress (σ_{P1}) (MPa)	Maximum shear stress (τ_{max}) (MPa)	Unwinding rotation (Degree)
Inner wires	417-786	359-400	780-966	398-538	54.63

The stresses and forces in the inner and outer wires using the analytical solution by Costello (1997) are summarized in the following tables.

Table I.4 Forces and moments in the wires using the solution of Costello (unwinding rotation is restricted)

	Axial force (kN)	Bending (N.mm)	Torque (kN.mm)	Contact force (N)
Outer wires	3.2	24	82	23.25
Inner wires	6.2	11	31	23

Table I.5Normal and shear stresses using the solution of Costello (unwinding rotation is restricted)

	Normal stress (σ) (MPa)	Shear stress (τ) (MPa)	Principal stress (σ_{P1}) (MPa)	Maximum shear stress (τ_{max}) (MPa)
Outer wires	331-349	86-90	353-373	177-186
Inner wires	953-968	117-118	967-982	483-491

Table I.6Normal and shear stresses using the solution of Costello (unwinding rotation is allowed)

	Normal stress (σ) (MPa)	Shear stress(τ) (MPa)	Principal stress (σ_{P1}) (MPa)	Maximum shear stress (τ_{max}) (MPa)	Unwinding rotation (Degree)
Inner wires	379-821	333-363	685-966	402-525	49.61

APPENDIX II

II.1 Experiments at McGill University

In the finite element analysis, plastification of the central aluminum tube and the spacer is predicted for the displacement prescribed. Therefore, the linear Hookean material law is inadequate to predict their behavior. Consequently, uniaxial tension tests were performed on the aluminum tube and spacer separately to obtain their nonlinear material law. The stress-strain curve of each component is required as input in ADINA to define the material properties.

Uniaxial tension tests on aluminum tube segments were performed at McGill University (Jamieson Structures Laboratory) using a uniaxial tension machine (Instron) with ±1.5% error. The speed of loading was 0.02 in/min elongation. Ten specimens of about 10 inch long were tested for the aluminum spacer and the tube. Both the central aluminum tube and spacer are tested exactly as they are in the OPGW, i.e., a hollow tube, and a helically twisted spacer.

Out of the ten tests, 8 specimens failed at the center of the specimen where the extensiometer was installed. The other two were failed at the end gripped to the tension machine.

The properties (area and modulus of elasticity) of the tube and spacer are as follows:

Table II.1 Aluminum tube and spacer properties

	Aluminum tube	Aluminum spacer
Area (mm^2)	10.28	10.17
E (MPa)	61,803	63,765

The test results of the aluminum tube and spacer are plotted in Figure II.1 and II.2, respectively. The modulus of elasticity obtained from the experiments is slightly higher than the nominal modulus of elasticity provided by the manufacturer (62 GPa). In the OPGW model, the linear portion of the material law used in ADINA is based on the nominal modulus of elasticity and a multilinear plastic behavior is calculated using the experimental results. The black solid line in the Figure II.1 is the material law used in the OPGW model. The ultimate

strength obtained in the test (146 MPa) is smaller than that specified by the manufacturer (162 MPa).

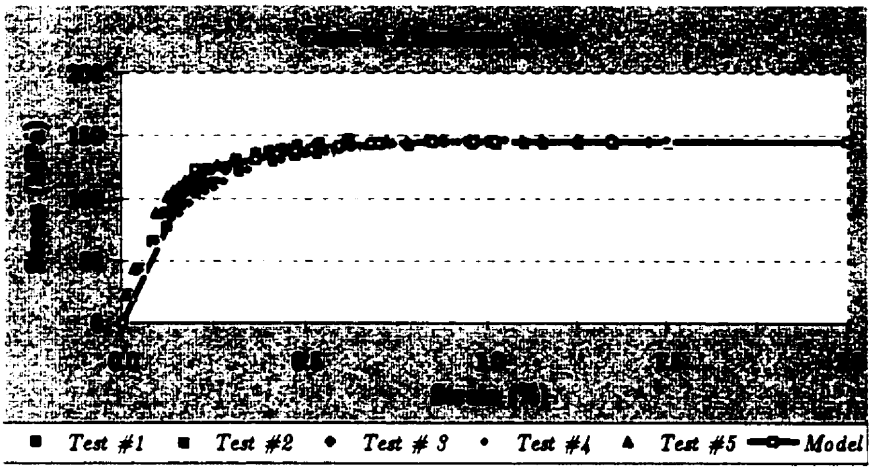

Figure II.1 Aluminum tube nonlinear material law (stress-strain curve)

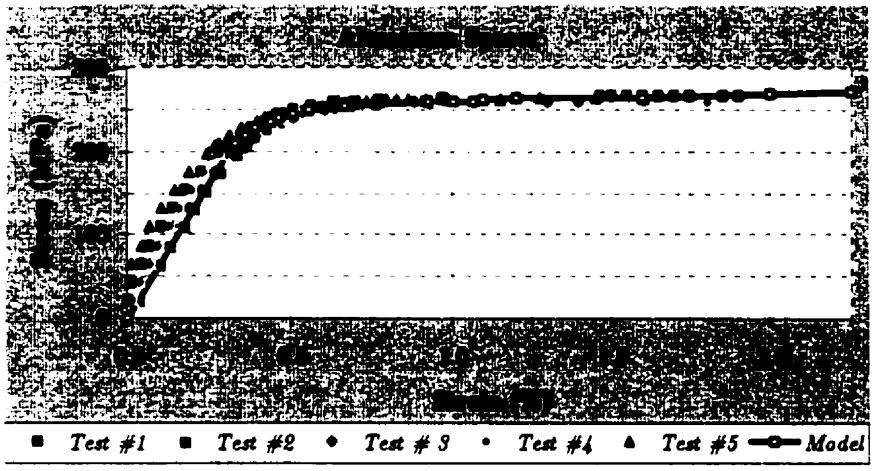

Figure II.2 Aluminum spacer nonlinear material law (stress-strain curve)

The aluminum spacer response is similar to that of the central tube. The actual modulus of elasticity is also larger than that of the experiments. Therefore, like the tube, a linear stress-strain behavior based on the nominal modulus of elasticity is used in the model up to the yielding point of the aluminum spacer, and for the plastic part, a multilinear plastic material law is obtained using the average of the experimental results. The black solid line in Figure II.2 is the stress-strain curve used in the OPGW model in ADINA. The ultimate strength of

the aluminum spacer (272 MPa) is slightly smaller than that specified the manufacturer (280 MPa).

II.2 IREQ Experiments

Institut de recherche d'Hydro-Québec (IREQ) has performed a 96-hour traction test on the 19 mm OPGW at maximum tension in normal operation (MTNO), i.e., 83.5 kN. The specimen was fabricated out of 60 m of OPGW. The cable length subjected to tension was 27.5 m. Dead-end assemblies at each end were prevented from twisting during the test. The reference length was 15 m after calibration and positioning of the displacement transducers. The cable was loaded to a 5 kN tension where all initial optical and physical measurements of the sample were taken. Then, the position of the rods and wedges were marked to evaluate the relative movement of one to the other, which followed by pulling at a rate of 5% MTNO (Maximum Tension in Normal Operation) per minute (3.73 kN/min). Figure II.3 schematically shows the experimental set-up at IREQ (IREQ 1994).

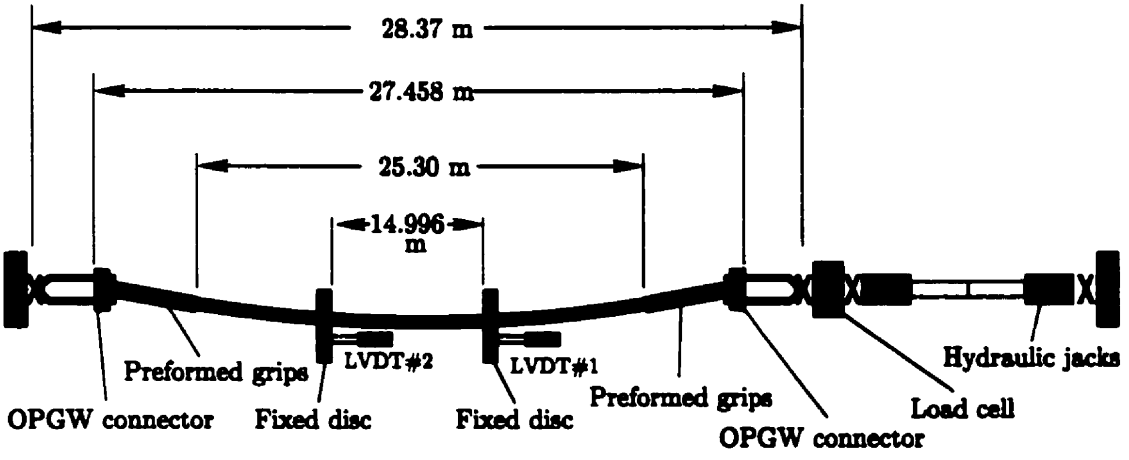

Figure II.3 Schematic IREQ experimental set-up

Two optical fiber groups of six and eight fibers were used in the experiments. The cable and optical fibers elongation (group of 8 fibers) versus the applied tension has been obtained and is plotted in Figure II.4. The elongation of the cable at the initial value of 5 kN was estimated at 0.028%. The total elongation of the cable reached 0.61%, where creep during 96 hours was 0.09% and permanent deformation was measured as 0.12%.

The elongation of the group of 6 and 8 optical fibers was evaluated at 0.52% and 0.48%. The elongation begins at the starting load of 5 kN and 15 kN for the 6 and 8 fiber group, respectively. The fiber elongation for the 19 mm OPGW was 0.48% and 0.52% for the 8 and 6 fiber groups, respectively. The fiber elongation of the 6 fiber group has exceeded the design requirement (0.5%). It is concluded that the difference between the two groups implies that the group blocking mechanism (loops at both ends) can act differently even on the same cable.

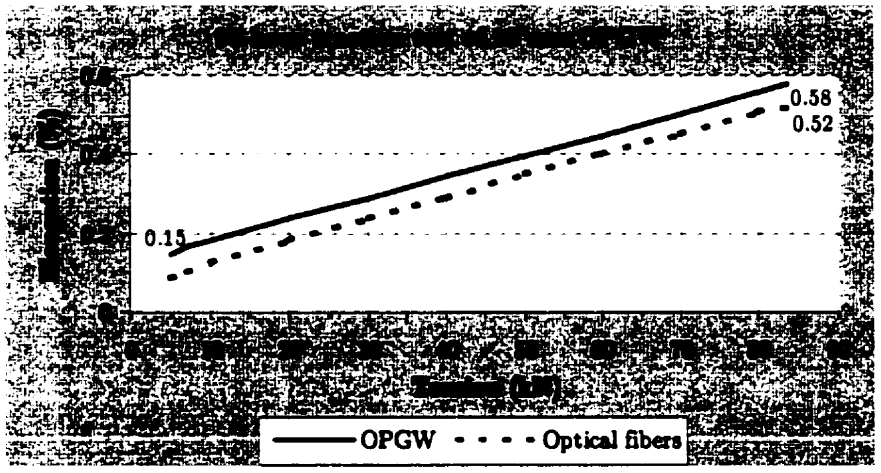

Figure II.4 Cable and optical fibers elongation versus tension

The maximum measured attenuations were 0.21 and 0.18 dB/km on the 8 and 6 fiber units, respectively. Meanwhile, permanent attenuations of 0.1 and 0.11 dB/km were measured for the 8 and 6 fiber groups, respectively. Permissible long-term attenuation is stated to be 0.0 dB/km. Although the permanent attenuation obtained is small, however the "zero" criterion is not met.

The smaller elongation of the fibers with respect to that of the cable is due to the excess length of the fibers (0.018%). The experiments indicate an overall linear load-displacement behavior for the cable and the fibers. The experiments were incapable of evaluating the behavior of the individual cable components, which are the inner and the outer wires, the central tube and the aluminum spacer. It is not evident if any of these components reaches their yielding point. However, the overall behavior of the cable seems to be in the linear range.

As it is reported, the permanent deformation of the cable is 0.12%; This plastic deformation is about 20% of the total elongation.